# Sampling and demodulation of RF signals modulated by multi-GBits/s data streams.

Róbert Horváth

## To cite this version:

Róbert Horváth. Sampling and demodulation of RF signals modulated by multi-GBits/s data streams.. Optics / Photonic. Université Grenoble Alpes, 2019. English. NNT : 2019GREAT130 . tel-03633523

HAL Id: tel-03633523
https://theses.hal.science/tel-03633523
Submitted on 7 Apr 2022

Communauté
UNIVERSITÉ Grenoble Alpes

# THÈSE

Pour obtenir le grade de

**DOCTEUR DE LA**
**COMMUNAUTE UNIVERSITÉ GRENOBLE ALPES**

Spécialité : **Optique et Radiofréquences**

Arrêté ministériel : 25 mai 2016

Présentée par

**Róbert HORVÁTH**

Thèse dirigée par **Jean-François ROUX**
et codirigée par **Béatrice CABON**

préparée au sein du **Laboratoire Institut de Microélectronique, Electromagnétisme et Photonique – Laboratoire d'hyperfréquences et de caractérisation**
dans **l'École Doctorale Electronique, Electrotechnique, Automatique, Traitement du Signal (EEATS)**

# Echantillonnage et démodulation de signaux RF modulés à très haut débit

# Sampling and demodulation of RF signals modulated by multi-Gbit/s data streams

Thèse soutenue publiquement le **14 juin 2019**,
devant le jury composé de :

**Pr Jean-Emmanuel BROQUIN**
Professeur des Universités, Grenoble INP, Président du jury
**Dr Anne-Laure BILLABERT**
Maître de Conférences, CNAM, Paris, Rapporteur
**Pr Guillaume DUCOURNAU**
Professeur des Universités, Université Lille 1, Rapporteur
**Pr Cyril RENAUD**
Professeur des Universités, University College London, Examinateur
**Dr Frédéric VAN DIJK**
Ingénieur de Recherche, 3-5 Labs, Palaiseau, Examinateur
**Dr Jean-François ROUX**
Maître de Conférences, Université Savoie Mont Blanc, Chambéry,
Directeur de thèse

**Pr Béatrice CABON**
Professeur Émérite, Grenoble INP, Co-directeur de thèse, Invitée
**Dr Julien POËTTE**
Maître de Conférences, Grenoble INP, Invité

# Résume

Les technologies de la fibre optique, de la photonique et des radiofréquences seront au cœur des réseaux de communication de la prochaine génération, tandis que les fréquences porteuses des signaux haut débit se déplaceront dans la gamme des ondes millimétriques (30 GHz - 300 GHz). Avec l'utilisation de fréquences porteuses élevées, ces systèmes de transmission nécessitent toujours la détection et la conversion basse de fréquence des signaux vers la bande de base pour le traitement du signal.

Dans cette thèse, nous proposons un système mélangeur optoélectronique hétérodyne, basé sur un dispositif original, un photo-mélangeur intégré, pour le traitement optique de données transmises dans une liaison de télécommunication en ondes millimétriques. Le dispositif proposé est une solution envisageable pour les mélangeurs situés du côté récepteur d’une liaison sans fil de réseau radio sur fibre. Le système fonctionne dans la plage de longueurs d'onde de 1,5 µm et tire parti des propriétés ultra-rapides d'un commutateur photoconducteur en InGaAs, associé à un laser à verrouillage de mode semi-conducteur.

La caractérisation du photo-commutateur a montré une durée de vie ultra-courte des photo-porteurs de 1,2 ps, ce qui garantit la bande passante élevée et la capacité à fonctionner en ondes millimétriques du dispositif. Les caractérisations du système ont permis d'obtenir une réponse relativement uniforme dans les domaines électrique et optique jusqu'à 164 GHz. Nous avons démontré les performances du système mélangeur optoélectronique par la conversion basse de fréquence et la démodulation d'un flux de données modulé QPSK à 2 Gbit/s.

Les commutateurs photo ultra-rapides sont également des candidats potentiels en tant qu'échantillonneurs optique dans les convertisseurs analogique-numérique.

Enfin, une analyse est présentée pour montrer le potentiel de commutation du photoconducteur InGaAs dans de tels dispositifs.

# Abstract

Fiber optics, photonic and RF technologies will be at the core of next generation communication networks, while the carrier frequencies are moving into the millimetre wave range (30 GHz – 300 GHz). Despite the use of high carrier frequencies, these transmission systems still require the detection and downconversion of modulated data-streams into the baseband for signal processing.

In this thesis we are proposing an optoelectronic heterodyne mixer system, based on a single device, for photonic assisted processing of data transmitted in a millimetre wave telecommunication link. The proposed scheme is a feasible solution for mixers at the receiver side of a Radio-over-Fibre network wireless link. The system is working in the 1.5 µm wavelength range and taking advantage of the ultrafast properties of an InGaAs photoconductive switch, in combination with a semiconductor mode-locked laser.

The characterization of the switch showed an ultrashort photocarrier lifetime of 1.2 ps, which ensures its high bandwidth and ability to work in the millimetre wave range. System characterisations obtained a relatively flat response both in the electrical and optical domains up to 164 GHz. We demonstrate the optoelectronic mixer system performance through the downconversion and demodulation of a 2 Gbit/s QPSK modulated data-stream.

Ultrafast photoswitches are also potential candidates as samplers in Analog-to-Digital Converters. Finally, an experimental study is given to show the InGaAs photoswitch potential in such devices.

# Acknowledgments

I would like to express my gratitude to my supervisors: to Jean-François Roux, for the numerous discussions, advices and help in the experiments, and to Béatrice Cabon for the discussions, advices and for pushing me to better organize my writings. Without their guidance and support during the 3 years of my PhD, this thesis wouldn't have been possible. I owe a special thanks to Julien Poëtte too, for helping me in the numerous experiments and for the many advices during the work.

I also would like to acknowledge the funding of this thesis project, which was part of the FiWiN5G Marie-Curie ITN Project (grant agreement No. 642355) funded by the European Union's Horizon 2020 research and innovation programme.

I'd like to thank the jury members, Jean-Emmanuel Broquin for being the president of the jury, Anne-Laure Billabert and Guillaume Ducournau for reviewing the manuscript, Cyril Renaud and Frédéric van Dijk for being the examiners. Thank you for accepting to be part of the jury and for your insightful comments and questions.

During the PhD, I've been working at both sites of IMEP-LAHC, taking advantages of the equipment and expertise of both. I thank all the people of the Le-Bourget-du-Lac site, all the permanents and also the PhDs, postdoc for the support and help. From the Grenoble site, first I'd like to thank the help of Nicolas Corrao, who was always available if I needed help in the experimental rooms. My gratitude is also for the administrative personnel for their kindness and help with the necessary paperwork: Valérie, Isabelle, Fabienne, Brigitte and Dalhila.

There are many people from the lab, who made the past 3 years unforgettable. I thank the company and all the nice moments of Mohamad, Aggeliki and a special thanks to Nisrine for all the discussions, tea and dinners, and company in Grenoble and during the travels. Thanks also to everyone else from the lab, officemates, the lunch group, from Chambéry or from squash evenings: Ali, Mederic, Licinius, Gizem, Bastien, Ugur, Miltiadis, Petros, Guiseppe, Dimitrios, Romain, Thibauld…

Thanks to the Fiwin5g project, I had the chance to spend 3 months at University College London with the Photonics Group. I thank the help and supervision of Cyril Renaud and I also thank Kasia Balakier and Haymen Shams for all the help and scientific discussions. Thanks to Luis, Ahmad and especially to Marc for making my time in London remarkable, I really enjoyed those months. And by being part of the project, I also got to know some great people involved in it, I hope we will meet again: Nisrine, Marc, Andrzej, Ahmad, Igor, Maria, Mu-Chieh, Hum and Mehmet…

My sincerest gratitude is for my family, for their love and support all along, and driving all the way to Grenoble for the defense.

I've met and became friends with many kind and generous people during the past years, and it is hard to acknowledge everyone who made it unforgettable. I'd like to thank all of my friends, who I didn't mention above, for the times during skiing, hiking and every moment in and around Grenoble.

# Table of contents

Résume ........ 1

Abstract ........ 3

Table of contents ........ 7

List of abbreviations ........ 10

General Introduction ........ 12

Chapter I Photoconductive switches and its applications ........ 14

I/1. Photoconductive devices ........ 15

  I/1.1. Photoswitch dynamics ........ 16

  I/1.2. Photoconductors for THz generation ........ 21

I/2. Photoswitch evolution ........ 22

  I/2.1. GaAs devices ........ 22

  I/2.2. $In_xGa_{x-1}As$ devices ........ 23

  I/2.3. Techniques to improve the quantum efficiency ........ 24

I/3. Photoswitch as a frequency mixer ........ 27

  I/3.1. Fundamentals of mixing ........ 28

  I/3.2. Mixing properties ........ 29

  I/3.3. Mixing with pulsed LO ........ 30

    I/3.3.a Undersampling ........ 31

  I/3.4. Electronic mixers ........ 34

  I/3.5. Photonic aided mixers ........ 34

    I/3.5.a Photonic mixers ........ 36

    I/3.5.b Optoelectronic mixers ........ 36

I/4. Photoswitch as a sampler ........ 38

  I/4.1. Sampling fundamentals ........ 39

  I/4.2. Analog-to-Digital converter challenges ........ 41

  I/4.3. Photonic Analog-to-Digital Converter types ........ 42

I/5. Mode-locked lasers ........ 44

I/6. Outline and Goals of the Thesis ........ 46

Chapter II InGaAs photoconductive switch ........ 48

II/1. The photoswitch samples ........ 49

  II/1.1. Switch fabrication ........ 51

  II/1.2. Characterisation setup ........ 52

II/2. Electrical Characterization ........ 53

  II/2.1. Coplanar waveguide simulation ........ 53

  II/2.2. Photoswitch RF response in the dark state ........ 55

II/2.3. Dark resistance in DC ........ 56
II/2.4. Photoswitch equivalent circuit model ........ 57
II/2.5. Improving the equivalent circuit model ........ 58
II/2.6. U-I characterization ........ 60
II/3. Optoelectronic characterization ........ 61
II/3.1. Measurement setup ........ 61
II/3.2. Dispersion of laser pulses ........ 62
II/3.3. Photoswitch response with sampling oscilloscope ........ 64
II/3.4. Measurement with opto-electronic autocorrelation ........ 66
II/3.4.a Simulation of the autocorrelation curve ........ 66
II/3.4.b Measurement setup ........ 67
II/3.4.c Typical measurement result ........ 69
II/3.4.d Measurement corrections ........ 70
II/3.4.e Curve fitting ........ 72
II/4. Conclusions on Chapter II ........ 74
Chapter III Semiconductor mode-locked laser stabilization ........ 76
III/1. Semiconductor mode-locked laser ........ 77
III/1.1. MLL samples used in this work ........ 77
III/1.2. Laser setup ........ 78
III/1.3. Laser optical properties ........ 79
III/1.4. Optical pulse characterization ........ 81
III/1.5. MLL heterodyning on a photodiode ........ 84
III/1.6. Phase noise of the electrical beating signal ........ 86
III/1.7. Origins of phase noise ........ 88
III/2. MLL stabilization ........ 89
III/2.1. External direct modulation ........ 90
III/2.2. All optical feedback – single loop setup ........ 91
III/2.2.a Principles of stabilization ........ 91
III/2.2.b Stabilization setup ........ 92
III/2.2.c Stabilization results ........ 94
III/2.3. All optical feedback – dual loop setup ........ 97
III/3. Stabilization summary ........ 100
III/4. Conclusions on Chapter III ........ 101
Chapter IV Photoswitch as an optoelectronic mixer ........ 102
IV/1. Heterodyne mixer of narrowband signals ........ 103
IV/1.1. Setup design ........ 103
IV/1.2. Conversion loss ........ 105
IV/1.2.a Discussion about the high conversion losses ........ 107

IV/1.2.b Simulation of the conversion loss ........................................ 109

IV/1.3. Heterodyning of two DFB lasers ........................................ 109

IV/1.3.a Conversion loss ........................................ 111

IV/1.3.b Simulation of the conversion loss ........................................ 112

IV/1.3.c System characterization ........................................ 112

IV/1.3.d Heterodyne detection results ........................................ 114

IV/2. Optoelectronic mixer for data-stream downconversion ........................................ 115

IV/2.1. QPSK modulation format for the data-stream ........................................ 116

IV/2.2. Data-stream demodulation – EVM and BER ........................................ 117

IV/2.3. Optically provided local oscillator - MLL ........................................ 119

IV/2.4. Optically provided local oscillator – DFB laser ........................................ 124

IV/2.5. Electrically provided local oscillator ........................................ 126

IV/3. Study of switch non-linearities ........................................ 129

IV/4. Applications of the optoelectronic mixer schemes ........................................ 132

IV/5. Conclusions of Chapter IV ........................................ 135

General conclusions ........................................ 137

References ........................................ 140

Publications ........................................ 150

APPENDIX ........................................ 151

APPENDIX A : Numerical model of the photoswitch ........................................ 151

APPENDIX B : Chromatic dispersion in optical fibres ........................................ 159

APPENDIX C : Chromatic dispersion measurement and compensation ........................................ 161

# List of abbreviations

| | |
|---|---|
| ADC | Analog to digital converter |
| APC | Angled Physical Contact |
| ASE | Amplified spontaneous emission |
| ASK | Amplitude shift keying |
| AWG | Arbitrary Waveform Generator |
| AWGN | Additive white gaussian noise |
| B2B | Back-to-back |
| BER | Bit Error Rate |
| BS | Base station |
| CL | Conversion loss |
| CPW | Coplanar Waveguide |
| CS | Central station |
| CW | Continuous wave |
| DCF | Dispersion compensating fibre |
| DFB | Distributed Feedback |
| DSO | Digital Sampling oscilloscope |
| ENOB | Effective number of bits |
| ESA | Electrical Spectrum Analyser |
| EVM | Error Vector Magnitude |
| FEC | Forward Error Correction |
| FFT | Fast-Fourier Transform |
| FP | Fabry-Pérot |
| FSK | Frequency shift keying |
| FSR | Free spectral range |
| FWHM | Full-width at half maximum |
| GaAs | Gallium arsenide |
| IEMN | Institut d'électronique de microélectronique et de nanotechnologie |
| IF | Intermediate frequency |
| IMEP-LAHC | L'Institut de Microélectronique Electromagnétisme et Photonique et le LAboratoire d'Hyperfréquences et de Caractérisation |
| InGaAs | Indium gallium arsenide |
| InP | Indium phosphide |
| LIA | Lock-In Amplifier |
| LNA | Low noise amplifier |

| | |
|---|---|
| LO | Local oscillator |
| LT-GaAs | Low-temperature grown GaAs |
| MLL | Mode-locked laser |
| mmW | Millimetre wave |
| MZM | Mach-Zehnder modulator |
| PC | polarization controller |
| PCA | Photoconductive antenna |
| PD | Photodiode |
| PIC | Photonic integrated circuit |
| PMT | photomultiplier tube |
| PN | Phase noise |
| PRBS | Pseudo random binary sequence |
| PSK | Phase shift keying |
| QAM | Quadrature Amplitude modulation |
| QPSK | Quadrature Phase shift keying |
| RF | Radiofrequency |
| RMS | Root-mean square |
| RoF | Radio over Fibre |
| SFDR | Spurious free dynamic range |
| SINAD | Signal to noise and distortion ratio |
| SMF | Single mode fibre |
| SNR | Signal to noise ratio |
| SSB-PN | Single side band phase noise |
| TDS | Time domain spectroscopy |
| UCL | University College London |
| UTC-PD | Uni-travelling carrier photodiode |
| VOA | Variable Optical Attenuator |
| VOD | Variable Optical Delay |

# General Introduction

The photoconductive effect was first discovered by accident in the late 19th century by an English engineer, Willoughby Smith (1828 - 1891). However, the understanding of the physics behind the effect came just around 50 years later between the two world wars following the works of the German physicist Robert Wichard Pohl. Today it is well known, that photoconductivity is a quantum effect where the absorption of photons is generating electron-hole pairs in the material, which leads to an increase in conductivity. All materials are photoconductive in principle, however in semiconductors the generated photocurrent is significantly higher and can be exploited.

Nowadays, the main application of photoconductivity is in photodiodes and phototransistors, among other types of photoconductive devices. The effect can also be used for measuring light intensity with photoresistors. Another important use of photoconductivity is utilizing the voltage difference across a p-n junction. The photon absorption in this junction results in a photovoltaic current flow across a load resistor, in this case we talk about the photovoltaic effect. This effect is mainly used in photovoltaic electricity generation in solar cells.

The focus of this thesis is on a photoconductive semiconductor used as an opto-electronic device, where we are exploiting the interaction of the optical field illuminating the semiconductor, and the applied electric field across the illuminated material. Photoconductive semiconductors are used for switching since the first demonstration of Auston in 1975. It is based on the conductivity change under laser illumination, the optical pulses are turning ON and OFF the switch. These devices are also used as a photomixer to generate free-space terahertz (THz) radiation, thanks to their possible short carrier lifetime in the picosecond range. The THz range is defined between 300 GHz and 3 THz, and the sub-THz range term is commonly used in the literature for frequencies between 100 GHz and 1 THz. These frequencies are commonly used for imaging and spectroscopy applications. In our work we are using the photoconductive switch for applications in the microwave (300 MHz – 300 GHz) range, which corresponds to wavelengths between 1 meter and 1 millimetre. Inside this range, defined as millimetre waves (mmW) between 30 GHz and 300 GHz, is a popular research area nowadays for telecommunication and radar applications. Their popularity lies in the wide unregulated spectrum in this frequency range which allows higher achievable bandwidths.

The most widely used material for semiconductor devices is Gallium arsenide (GaAs), mostly because of their good performances and sensitivity to 800 nm wavelength light, produced by the popular titanium-sapphire lasers at that time of early researches in the ‘70s and ‘80s. In the past two decades the interest grew toward materials sensitive to 1550 nm wavelength light, which wavelengths are used in telecommunication systems. The development of fibre lasers and semiconductor laser sources also fuelled these researches. A compound material of indium gallium arsenide (InGaAs) proved to be an efficient absorber of wavelength in the 1.5 µm range.

In our work, we are presenting a photoswitch compatible with the telecom wavelengths, made of InGaAs. The aim is to demonstrate the switch performance for opto-electronic mixing applications, like the use as a hybrid mixer for heterodyne detection in a Radio over Fibre (RoF) system, which is a promising application for such devices. This project is part of the European Union funded FiWin5G ITN project, which aims to study and develop solutions for the next generation of telecommunication networks. Another possible use of the photoswitch is as an optoelectronic sampler for Analog-to-digital conversion. In the first chapter we review the necessary background for these applications and corresponding state-of-the-art devices. One of the most important property of a photoconductive device is its carrier lifetime, for fast and high frequency operation it has to be in the picosecond or even in the sub-picosecond range. The lifetime measurement is one of the key characterizations in the second chapter, where we are also characterizing our photoconductive switch samples in the electronic and opto-electronic domain. To fully take advantage of the ultrafast capabilities of the switch, it has to be operated with picosecond optical pulses with a high repetition rate in the GHz range. For this reason, in Chapter III we are characterizing a semiconductor mode-locked laser (MLL) providing pulses with 24.55 GHz repetition rate and picosecond pulsewidths. The laser stability is analysed, and a stabilization setup is built to improve the timing jitter of the laser output pulse train.

Mixing applications with the photoswitch and the MLL source are demonstrated in Chapter IV, and results are compared using different local oscillator sources. We evaluate the mixing performance with the downconversion and demodulation of wideband QPSK modulated signals, which was not done before with photoconductive switches. Analog to digital conversion is also benefiting from the low jitter laser source, the stable high frequency provided by the laser can overcome the limitations of electronic oscillators and increase the ADC resolution. First assessment of the photoswitch non-linear characteristics, which are important to be low for ADC application, was performed and is presented at the end of the last chapter.

# Chapter I

# Photoconductive switches and its applications

I/1. Photoconductive devices ........ 15
  I/1.1. Photoswitch dynamics ........ 16
  I/1.2. Photoconductors for THz generation ........ 21
I/2. Photoswitch evolution ........ 22
  I/2.1. GaAs devices ........ 22
  I/2.2. $In_xGa_{x-1}As$ devices ........ 23
  I/2.3. Techniques to improve the quantum efficiency ........ 24
I/3. Photoswitch as a frequency mixer ........ 27
  I/3.1. Fundamentals of mixing ........ 28
  I/3.2. Mixing properties ........ 29
  I/3.3. Mixing with pulsed LO ........ 30
    I/3.3.a Undersampling ........ 31
  I/3.4. Electronic mixers ........ 34
  I/3.5. Photonic aided mixers ........ 34
    I/3.5.a Photonic mixers ........ 36
    I/3.5.b Optoelectronic mixers ........ 36
I/4. Photoswitch as a sampler ........ 38
  I/4.1. Sampling fundamentals ........ 39
  I/4.2. Analog-to-Digital converter challenges ........ 41
  I/4.3. Photonic Analog-to-Digital Converter types ........ 42
I/5. Mode-locked lasers ........ 44
I/6. Outline and Goals of the Thesis ........ 46

The central element of this thesis is an InGaAs photoconductive switch. In this first chapter, an introduction is given of the fundamentals of photoconductive switches along with the state-of-the-art devices. The applications are also introduced with competing technologies.

## I/1. Photoconductive devices

Photoconductive materials are generating free charge carriers (electron-hole pairs) by the absorption of photons. The energy of the photons has to be around the band-gap energy of the material 0 for efficient absorption. Absorbing one photon with enough energy is exciting an electron from the valence band to the conduction band, where it can move, while a hole remains in the valence band. The presence of the generated free carriers is changing the conductivity of the material which can be exploited for various applications.

The photoconductive switch (or photoswitch) is an opto-electronic photoconductive device which allows the detection of optical signals, while changing the properties of an electrical transmission line. It is composed of a coplanar waveguide interrupted with a gap (a discontinuity) made of photoconductive material. The first photoconductive switch concept was described by Auston in 1975 [2]. A simple illustration of a photoconductive device cross section is shown in Figure 1-1 and a top view is shown in Figure 1-3. Two electrodes are surrounding a gap of semiconductor material and an electrical potential between the electrodes (bias) is building up an electric field. When the gap is illuminated free carriers are generated. These electrons and holes are accelerated along the electric field and recombined after a short time. In the close proximity of the electrodes the electrons will be collected by them before recombination, this results in a generated photocurrent. The increasing carrier concentration during illumination means an increase of the conductivity (which is a decrease of the resistivity). The conductivity $\sigma$ is proportional to the carrier concentrations times their mobility (Eq. (1)).

$$\sigma = q(N\mu_n + P\mu_p) \tag{1}$$

Where $q$ is a single electron charge, $N$ and $P$ are the concentration of electrons and holes respectively, $\mu_n$ and $\mu_p$ are their mobility. These mobilities are one of the important properties of a photoconductor.

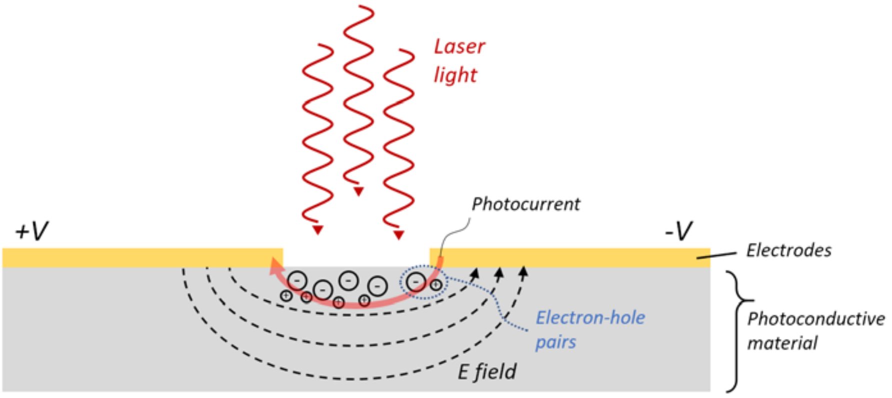

*Figure 1-1 Schematic of a photoconductive device.*

When the illumination is turned off, the current flow will disappear as the carrier generation stops and all the free charges are recombining with the holes. The time of recombination is called the carrier lifetime.

In the work Auston [2], the used silicon (Si) material has a long carrier lifetime, to overcome this Auston developed a push-pull method to increase the switch response speed. A first laser pulse illuminates the gap with 530 nm wavelength light and generates carriers on the top of the Si and setting the switch to ON state. A second delayed pulse illuminating with 1060 nm wavelength generates carriers in the full thickness of the silicon, creating a short circuit between the electrodes and the ground, thus, eliminating the dependence on recombination for the setting of the OFF state. However, the ON state still depends on the carrier lifetime. Figure 1-2 is showing an illustration of the method.

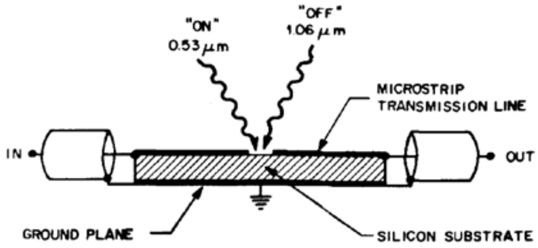

*Figure 1-2*
*Photoconductive switch design by Auston. Source:* D. H. Auston, Appl. Phy. Lett. Vol. 26, No 3, 1975 [2]

The time of recombination is another important property of the material and can be decreased with several techniques. By introducing defects or traps as recombination centres in the semiconductor, we can accelerate the recombination process, thus decrease the carrier lifetime. For ultrafast applications, the lifetime has to be in the order of picoseconds, state-of-the-art devices are having carrier lifetimes of 0.2-0.3 ps [1]. Other material properties of photoconductors, the dark resistance and breakdown voltage are to be considered for ultrafast applications. Controlling all these parameters at the same time in the material is challenging and requires compromises during fabrication. The different materials and their manipulation during fabrication to obtain superior performances are detailed in Section I/2.

### I/1.1. Photoswitch dynamics

The current and resistance change of photoconductors under illumination can be derived from the continuity equations for electrons and holes, defined with equations (2) and (3). These basic semiconductor equations are describing the static and dynamic behaviour of carriers in a semiconductor under external influences, like an optical excitation, they are thoroughly described in [3] and [4]. They can be directly formed using the classical first Maxwell equation of Ampere's law, completed with Maxwell's addition of the displacement term. We define the illuminated area of the photoconductor with a width $W$ and length $L$ as it is shown in Figure 1-3. The photon penetration depth in the semiconductor material is defined as $1/\alpha$, where $\alpha$ is the absorption coefficient. We assume that one absorbed photon is generating one electron, and that all the photons are absorbed in the volume of $V = W*L*1/\alpha$. Similarly to Eq. (1), $N$ and $P$ are denoting the electrons and holes respectively, in all the following equations. Equations (2) and (3) are showing that the change of carrier concentration is the difference of generation, recombination and trapping, and the net current flow in and out of the volume under investigation.

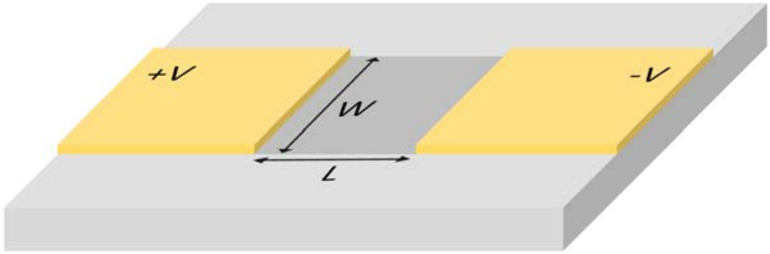

*Figure 1-3 Illustration of the photoconductive gap with its dimensions. Usually, these dimensions are in the micrometre range*

$$\frac{\partial N(\mathbf{r},t)}{\partial t} = G(\mathbf{r},t) - \frac{N(\mathbf{r},t)}{\tau_N} + \frac{1}{q}div(\vec{J}_N) - B_N[N(\mathbf{r},t)P(\mathbf{r},t) - N_i^2] \tag{2}$$

$$\frac{\partial P(\mathbf{r},t)}{\partial t} = G(\mathbf{r},t) - \frac{P(\mathbf{r},t)}{\tau_P} - \frac{1}{q}div(\vec{J}_P) - B_P[N(\mathbf{r},t)P(\mathbf{r},t) - N_i^2] \tag{3}$$

Where *G(***r***,t)* is the electron-hole pair photogeneration rate in cm$^{-3}$/s. In the second terms $\tau_N$ and $\tau_P$ are the lifetime of electrons and holes respectively and *N(***r***,t)* and *P(***r***,t)* are the electron and hole concentrations, measured in cm$^{-3}$. These second elements of the equations are representing the trapping rate of electrons and holes by the defects in the semiconductor. The electron and hole current densities are defined with $J_N$ and $J_P$ in A/cm, while $q$ is the electron charge. $B_N$ and $B_P$ are the recombination rate of electrons and holes with the intrinsic carriers of $N_i$.

The defects are introduced for example with doping or ion-implantation, and they are creating an EL-2 electron trapping level in the bandgap of the semiconductor. This trapping level is causing the free electrons in the conduction band not to recombine with the holes in the valence band, instead, they get trapped by the partly ionized donor atoms with a characteristic time of $\tau_N$. These trapped electrons after the characteristic time of $\tau_P$ are recombining with the holes in the valence band. This non-radiative process is much faster than the direct recombination of electron and holes and allows to construct ultrafast photoconductors by introducing defects in the material. The $\tau_N$ and $\tau_P$ characteristic times can be described with the Shockley-Reed-Hall model [5], see eq. (4).

$$\tau_P = \frac{1}{\sigma_P v_{th,P}[N_T^+]} \qquad \tau_P = \frac{1}{\sigma_N v_{th,N}[N_T^0]} \tag{4) a,b (}$$

Where $\sigma_P$ and $\sigma_N$ are the electron and hole capture cross sections, $v_{th,P}$ and $v_{th,N}$ are the electron and hole average thermal velocities. $N_T^+$ is the electron trap concentration, and $N_T^0$ is the hole trap concentration, introduced by the material defects.

The current densities can be defined with equation (5) for electrons and for holes with equation (6), they consist of a drift component caused by an electric field and a diffusion component caused by the carrier-concentration gradient [4]. They are derived from the Boltzmann transport equation.

$$\vec{J}_N(\mathbf{r},t) = q\left[\mu_N N(\mathbf{r},t)\vec{E}(\mathbf{r},t) + D_N \overrightarrow{grad}\big(N(\mathbf{r},t)\big)\right] \tag{5}$$

$$\vec{J}_P(\mathbf{r},t) = q\left[\mu_P P(\mathbf{r},t)\vec{E}(\mathbf{r},t) - D_P \overrightarrow{grad}(P(\mathbf{r},t))\right] \tag{6}$$

$$\vec{J}_{Total} = \vec{J}_D + \vec{J}_N + \vec{J}_P \tag{7}$$

Where $\mu_N$ and $\mu_P$ are the electron and hole mobilities, $E$ is the electric field in the photoconductor and $D_N$, $D_P$ are the carrier diffusion constants. $J_D$ is the displacement current, defined with eq. (8).

$$\vec{J}_D(\mathbf{r},t) = \frac{\partial \vec{D}(\mathbf{r},t)}{\partial t} = \varepsilon_0 \varepsilon_r \frac{\partial \vec{E}(\mathbf{r},t)}{\partial t} \tag{8}$$

The electric field can be calculated from the charge concentrations using the Poisson equation:

$$div\big(\epsilon_0 \epsilon_r E(\mathbf{r},t)\big) = q(P(\mathbf{r},t) + N_T^+(\mathbf{r},t) + N_T^0(\mathbf{r},t) - N(\mathbf{r},t)) \tag{9}$$

The previous equations can be simplified with some assumptions while considering special circumstances.

1. For low carrier injection, as the result of low optical illumination, the Poisson equation can be eliminated by assuming a constant electric field in the gap made only by a constant bias voltage of $V_{bias}$ over the electrode length of $L$, which is considered much longer than the photon penetration depth *(1/α)*. As it is a constant field in time, the displacement current in equation (8) becomes zero.

$$|\vec{E}| = \frac{V_{bias}}{L} \tag{10}$$

2. In case of the low power optical excitation, the density of the photogenerated carriers is smaller than the density of the traps, which results in constant carrier lifetimes ($\tau_N$, $\tau_P$). Moreover, if $\tau_N$ and $\tau_P$ are in the picosecond range, we can neglect the drift and diffusion processes, as the carriers do not travel a long distance before being trapped. This leads to the simplification of equations (5) and (6).

$$\vec{J}_N(\mathbf{r},t) = q\mu_N N(\mathbf{r},t)\vec{E}(\mathbf{r},t) \tag{11}$$

$$\vec{J}_P(\mathbf{r},t) = q\mu_P P(\mathbf{r},t)\vec{E}(\mathbf{r},t) \tag{12}$$

3. The radiative recombination rate in the semiconductor is very low as compared to the weight of the trapping process, therefore the recombination rate components ($B_N$ and $B_P$) of eq. (2) and (3) are negligible. Because of the previous simplifications the drift component of eq. (2) and (3) can be neglected too, because of the low value of the divergence.

$$\frac{\partial N(\mathbf{r},t)}{\partial t} = G(\mathbf{r},t) - \frac{N(\mathbf{r},t)}{\tau_N} \tag{13}$$

$$\frac{\partial P(\mathbf{r},t)}{\partial t} = G(\mathbf{r},t) - \frac{P(\mathbf{r},t)}{\tau_P} \tag{14}$$

With these 5 equations (10 to 14) we formed a simplified system of equations, and we can calculate the current and resistance dynamics of the photoswitch under optical illumination. Considering that the currents are flowing only in a thin upper layer of the semiconductor, which can be defined with the absorption depth *1/α,* and it is much smaller than the electrode distance *L*, therefore the flow is in a cross section of *S = W*1/α*, the current can be calculated from the current densities in eq. (7) by integrating it over *S*.

$$\begin{aligned} I(t) &= \iint_S \vec{J}_{Total}\, dS = \left[\vec{J}_N(\mathbf{r},t) + \vec{J}_P(\mathbf{r},t)\right]\frac{W}{\alpha} \\ &= q\left[\mu_N N(\mathbf{r},t) + \mu_P P(\mathbf{r},t)\right]\frac{V_{bias}}{L}\frac{W}{\alpha} = \sigma(t)\frac{V_{bias}}{L}\frac{W}{\alpha} \end{aligned} \tag{15}$$

Where *σ(t)* is the conductance. The resistance can be calculated from the above expression with the conductance, expressed with equation (1) on page 15.

$$R(t) = \frac{V_{bias}}{I(t)} = \frac{\alpha L}{W\sigma(t)} \tag{16}$$

In equation (15), the electron and hole concentrations are dependent on the generation rate through equation (13) and (14), and this generation rate depends on the optical excitation. Therefore, we can consider the photoconductive switch as an optically controlled resistance. For a precise simulation the dark resistance ($R_{dark}$) should be also taken into consideration, which is defined by the residual free carriers at equilibrium: $N_0$ and $P_0$. The metal electrode geometry of the switch deposited on the semiconductor is creating a capacitance, which can be modelled by a single equivalent capacitor. A basic equivalent circuit of photoswitches is illustrated in Figure 1-4.

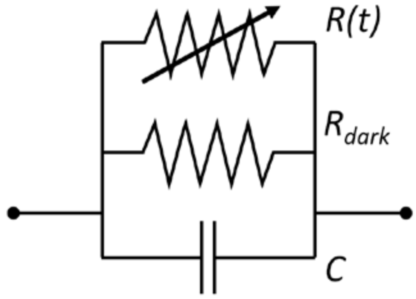

*Figure 1-4*
*Equivalent circuit of a photoconductive switch*

The capacitance *C* ideally is as low as possible in the < 20 fF ensuring a fast response, while the ideal dark resistance is in the > 100 kΩ range to have a low level of feedthrough signal.

The current and resistance dynamics of the photoswitch can be simulated with equation (15) and (16). If we use a pulsed illumination, where a femtosecond laser is providing the optical signal, we can approximate the pulse shape with a gaussian pulse and write the optical power of one pulse with equation (17).

$$P(t) = P_0 e^{-\left(\frac{t}{\tau_l}\right)} \tag{17}$$

Both the electron and hole lifetimes define the result curve shapes. Typically, the electron lifetime is in the picosecond range and the hole lifetime is in the order of tens of picoseconds. These two decays are resulting in a dual exponential curve for the photoswitch response. Typical calculated response curves are illustrated in Figure 1-5 and Figure 1-6, showing the response of the photoswitch resistance and current respectively, to an ultrashort laser pulse. The simulation was performed with Matlab, with an in-lab developed script [6]. A thorough description of the simulation method can be found in *APPENDIX A*. Here, the results are based on the simulation of a photoswitch that has very similar characteristic parameters as the component that we will use in this thesis. Chapter II is detailing the characterisation and experiments to determine the device parameters.

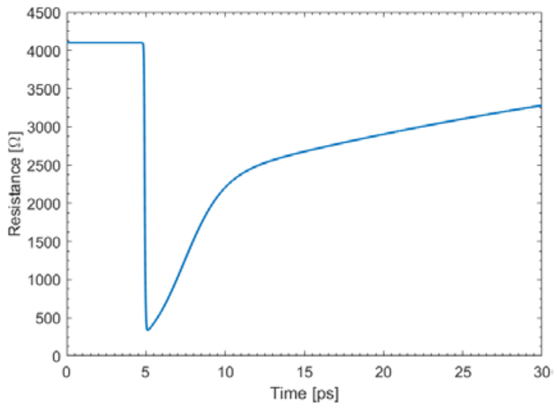

*Figure 1-5*
*Typical calculated resistance response of a photoswitch to an optical pulse*

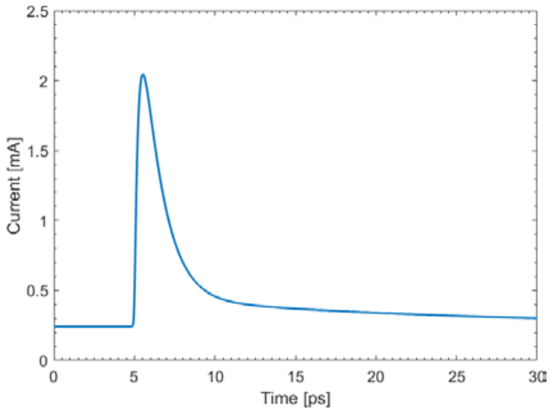

*Figure 1-6*
*Typical calculated current response of a photoswitch to an optical pulse*

The response curves have a fast initial jump, in accordance with the optical intensity increase as the laser pulse arrives to the semiconductor. Consequently, the device resistance, which is initially the dark resistance of 4.1 kΩ, goes down to 330 Ω within 100 fs (the exciting optical pulse width), as seen in Figure 1-5. This corresponds to the generation of a current pulse, as in Figure 1-6. The fall time of the current is determined mainly by the $\tau_N$ characteristic time. The simulation was done with an optical pulse of 100 fs and with lifetimes of $\tau_N = 1.2$ ps; $\tau_P = 20$ ps, while a bias voltage is set at 1 Volts. The dual-exponential shape is clearly observable on the curves. After all the free carriers recombined or get captured, the signal returns to its initial value. Thanks to the bias voltage, a low level of feedthrough signal will appear on the photoswitch, with a current of 0.24 mA.

## I/1.2. Photoconductors for THz generation

Photoconductive switches are most widely used for the detection and generation of THz waves, in this domain they are also frequently called photoconductive antennas (PCA), as they are directly radiating the THz signal. In the generation process, the electrodes are electrically biased and the gap between them is illuminated by a laser. There are two options possible [1]: the use of ultrashort laser pulses emitted from a femtosecond mode-locked laser (Figure 1-7/a), or simultaneous illumination of two continuous wave (CW) laser with a frequency difference (Figure 1-7/b). In the first case, the ultrashort pulses are generating THz pulses. The rise time of these pulses corresponds to the laser pulse rise time while the pulse width and shape depends on the carrier lifetime of the material. In the frequency domain the generated ultrashort pulses have an extremely wide bandwidth up to the THz domain. In this setup the photoconductive antenna is frequently called photoconductive switch. For the second case the two CW lasers wavelength (frequency) difference is in the range of THz and the photoconductor will emit a continuous Terahertz signal with a frequency corresponding to the frequency difference of the CW lasers, in this case the device is frequently called photomixer.

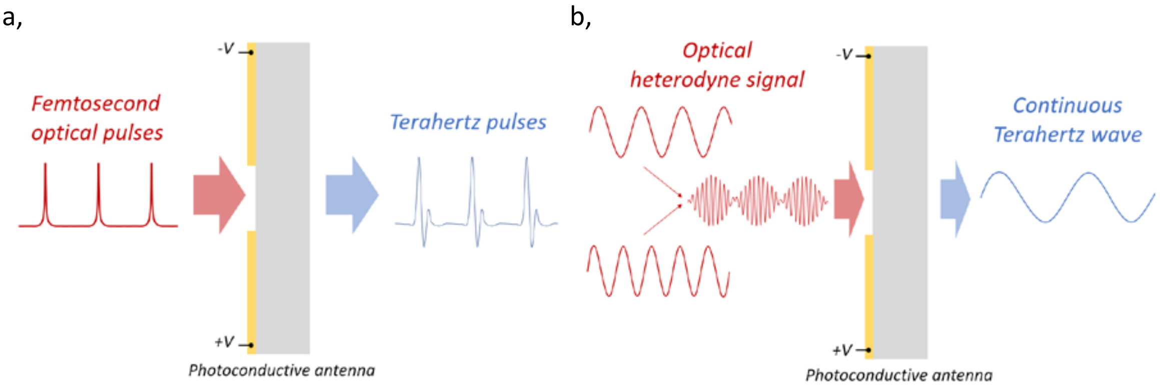

*Figure 1-7*
***a**: Terahertz pulse generation and **b**: CW terahertz generation with photoconductive antenna*

Before and during the ‘90s, very few researches were addressing the THz domain, mainly because of the lack of efficient and convenient THz sources. Since the exploitation of photoconductive switches and lasers for THz generation, the number of scientific papers concerning the THz domain is exponentially increasing from the years 2000s [7]. Terahertz waves can be used for many applications [8], starting from spectroscopy, imaging, sensing, biomedical applications and telecommunication. Many materials have unique spectral signatures at THz frequencies, which makes it useful for material characterization and identification. Also, many optically opaque materials are transparent for THz waves. In the telecommunications field the unused wireless frequencies above 100 GHz and in the unregulated spectrum above 300 GHz motivates the research to develop telecommunication systems using the THz waves [9][10]. However, several passive services exist above 300 GHz for radio-astronomy and earth observation, which needs to be protected from the possible interferences by THz communications. Figure 1-8 shows the free-space loss and resonance peaks up to 3 THz [9]. Suggested bands chosen for long- and medium distance, and indoor applications are marked in the figure.

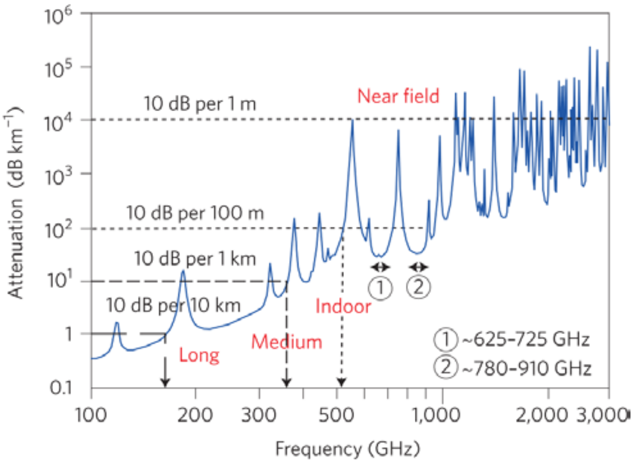

*Figure 1-8*
*Free space path loss per km for frequencies up to 3 THz. Source:* T. Nagatsuma et al. Nature, 2016 [9]

The THz range also has the advantage of frequent frequency reuse due to the high free-space loss and the several water absorption peaks at higher frequencies [11], as we can see the numerous peaks in the figure corresponding to this. The high losses can also be seen as a disadvantage for the restriction of high-distance communication. Recent researches have already demonstrated high bandwidth and high data-rate wireless communication at 300 GHz [12] or even at 600 GHz [13].

## I/2. Photoswitch evolution

The first devices by *Auston* were made of silicon (Si) ([2] and [14]), later gallium-arsenide (GaAs) was used thanks to its good carrier mobility and direct bandgap. In particular, GaAs deposited with molecular beam epitaxy (MBE) at low temperatures (LT-GaAs), proved to have very good properties with sub picosecond carrier lifetime (1.6 ps in [15] and 0.27 ps in [16]). Many of the devices are used for THz generation as photoconductive antennas. In the following state of art review, we are looking at photoconductive antennas and switch designs. An excellent review of PCAs by *Burford* and *El-Shenawee* was done in 2017 [8], the following review is partly based on their work.

### I/2.1. GaAs devices

The bandgap of 1.42 eV in GaAs requires the illumination with 800 nm wavelengths or below, which allows the use of the popular titanium-sapphire mode-locked lasers. Nowadays the best performing photoconductors for THz generation and detection are made of LT-GaAs. The benefits of the low temperature growth around 200°C - 250°C, are the rather higher carrier mobility due to the high level of crystallinity and the excess arsenide within the crystal to create point defects. These defects are helping the recombination and reduces the carrier lifetime. It also has a high resistivity due to the small number of free carriers. An example from 1991 for LT-GaAs was published by *Gupta et al.* from the United States with 0.4 ps carrier lifetime grown at 200°C [17]. The result showed a moderate electron mobility of 120-150 cm$^2$/Vs and high resistivity.

A popular method of reducing the carrier lifetime is by performing ion-implantation. An example was proposed by the team of *A. Krotkus* from Lithuania and *C. Jagadish* from Australia [18], in which they were implanting As ions into the GaAs semiconductor to create defects. An ultra-fast lifetime of 0.2 ps was achieved, however the mobility become very low and it also resulted in a low resistance. An annealing process at 600°C was required to increase the mobility to 2000 $cm^2/Vs$ and to increase also the resistance, which also resulted in a carrier lifetime increase to 1 ps. Further annealing at 800 °C increased the lifetime up to 10 ps. This shows the difficulty of achieving good values in all the parameters needed for ultrafast operation.

It is possible to reduce the lifetime of GaAs with carbon irradiation too [19]. Semi Insulating (SI) GaAs without irradiation is showing lifetimes in the range of 70 ps, after carbon irradiation 0.55 ps was achieved. The device was used for THz detection in a 1.5 THz bandwidth.

In IMEP-LAHC laboratory, LT-GaAs samples with beryllium doping was used in 2005 [5], (at that time it was LAHC laboratory in Le-Bourget-du-Lac), and studied in a collaboration with the team of *A. Krotkus* in 2002 [20]. Beryllium doping is another method to control the optoelectronic properties and to reduce the lifetime, the samples had a mobility of 540 $cm^2/Vs$ and a carrier lifetime of 0.5 ps.

As we saw, there are several methods to improve the GaAs properties with various degrees. At the end of the '90s, the interest started to increase towards materials working with 1550 nm illumination. At this wavelength smaller size and simpler laser are available. There were researches using the GaAs with 1550 nm, but the efficiency was much lower than in case of 800 nm illumination. A two-step absorption process makes it possible to work at this sub-bandgap wavelength and it requires interband transition of electrons with midgap states or non-linear two-photon absorption. In [21] with LT-GaAs, an efficiency of 10% was obtained compared to 800 nm excitation.

Another alternative to LT-GaAs has been introduced by the group of *A. Gossard* in the United States, they proposed a structure composed of self-assembled layers of erbium-arsenide (ErAs) islands in GaAs semiconductor [22]. The advantage of the structure is the possibility to control the response time and resistance by precise engineering of the layers. A carrier lifetime of 0.12 ps was measured with a low electron mobility of 100 $cm^2/Vs$. The layered GaAs:ErAs structure can be used with 1550 nm wavelengths too.

There are also techniques to increase this low efficiency with complex designs of the electrodes, as it will be shown in section I/2.3. Nonetheless, a compound material of InGaAs turned out to be an efficient alternative for the longer wavelengths.

### I/2.2. $In_xGa_{x-1}As$ devices

Compared to GaAs devices, InGaAs is not yet that well established technology, significant improvements were achieved only in the past 10-20 years. The bandgap of 0.8 eV allows the InGaAs material to work with 1550 nm wavelength sources. This wavelength also has the advantage of using the well-established fibre-technology in the systems.

Some researches were investigating the low temperature growth InGaAs similarly to GaAs. A Be doped bulk LT-InGaAs was fabricated in [23], it showed a relatively low resistance of 700 Ω and low carrier mobility of 100 cm$^2$/Vs, however with a good lifetime of 0.35 ps.

Similarly to GaAs, ErAs island embedding can also enhance the InGaAs properties. The method is improving the crystal quality and carrier mobility [24]. As the result of ErAs, the Fermi level is slightly modified in the structure, resulting in an unwanted free carrier concentration. To overcome this problem, beryllium was added as a p-type donor. A 0.3 ps lifetime and 200 cm$^2$/Vs carrier mobility was achieved with this technique.

Ion-irradiation is also possible to improve the material properties, however this results in a low resistance. In [25] brome irradiation of InGaAs showed a carrier lifetime of 0.2 ps and a good mobility.

Another method for improved properties is to construct a superlattice structure of InGaAs and InAlAs layers [26]. The InAlAs layers are transparent to 1550 nm wavelengths, their role is to add a high concentration of deep-electron traps, acting as a recombination layer via tunnelling process. The InGaAs layer is beryllium doped to reduce the free electron concentration. A mobility of 1900 cm$^2$/Vs was achieved with a very good resistance of 0.12 MΩ. The detected THz pulse width were measured to be 0.75 ps. Recently, this technological approach has gained in performances and has allowed the development of very sensitive components for THz time domain spectroscopy (TDS) setups, the group of *B. Globisch* in Germany demonstrated a TDS system with a Signal-to-Noise ratio of 55 dB at 4 THz [27] achieved with beryllium doped InGaAs/InAlAs superlattice.

Ion-implantation of the InGaAs material can also improve the performances. Iron (Fe) implantation reduced the emitted THz pulsewidth from 0.68 ps to 0.57 ps compared to the unimplanted case, the calculated mobility was 1500 cm$^2$/Vs for the ion-implanted InGaAs [28]. While this mobility is lower compared the unimplanted InGaAs, an increase was observed in the THz radiation amplitude.

The InGaAs photoconductive switch used in this thesis is implanted with nitrogen ions [29]. The mobility was reported to be around 6900 cm$^2$/Vs with a relatively good dark resistance of 6 kΩ, and as we will show in Chapter II, the lifetime is in the picosecond range.

As a summary, the sensitivity to 1.5 µm wavelengths is an important advantage of InGaAs devices, however their dark resistance compared to GaAs is lower and their low breakdown voltage is also amongst the disadvantages. Despite these, good properties and performances can be achieved with some of the variously manipulated InGaAs photoconductors. Comparing to GaAs materials, the reported THz field amplitude for these devices is still lower [1].

In the next section (I/2.3) we review the widely used techniques to improve the photoconductor efficiencies. This includes fabrication of the electrode structures at nano-scale level, which is a technology that became available widespread only in the past decade.

## I/2.3. Techniques to improve the quantum efficiency

### *Interdigitated structures*

One main limitation of the efficiency is originating from the geometry of the electrodes on the photoconductor. While an ultrafast photoconductor is illuminated, only the carriers generated in a few hundred nanometres distance from the electrodes can considerably contribute to the generated THz signal, as it is explained by *N. T. Yardimici* and *M. Jarrahi* in [30]. The quantum efficiency is defined as the ratio of carriers collected by the electrodes and the number of photons illuminating the photoconductor. To increase the area where the carriers can reach the conductor, interdigitated structures are used where thin “fingers” connected to the electrodes were fabricated with a width in the µm range with a gap between them also in the µm range. An illustration of this interdigitated structure is shown in Figure 1-9.

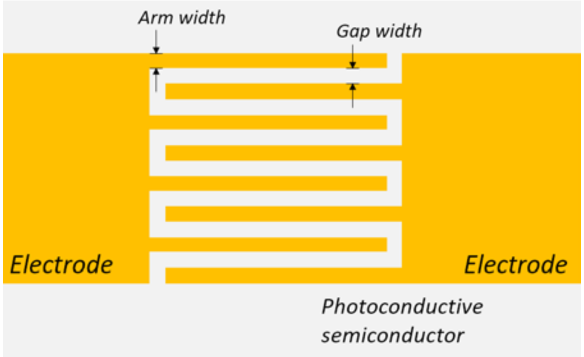

*Figure 1-9*
*Interdigitated structure illustration*

The neighbouring arms are connected to opposite electrodes, creating an interweaving structure. The fingers are increasing the area where the carriers can be collected but on the other hand the illuminated area is decreasing by the shadowing effect of the metal electrodes.

One of the first photoconductor example with interdigitated structure was demonstrated by *Chen et al.* in 1991 [31]. They observed that a reduction in electrode spacing by 100 times from 20 µm to 0.2 µm by using the interdigitated structure is improving the responsivity 100 fold. This small gap is in the range of the carrier transit time for a carrier lifetime of 1 ps. *Brown et. al.* [32] showed with theoretical calculations that the quantum efficiency is dependent on the electrode length and gap width. There is a trade-off between high quantum efficiency and ultrafast operation of the semiconductors: the faster the semiconductor (shorter the lifetime) the shorter the carrier travel distance before recombination or trapping, therefore less carriers can be collected. The interdigitated structure therefore significantly improved the photoconductor switch’s and antenna’s efficiency by increasing the effective area.

### *Efficient resonant structures*

Another way to increase the efficiency is by increasing the absorption rate of the illuminating light. The fabrication of resonant structures in the semiconductor can significantly improve the absorption efficiency. A solution proposed at IEMN laboratory (*Institut d'électronique de microélectronique et de nanotechnologie*) by *Peytavit et al.* [33] based on a Fabry-Pérot resonant cavity constructed between two gold layers. Figure 1-10/a (*Source:* [34]) illustrates the light path with several reflections between the gold layers. Figure 1-10/b shows the enhancement of quantum efficiency when the LT-GaAs thickness corresponds to a multiple of the quarter-wavelength (λ/4).

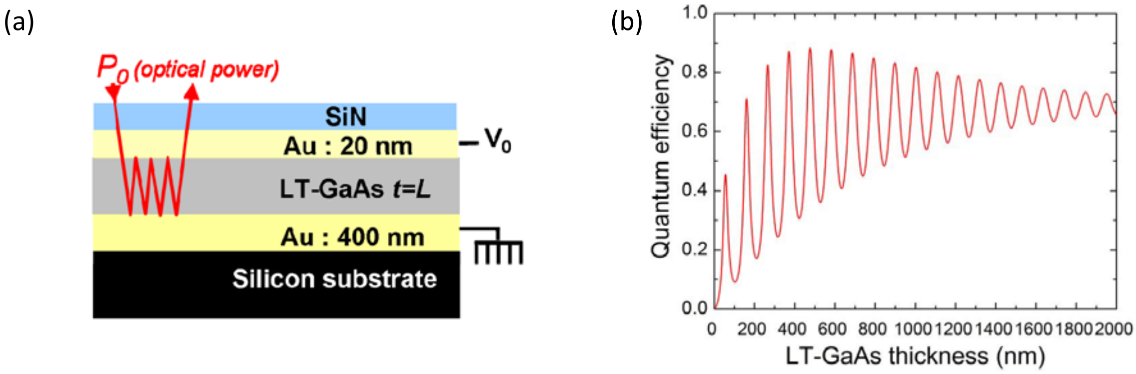

*Figure 1-10 Source: E. Peytavit et al., IRMMW-THz Conference, 2013 [34]*
***(a):** Illustration of the resonant structure with the reflected light path.*
***(b):** Quantum efficiency dependence on the LT-GaAs thickness of the structure of a,*

The Au layers are serving as the electrodes and the mirrors for the cavity and the sub-micron distance between them also increases the electrical DC field in the GaAs layer. With these devices, a microwave signal conversion loss of 22 dB was achieved at 100 GHz (with 780 nm wavelength illumination), which is an improvement of 40 dB compared to other photoconductors [35].

*Nanoplasmonic structures*

One of the most promising technology for photoswitch improvement is the fabrication of nanoplasmonic structures. Nanostructured metals can enhance the optical response due to the interaction of metal surface plasmons with the incident light [36]. Surface plasmons are electron-plasma oscillations existing at the metal-dielectric interface [30]. Due to this effect, near the plasmonic structures, the photo absorption is enhanced, increasing the carrier generation in the close proximity of the electrodes. This leads to an increased number of photocarriers reaching the electrodes before recombination [37], suggesting higher achievable radiation power for emitters and higher sensitivity for detectors. In [37] a comparison was performed with an LT-GaAs photoconductive antenna with a gap of 20 µm without plasmonic contact electrodes, and with plasmonic contact electrodes composed of 200 nm wide arms with 100 nm gaps. An illustration of the plasmonic contacts is shown in Figure 1-11, with the electrons, electric field, electrode and gap sizes, and the needed orientation of the incident optical field.

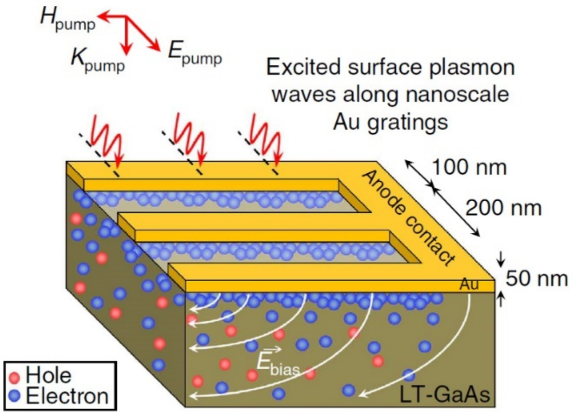

*Figure 1-11*
*Illustration of the plasmonic contacts*
*with the incident optical field orientation.*
*Source:* Berry et al. Nature
communications, 2013 *[37]*

While illuminated, the plasmonic electrodes are exciting surface plasmon waves along the grating interface. These waves are allowing the transmission of a large portion of the optical signal into the photo-absorbing substrate. These devices were dedicated to THz wave radiation and the reported improvement of radiation power thanks to the plasmonic surface is 50 fold higher than the conventional case, and for detection, a 30 fold improvement in photocurrent was observed [37], as compared to a non-plasmonic device.

Other plasmonic techniques includes plasmonic light concentrators, large area nanoantenna arrays or plasmonic nanocavities [30]. These solutions are aiming to enhance the absorption of the photoconductor and reduce the carrier transport length. As a result, they are reducing the trade-off between high quantum efficiency and ultrafast operation. The fabrication of plasmonic structures, a very precise, advanced technology is required.

*Plasmonic and resonant structures*

*M. Billet et al.* [38] used LT-GaAs with a Fabry-Pérot (FP) cavity and a plasmonic diffraction grating to enhance the absorption efficiency of 1550 nm wavelength illumination. The FP cavity is similar as we mentioned previously, however instead of an Au plate, a grating is constructed at the top of the structure as shown in Figure 1-12.

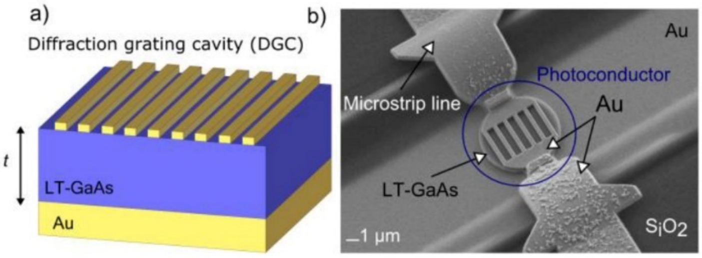

*Figure 1-12*
*Fabry-Pérot cavity with a diffraction grating to increase the LT-GaAs absorption efficiency for 1550nm wavelengths.*
*Source:* Billet et al. IRMMW-THz conference, 2017 *[39]*

It was shown, that the grating is allowing the excitation of waveguide modes in the structure and increased the efficiency by 3 times. Microwave signal conversion losses of 65 dB was also observed [39].

These listed techniques details only the most promising methods of improving the photoconductor by designing the appropriate structures, which would also improve the performances of the applications detailed in this thesis. The photoconductor devices presented in Chapter II has an interdigitated switch geometry with gap and arm width of 3-5 µm. The improvement of this structure with these techniques are not the topic of the thesis and the necessary resources were not available at that time.

## I/3. Photoswitch as a frequency mixer

In this thesis, we are focusing on the semiconductor performance at lower frequencies in the microwave and the millimetre wave range and not in the THz range. One application is the use as a frequency mixer, the fundamentals of mixing is introduced in this section. Other application is the use as a sampler in Analog to digital converters (ADCs), the fundamentals are detailed in the following section I/4, while some ADC properties already introduced in this section.

### I/3.1. Fundamentals of mixing

Mixing of signals is a fundamental process for radiofrequency applications. The up- or downconversion of signals in the frequency domain is one of the most important function in signal processing. Usually, a frequency mixer has two input ports with incoming signals at different frequencies, they are called the radiofrequency signal (RF) and local oscillator signal (LO). At the output port the mixed products can be measured at the intermediate frequencies (IF). A basic mixing scheme is illustrated in Figure 1-13.

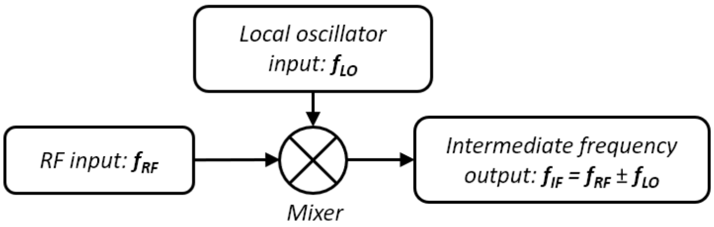

*Figure 1-13*
*Mixing of frequencies*

The frequency mixing can be deduced from time domain signals with the following equations (18) and (19). We define the RF signal as $X_{RF}(t)$ and the LO as $X_{LO}(t)$, the mixing output signal is $X_{IF}(t)$.

$$X_{RF}(t) = X_{RF}\ a(t)\ sin(2\pi f_{RF}t + \theta(t)) \tag{18}$$

$$X_{LO}(t) = X_{LO}\ sin(2\pi f_{LO}t) \tag{19}$$

Where $f_{RF}$ and $f_{LO}$ are the RF and LO frequencies respectively. The terms $a(t)$ and $\theta(t)$ are possible amplitude and phase modulations of the RF signal. The IF signal at the output can be calculated by multiplying the RF and LO:

$$\begin{aligned} X_{IF}(t) &= X_{RF}(t) * X_{LO}(t) = X_{RF}\ a(t)\ sin(2\pi f_{RF}t + \theta(t)) * X_{LO}\ sin(2\pi f_{LO}t) = \\ &= \frac{1}{2} X_{RF}\ a(t)\ X_{LO}[cos(2\pi(f_{RF} - f_{LO})t + \theta(t)) - cos(2\pi(f_{RF} + f_{LO})t + \theta(t))] \end{aligned} \tag{20}$$

As the result of the mixing we will have two components at the frequencies $(f_{RF} - f_{LO})$ and $(f_{RF} + f_{LO})$. In case of the lower frequency we talk about downconversion, if the output has a higher frequency than $f_{RF}$ we talk about upconversion of signals. In practical systems the frequency components not under treatment are filtered out to reduce possible interferences. There are numerous applications of mixing, for example in a telecommunication transmission system it can be used for signal downconversion for data-processing, or upconversion for transmission or signal frequency re-positioning to avoid interference in a dense communication channel.

## I/3.2. Mixing properties

There are some important properties of mixing, which are defining the performances of a frequency mixer.

*Conversion loss*

The ratio between the signal to be down (or up) converted and the mixed signal power is called the conversion loss (CL) or in some occasions, when there is a gain during the process, the conversion gain. This value, expressed in decibels, shows the efficiency of the conversion and usually has a dependence on the local oscillator power. As there can be several mixed products, we calculate the CL considering only one IF signal we are interested in. The calculation is written in Equation (21).

$$Conversion\ Loss\ \left(CL^{dB}\right) = 10 * log_{10}\left[\frac{P(f_{RF})^{mW}}{P(f_{IF})^{mW}}\right] = P(f_{RF})^{dBm} - P(f_{IF})^{dBm} \qquad (21)$$

*Bandwidth and frequency range*

The mixer frequency range is defining the frequencies where the mixer has the same performance. The difference between the lower and upper frequency is the mixer bandwidth. There could be different ranges for the RF and LO inputs. It is also possible that the mixer has a wider operating frequency range than its bandwidth, which means that it works only for low bandwidth input RF signals.

*Isolation*

In an ideal mixer the IF output contains only the mixed products, however in many real life cases the LO and RF signals can be seen at the output with various degrees. If the isolation is low the feedthrough signals of RF and LO can cause problems for the devices following a mixer, for example saturating an IF amplifier. The isolation between the LO and RF signals is also important to prevent backward propagation of signals in a system, for example if the RF signal is a received signal by an antenna, the LO signal could radiate through this antenna due to the low isolation. Optoelectronic mixers have particularly good isolation between the RF and LO signal because one signal is in the optical domain and the other is in the electrical domain.

*Mixer non-linearity*

Mixers are using a non-linear element or a time-varying element for frequency conversion [40]. One of the most important non-linear property is the third order intercept point (IP3) which is the theoretical power of the fundamental output IF signal when the third order intermodulation product has the same power level. In practice, this point cannot be measured directly because it is usually at a higher power level than the 1 dB compression point of the system.

*Spurious free dynamic range in mixers*

The spurious free dynamic range (SFDR) can show the operating range where the devices can perform with good characteristics. The non-linear mixing process is creating intermodulation products. The SFDR is the range between the maximum fundamental signal level where the third order intermodulation product has the same level as the noise floor and the noise floor [40]. Third order intermodulation products can be the following: $2*f_{RF}\pm f_{LO}$, $2*f_{LO}\pm f_{RF}$. SFDR is given in decibel scale and for mixers it is usually measured with a dual tone experiment, when two signals are set as an input with a minimal frequency difference.

The SFDR in Analog to Digital Converts (ADCs), which is another application we will detail in section I/4, is defined differently. It is usually measured as a ratio of the signal level to the highest spurious signal level which falls in the frequency range of *DC* to $f_s/2$, where $f_s$ is the sampling frequency. It can be given in *dBc*, where the reference is the signal level (*c* refers to the carrier) or *dBFS* where the reference is the full-scale (FS) level of the ADC [41].

### I/3.3. Mixing with pulsed LO

Using a pulsed signal and a continuous signal as the LO, we can also perform mixing which can be also seen as the sampling of the signal. Sampling is one of the essential functions of an ADC. The digital signals containing the data are modulated in an analog carrier signal and are transferred to the receiver through a channel, the receiver needs to convert the analog signal to digital for signal processing. The conversion is done with sampling and digitization in an ADC.

The local oscillator input in this case is a pulse train (*p(t)*) with a repetition rate of $f_s = 1/T$, where *T* is the pulse period. A schematic of the mixing is illustrated in Figure 1-14. We mark the sampled output signal with *s(t)*.

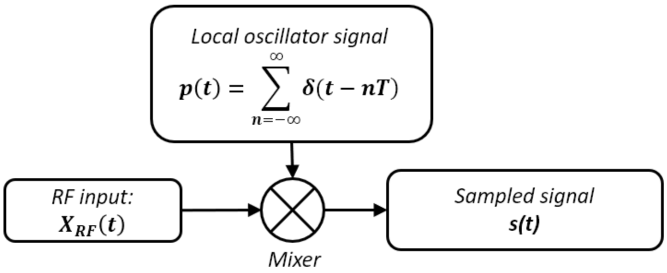

*Figure 1-14*
*Mixing with sampling*

According to the Shannon criteria (equation (22)), the sampling frequency should be at least twice as the maximum frequency of the input RF signal in order to be able to reconstruct all the information.

$$f_s \geq 2f_{max} \tag{22}$$

Where $f_{max}$ is the maximum frequency of the RF input signal. We mark the minimum frequency as $f_{min}$, and the bandwidth *BW* as the difference of the maximum and minimum frequency: $BW = f_{max} - f_{min}$. Figure 1-15 is illustrating a 10 MHz sinusoidal signal sampled with 100 MHz repetition rate pulses. The left column shows the time domain signals and the right column shows the corresponding signals in the frequency domain. The pure sinusoidal signal only has a single peak at 10 MHz in the frequency domain, while the periodic sampling signal has several peaks at 100 MHz and its harmonics. If we mix these two signals, which means the sampling of the sinusoidal with the pulses, in the time domain we will see the periodic samples of the signal, in the frequency domain it contains several copies of the original signal replicated around the sampling peaks. Around one harmonic of the sampling signal we have two copies of the RF.

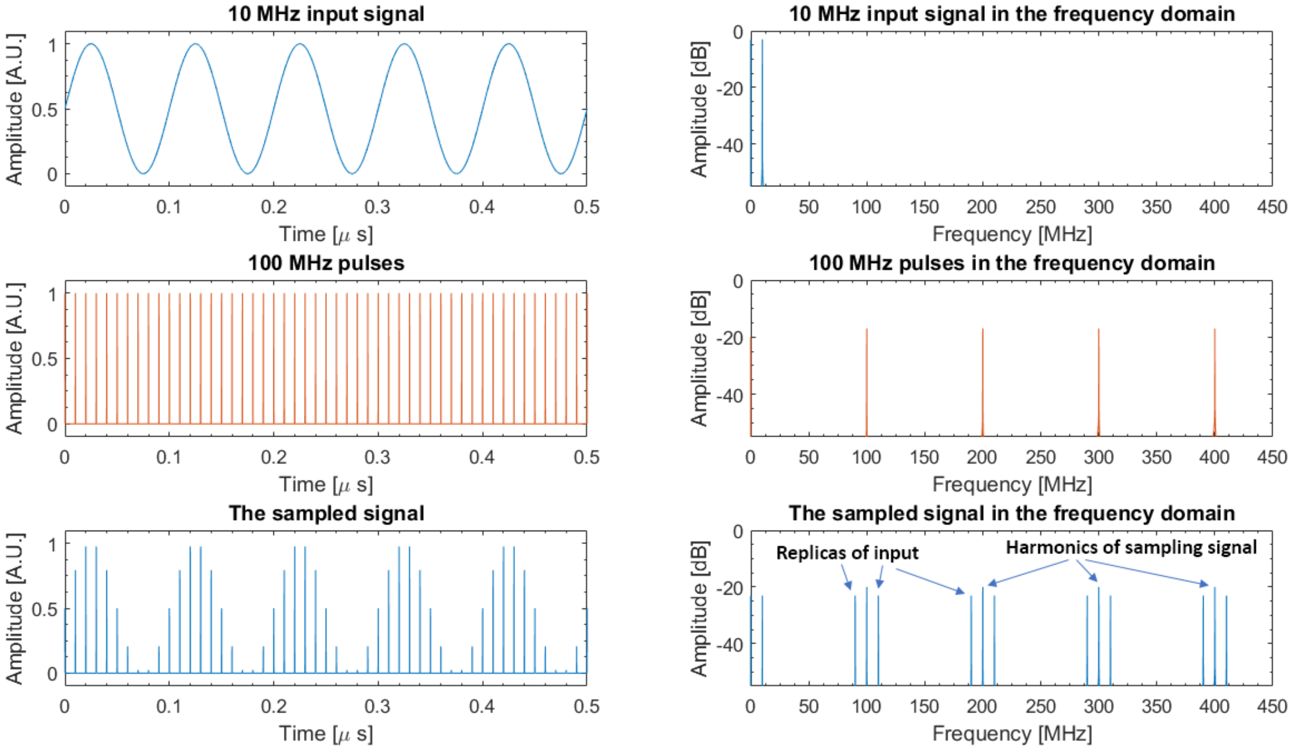

*Figure 1-15 Illustration of a sinusoidal signal sampling in the time domain and the frequency domain*

The following equations (23) and (24) are detailing the mixing mathematically. The multiplication in the time domain is equivalent with a convolution in the frequency domain.

$$s(t) = X_{RF}(t) * p(t) = X_{RF}(t) * \sum_{n=-\infty}^{\infty} \delta(t - nT) \tag{23}$$

$$S(f) = X_{RF}(f) \otimes P(f) = X_{RF}(f) \otimes \sum_{n=-\infty}^{\infty} \delta\left(f - \frac{n}{T}\right) = \sum_{n=-\infty}^{\infty} X_{RF}\left(f - \frac{n}{T}\right) \tag{24}$$

The result of equation (24) also shows that the output signal in the frequency range contains multiples of the signal with frequency distances of the sampling frequency.

### I/3.3.a Undersampling

As we are using higher and higher frequencies in the new generations of telecommunication systems, the sampling frequencies also have to increase. However above 10 GHz it is challenging to have a stable sampling signal for high quality sampling [42]. However, it is still possible to sample signals on a high carrier frequency with lower sampling frequency under certain conditions, in case we are not aiming to reconstruct the real time domain signal, but only the signal modulated onto the high frequency carrier. In this case the modulation has a frequency bandwidth which is only a fraction of the carrier frequency. After sampling the RF signal has replicas in the frequency ranges called Nyquist zones [43]. Nyquist zones are portions of the spectrum with frequency limits of $n * \frac{f_s}{2}$ to $(n+1) * \frac{f_s}{2}$ . This method is called undersampling or bandpass sampling. There are some constraints for choosing the $f_s$ frequency for optimal sampling [44], it has to be between the following limits:

$$\frac{2f_u}{n} \le f_s \le \frac{2f_l}{n-1} \tag{25}$$

Where $f_l$ and $f_u$ are the lower and higher frequency limits of the wideband signal respectively, the bandwidth (BW) can be defined with the expression $BW = f_u - f_l$. The integer $n$ is defined as:

$$1 \le n \le I_g\left[\frac{f_u}{BW}\right] \tag{26}$$

Where $I_g$ is the lower integer function. These equations are showing that the $f_s$ sampling frequency should be at least twice the BW. Figure 1-16 is showing the preferred sampling rates as function of the highest frequency component of the signal. $B_{GT}$ is the guard band between the replicas of the modulated signal. Figure 1-17 is illustrating the Nyquist bands and an undersampled signal with its replicas after sampling.

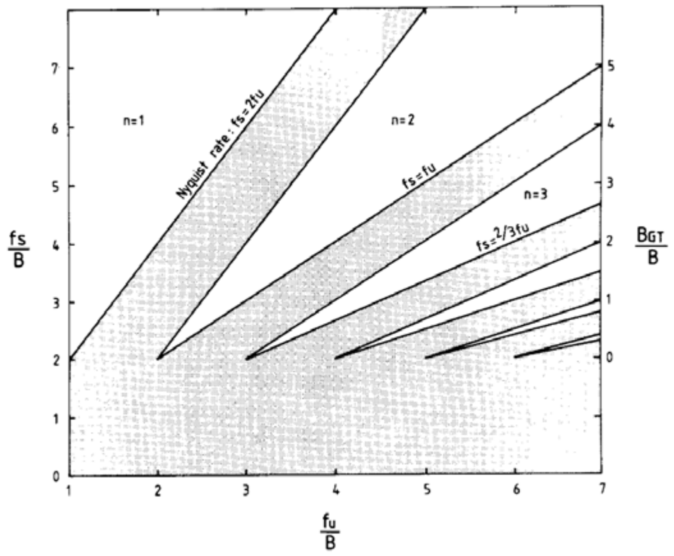

*Figure 1-16*
*Preferred sampling rates for undersampling concerning the inverse relative bandwidth of the signal. B≡BW in the figure.*
*Source:* R. Vaughan et al., The theory of bandpass sampling *[44]*

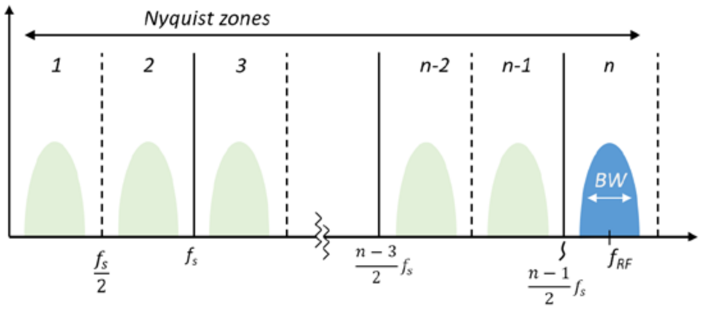

*Figure 1-17*
*Illustration of undersampled output signal in the frequency domain with the Nyquist zones. The original signal with BW bandwidth is downconverted into all the zones.*

Figure 1-18 is illustrating a high frequency signal sampled with a lower frequency, left column are the time domain signals and the right column is showing the frequency domain. An 80 MHz sinusoidal signal is sampled with 10.97 MHz repetition rate pulses. The bottom row shows the sampled signal in the time and frequency domain, we can see similar result as in the previous case: replicas of the sinusoidal signals are on both sides of the sampling signal's frequency components. In addition, also the sampling signal's harmonics are present at $m$*10.97 MHz. This spectrum can be interpreted with equation (24) as the spectral components are around the signal to be sampled (80 MHz in this case) with 10.97 MHz spacing:

$$S(f) = (80\text{ MHz} \pm n*10.97\text{ MHz}) + m*10.97\text{ MHz}$$

If our signal is modulated with *BW* bandwidth (for example with digital data stream), at the output we see the replicas with the modulation. With careful selection of the sampling signal, the modulation can be converted down to the intermediate frequency where signal processing is performed.

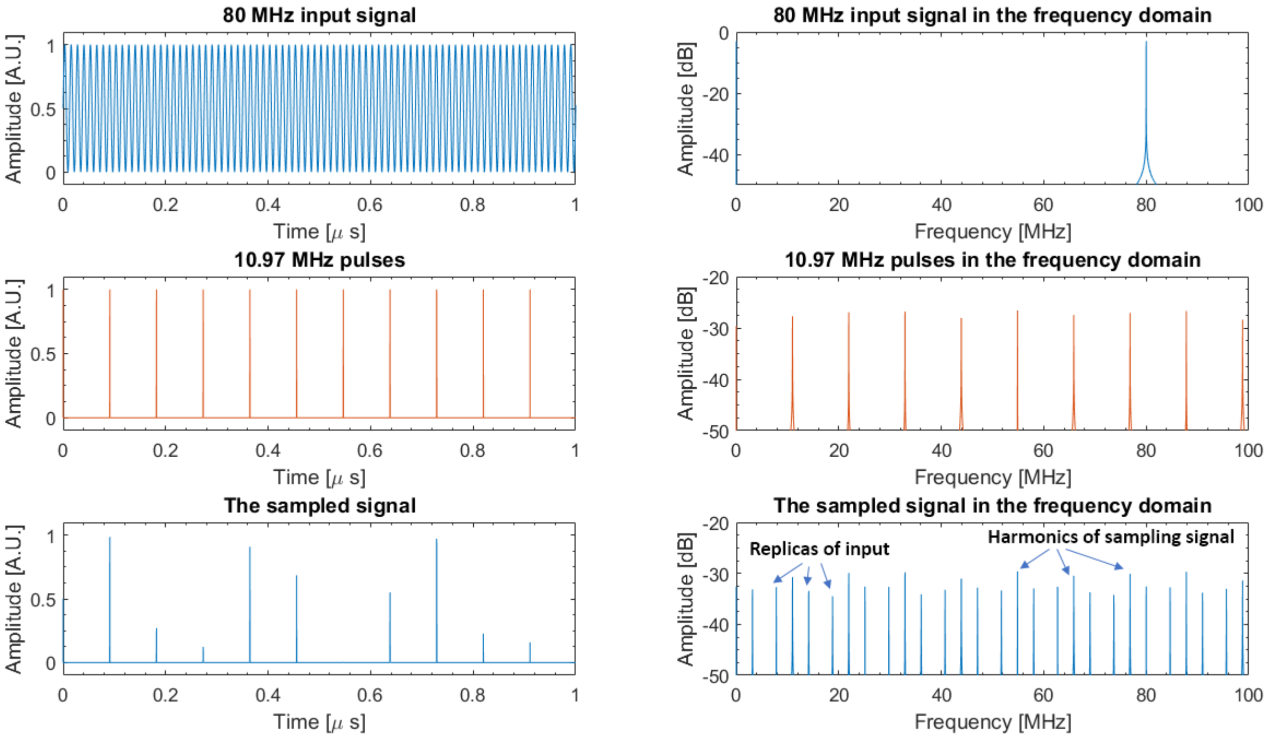

*Figure 1-18 Example for undersampling of an 80 MHz sinusoidal signal with 10.97 MHz pulses.*

In the previous Figure 1-18 the undersampling was demonstrated on a sinusoidal signal, representing a single frequency. If the input signal is modulated in BW bandwidth, as the result of the sampling, all the sampled harmonics will contain this modulated signal with BW bandwidth (we note that the harmonics of the sampling signal at n*10.97 MHz will not be the modulated signal). This effect restricts the maximum BW of the modulation due to the possible interferences caused by the neighbouring harmonics. To avoid the interferences, it is required to select carefully the input signal frequency the sampling signal frequency too, as shown in Figure 1-16, so the output harmonics can be still distinguishable with the BW bandwidth. Additional harmonics can also appear due to the high non-linearities of the sampler device, if their level is too high, the signal processing could be impossible. It is important to mention, that the modulation on the input signal should be optimized, to minimize the spectral components with significant power level outside its useful modulation spectrum.

## I/3.4. Electronic mixers

There are several types of fully electronic mixers exist for the millimetre-wave frequencies. Semiconductor devices are available in the 100 GHz range, for example a Schottky barrier diode [45] with a conversion loss of 7 dB at 120 GHz. However, its maximum output power is limited at -4 dBm at 120 GHz for up-conversion. More complex devices, like a superconductor-insulator-superconductor (SIS) mixer [46] is working between 129-174 GHz, the main disadvantage is its operating temperature of 35 Kelvin. Hot electron bolometer devices are another example for mixing at sub-THz frequencies with an LO of 694 GHz in [47], however they also require extreme temperature control at 20 Kelvin. These complex setups are mostly bulky for telecommunication applications where the device footprint and power consumption are of high importance.

Conventional electronic mixers working at these high frequencies are requiring electrically generated local oscillator signals in the millimetre wave range. Another type of mixers are the subharmonic mixers, which are using the harmonic multiple of one of the input signals. Electrical oscillators, like voltage controlled oscillators (VCOs), are generating continuous wave signals with excellent phase noise in the MHz and lower-GHz range. In signal generators this VCO's output signal is sent through a frequency multiplier chain to generate frequencies of tens of GHz and above. Generating mmW carrier signals in laboratories in fully electronic systems, is also achieved with the frequency multipliers, as an example, in [48] for a communication link at 0.34 THz the LO signal was generated from 20.3 GHz through x8 multiplier chain, and a Schottky varactor based doubler. However, with every doubling step the phase noise is increasing with at least 6 dB [49], following the rate of $20*\log_{10}(N)$, where $N$ is the multiplication factor. This means that low-phase noise signals are difficult to achieve in the mmW range. There are electrical oscillators based on impact-ionization-avalanche-transit-time (IMPATT) diodes working in the mmW range, but their phase noise is poor due to the avalanche breakdown process [49]. Another limitation at high frequencies of these oscillators is that they have to be integrated close to the mixer, to minimize the high propagation losses of electrical waveguides.

## I/3.5. Photonic aided mixers

In case the mixer has optical and electrical input signals, we are talking about photonic assisted mixing. These devices are benefiting of the several advantages of using optoelectronic systems [50] [51]:

- High isolation between the optical and RF signals
- The high bandwidth in the optical domain (THz bandwidth)
- Low loss of optical signal propagation in optical fibres

- As the consequence of the low loss, remote distribution of optical clock signals is simple

These mixers are taking advantage of generating millimetre wave frequencies in the optical domain where the mmW frequency is determined by at least two distinct optical modes. The frequency *Δf* can be calculated from the wavelength of two adjacent modes with the expression in equation (27).

$$\Delta f = f_2 - f_1 = \frac{\lambda_2}{c} - \frac{\lambda_1}{c} = \frac{c(\lambda_1 - \lambda_2)}{\lambda_1 \lambda_2} \tag{27}$$

Where $c$ is the speed of light, $f_1$ and $f_2$ are the frequency of the two optical modes and $\lambda_1$ and $\lambda_2$ are the wavelength of the two optical modes.

The optical modes can be directly generated as an optical comb like in a mode-locked laser, or by combining the signals of two or more single mode lasers, or by modulating a single mode source. These optical solutions for mmW frequencies can provide signals with better stability and quality compared to electrical generation. All these solutions have different level of complexity and different advantages. In the present work we are using an optical comb provided by a mode-locked laser (MLL) for an optically generated local oscillator signal. MLLs have a very good frequency stability, the devices made of semiconductor materials have a small footprint and achievable frequencies in the mmW range. An important advantage of optoelectronic solutions with semiconductors is the possibility of integrating several functions (laser, amplifier, multiplexer, modulator, photodiode) on a single semiconductor chip called a photonic integrated circuit (PIC), as it was already demonstrated [52]. The field combining the high-speed electronics and photonic techniques is called Microwave Photonics, where microwave signal generation, processing and transmission is performed with the help of photonics, benefiting from its advantages [53].

The photonic assisted mixers can be distinguished into 3 groups by their application or mixing method.

*Photomixers*

Photomixers are usually the previously discussed photoconductive devices used for THz generation [54], where the two input continuous wave optical signals with detuned wavelengths are mixed, and a continuous wave radiation (or electrical signal) is generated with a frequency corresponding to the wavelength difference. These devices are usually biased with a DC voltage.

*Photonic mixers*

This type of mixer is performing the mixing in the optical domain. The electrical signals are converted into the optical domain by modulating continuous wave laser beams [55] or can be directly generated by optical elements. The mixed optical signal is then detected with a photodiode, and the output electrical signal of the photodiode is connected to the signal processor. A schematic of the mixing method of photonic mixers is illustrated in Figure 1-19.

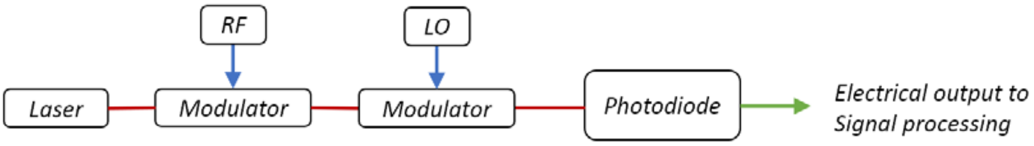

*Figure 1-19 Schematics of photonic mixers. The electrical RF and LO signals are converted into the frequency domain*

*Optoelectronic mixer*

If the mixer has an electrical and an optical input, and the output is an electrical signal containing the mixed products, we are talking about optoelectronic mixers. Their advantage is that the mixer element is also the optical detector in one device. A schematic of the mixing method is illustrated in Figure 1-20.

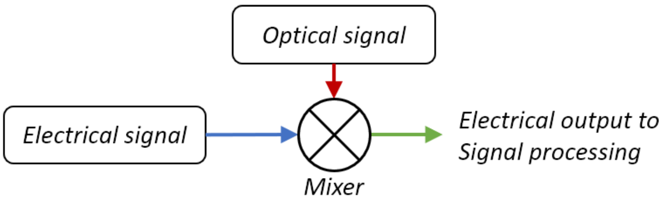

*Figure 1-20 Schematics of optoelectronic mixers. The electrical output contains the mixed products of the input optical and electrical signals*

### I/3.5.a Photonic mixers

Photonic mixers are utilizing various non-linear electro-optic modulators. These devices can be phase-modulators, Mach-Zehnder Modulators (MZMs) in series, or dual-parallel Mach-Zehnder Modulator (DP-MZM) [56]. Their advantage is a high bandwidth in the optical domain, however the systems are limited by the electrical bandwidth of the modulators and photodiodes. In [56] the mixing scheme allowed mixing in the 2 GHz to 26.5 GHz range due to the limit of the electrical hybrid coupler, combining the signals of two photodiodes. However, using higher bandwidth coupler can increase the bandwidth. Commercially available MZMs have a bandwidth of 40 GHz. Unpackaged devices achieved 70 GHz electrical bandwidth and 100 GHz optical bandwidth [57]. Recently, a Lithium Niobate modulator integrated on Silicon achieved an ultra-wide bandwidth beyond 100 GHz [58].

Their disadvantage is due to the inherently non-linear elements, the spurious free dynamic range is low, which can be improved with optimized control of the DP-MZM. In [59] a group from Australia achieved an SFDR of 127 dB*Hz$^{4/5}$ which is 22 dB higher as conventional mixer based on DP-MZM.

### I/3.5.b Optoelectronic mixers

Several opto-electronic devices can be used as mixers: phototransistors [60], electro-absorption waveguide [61] or PIN[1] photodiodes [62]. Another types of photodiodes, the Uni-travelling carrier photodiodes (UTC-PDs), are promising devices with high optoelectronic bandwidth, demonstrated

---

[1] *The* PIN *abbreviation is referring to a 3 layer photodiode structure with p-i-n doped regions. P: p-doped semiconductor, I: intrinsic semiconductor; N: n-doped semiconductor*

up to 310 GHz [63]. The output pulsewidth was measured to be 0.97 ps while illuminating it with 280 fs optical pulses with 1550 nm wavelength. A recent work from University College London (UCL) demonstrated a UTC-PD for optoelectronic mixing working at 600 GHz [64]. A conversion loss of 21.8 dB was also demonstrated using UTC-PD with -2.8 V bias and 18 dBm optical power [65]. These devices present the state-of-art of optoelectronic mixers. Their advantage is the low conversion loss, small footprint and the capability to handle relatively high optical powers of 50 - 100 mW with 1550 nm wavelengths. They are also capable of mixing of wideband signals, a 10 GHz wide NRZ-OOK signal downconversion was demonstrated in [65] at a carrier frequency of 35 GHz. As a downside, the systems utilizing UTC-PDs have to be optimized for optical power and bias voltages because of the PDs non-linear behaviour. The conversion loss and efficiency have a non-linear dependence on the optical power and also on the applied bias voltage. Therefore, its performance can drastically change if they are not operated in the optimum point. These devices should be excited by high optical power in order to screen the internal voltage of the PN junction.

Mixing schemes with UTC-PDs also require additional electrical components: bias-T and bias source for the PD bias, and because of a single input/output port of the UTC photodiodes, an RF power divider is needed to extract the IF signal. A schematic of a mixing setup with UTC-PDs is illustrated in Figure 1-21.

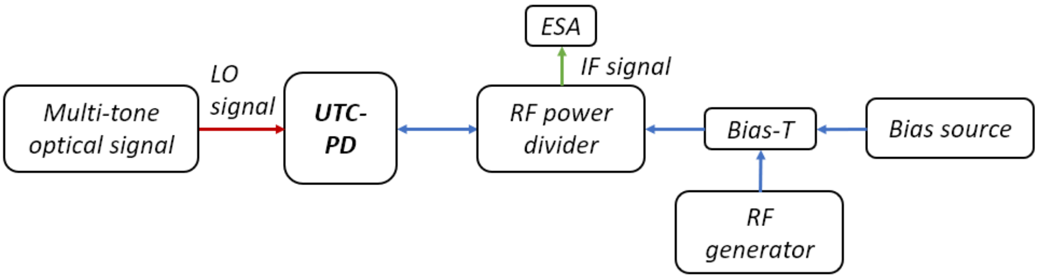

*Figure 1-21 Illustration of a mixing setup with a UTC-PD*

The broadband RF power divider usually has a one way loss of 6 dB, which attenuates the input RF signal to the PD, and attenuates again the extracted IF signal. It also presents a limit for the mixing bandwidth, as the commercially available broadband coaxial dividers are working up to 70 GHz (from DC). Rectangular waveguide diplexers can go until higher frequencies, but the lower frequency limit will be also in the millimetre range.

Photoconductive switches were also used for optoelectronic mixing as it was mentioned in section I/2.1 and I/2.2. A GaAs device was used to downconvert frequencies up to 320 GHz with a conversion loss of 27 dB [35] and an optical power of 19.7 dBm.

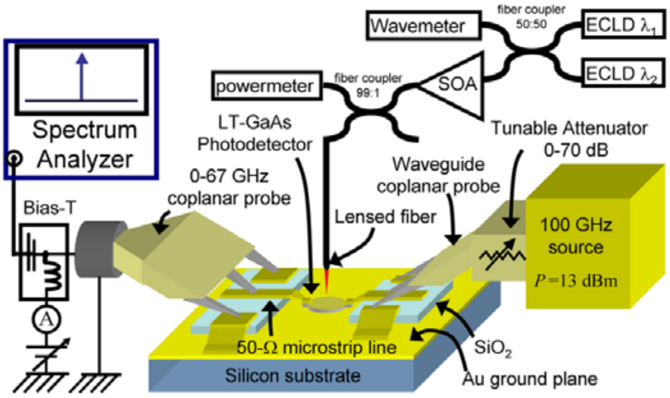

*Figure 1-22*
*Illustration of the mixing setup with photoswitch and two heterodyned single mode lasers as the LO source*
*Source:* E. Peytavit et al. Applied Physics Letters, 2013, *[35]*

The switch was illuminated by heterodyning two lasers with wavelengths in the 780 nm range, the setup is illustrated in Figure 1-22. Another device made of LT-GaAs for 1550 nm wavelengths with resonant structures was proposed in [39]. The measured conversion loss of 65 dB was achieved with 17 dBm optical power. A group in Korea was also experimenting with InGaAs photoswitch application for optoelectronic mixer [66]. In their setup, the measured conversion loss was dependent on the optical LO frequency, as the LO bandwidth was limited to a few hundred MHz, mainly due to the long carrier lifetime of the undoped InGaAs material. With an average optical LO power of 6 dBm and 10 GHz the CL was measured between 51-56 dB for input RF frequencies up to 20 GHz. This CL decreased to 25-35 dB in case of using 1 GHz LO frequency.

These devices, based on photoswitches, do not have the low conversion losses as UTC-PDs, their advantage is the less complex setups for mixing. External biasing of the device is not required for their operation, and because of the coplanar waveguide design, they have two electrical input/output ports for the RF and IF signals. An illustration of the mixing setup is shown in Figure 1-23.

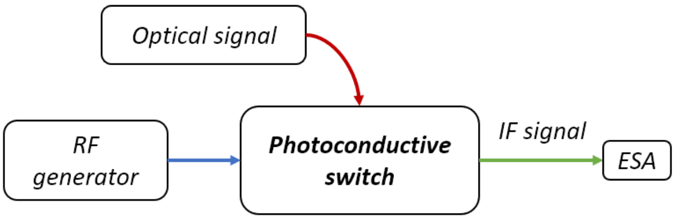

*Figure 1-23*
*Illustration of the mixing setup with photoconductive switches*

In this thesis we are using a similar approach as in [66] and as presented in the above setup. Our proposed device is having a much higher bandwidth thanks to the picosecond response time of the active semiconductor layer. In Chapter IV, we will demonstrate the setup's performance with the downconversion of data-stream modulated electrical signals with an optically provided LO signal.

## I/4. Photoswitch as a sampler

Photoconductive switches can be also utilized as samplers of analog signals thanks to their fast response of laser pulses. In section I/3.2 we were discussing about the mixing with sampling where the focus was on the frequency domain for signal downconversion. In this application we are focusing on the time domain signals. In a sampler device, an RF input signal is sampled to the output thanks to a clock signal. The clock is periodically opening and closing a switch for a very short time to allow through a sample of the RF signal. Ultrashort laser pulses are used as clock signals illuminating a photoconductive switch which has an electrical RF input signal. At the output, the sampled signal as pulses is present, the concept of the sampling is illustrated in Figure 1-24.

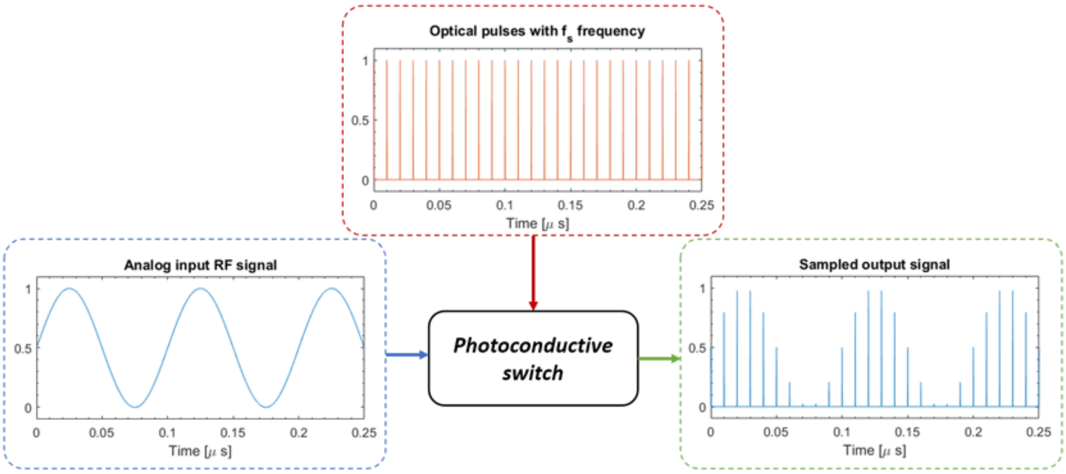

*Figure 1-24 Schematics of RF signal sampling with photoconductive switch and pulsed optical signal*

## I/4.1. Sampling fundamentals

Sampling is a fundamental function of Analog-to-Digital Converters (ADCs). Most of the modern telecommunication systems are working with digital data, for the transmission it needs to be transformed into an analog signal through the modulation of a carrier signal. At the receiver side, this analog signal is transformed back into digital data with ADCs. During the conversion, the short samples of the analog signal after the sampling are quantized. During quantization, digital bits are assigned to the signal levels of each sample. The number of bits determines how many equally distanced levels are distinguished. The number of levels therefore can be an integer power of two. This integer also defines the ADC resolution, for example if we quantize to 4 bits, it means $2^4 = 16$ different levels for all the combinations of the bits, which makes a 4-bit ADC. An illustration of an analog signal with the quantized signal is shown in Figure 1-25.

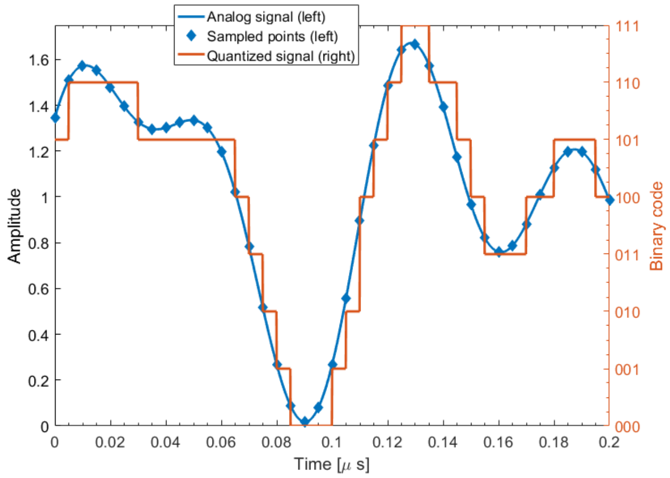

*Figure 1-25*
*Analog signal with sampled points and corresponding quantized signal. Sampling rate is 200 MHz.*

We can see samples taken periodically at every 5 ns (200 MHz sampling rate) of the signal and a quantized level was assigned to each of it, depending on which quantization level the sampled level has the lowest difference to. The example shows a 3-bit quantization with the assigned binary code for each level. The difference between the analog signal and the quantized signal is called the quantization error. The shown 3-bit example presents an ideal case, where there is no noise to interfere with the quantization. However, in real life case, many types of impairments are present: amplitude noise, timing noise, phase noise, thermal noise, shot noise and non-linearities in the system. All these disturbances are reducing the effective resolution. The measure of the real resolution of an ADC is called effective number of bits (ENOB) [67]. If the limiting factors are the nonlinear effects and amplitude noises, the resolution depends on the signal to noise and distortion ratio (SINAD). The SINAD can define the ENOB in this case [67].

$$ENOB = (SINAD[dB] - 1.76)/6.02 \tag{28}$$

The timing noise of the clock signal is called jitter, it shows the deviation of the clock from its ideal timing position. If the timing jitter of the clock is the dominant factor of noise, ENOB can be calculated with the following equation [67].

$$ENOB = log_2\left(\frac{1}{\sqrt{3}\pi f_s \sigma_j}\right) \tag{29}$$

Where $f_s$ is the sampling rate and $\sigma_j$ is the root mean square (rms) timing jitter. The jitter is having a bigger effect on higher resolution sampling. In Figure 1-26 an illustration of the sampling of the same signal with 3 and 5 bits are drawn with the same level of random jitter added to the clock. On the left, while the signal is quantized with 3 bits (8 levels), only one sample's attribution has changed (marked with red arrow) due to the deviation of sampling position caused by the jitter. With 5 bits ($2^5 = 32$ levels) sampling, 7 positions have changed compared to the jitter free sampling.

Figure 1-26 also illustrates the finer quantized curve while using 5 bits resolution compared to 3 bits. Due to the increased number of quantization levels the quantized signal follows the original continuous curve more accurately, therefore the quantization error is reduced. The sampling rate is again 200 MHz for both cases in Figure 1-26.

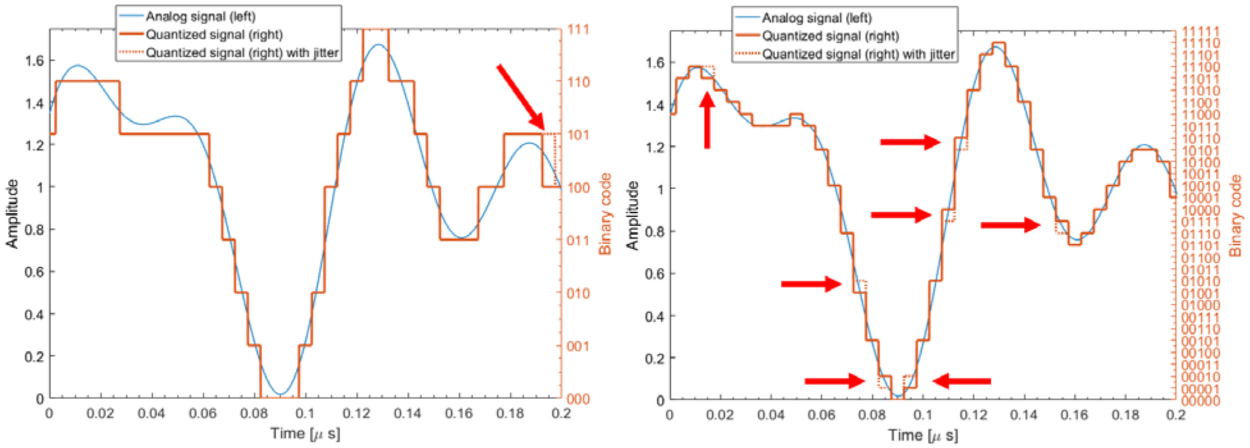

*Figure 1-26 Illustration of the jitter effect on the quantized signal for 3 bits (left) and 5 bits (right), sampling rate is 200 MHz.*

In ADC it is not just the resolution which we can increase to achieve better performance, but also the sampling rate can be increased too. In Figure 1-27 the previous signal is illustrated with doubled sampling rate of 400 MHz for 3 and 5 bits quantization. For both cases, we can see that the number of quantization uncertainty have increased in case of a jittered clock. The figure on the right side shows that the higher sampling rate had a more prominent effect on the higher bitrate sampling, resulting in a more accurate sampled signal, compared to the previous Figure 1-26. Meanwhile in case of 3 bits, the higher sampling rate did not make the sampled signal significantly more accurate.

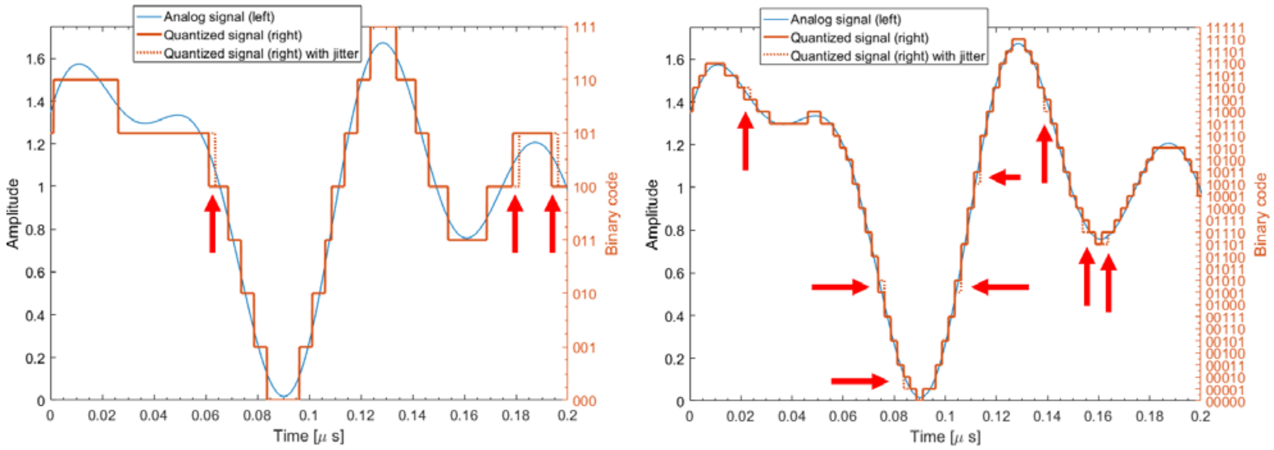

*Figure 1-27 Illustration of the jitter effect on the quantized signal for 3 (left) and 5 (right) bits for doubled sampling rate to 400 MHz*

## I/4.2. Analog-to-Digital converter challenges

Sampling at higher and higher frequencies, the jitter is becoming an increasingly dominant limit in electrical ADC systems, due to the difficulty of generating high quality electrical clocks, as it was described in section I/3.4. In 2012, *A. Khilo* presented in a survey [42] an updated Walden-plot (first constructed by *R. Walden* in 2008 [68]) illustrating the state-of-art analog to digital converters, showing the achieved ENOB by the analog input frequency. The plot is presented in Figure 1-28, it illustrates the performance of the best ADCs found in the literature. The dashed lines are the constant jitter levels needed to the corresponding ENOB - input frequency pairs. The 1 ps jitter limit was reached for electronic ADCs in 1999 and the 100 fs limit in 2007. The graph shows that the best electronic ADCs are having a jitter of 60-80 fs with 100 MHz – 400 MHz input signals. *Khilo* predicts that to increase this limiting with an order of magnitude could take a decade of research. The 10 fs limit was reached in the past years in laboratory environments, using high performance mode-locked lasers, as it is presented in *Khilo*'s paper. Important to note, that all the photonic ADCs in Figure 1-28 are performing undersampling, shown with stars in the figure.

Until the end of the 20th century, the development of electronic ADCs was following the evolution of integrated technology, the usage of photonic solutions did not worth the time and cost of research because they couldn't offer the improvement in speed to make them attractive. Recently, in the electronic sampling systems the signal to noise ratio is reaching the static and dynamic limitations. Adding to that, the rapid evolution of mode-locked lasers (MLL) renewed the interest in photonic solutions, high speed lasers are already commercially available with order of magnitude better timing stability than the electronic clocks. For example, a 100 MHz repetition rate fibre laser from Menlo Systems is available with <2 fs rms timing jitter [69]. As a result, higher sampling frequency with higher ENOB can be achieved with MLL pulses.

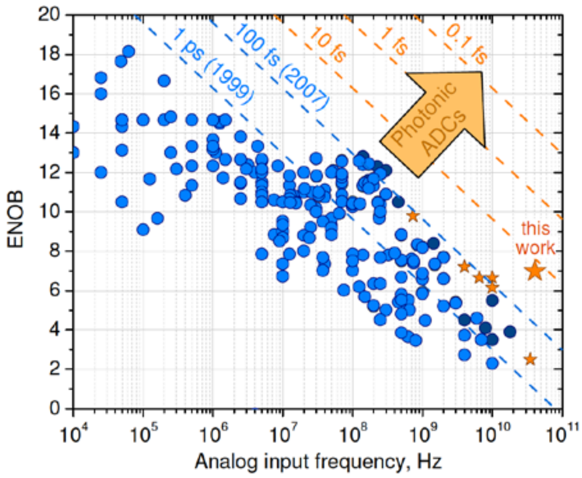

*Figure 1-28*
*Walden plot showing the ENOB and input frequency of ADCs. "This work" refers to work in [42]. blue and dark blue circle represents ADC. Stars shows some high performance photonic ADC. The dashed lines are the needed constant jitter to the corresponding ENOB – input frequency pairs.*
*Source:* A Khilo et al. Optics Express, 2012 *[42]*

### I/4.3. Photonic Analog-to-Digital Converter types

Photonic ADCs are using photonic technology to overcome the limits of electronics. The different technologies can be divided into 4 main categories.

- Photonic-assisted ADC: electronic ADCs with the use of photonic technology to improve one or more limiting factors, sampling and quantization is done in the electronic domain.
- Photonic sampling with electronic quantization: sampling is done in the photonic domain and the quantization is done in the electric domain.
- Electronic sampling with photonic quantization: sampling is done in the electronic domain and quantization in the photonic domain.

- Photonic sampling and quantization: sampling and quantization are done in the optical domain.

The different ADCs can be categorized in these four categories, as *George C. Valley* illustrated it in [67], his diagram is shown in Figure 1-29.

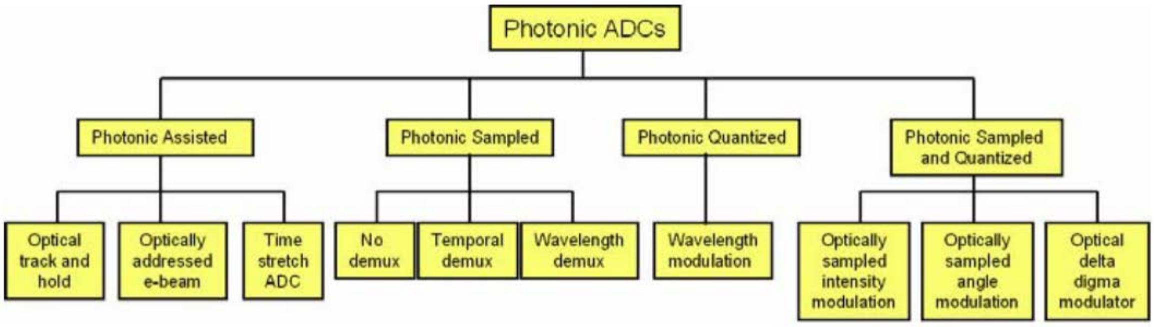

*Figure 1-29 Illustration of the photonic ADC categories. Source:* G. C. Valley, Optics Express, 2007 *[67]*

The photoconductive switch used as a sampler is in the category of photonic assisted ADC, where the low-jitter optical pulses are replacing the electrical clocks. The scheme was first demonstrated by *Leonberger* and *Diadiuk* in 1983 [70]. The team of *R. Urata* in 2003 [71] demonstrated photoconductive sampling of 40 GHz signal with 160 MSamples/s achieving an ENOB of 3.9 bits. A recent work by a group at *Thales* showed the photonic sampling of a signal with 750 MHz bandwidth at 29.5 GHz carrier achieving an ENOB of 5.9 bits [72]. While the RF input signal frequency is in the microwave and lower millimetre wave range, we can see an increase in the bandwidth of the signal with the newest researches. This is allowed by the high frequency mode-locked laser development, which can provide pulse repetition rates in the millimetre wave regime [73]. This allows the use of high-bandwidth telecommunication networks, where the data rates can reach tens of Gbit/s. The Walden-plot shown in Figure 1-28 is not practical to illustrate the newest researches as it is not giving any information about the bandwidth of the samplers, which is becoming more and more important, the superior performance means a higher sampled signal bandwidth.

Another category of photonic ADCs is transforming the RF signal into the optical pulses. Photonic sampling architectures are using an electro-optic modulator (for example an MZM) to convert the electric signal into the optical domain. The pulses then are received by a high speed photodiode. The use of optoelectronic devices raises several issues with this solution. The modulator and photodiode both have to be linear in the operating range. The photodiode must be fast enough to follow the rapid changes in the amplitude of the optical signal and the connecting electronic quantizer must be as fast as the photodiode, therefore this solution doesn't reduce the necessary speed for the electronics [74]. A solution for the electronics' speed problem is demultiplexing the signal in time or in wavelength into arrays of photodiodes, this can enable the use of slower photodiodes and electronic quantizer. Wavelength-division multiplexing was used in the work of *Khilo et al*.[42]. Another research by *Fok et al*. [75] achieved 10 GSample/s also with wavelength multiplexing.

Stretching the optical signal in time can also be used to improve the ADC performance. The wideband optical pulse is first stretched with a high dispersion fiber, then the dispersed, few ns long pulse is modulated by an electro-optic modulator with a short segment of an RF pulse. After the modulation, the pulse is stretched in time further with another high dispersion fiber. The optical signal is received by a photodiode before the electronic ADC. To use this solution in continuous time, the pulses are needed to be stretched to the interpulse time. After the second stretching, a wavelength division multiplexer divides the signal, the channels will be slightly overlapped, which can be used as mismatching calibration during the final interleaving [76]. The advantage of this solution is that it doesn't require fast photodiodes, GSample/s speeds can be achieved with an array of slower photodiodes.

There are intensive researches in every category, and impressive results are achieved, but a commercially available photonic ADC does not exist yet. A huge challenge is the integration of the optical and electronic components into a single chip [77]. One of the best performances was achieved in 2015 by a group at University of California. *Esman et al*. developed a photonic assisted ADC with an ENOB of 7 bits, by sampling a 5 GHz bandwidth signal with 40 GHz carrier [78]. The pulsed laser source was operated at 10 GHz. The work by *A. Khilo et al*. [42] was introducing a photonic ADC digitizing a 41 GHz signal with 2.1 Gs/s, and with 7 ENOB, the group also proposes a feasible solution to integrate every part of the ADC in a single chip using silicone photonic technology.

Each of the above solutions has its advantages, and challenges. As the photonic assisted ADCs are a promising a huge advancement in the DC technology, we are investigating the feasibility of using the photoswitch presented in this thesis as the sampler device for such ADCs. The main advantages of the photoswitches are the easy fabrication, and it can be easily integrated with semiconductor ADC. The output of the device is a sampled RF signal which can be directly digitalized. However, the non-linear behaviour of the sampler device is dramatically reducing the achievable ENOB bits of the ADC. At the end of Chapter IV in this thesis, we will analyse the non-linearities presented by the photoswitch to assess its possible performance in ADCs.

## I/5. Mode-locked lasers

Photonic Analog to Digital Converters and sampling mixers are taking advantage of the optical pulses provided by mode locked lasers (MLLs). MLLs are emitting an optical pulse train with femtosecond or picosecond pulsewidths. The stable pulse trains are suitable to use as a clock in high performance sampler devices in ADCs. The locking term in MLLs is used to describe the phase of the individual longitudinal modes in the laser cavity. They are locked, if the phase difference between the modes is constant, which results in a pulsed emission instead of a continuous-wave (CW) lasing. The frequency difference of the modes corresponds to the free spectral range of the laser, which is also the repetition rate of the pulses. The free spectral range is determined by the length of the laser cavity. In principle this means, that the frequency is not tuneable, but determined at fabrication [79].

### *Fibre lasers*

One popular type of MLL are mode-locked fibre lasers. They composed of a rare-earth doped fibre with high amplifying gain pumped by a CW laser. The achieved pulsewidths are in the femtosecond range, with possible high optical power outputs (>500 mW average optical power). One commercial example is the previously mentioned Menlo Systems C-Fibre laser with 80 fs pulsewidth and 100 MHz repetition rate and low jitter of <2 fs [69]. During the characterisation we are using this laser as the optical source. These types of lasers have the lowest jitter levels, a record low integrated jitter of 14.3 attosecond was achieved in 2014 by a Korean group [80] with a free-running ytterbium-fibre laser, and with a repetition rate of 188 MHz and 1.05 µm wavelength.

### *Glass lasers*

Mode locked laser can be fabricated on rare-earth doped glass too. The group of *F. X. Kärtner* in Germany fabricated a mode-locked laser on CMOS platform [81]. An Erbium doped aluminium-oxide glass was used as a gain medium, and a nonlinear interferometer as a saturable absorber. The glass for the laser structure was deposited on Silicon dioxide. They achieved 4 mW output power and 1.2 GHz repetition rate, while the pulsewidth potentially can be 217 fs (however, it was not measured, just assumed from the optical bandwidth). The jitter performance of this laser was not measured, because of the instabilities due to the Q-switched mode-locking. Also, the laser was emitting in the 1.9 µm wavelength range. Silica waveguides can be also used to construct MLLs, in [82] an erbium doped region was formed in the waveguide which needed a pumping laser power of 400 mW. The output pulses had 440 fs pulsewidth and a repetition rate of 394 MHz and emitting in the 1.5 µm wavelength range. Compared to InP based devices, the output power was lower, reaching only 1.2 mW, however, a very low 24 fs integrated jitter was measured.

### *Semiconductor lasers*

Other type of mode locked lasers is based on semiconductor materials. Their output power is usually is in the 10s of mW range. A popular choice of material is an InAs/InP based quantum dot structures [73]. InP semiconductor-based mode-locked lasers have the advantage of the compact size and can provide laser signals with relatively stable frequency, with a free-running integrated jitter in the picosecond range. Another advantage is that they are emitting in the 1.5 µm wavelength range, a widely used wavelength in the telecommunication system. Higher repetition rates are also available for semiconductor pulsed lasers, a 134 GHz repetition rate MLL with 800 fs pulses was achieved on InP substrate [83]. The same group also demonstrated MLLs with even higher oscillation frequencies at 346 GHz with a 120 µm cavity and 20mW peak pulse powers [84].

In this thesis we are using an InP based semiconductor mode-locked laser, provided by III-V Lab, France. The laser is presented in Chapter III, it is a passively mode locked quantum dash MLL with 24.5 GHz repetition rate. As these lasers are not as stable as fibre or glass lasers, we are constructing an all-optical feedback loop to stabilize the laser output with self-injection feedback. This setup allows to reach sub-ps jitter values, suitable to use as a high quality clock.

## I/6. Outline and Goals of the Thesis

In this first introductory chapter, we described the physical behaviour of photoconductive switches and their main applications. States of the art devices were introduced with advanced photoconductive technology. We introduced the three main applications where photoconductive devices are used for. The detection and generation of THz waves is the most frequent application for such devices. Optoelectronic mixing in the mmW range with photoswitches is an area not yet in the mainstream of research interest mainly due to their low conversion efficiency. However, optimizing the design of the device might lead to better performances. As the third application, the photonic assisted sampling is a very promising technique, it can offer at least an order better performance than fully electronic solutions.

In the following Chapter II, we are characterising an InGaAs photoconductive switch. We are showing its ultrafast response time by an opto-electronic autocorrelation experiment. This response being in the picosecond range suggests and ultrawide optical, and optoelectronic bandwidth of the photoswitch in the millimetre wave range. An equivalent circuit model is constructed for the electrical modelling of the switches.

In Chapter III, an InP based semiconductor mode-locked laser is presented and characterised. We describe a passive feedback method for the stabilization of the laser output signal. As the result, the stable optical pulses in the picosecond range and with 24.55 GHz repetition rate provides a high quality microwave signal generation. We propose to use the laser as the optical source for optoelectronic mixing applications with the photoconductive switch. The stable optical pulses can also be used as the sampling clock.

In the fourth chapter, after the characterisation of the two devices, we are aiming to show their performance used together through applications. The switch and the laser source are combined to perform optoelectronic mixing. The mixer is demonstrated through downconverting QPSK modulated data-stream signals from the microwave frequency band around 20 GHz. The data-stream bandwidths up to 2 Gbit/s, are showing that the mixer can be operated with wide bandwidth signals. Different solutions are proposed based on the photoswitch used with different method of optical frequency generation. The demonstrations are also showing that the data-stream modulation can be applied either on the optical signal or on the electrical signal. The setups are feasible solutions in the Radio-over-fibre receivers as they propose a simple frequency downconverter. An introductory characterisation of the non-linearities of the sampling function is also given to show the feasibility of sampling with this photoswitch.

Finally, a conclusion will summarize the main results of this thesis and will open the discussion for further development.

# Chapter II

# InGaAs photoconductive switch

II/1. The photoswitch samples ........ 49
  II/1.1. Switch fabrication ........ 51
  II/1.2. Characterisation setup ........ 52
II/2. Electrical Characterization ........ 53
  II/2.1. Coplanar waveguide simulation ........ 53
  II/2.2. Photoswitch RF response in the dark state ........ 55
  II/2.3. Dark resistance in DC ........ 56
  II/2.4. Photoswitch equivalent circuit model ........ 57
  II/2.5. Improving the equivalent circuit model ........ 58
  II/2.6. U-I characterization ........ 60
II/3. Optoelectronic characterization ........ 61
  II/3.1. Measurement setup ........ 61
  II/3.2. Dispersion of laser pulses ........ 62
  II/3.3. Photoswitch response with sampling oscilloscope ........ 64
  II/3.4. Measurement with opto-electronic autocorrelation ........ 66
    II/3.4.a Simulation of the autocorrelation curve ........ 66
    II/3.4.b Measurement setup ........ 67
    II/3.4.c Typical measurement result ........ 69
    II/3.4.d Measurement corrections ........ 70
    II/3.4.e Curve fitting ........ 72
II/4. Conclusions on Chapter II ........ 74

In this chapter the InGaAs photoconductive switches are described and electronic and opto-electronic characterization is performed to obtain its static and dynamic properties.

## II/1. The photoswitch samples

The fundamental element of this thesis are the photoconductive switch samples, they are provided by University College London (UCL). The design and fabrication were done in the United Kingdom, with the designs of *Dr. Chris Graham* from UCL. A basic characterization and sampling experiment have already been performed in 2012 at UCL [29]. Taking his work as a starting point, we also performed the electrical characterisation of the samples in terms of dark resistance, I-V curve and frequency response, detailed in section II/2. The electro-optic characterization measuring the switch response time to femtosecond laser pulses is detailed in section II/3.

Two substrates were available, each with several switch samples. A smaller substrate, identified as “S”, with 24 switches, and a larger one, identified as “L” with 30 switches. A photograph of the smaller substrate through a microscope is shown in Figure 2-1, the real size is around 4 x 3 mm$^2$.

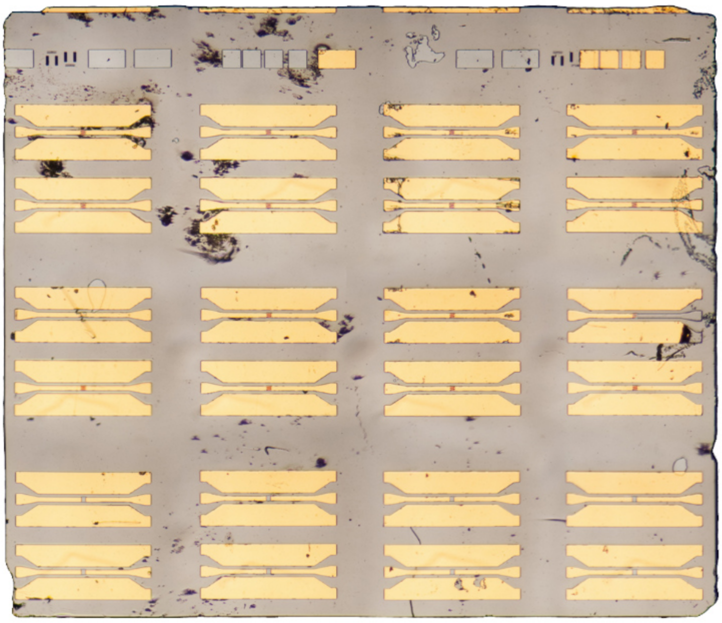

*Figure 2-1*
*Substrate "S" magnified view*

The substrate material is semi insulating iron doped indium phosphide (Fe:InP), seen with grey colour in Figure 2-1. The yellow colour is the deposited conductors made of gold. A magnified view of one switch sample is illustrated in Figure 2-2. It has a size of 750 x 270 µm$^2$ and consists of a coplanar waveguide (CPW), without ground at the bottom of the substrate. The waveguide has an inner conductor width of 25 µm and a gap of 16 µm. The outer conductors are serving as the ground.

The CPW line is interrupted by a gap in the middle, where the InGaAs switch structure can be found as a mesa. This mesa has a size of 25 x 25 µm$^2$ and is made of indium gallium arsenide (InGaAs). Electrodes with interdigitated arrangement were deposited on top of it. Three different electrode geometries were designed, magnified views are showing all three in Figure 2-3, and TABLE 1 details their geometries. The types are identified by the width of the fingers and the width of the gap between the fingers. There are 8 switches on the S sample without any fingers on the mesa, we identify them as “N”.

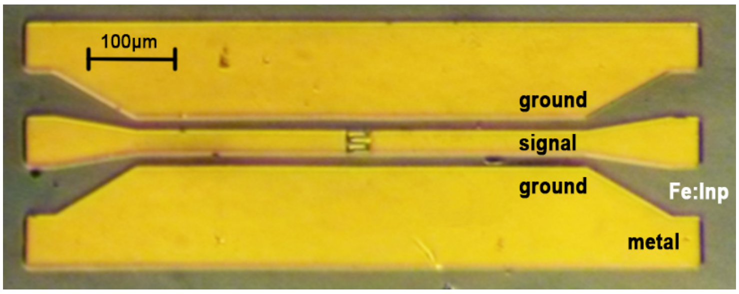

*Figure 2-2*
*Magnified view of a switch*

The CPW line has a characteristic impedance of 50 Ω. Close to the sample edges the CPW widens, while keeping the 50 Ω impedance. This widened CPW makes it possible to connect the switch to coplanar electrical RF probes during the experiments. The geometry allows to use probes with pitch sizes of 100 µm or 150 µm. All the switch samples on both substrates are identical in size and material, the only differences are the geometry of the interdigitated structures.

*TABLE 1 GEOMETRIC PROPERTIES OF SWITCHES ON EACH SAMPLE*

| Type | Finger width | Gap width | Number of fingers # | Number of switches |
|---|---|---|---|---|
| 3:3 | 3 µm | 3 µm | 4 | S: 8<br>L: 6 |
| 3:5 | 3 µm | 5 µm | 4 | S: 8<br>L: 18 |
| 5:5 | 5 µm | 5 µm | 3 | S: -<br>L: 6 |

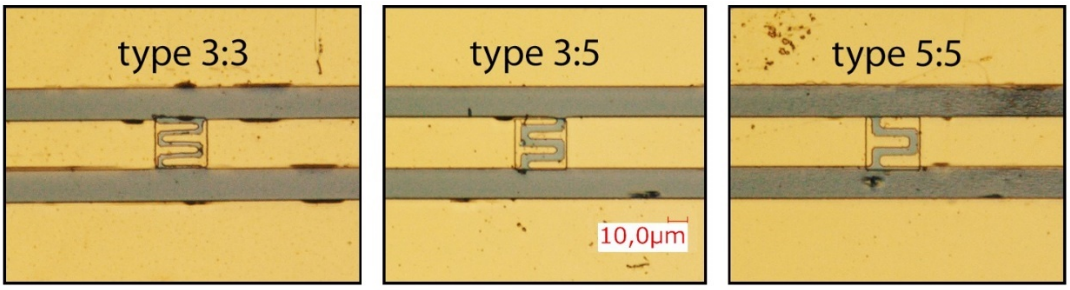

*Figure 2-3 Microscope view of the 3 switch types*

The identification of each switch is following a matrix style rule. A top view orientation was selected by arranging the substrates with an identifiable excess deposited metal, as we can see some squares on the top of the S substrate in Figure 2-1. In this orientation the switches in one row are the same type, arranged in groups of two, we assign a number to each row of groups of two, and a letter to each column A, B, C or D. The first part of a switch ID identifies the “S” or “L” substrate, and the second character identifies the column. The third character is the row number, and the last number is 1 or 2, which selects the top or bottom switch in the group of two.

One ID can be constructed as the following:

{ L , S } { A , B , C , D } { 1 , 2 , 3 , 4 , 5 } - { 1 , 2 }

Figure 2-4 illustrates the two samples with all the switch IDs and their locations. For instance, the switches *SA2-2* and *SC1-1* will be later on investigated (see Table 6.), they are both type 3:5, with 3 µm wide fingers and 5 µm gap between them.

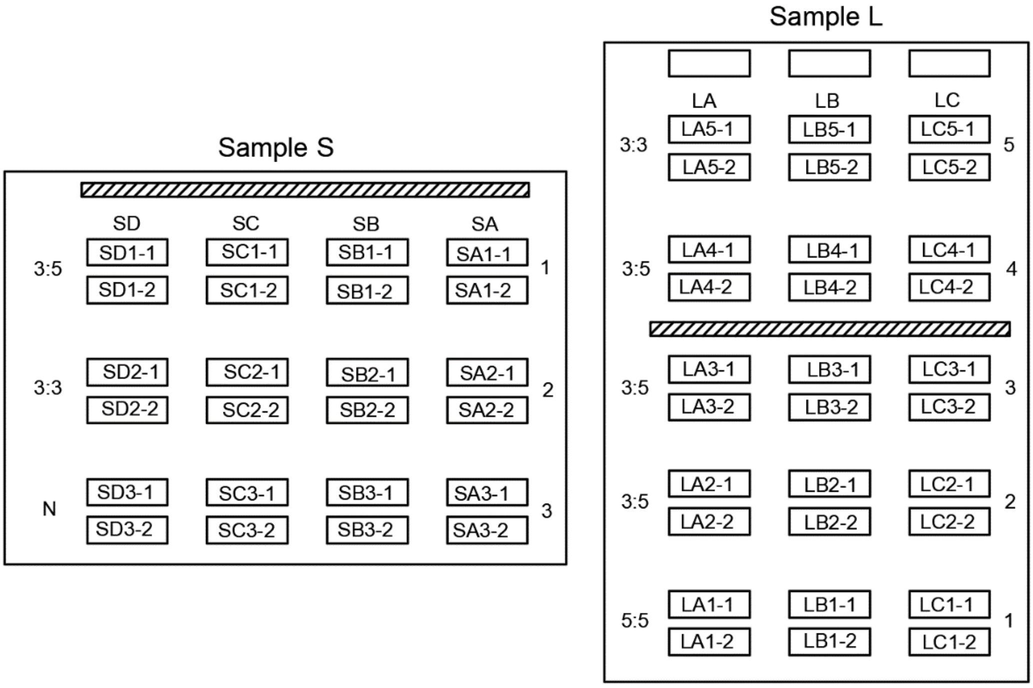

Figure 2-4 Switch IDs

## II/1.1. Switch fabrication

The photoswitch samples were available readily for this thesis. They were fabricated in 2012 at UCL and University of Surrey in the United Kingdom. In the publication by *Dr. Chris Graham et al.* [29] the fabrication process is detailed thoroughly, here we detail some of the descriptions of the processes from the paper, which are essential to know to properly understand the photoswitches.

The material structure is composed of 5 layers on top of each other. The substrate is Fe:InP semi-insulating material. On top of this a 300 nm thick InGaAs layer is matched with 80 nm Fe: InP buffer. The InGaAs layer is followed by a 50 nm thick n doped InGaAs layer to enhance the ohmic contact of the electrodes and the semiconductor. This is followed by a 50 nm thick n-doped InP layer as an etch stop layer. The 25 x 25 µm$^2$ mesa structure is fabricated by wet-etch and photolithographic methods from this layered structure. After the deposition of metallic alignment marks, the ohmic contact layer, etch stop layer and InGaAs layers were removed with wet etch and well established reagents, to form the 400 nm thick mesa. The electrodes with 20 nm chromium and 350 nm gold layers were deposited on the mesa and similarly the coplanar waveguide structure on the substrate. Selective etch method was used to remove the n-doped layers between the fingers by using the metal electrodes as the mask. This isolates the electrodes electrically. An illustration of the material structure after the full fabrication process is shown in Figure 2-5, this figure is a cross section at the position of the mesa.

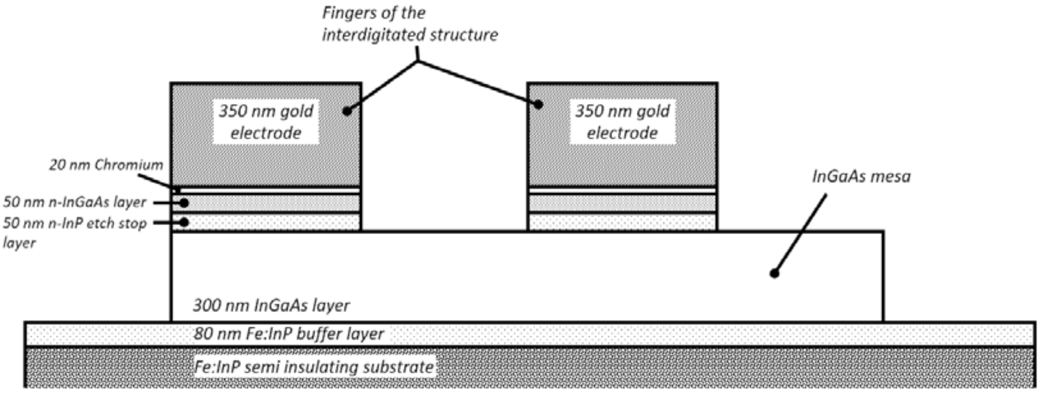

*Figure 2-5 Cross-section of the photoconductive switch. Vertical and horizontal dimension are not in scale*

Before the etching, the samples were nitrogen-ion implanted at University of Surrey. As the result of the ion-implantation, the irradiated ions displaced the gallium and arsenide atoms in the material. These displacements are producing vacant gallium and interstitial arsenide sites and creating an EL-2 trapping level (around 0.71 eV) in the bandgap [85], and ensures a picosecond carrier recombination time. The illustration of the electron band structure is shown in Figure 2-6. The implantation energy was 4 MeV with $10^{13}$ cm$^{-2}$ fluence. With this energy the ions are coming to a rest deep in the substrate. The sample was heated to 200°C during the implantation. This method required no annealing step in contrast to iron doped InGaAs. A trap concentration of $5*10^{17}$ cm$^{-3}$ was estimated which makes an estimated average recombination time of around 1 ps.

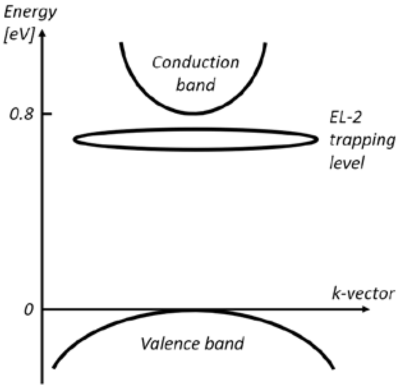

*Figure 2-6 Illustration of the InGaAs bandgap with the EL-2 trapping level created by the ion-implantation*

The InGaAs bandgap of 0.8 eV means that it is sensitive to 1.5 µm wavelengths. These wavelengths are widely used in today’s telecommunication networks, making the photoconductive switch compatible with modern systems.

### II/1.2. Characterisation setup

The characterization and experiments described in this chapter and in the following ones, were performed on an RF probe station (Karl Süss PM8), on-wafer with coplanar waveguide electronic probes directly connected to the two sides of the switch. The probes are from Cascade Microtech , from their Infinity Probe® series, and were used for both DC and RF measurements. During the measurements we used two types: i40 GSG-150, and i67 GSG-100. They had 150 µm and 100 µm pitch sizes respectively and verified for DC to 40 GHz and to 67 GHz bandwidths. The illuminating laser beam was guided to the switch mesa through an optical fibre and it was positioned with a third probe arm on the probe station. The used fibre was a pig-tailed single mode fibre with a clean-cut end, illuminating the switch from the top with a small tilt. The fibre end was set in a distance from the switch to have the laser spot as big as possible while the whole spot is inside the switch area. Because of the small dimensions, the probe and fiber positioning was done with the help of a microscope, the tilt of the fibre probe ensured that the view is not obstructed, and it also prevented the back reflection of the laser beam from the switch surface into the fibre. A photograph of the setup is shown in Figure 2-7. Considering the energy of the optical pulses, the temperature change of the device is negligible and will not have any effect on the performance, therefor the temperature control of the device is unnecessary. In addition, the laboratory environment where the measurements were performed was temperature and humidity controlled.

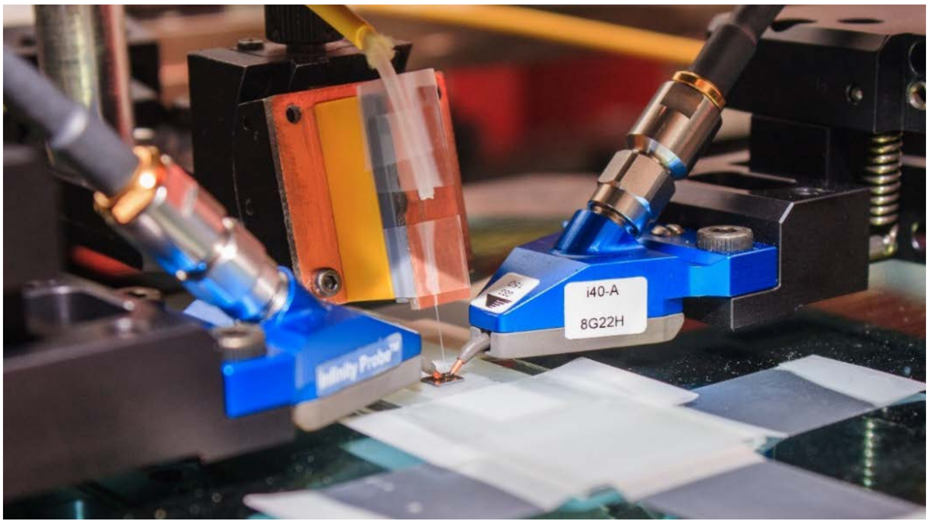

*Figure 2-7 Setup on the probe station with two RF probes and the fibre holder*

## II/2. Electrical Characterization

The electrical characterization of the photoswitch is aimed to obtain its static and dynamic electrical properties. The measurements included the frequency response measurement, dark resistance and U-I curve. Using the results, we could construct a basic lumped element electrical model of the switch.

### II/2.1. Coplanar waveguide simulation

The photoswitch consists of a coplanar waveguide without ground at the bottom, on an Indium-phosphide substrate. This waveguide has a characteristic impedance around 50 Ω, both for the central part and the wider part at the sides. We made simulations to confirm its impedance from the geometry. There are various software available to calculate the characteristic impedance of transmission lines. It is also possible to calculate it numerically with approximate closed form expressions [86]. We are using a simple tool, called TX-Line from National Instruments (formerly known as AWR Corporation). The geometry of the switches' CPW line are detailed in TABLE 2 for the probe pad section and the central section. The values are estimated from magnified images of the sample by comparing the geometric features to the 25 µm * 25 µm central mesa.

*TABLE 2 SWITCH WAVEGUIDE GEOMETRY*

| | CPW line | Probe connection pad |
|---|---|---|
| Gap width | 16 µm | 52 µm |
| Signal conductor width | 25 µm | 57 µm |

For the calculation the precise value of the substrate permittivity (InP material) is also needed. InP permittivity is $\varepsilon$ = 12.4, which does not change due to the ion implantation [29].

The above values are giving a 56.4 Ω characteristic impedance for the CPW at the probe connection and 51 Ω for the central CPW. The RF probes and most of the used equipment have an impedance of 50 Ω. We modelled the effect of this small impedance mismatch to show that its effect is not significant, the impedance matching is good. We used the Microwave Office (MWO) software from National Instrument (formerly known as AWR Corporation). The simulator software is capable of simulating microwave circuits with lumped elements and also with distributed elements, its built-in library contains various transmission line structures. It is not a 3 dimensional electromagnetic simulator, the transmission lines (coaxial, microstrip line, coplanar waveguide etc.) are defined with the substrate and the geometry, and the software computes the appropriate equations for the chosen transmission line. With this software we are able to design and simulate planar microwave circuits easily and fast with a good accuracy. The model of the switch's transmission line included the short 30 µm long pad for the RF probes, the 70 µm long tapered CPW which converts between the wide and narrow CPW lines, and the 420 µm long CPW around the switch mesa. The switch mesa was not included, here we are investigating only the CPW lines. The schematic view of the model is illustrated in Figure 2-8.

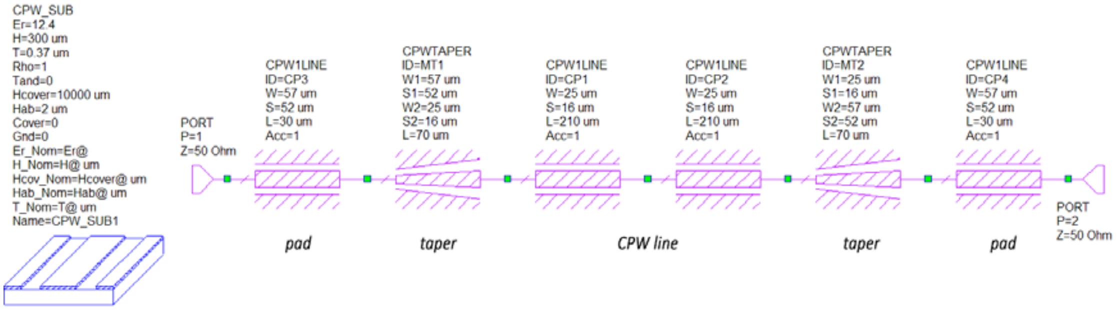

*Figure 2-8 Microwave Office model of the CPW waveguides*

The simulation was done with a lossless substrate (*tanδ = 0*) and perfect conductors. All the elements were between two 50 Ω ports in order to analyse the S-parameters of the circuit. The simulation results are drawn in Figure 2-9, left axis for $S_{11}$ , right axis for $S_{21}$ parameter. The $S_{21}$ curve shows that up to 200 GHz we have only 0.4 dB loss due to the mismatch, the $S_{11}$ reflection parameter is below -20 dB up to 190 GHz, which is considered a good matching.

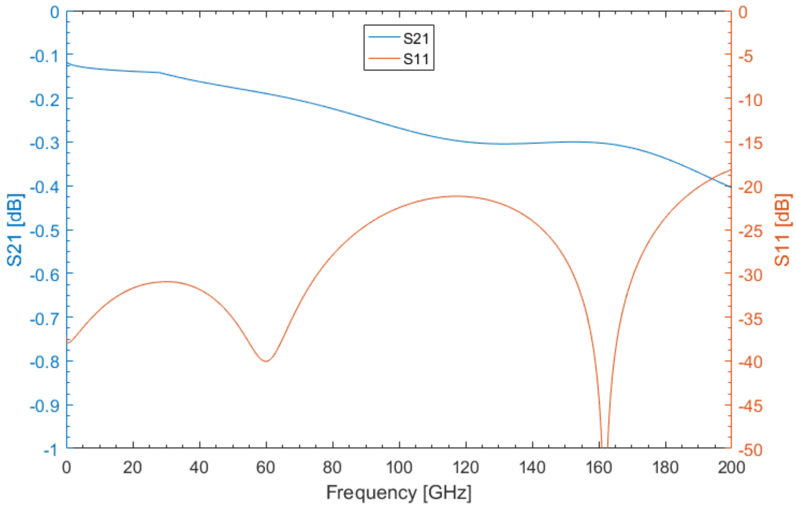

*Figure 2-9*
*Simulated $S_{11}$ and $S_{21}$ parameters of the circuit in Figure 2-8*

## II/2.2. Photoswitch RF response in the dark state

As the first measurement of the characterization we investigated the frequency response of the non-illuminated samples with a Vector Network Analyser (VNA, Anritsu 3739D 40 MHz – 65 GHz). The VNA was calibrated with the RF probes, so their contribution is not present in the results. The i67 probes were used, directly connected to the VNA. We obtained the S-parameters up to 65 GHz, limited by our equipment. We measured the S-parameters for all the switches on both samples. The results for the *S* sample are illustrated in Figure 2-10 ($S_{11}$ parameter) and in Figure 2-11 ($S_{21}$ parameter), and for the *L* sample in Figure 2-12 ($S_{11}$ parameter) and in Figure 2-13 ($S_{21}$ parameter). The 3 different types of switches can be easily distinguished from the results, due to their different properties. The curves corresponding to the blank switches are showing the highest losses.

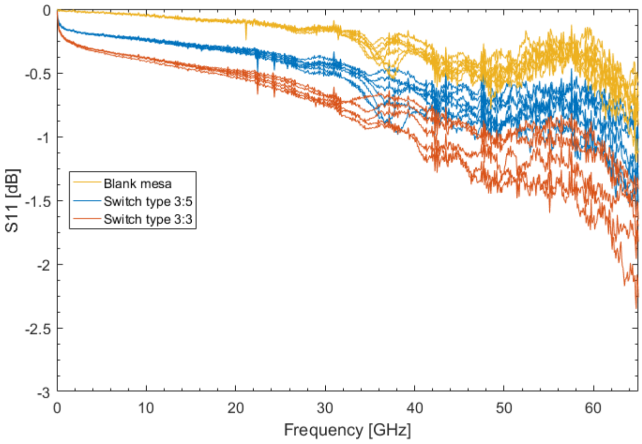

*Figure 2-10*
*Measured $S_{11}$ parameters for the S sample switches*

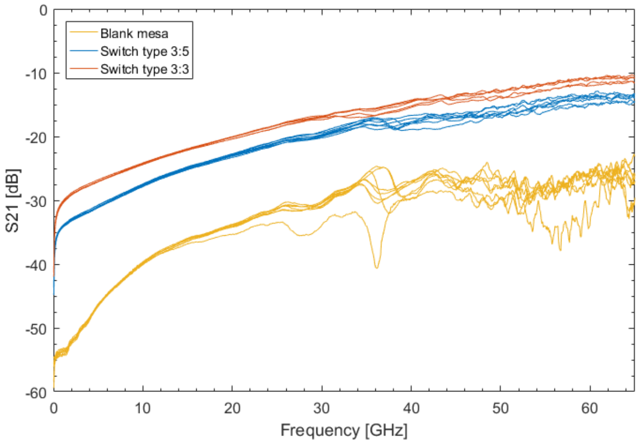

*Figure 2-11*
*Measured $S_{21}$ parameters for the S sample switches*

The results show that the feedthrough of the signal is increasing over the frequency and it is also depending on the switch type because the different switches have different capacitances depending on the finger number and gap size.

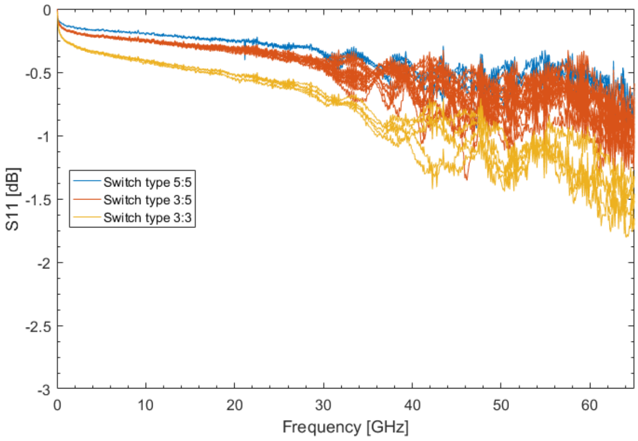

*Figure 2-12*
*Measured $S_{11}$ parameters for the L sample switches*

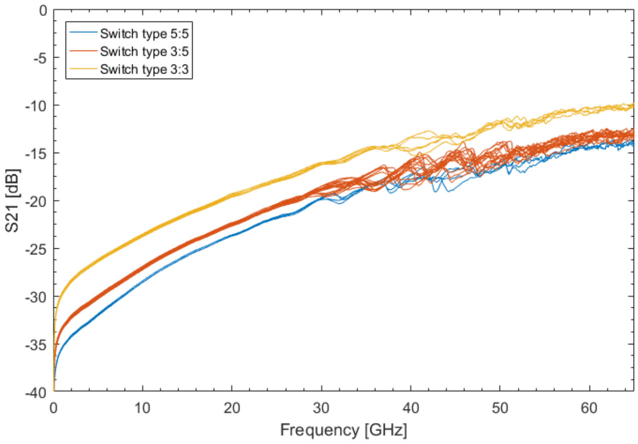

*Figure 2-13*
*Measured $S_{21}$ parameters for the L sample switches*

In Figure 2-14 and Figure 2-15 the same types of switches are compared from the two samples, it shows that practically there is no difference between the two samples.

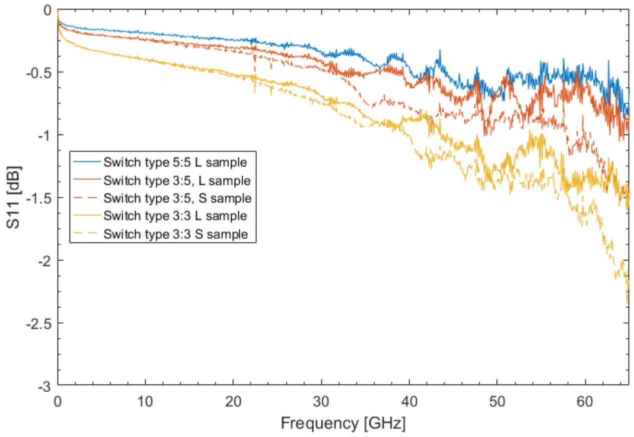

*Figure 2-14*
*$S_{11}$ parameters, comparing the two samples*

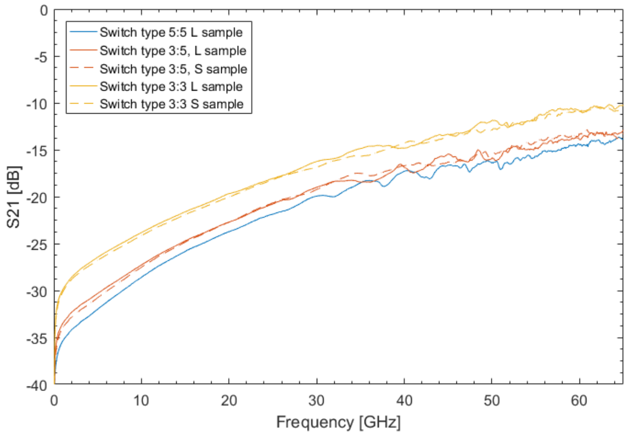

*Figure 2-15*
*$S_{21}$ parameters, comparing the two samples*

In all the previous measurement curves we can observe that at higher frequencies the curve is less smooth, mainly above 40 GHz. This could be attributed to the background noise and the device features at high frequencies. Some of the switches was measured also in a narrower 35 GHz calibrated band between 30 GHz and 65 GHz, with the VNA to rule out the possibility that this is due to the imperfect wideband VNA calibration. The wide and narrower results show a very good fitting, confirming the measurements.

## II/2.3. Dark resistance in DC

The dark resistance measurement was done by using a digital multimeter between the two sides of the inner conductor of the coplanar waveguide. For photoswitches, this value is preferably high, in order to have a good RF isolation of the switch. We measured the resistance at DC level where we obtained values in the 40 – 100 kΩ range. The 3 types of switches have different resistances, the measured minimum and maximum value for each type are the following:

- Type 3:3 : 37-57 kΩ
- Type 3:5 : 80-104 kΩ
- Type 5:5 : 73-76 kΩ

Some switches are showing values significantly different than the average for its type, which are not included in the above list. For example, switch SB1-1 (type 3:5) is measured to be 18 kΩ which is the fraction of its supposed value by the measurement of the other samples of the same type. This could be a result of a manufacturing fault making two electrodes closer to each other. Investigating that switch with a microscope we didn't observe any imperfections, however we had limited magnification. On the RF response measurement in section II/2.2 these switches with the unexpected dark resistance showed the same performance as the others, so we can conclude that the difference is not due to the semiconductor material difference.

In an earlier measurement at UCL a dark resistance of 6 kΩ was measured [29]. There is no indication in the paper about the measurement setup, but it is most likely that it was not performed at DC level. The higher dark resistance measured by us, is also confirmed by the $S_{21}$-parameter measurement curves in Figure 2-15. At lower frequencies a sharp drop is observable, at the minimum measured frequency with the VNA of 40 MHz, it is reaching values below -40 dB, which in a system of 50 Ω connections indicates an equivalent dark resistance of >10 kΩ.

### II/2.4. Photoswitch equivalent circuit model

Based on the S-parameter and the dark resistance measurement we can construct a simple equivalent circuit of the switch and determine its equivalent capacitance. The circuit is modelling the switch electrical behaviour in the dark state without optical illumination, therefore it is not sufficient to model the dynamic optoelectronic behaviour of the switch. The circuit is a simple parallel resistance-capacitance (R-C) pair. Where the resistor models the dark resistance ($R_{dark}$), and the capacitor ($C_p$) models the switch capacitance. This equivalent circuit was first proposed by *D. Auston* in the late '80s [87]. We investigated two models, one with the previous model of the coplanar waveguide, and the other one is without it. In the second case the equivalent capacitor and resistor contains the waveguide capacitance too, therefore gives an equivalent capacitance for the full sample not just the switch mesa as in the first case. The simulation was done with the previously used MWO software, an illustration of the model with the CPW line is shown in Figure 2-16.

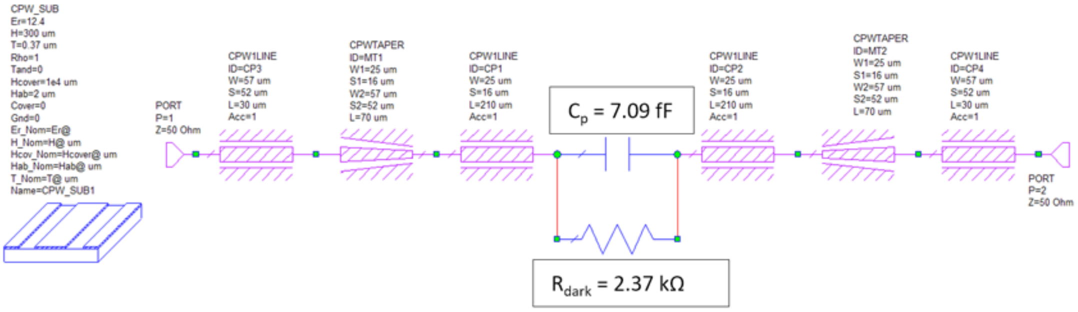

*Figure 2-16. Switch model with the CPW line and the R-C equivalent circuit*

In the simulation we were fitting the S-parameter curves of the model on the measurement curves by adjusting the resistor and capacitor values. The result of the best fitting has the values for $R_{dark}$ = 2.37 kΩ and for $C_s$ = 7.89 fF for a type 3:3 switch, the fit is illustrated in Figure 2-17, the curves are compared to the measurement results. The model has a good agreement with the measured $S_{21}$ curves for frequencies above 10 GHz. In the model we used lossless waveguides, which can explain the difference in the $S_{11}$ curves.

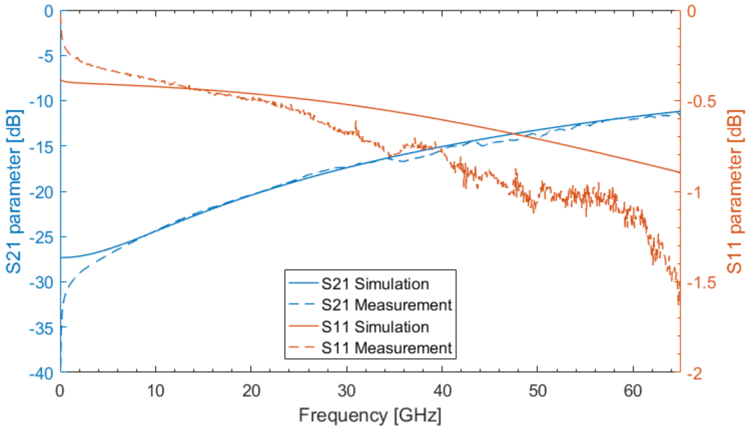

*Figure 2-17*
*Measurement and fitting of a type 3:3 switch with the model of Figure 2-16.*

The fitted values (maximum and minimum for all measured switch) for the three switch types are listed in the next table (Table 3) with and without the waveguide built-in model. In case the CPW line is also simulated, the needed capacitance in the equivalent R-C circuit is 0.1 – 0.2 fF lower, which indicates that this transmission line has a capacitance around this value.

*Table 3. Photoswitch equivalent circuit fitted values for simulation*

| | With CPW model | | Simple R-C circuit | |
|---|---|---|---|---|
| | *Resistance [kΩ]* | *Capacitance [fF]* | *Resistance [kΩ]* | *Capacitance [fF]* |
| Type 3:3 | 2.1 – 2.2 | 7.9 – 7 | 2.22 – 2.3 | 8.1 – 7.1 |
| Type 3:5 | 3.7 – 4.1 | 5.7 – 5.5 | 4 – 4.3 | 5.83 – 5.35 |
| Type 5:5 | 5.05 | 5.13 | 4.9 | 5 |

The values of the fitted capacitances between 5 fF and 8.1 fF are suggesting a wide electrical bandwidth of the switch and a short response time. In a 50 Ω system, this capacitance and resistance values are giving an electrical characteristic time around 300 fs for the switch.

## II/2.5. Improving the equivalent circuit model

The simple R-C model does not satisfy the lower frequencies of the measurement. The equivalent resistance in the model is in the 2-5 kΩ range, while the sharp drop in the measurement curves ($S_{21}$) suggests that the resistance increases significantly below 5 GHz, confirmed by the dark resistance measurement. Around DC it is tens of kΩ which decreases fast with increasing frequencies until it reaches a resistance as in the previous model.

An improved model has been designed to satisfy the lower frequency range, it contains 3 parallel components. The first component is modelling the dark resistance ($R_{dark}$) with the measured value in section II/2.3. A second component is a main capacitor ($C_p$), modelling the equivalent capacitance of the switch, its value is important mainly at higher frequencies (>15 GHz). The third component is a series R-C ($R_s$ and $C_s$), which is acting as a high pass filter to model the sharp decrease in the curve around 1 GHz with a resistor value similar to the previous model and a capacitor around 70 fF. These two values define a cut-off frequency around 4 GHz for this circuit branch, so at higher frequencies the resistance of the switch model is approaching the resistance value in this branch. The circuit is illustrated in Figure 2-18. With this model we are correctly modelling the measured dark resistance at DC and the lower dark resistance at higher frequencies.

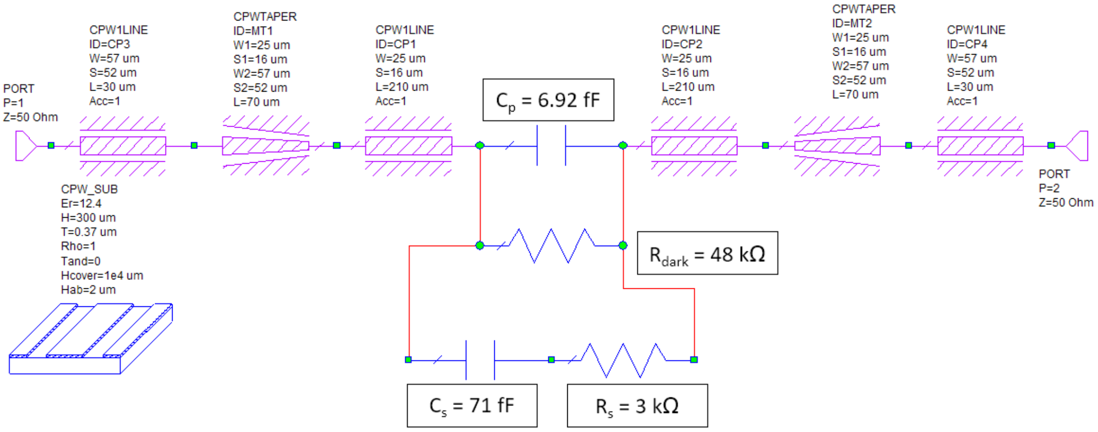

*Figure 2-18 Schematics of the improved equivalent model of the photoswitch*

The values of the 4 components are optimized to fit the measurement curve. For the single resistor, we set the dark resistance value measured for the corresponding switch, which in case of the SC2-2 switch (type 3:3) is: $R_{dark}$ = 48 kΩ. The single capacitor value is similar to the one in the previous basic circuit: $C_p$ = 6.9 fF. The best fit was achieved with values for the series R-C of $R_s$ = 3 kΩ and $C_s$ = 71 fF. The result curve with these parameters is illustrated in Figure 2-19.

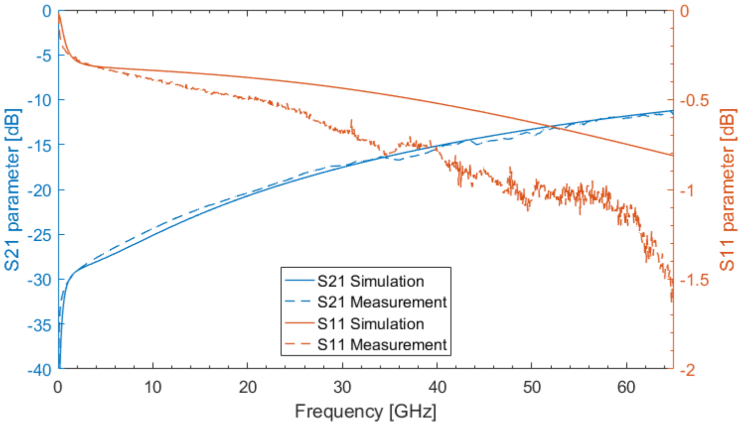

*Figure 2-19 Measurement and fitting with the improved circuit of a type 3:3 switch with the model of Figure 2-18*

We can see that the simulation has a very good fit on the measured $S_{21}$ values.

Despite the accurate model, the role of the circuit elements is not properly understood, it needs further investigation to understand the physical meanings behind all the elements of the circuit.

## II/2.6. U-I characterization

The photoswitches were characterized with the output current versus bias voltage to analyse its dark current, and non-linearities. In Chris Graham's paper [29], U-I curves were measured in the dark state and under continuous wave illumination with optical powers up to 50 mW, illustrated in Figure 2-20.

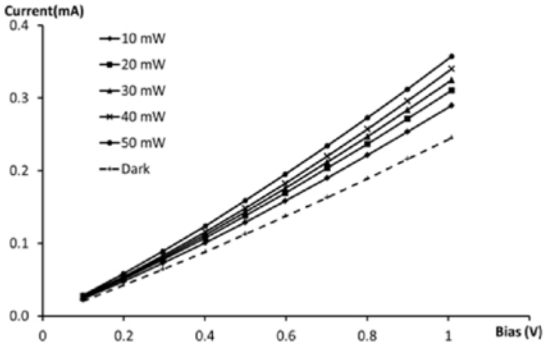

*Figure 2-20*
*U-I curves of a type 3:5 switch Source:* C. Graham et al, Optics Express, 2012 [29]

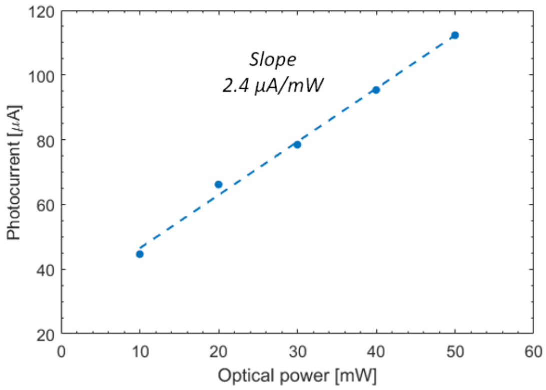

*Figure 2-21*
*Photocurrent drawn from data in Figure 2-20 with 1 V bias*

The bias was swept up to 1 Volts. The dark state measurement indicates a closely linear curve, translating it into the dark resistance, its value is around 5.9 kΩ ± 0.3 kΩ. An increase in the photocurrent is also observed with increasing optical powers, Figure 2-21 shows the photocurrent by the optical power for 1 Volt bias (*photocurrent = current under illumination - dark current*). The slope gives a responsivity of 2.4 µA/mW.

We performed the same measurement, the switch was DC biased from one side, and the current was measured on the other side. We swept the bias from 0 to 4 Volts and we did not illuminate the switch. Figure 2-22 shows typical curves for the 3 switch types.

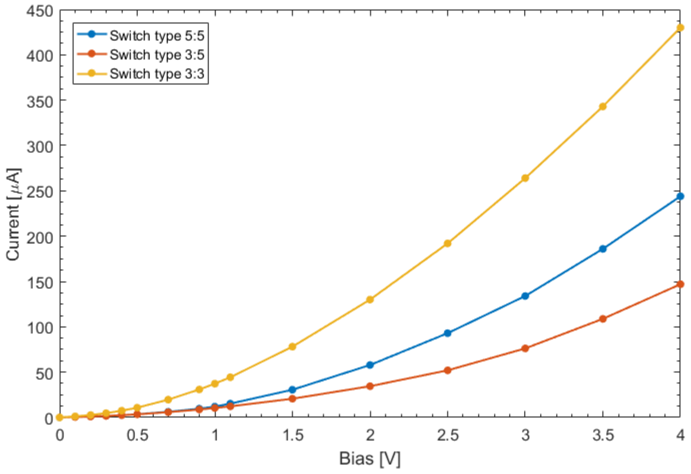

*Figure 2-22*
*Bias voltage - dark current curves of the 3 switch types*

Our measured curves are differing from the one in Figure 2-20 obtained at UCL. The lower level of currents measured by us, indicates the previously obtained higher dark resistance too. These differences suggest that the devices measured at UCL and by us, are a bit different. This difference is unknown, one possibility can be a slightly different deposited metallic structure.

For the photocurrent measurement we used a continuous wave optical signal with 1.94 mW optical power. We measured type 3:5 photoswitch with the lowest dark resistance, in order to have the highest dark current available.

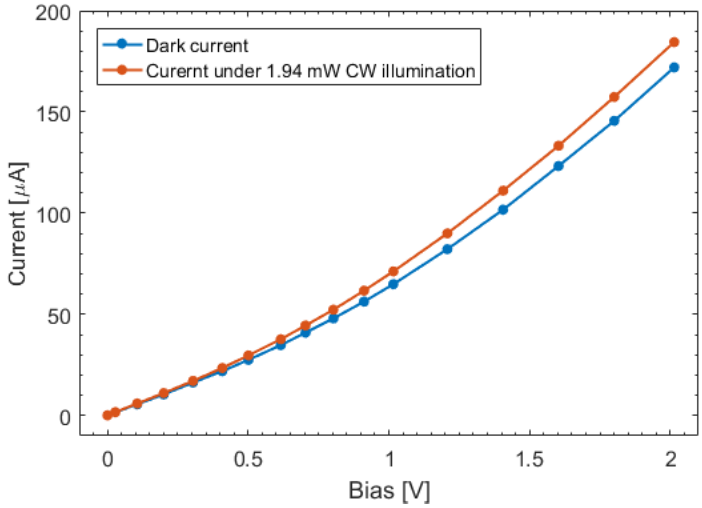

*Figure 2-23*
*Dark current and current under illumination of switch SB1-1 (type 3:5)*

The difference between the dark current and the current under illumination is the photocurrent, which is 6.3 µA at 1 V bias, therefore our measured responsivity is 3.24 µA/mW which is in the same order as it was measured at UCL.

## II/3. Optoelectronic characterization

One of the most important properties of a photoswitch is its response time, as it was discussed in the first chapter in I/1.1. The response time is directly connected to the recombination time of the photogenerated carriers. In the optoelectronic characterisation, we are deducing this characteristic time by measuring the opto-electrical response of the photoswitch to ultrashort optical pulse illumination.

### II/3.1. Measurement setup

The setup is similar to the electrical characterisation setup as it is illustrated in Figure 2-7 in section II/1.2. The photoswitch is electrically connected with i40 Infinity Probes to a power supply on one side and a Lock-In Amplifier (LIA) or a sampling oscilloscope on the other side. In order to measure the response time accurately, it is necessary to use an exciting source which has an exciting time at least an order shorter than the measured response time. It is expected that the photoswitch response is in the picosecond range around 1-2 ps. Therefore, an ultrashort laser pulse with a pulsewidth of 100 femtoseconds is suitable to measure this response. We are using a Menlo Systems C-Fibre A laser (online datasheet: [69]), it is providing < 90 fs laser pulses with 100 MHz repetition rate. The output optical pulse train in free space can have an average optical power up to 500 mW. Optical fibres were used to guide these pulses to the photoswitch for illumination.

## II/3.2. Dispersion of laser pulses

The ultrashort laser pulses have a wide bandwidth in the optical domain, which consist of tens or even thousands of optical modes separated with the pulse repetition rate frequency. The bandwidth in which these modes are confined could reach 100 nm. Our femtosecond laser has a central wavelength of 1560 nm and 3 dB bandwidth around 70 nm, with thousands of optical modes separated with 100 MHz distance, which is around 0.8 picometer in wavelength. An illustration of the optical spectrum is shown in Figure 2-24, the figure is taken from the laser datasheet.

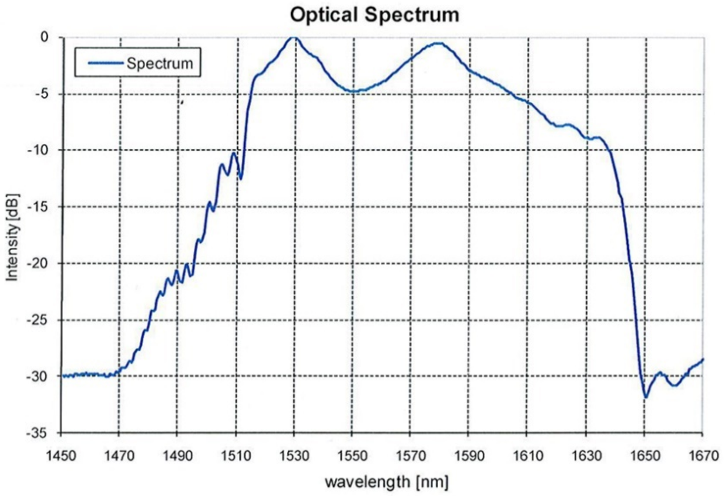

*Figure 2-24*
*Optical spectrum of the Menlo femtosecond laser. Source: datasheet of the laser [69]*

To guide the laser beam to the switch we are using standard SMF-28 (Single Mode Fibre) optical fibre, online datasheet can be found in [88]. These fibres are widely used in telecommunication networks, they are single mode fibres with 0.2 dB/km loss and can be used in the 1300 nm and 1550 nm wavelength ranges. The core has a diameter of 8.2 µm.

In optical fibres the propagating light suffers from dispersion effects, which causes pulse broadening. These effects are in proportion with the optical bandwidth of the optical signal, the wider the bandwidth, the longer the optical pulse becomes for the same propagation length. A detailed description of dispersion effects is given in APPENDIX B.

In optical telecommunication systems the dispersion in fibres results in an interference of adjacent transmitted symbols due to the broadened time domain signal. As these signals usually have a lower bandwidth than femtosecond pulses, they can propagate for kilometres in the fibre and the receiver can still decode the transmitted data. If the transmission is for hundreds of kilometres, to overcome the dispersion problem they are using dispersion compensating fibres which has an opposite dispersion coefficient than the standard fibre. Concatenating standard and compensating fibres, the transmission is possible for thousands of kilometres through fibres.

The dispersion effect is more apparent during the propagation of ultrashort pulses. Due to the wide optical bandwidth of the 100 femtosecond long pulses, after propagating through only 1 meter of standard SMF-28 optical fibre these pulses are widening to almost 2 picosecond width. In our setup we have to use fibres to guide the laser to the switch and due to the equipment arrangement, it has to be at least 1 meter long. The 2 ps optical pulses are not practical for our measurement, it is in the same order as the expected photoswitch response. To overcome this problem, similarly to optical transmission systems, we are using a dispersion compensating fibre (DCF). We choose a dispersion compensating model from Thorlabs, named DCF-38 fibre. In Appendix C, we demonstrate with experiments the pulse broadening of a femtosecond pulse after propagating through different lengths of SMF-28 and we also demonstrate the dispersion compensation with the DCF. We determined experimentally the required fibre length ratio of 1:2 for SMF and DCF fibres for optimal compensation of the dispersion. During propagating in the SMF fibre the pulse broadens, then while propagating through the DCF fibre it is compressed back close to its original shape. In our experiments we are using a 2.94 m long SMF-28 fibre connected to a 1.53m DCF-38 fibre. The optical autocorrelation measurement of the original pulse and the compensated pulse is illustrated in Figure 2-25 for 4 cases. Two sets of cables were available with identical measured lengths, however due to the loose jacket the length can vary with ± 10mm. The cables were marked with either A or B, both for SMF and DCF types presenting 4 possible combinations, and because of the uncertain lengths the measured pulse widths are different.

The results are suggesting that the two DCF cables has the same length, because they have a similar result if used with the same SMF fibre (e.g.: yellow curve *DCF A + SMF B* and green curve *DCF B + SMF B*). The width of the pulses for the longer case (autocorrelation width at 1/e height) is 218 fs, while for the other result it is 128 fs, assuming a gaussian shape, it is 90 fs width . This latter is the same as the original laser pulse width (blue dashed curve). According to our experiments in Appendix C, during the propagation through these fibres the pulse first broadens to 3.5 ps (real width estimated from the autocorrelation curve assuming a Gaussian pulse) after propagating in 2.94 meters of SMF-28 fibre, then it is compressed back to 90 fs with the 1.53 meters of DCF-38 fibre. We were using the combination of DCF-A + SMF-B, seen with yellow in Figure 2-25, this compressed pulse is illuminating the photoconductive switch during the characterization.

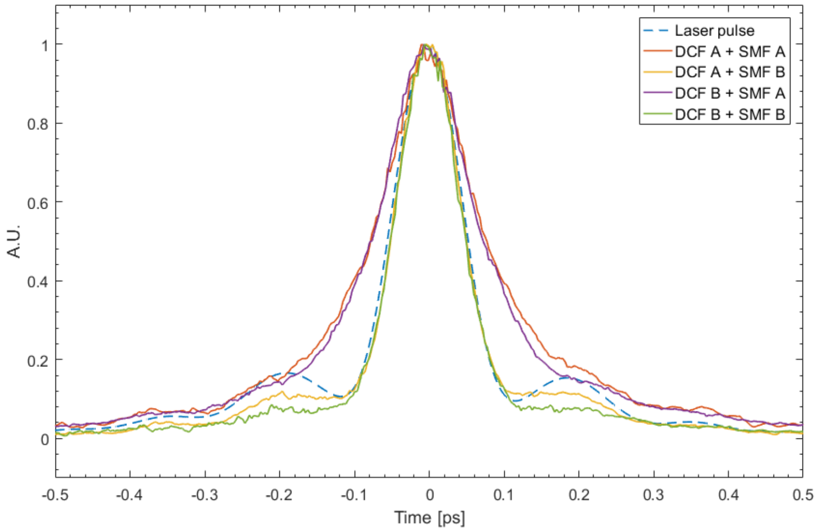

*Figure 2-25*
*Pulse width of the dispersion compensated laser pulse*

At first, in section II/3.3 we are showing the photoswitch response measured with a high-speed sampling oscilloscope. Then in section II/3.4 we use an optoelectronic pump-probe experiment to measure the response with femtosecond resolution.

## II/3.3. Photoswitch response with sampling oscilloscope

One way to measure the electrical response of the photoswitches to femtosecond optical pulses is to use a fast sampling oscilloscope. These types of scopes are used to measure repetitive signals by taking couple of samples from one period, while incrementing the sampling position in each period [89]. This technique allows to measure periodic signals with faster features than the sampling rate of the oscilloscope by reconstructing the signal from the samples taken from several periods. The setup is illustrated in Figure 2-26, we illuminate the photoswitch with the laser pulses and while biasing one side with a DC voltage, the oscilloscope on the other side records the generated electrical pulses. We used a Tektronix DSA-8300 oscilloscope with Tektronix 80E10 TDR sampling head. An electrical high-bandwidth DC-block was used before the sampling head to filter out the DC feedthrough of the photoswitch, which allowed to set the sensitivity according to the relative pulse height and not the absolute signal level containing also the constant DC feedthrough signal.

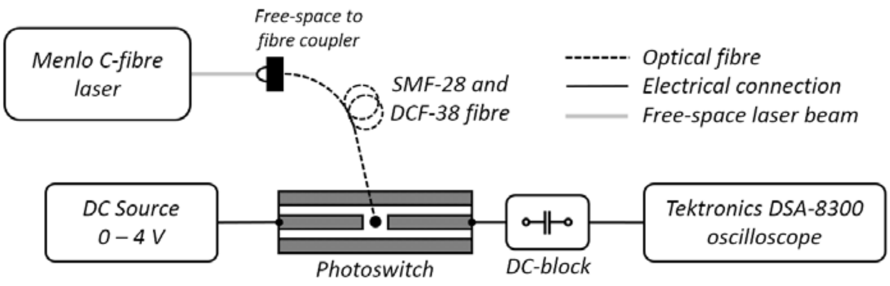

*Figure 2-26 Photoconductive switch measurement setup with a sampling oscilloscope*

The sampling head has a frequency bandwidth of 50 GHz and an incident pulse rise time of 12 ps. We choose the switches SA2-2 (type 3:3) and SC1-1 (type 3:5) (see switch geometries on page 50, TABLE 1) for the measurement. Figure 2-27 illustrates the measured electrical pulses of the photoswitch SA2-2.

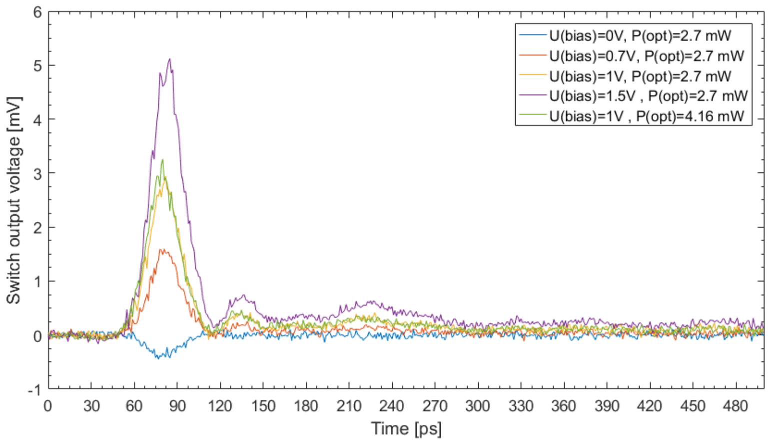

*Figure 2-27 Measured pulses with the fast sampling oscilloscope for SA2-2 switch*

During the measurement we varied the bias voltage and the optical power of the illuminating beam. We can observe that the pulse level is increasing with higher bias voltage and also with higher optical powers. We can also observe some small peaks following the main pulse, these are attributed to the electrical reflections of the pulse in the measurement setup. Fitting a Gaussian pulse on the measurement we can obtain the electrical pulse widths for all the measurements, one fitting example can be seen in Figure 2-28.

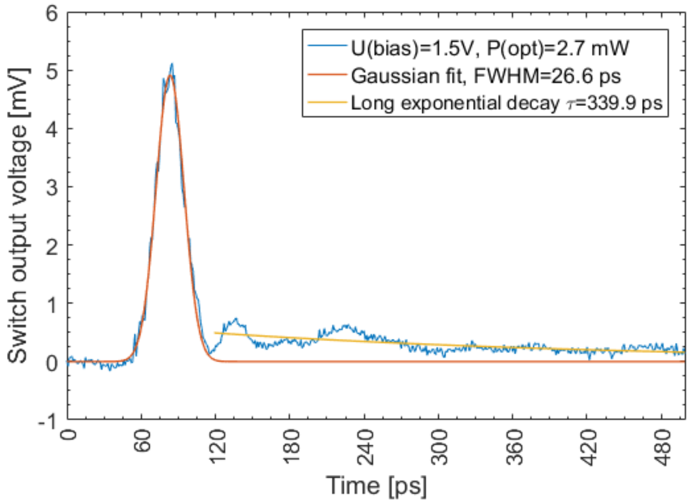

*Figure 2-28*
*Fitting example of the fast sampling oscilloscope result measuring SA2-2*

A gradual exponential decrease is also present after the pulses, this low level signal can be the effect of the hole recombination. The Full-Width at Half Maximum (FWHM) values of the Gaussian fittings are detailed in *Table 4* for all measurement. The longer decay values and the peak of the gaussian fitting are also presented. The pulsewidths are around the same for all the measurements, for both switch types. This 26 ps is a much higher value than we are expecting from the nitrogen-ion implanted photoconductive material. This relatively long response shows that the measurement is limited by the equipment speed, it is not able to measure shorter pulses than this width.

*Table 4 Sampling oscilloscope measurement properties*

| Switch ID (Ref. p. 51) | Bias [V] | $P_{opt}$ [mW] | Pulse FWHM [ps] | Long Exponential Decay [ps] | Peak voltage [mV] |
|---|---|---|---|---|---|
| SA2-2 | 0 | 2.7 | - | - | -0.42 |
| SA2-2 | 0.7 | 2.7 | 26.4 | 284 | 1.5 |
| SA2-2 | 1 | 2.7 | 25.74 | 366.6 | 2.8 |
| SA2-2 | 1.5 | 2.7 | 26.6 | 340 | 4.9 |
| SA2-2 | 1 | 4.16 | 26.56 | 319.1 | 3 |
| SC1-1 | 0 | 4.16 | - | - | -0.6 |
| SC1-1 | 0.5 | 4.16 | 27.9 | 224 | 0.8 |
| SC1-1 | 1 | 4.16 | 27.49 | 280.6 | 1.9 |
| SC1-1 | 1.5 | 4.16 | 25.69 | 309 | 3.25 |

In [29] a similar measurement was performed on the photoswitches with a higher-bandwidth equipment. In their measurement the FWHM of the Gaussian fitting is 10.87 ps, which is still an equipment limited value.

In our measurement, we observed higher peak voltages in case of type 3:3 (SA2-2) switch compared to type 3:5. In case of 1 V bias, with the same optical power (4.16 mW) a peak of 3 mV was measured for type 3:3 and 1.9 mV for the other. A lower optical illumination power (2.7 mW) still produced a higher peak of 2.8 mV. This shows a higher level generated electrical pulse for type 3:3 switches.

## II/3.4. Measurement with opto-electronic autocorrelation

The real photoswitch response time could be measured with an ultrafast oscilloscope with a time resolution below picosecond range, however today’s technology does not have these extreme low resolutions. In this section, we are introducing a solution to measure the temporal response, based on an opto-electronic pump and probe experiment. In this setup the measurement resolution is not affected by the bandwidths of electrical equipment, the limit is determined by the femtosecond optical pulse width exciting the photoswitch.

This measurement method with two optical pulses illuminating the photoconductive material at the same spot was first introduced by the group of *F.W. Smith* and *G. Mourou* in 1989 [15]. The limiting factor in their experiment was the 5 ps pulsewidth of the used mode-locked dye lasers, which is longer than the response time of the tested LT-GaAs material. Their measurement result is shown in Figure 2-29, it features a symmetric peak around the zero with a characteristic decay.

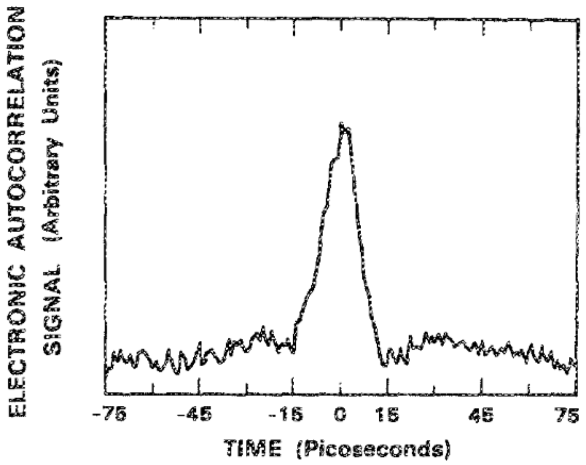

*Figure 2-29*
*LT-GaAs photoconductor response as measured by*
F.W. Smith et al., Appl. Phys. Lett., Vol 54, 1989 [15]

### II/3.4.a Simulation of the autocorrelation curve

We expect a similar curve as in Figure 2-29 from our experiment, which is an autocorrelation signal of the switch response. We simulated the photoswitch response curve in Chapter I/1.1, illustrated in Figure 1-6. The autocorrelation trace of this curve is symmetric and also has the dual exponential feature. The simulated autocorrelation trace for the response of Figure 1-6 is illustrated in Figure 2-30 after normalization.

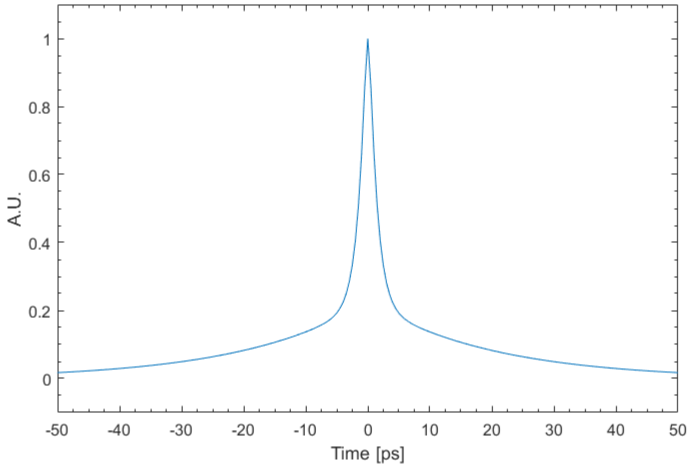

*Figure 2-30*
*Calculated autocorrelation of the switch response*

The autocorrelation curve shows a sharp peak around zero (when the two pulses completely overlap), with a fast exponential decay ($\tau_N$ = 1.2 ps), and a slower exponential decay ($\tau_P$ = 20 ps) with a lower amplitude. The fast decay corresponds to the electron lifetime while the slower decay can be attributed to the hole lifetime in the semiconductor material. By fitting a dual exponential curve on the autocorrelation with the right weighting of the components, we can deduct the lifetimes of the carriers as we will see in this section.

The simulation is fitting the model parameters on several different measurement results to obtain the physical properties of the switch. The used values for the lifetimes in Figure 2-30 are already the fitted values on the measurement results. The details of the simulation are explained in APPENDIX A.

### II/3.4.b Measurement setup

The photoswitch sample was placed on an RF probe station like as before. From one side, with an Infinity i40 probe, the switch is DC biased with a constant voltage (from an Agilent E3620A power supply) and connected to the Lock-In Amplifier (Stanford Research Systems SR510) on the other side. The setup is illustrated in Figure 2-31. The illuminating laser is also the same as in the previous experiment: a Menlo fibre laser emitting 90 fs laser pulses. Before coupling the laser beam into the optical fibres to guide them to illuminate the switch, we construct an optical autocorrelator with free-space optical components, it can be seen on the left side of Figure 2-31. As the first step, the free-space beam is split into two beams with an optical beam-splitter. In one of the paths we place a motorized optical delay line to be able to vary the length of the path. With additional mirrors we construct the second path to a length corresponding to the centre state of the delay in the first beam path. The two beams than re-joined with another beam-splitter and then coupled into an optical fibre. The fibres are the ones explained in section II/3.2, 2.94 meters of SMF-28 fibre connected to 1.53 meters of DCF-38 to have an almost dispersion free optical pulse with 90 fs width. The fibre is positioned accurately to illuminate the 25 x 25 $\mu m^2$ switch mesa on the samples.

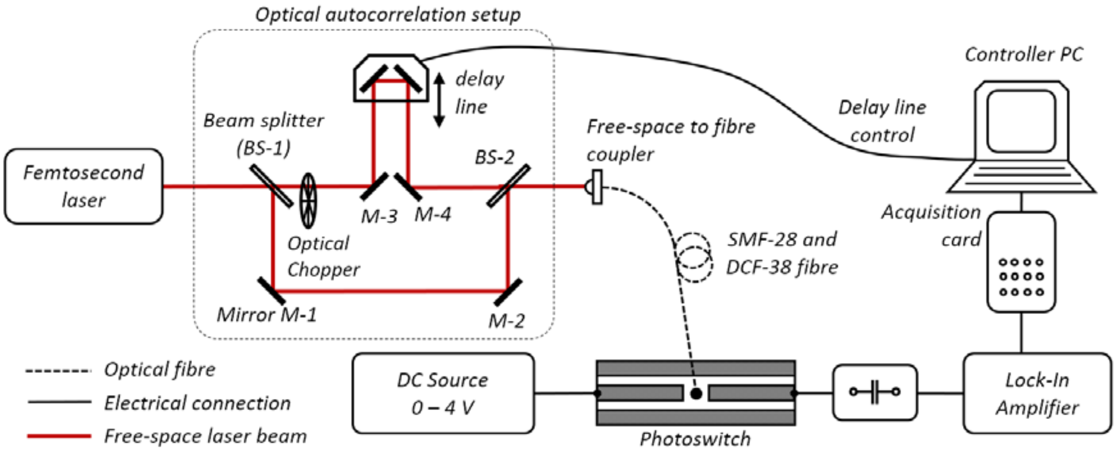

*Figure 2-31 Setup schematics of the photoswitch pulse response measurement*

This setup allows to have two identical laser pulses propagating through the optical fibres with a variable delay time, controlled with a computer. In one measurement we are sweeping the delay around the zero-delay point and for each step the switch electrical output signal is measured with a LIA (Stanford Research Systems SR510). A DC-blocker is used before the LIA input to filter out the DC feedthrough signal of the switch, allowing a higher sensitivity setting. We could set it in the 100 µV range instead of the 1-10 mV range because of the feedthrough signal compared to the low level generated pulse.

The LIA is locked on the rotation frequency of a mechanical chopper placed in the delayed beam path, which periodically blocks (turns ON-OFF) one of the beams. This acts as a filter, reducing the noise level during the measurement. The chopper frequency is in the 1-2 kHz range. The LIA is also amplifying and integrating the switch output signal, then the LIA output is received by an acquisition card (National Instruments USB-6221) connected to the PC. At each step on the delay line, a data point is recorded, the steps are converted into time delay, therefore we create a curve of the switch output versus the delay. The minimum temporal resolution is limited by the smallest step the step-motor can take (with a Standa 8SMC1-USBhF-B2 controller). In our system the minimum step is 0.125 µm, translating this into delay time while taking into account that one step counts as an increase of twice the step distance in the optical beam path because of the corner mirror, it corresponds to 0.834 fs time delay.

During this measurement the data points are giving an autocorrelation trace of the photoswitch response, which can be measured thanks to the non-linear behaviour of the photoswitch. As the first optical pulse illuminates the switch, it induces a resistivity drop, which creates an electrical pulse propagating along the CPW line. The pulse has the dual-exponential characteristics as it was simulated in the first chapter in I/1.1. When the second optical pulse arrives, new photocarriers are generated. If the resistance of the PSW has not recovered its dark value, the electrical field in between the PSW electrodes is lower than its initial value. Consequently, the photocurrent generated by the 2$^{nd}$ pulse is a bit lower. This will be true until the delay in between the 2 pulses is long enough so that the PSW has recovered its equilibrium state [90]. As the second pulse's delay is varied, this means that for each delay step a bit different current pulses are propagating along the CPW and integrated by the LIA. The result is an autocorrelation dip, observed around the zero delay, which curve composes of exponential decays with the characteristic recombination times of electrons and holes in the photoconductor material.

### II/3.4.c Typical measurement result

A typical measured response curve is illustrated in Figure 2-32. The measured switch was the SB1-1 with 3V DC bias. This curve has to be processed before we are able to fit the dual exponential and obtain the characteristic decay times.

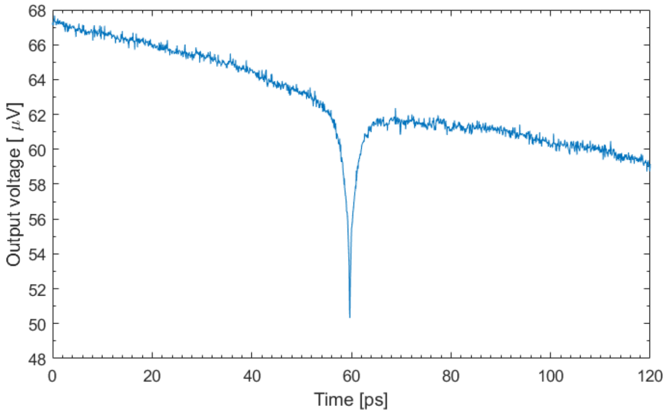

*Figure 2-32*
*Typical result of the pump-probe experiment*

The measurement was recorded with 50 fs steps, which is equal to 7.5 µm steps with the step motor. The photoswitch output was connected to the voltage input of the LIA. The sensitivity level was set to the highest where the maximum measured level can still be inside the sensitivity range, in the case of the example above it was 100 µV. The integration time was equal 100 ms, meaning that the step motor has to hold one position at least for this duration of time. The measured delay range is 120 picoseconds in order to be able to measure the longer decay of the switch too. This full delay range is corresponding to 180 mm movement of the motorized delay line. These settings gave a minimum scanning time of: *120ps / 50fs * 100ms = 240s* (4 minutes). In real it takes a bit longer because we are holding one step position a bit longer (120-130 ms) than the integration time in case there are some fast vibrations after the sudden stop of the step motor. Setting smaller step distance would increase the measurement time and would give a result with a better resolution. However, having a longer recording time (over 10 minutes) we noticed increasing disturbances in the measurement which were present in a sudden step or in an irregular steepness change of the slope. The source of these disturbances is unknow, the setup has a high sensitivity for any mechanical movement and also the electromagnetic background noise. Due to this, we limited the maximum measurement time in exchange of the resolution. Even with the lower resolution, the resulted curves are eligible for analysis of the temporal response of the photoswitches. The next section is explaining the compensation for the setup imperfections.

### II/3.4.d Measurement corrections

Before analysing the data, we need to consider some limitations of the measurement. The two beams are joined with a beam splitter into one beam and focused into an optical fibre with a collimator lens. In the free-space optical setup the beams are guided with mirrors to the delay line, the beam splitters and the collimator lens. These mirrors have to be aligned perfectly to have the two beams completely parallel after the final beam splitter to focus it into the lens. The delay line also has to be fixed completely parallel with the laser beams, so at the start and end position of the measurement the beam is reflected to the same position by the corner mirror. If this condition is not met, the reflected beam spot will be shifting with increasing delays, and it won't be optimally coupled into the fibre. It is challenging to achieve complete parallelism, even with the best setup, we were able to measure a decreasing (or increasing) optical power in the fibre by different delay positions, which also generates a lower (or higher) level voltage at the output of the switches with the delay movement. Figure 2-33 illustrates a curve, measured with only the delayed beam illuminating the switch. It shows the average output voltage of the photoswitch through 120 ps delay. The slope indicates that the output voltage is decreasing because of the lower optical power coupled into the fibre. Between the start and end position, we measured an optical power difference of 0.05 mW, while the maximum power was 1.5 mW.

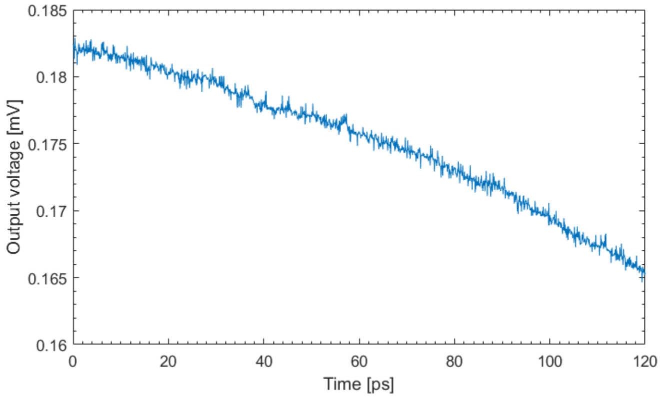

*Figure 2-33*
*Switch output voltage decrease as the coupled one optical beam's power decreases by the delay, illustrating the dependence of the output on the laser beam coupling accuracy*

The results can be compensated with this slope, representing the inconsistent optical coupling. We are measuring the response in a wide time range of 120 ps, so we can be sure that at the start end the end the switch response has minimum effect on the curve. We fit a polynomial using the first and last 15 ps of the measured signal with keeping the 90 ps distance of them, and we subtract this polynomial curve from the measurement. An example for this process is illustrated in Figure 2-34, the orange coloured curve shows the fitted slope. Figure 2-35 shows the curve after the subtraction of the orange curve from the blue curve in Figure 2-34. This compensation is just an estimation of the slope, there is still an uncertainty of the real slope, however this subtraction proved to be a good method.

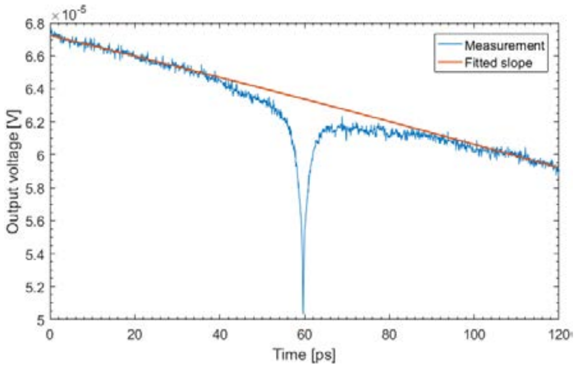

*Figure 2-34 Example measurement with the fitted slope*

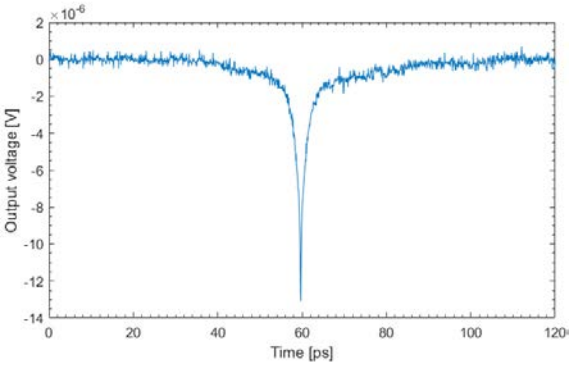

*Figure 2-35 Example measurement with compensation of the free space coupling mismatch*

Another limitation is due to the interference of the two laser beams. They are the copies of each other with the same properties, and when they are completely aligned in space and time, we can observe an interference peak. This interference peak gives the signal seen in Figure 2-36. In the autocorrelation measurement, this peak gives a false minimum of the signal and needs to be compensated, it is not a signature of the optoelectronic behaviour of the photoswitch. One way to minimize the interference, therefore the false peak level, is to use a half-wave plate in one of the beam-path and rotate the beam's polarization with 90° (to make the two beams cross polarized). We performed a couple of measurements to find the optimum polarization position, however a small interference peak was still observable. In our analysis of the results we remove the data points corresponding to the interference and exchange them with a constant value connecting the data points outside the area.

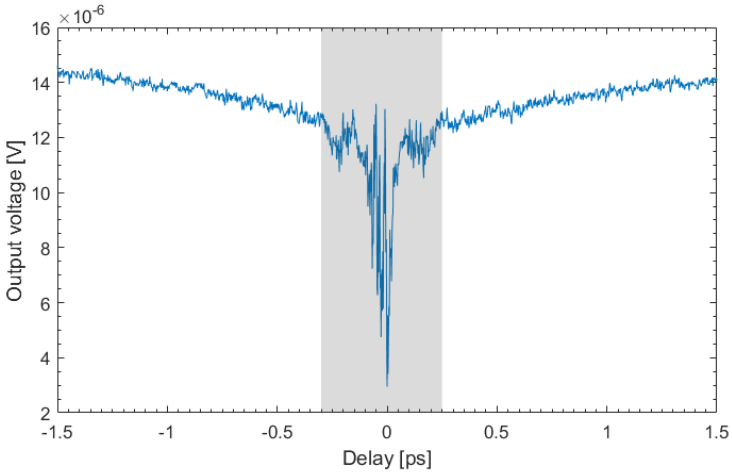

*Figure 2-36 Interference peak in the optoelectronic autocorrelation experiment*

Therefore, while calculating the exponential fitting, this interference will not play a role in the fitting values. Because of this, we do not have information about the real peak value, it can be just assumed form the crossing point of the two side fittings on the curve, however it is not important for the measurement to know this peak value. The identified time range for the interference is marked with grey in Figure 2-36 (the illustration shows the maximum interference), it is 0.55 ps wide.

### II/3.4.e Curve fitting

After compensating the measurement artefacts, we normalized and inverted the curves to fit a dual exponential on both sides. A similar function was fitted in [91] in a photoconductive switch response with three relaxation process to obtain the characteristic lifetimes of the photoconductor. Here we found that two element process can describe the result well. Equation (30) shows the fitting function on one side of the autocorrelation curve.

$$A * exp\left(-\frac{t}{T_f}\right) + B * exp\left(-\frac{t}{T_s}\right) \tag{30}$$

Where $A$ and $B$ are scaling parameters, $T_f$ is the decay time of the fast exponential and $T_s$ is the decay time for the slow exponential. The two observable decays are originating from carrier dynamics. The fast decay with a higher level is characterizing the electron trapping time, while the longer and lower level decay can be attributed to the contribution of the holes to the current provided by the photoswitch. This hole current is lower because of the reduced mobility of the holes compared to the electrons [91].

In Figure 2-37 the compensated measurement curve is seen with light blue colour as an example of the measurement result. It is normalized to the maximum level (the level where we removed the interference contribution). The black dotted curves are the dual exponential fits on both sides. With orange colour we illustrated the exciting laser pulse intensity shape after the fibre propagation, as it can be seen it is much shorter than the measured response. The lower level of the slower exponential is also observable. The measured curve is not perfectly symmetric in the illustration, one possible reason is the mentioned uncertainty in the slope prediction, it was not corrected completely, and it also can be due to the measurement noise. This small difference on the two side of the curve is affecting mostly the longer decay parameters, therefore we cannot deduct a precise value for the hole lifetime. However, the effect is minimal for the fast decay due to its much faster properties. The illustrated fitting has the parameters detailed in TABLE 5.

*TABLE 5 FITTING PARAMETERS FOR THE EXAMPLE RESULT CURVE OF FIGURE 2-37*

| *Left side* | | | | *Right side* | | | |
|---|---|---|---|---|---|---|---|
| A [A.U.] | $T_f$ [ps] | B [A.U.] | $T_s$ [ps] | A [A.U.] | $T_f$ [ps] | B [A.U.] | $T_s$ [ps] |
| 0.9735 | 1.27 | 0.257 | 9.5 | 0.9867 | 1.29 | 0.25 | 16.37 |

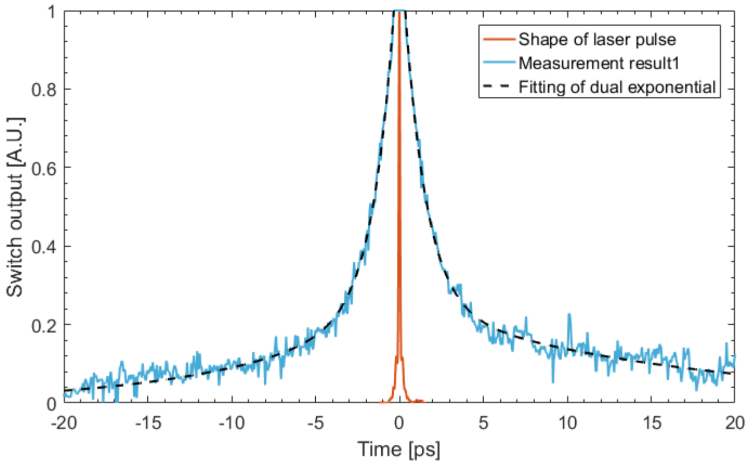

Figure 2-37
Fitting of the exponentials on both sides of an example result curve; orange curve is the femtosecond laser pulse after fibre propagation

The fitting parameters are similar for the fast component for both sides, a decay of 1.27-1.29 ps shows the ultrafast properties of the InGaAs photoconductive switch. This decay time characterizes the recombination time of the photogenerated carriers in the semiconductor. We performed the measurement in all the available switch types to investigate the effect of the electrode geometry. Measurement was also done with different bias voltages, and with different optical powers in some cases. The results have a big variance, the fast decays fittings were between 0.8 ps to 1.8 ps which is attributed more to the measurement error due to the noise and compensation predictions than the real difference in the response time of the switches, which is confirmed by repetitions of the measurement on the same switch resulting in values with a high variance. A summary of the average of the fitted parameters for different switch types are in TABLE 6. In the analysis we made an average for the switch types from several measurements, which removed the extreme values and give an average for the decay time between 1 ps and 1.3 ps. In the table we indicate the rising fast exponential time as $T_{rise}$, and the falling fast decay as $T_{fall}$.

The optical powers of the two beams, if it's not stated otherwise were 2.5 mW for the fixed beam ($P_1$) and 1.45 mW for the delayed beam ($P_2$). The delayed beam power was measured after the optical chopper, which also contributes to the average optical power measured by our power meter. This means that for the time window when the chopper lets the beam through, the average optical power is around 2.9 mW for $P_2$. We also measured the response for attenuated second optical beams too.

Table 6 Results of the photoswitch response measurements

Optical powers: fixed beam $P_1$=2.5 mW; delayed beam: $P_2$=1.45 mW

| type 3:5 | | | | |
|---|---|---|---|---|
| | 3V bias | | 2V bias | |
| Average [ps] | $T_{rise}$ | $T_{fall}$ | $T_{rise}$ | $T_{fall}$ |
| | 1.25 | 1.22 | 1.24 | 1.14 |

| type 3:3 | | | | |
|---|---|---|---|---|
| | 3V bias | | 2V bias | |
| Average [ps] | $T_{rise}$ | $T_{fall}$ | $T_{rise}$ | $T_{fall}$ |
| | 1.06 | 1.22 | 1.15 | 1.13 |

| type 5:5 | | | | |
|---|---|---|---|---|
| | 3V bias | | 2V bias | |
| Average [ps] | $T_{rise}$ | $T_{fall}$ | $T_{rise}$ | $T_{fall}$ |
| | 1.17 | 1.24 | 1.29 | 1.02 |

Attenuated second beam, 3V bias for all measurement

| type 3:5 | | | | |
|---|---|---|---|---|
| | $P_2$=1.45 mW | | $P_2$=0.75 mW | |
| Average [ps] | $T_{rise}$ | $T_{fall}$ | $T_{rise}$ | $T_{fall}$ |
| | 1.27 | 1.27 | 1.29 | 1.21 |

| type 3:3 | | | | |
|---|---|---|---|---|
| | $P_2$=1.45 mW | | $P_2$=0.75 mW | |
| Average [ps] | $T_{rise}$ | $T_{fall}$ | $T_{rise}$ | $T_{fall}$ |
| | 1.22 | 1.04 | 1.30 | 1.17 |

The values show no significant difference for different types of switches, different bias voltages or optical powers. The consequent results show that the response time does not depend on the switch geometry in the tested range of bias voltage or optical power. However, it can be the case that the difference is so subtle, that with the sensitivity of our measurement it cannot be differentiated due to the noise. A saturation effect of generated photocarriers is also not observed, which would be indicated by the longer decay times in case of higher optical powers.

The average value for the recombination time is in the range of 1.1 ps - 1.3 ps. This fast response time predicts that the device is capable of handling high frequency repetition rate optical pulses of at least 200 GHz (5 ps pulse repetition rate) for sampling function. In theory and in an ideal case where the electrical components are not limiting, the photoswitch would be able to generate distinguishable pulses even at a rate of 500 GHz, but only with limited power due to the fact that the 2 ps pulse distance at 500 GHz is very close to 1.2 ps average lifetime of the semiconductor.

## II/4. Conclusions on Chapter II

In this chapter we described the InGaAs photoconductive switches and characterized them. Based on the electrical characterization with a Vector Network Analyser we were able to build a simple equivalent circuit and model the switch as an R-C pair. The circuit model gave us the equivalent capacitance of devices. An improved model for simulation was proposed, however it needs further investigations to understand the model elements relation to physical properties. The dark resistance and bias voltage to switch current relation was also characterized.

An optoelectronic characterization was also performed in order to measure the switch response time to femtosecond optical pulses. We showed that using fast sampling oscilloscope for the response measurement we are limited by the equipment's speed. Therefore, we constructed and electro-optic autocorrelation experiment, where we illuminate the switch through an optical autocorrelator, and measure the switch response. We obtained from the autocorrelation signal through fitting a dual-exponential curve, the electron and hole lifetimes of the semiconductor. The electron lifetime is around 1.2 ps, which allows the high-frequency operation of the switch at least up to 200 GHz. We also observed that the hole lifetime has a lower influence on the response with around the fourth in amplitude, however for a longer decay time above 10 ps.

These ultra-fast properties of the switch make it able to operate as sampler or mixer device for frequencies reaching the lower sub-THz range. In the next chapter we are characterizing a semiconductor mode-locked laser with a pulse repetition rate of 24.5 GHz. In Chapter IV we are using the two devices, the photoswitch and the laser as an optoelectronic mixer.

# Chapter III

## Semiconductor mode-locked laser stabilization

III/1. Semiconductor mode-locked laser ........................................................ 77
    III/1.1. MLL samples used in this work ........................................................ 77
    III/1.2. Laser setup ........................................................ 78
    III/1.3. Laser optical properties ........................................................ 79
    III/1.4. Optical pulse characterization ........................................................ 81
    III/1.5. MLL heterodyning on a photodiode ........................................................ 84
    III/1.6. Phase noise of the electrical beating signal ........................................................ 86
    III/1.7. Origins of phase noise ........................................................ 88
III/2. MLL stabilization ........................................................ 89
    III/2.1. External direct modulation ........................................................ 90
    III/2.2. All optical feedback – single loop setup ........................................................ 91
        III/2.2.a Principles of stabilization ........................................................ 91
        III/2.2.b Stabilization setup ........................................................ 92
        III/2.2.c Stabilization results ........................................................ 94
    III/2.3. All optical feedback – dual loop setup ........................................................ 97
III/3. Stabilization summary ........................................................ 100
III/4. Conclusions on Chapter III ........................................................ 101

In this chapter we are characterizing a semiconductor mode-locked laser with an oscillation frequency of 24.55 GHz. In order to stabilize the laser output signal, an all optical feedback loop is constructed.

## III/1. Semiconductor mode-locked laser

In Chapter I, section I/5 we discussed about the different types of mode-locked lasers and their properties. In our system, we are utilizing semiconductor passively mode-locked lasers. Their advantages are the small size, simple operation, integrability in photonic systems and achievable pulse repetition rates in the range of hundreds of GHz and very low RF beating linewidths. As the down side, compared to the bulky fibre mode-locked lasers, semiconductor MLLs have lower stability and lower output powers. They can provide an average optical power in the 10s of mW, and usual timing jitter levels in the order of 100s of femtosecond.

In the ’80s, the first researches of semiconductor MLLs were based on laser diodes fabricated as a bulk active material, first demonstrated in [92] or as a quantum well (QW) diode in [93]. Later, Quantum dot (QD) based devices are proved to have better performance than the previous ones [94]. As an inherent property of the quantum dot laser diodes, compared to QW devices, these lasers have lower threshold current and fast carrier dynamics, their noise is also lower due to the lower intracavity losses and larger differential gain. Improved performances in terms of pulse duration, jitter and peak power was observed and their spectral bandwidth is also significantly broader [95]. In our work, quantum-dot laser diodes were available with self-oscillation frequency of 24.55 GHz. We are characterizing these QD devices in this chapter, and also construct a stabilization all optical feedback loop to further improve the performance in terms of stability of the output pulse train.

### III/1.1. MLL samples used in this work

In our system experiments, we used indium-phosphide (InP) based semiconductor quantum dot/dash mode-locked lasers provided by III-V Lab, Palaiseau, France. They are composed of a Fabry-Perot cavity with 6 quantum-dash layers. Passive mode-locking is observed without any saturable absorber section [73][96]. The lasers we used were providing pulse trains in the 1.55 µm - 1.58 µm wavelength range with the repetition rate of 24.55 GHz. Two samples were available, one of it was provided as a chip mounted on a ceramic substrate. A photograph of the 24.55 GHz MLL chip is shown in Figure 3-1, the laser is the black chip in the middle wire bonded to the stripline, in the following we are referring to the whole structure as the laser chip. The other sample of the 24.55 GHz laser is in a butterfly package, seen in the photo in Figure 3-2.

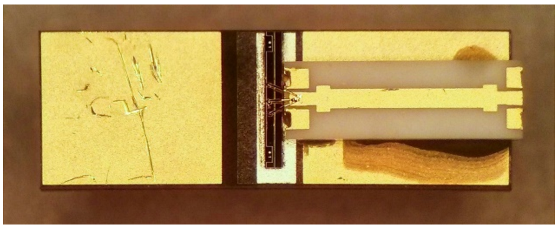

*Figure 3-1 MLL chip on a ceramic substrate. The wire bonded vertical dark chip is the MLL*

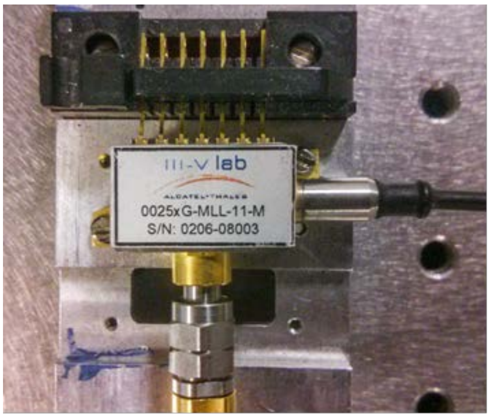

*Figure 3-2 MLL laser in a butterfly package*

### III/1.2. Laser setup

The butterfly package has an SMF-28 standard optical fibre output and it is possible to control the laser chip temperature through the electrical pins of the package. Biasing the laser was done through an electrical V type (DC to 65 GHz, 1.85 mm) connector. This connector serves also for direct RF modulation of the laser signal. In the butterfly package a lensed fibre is aligned optimally to couple the laser output into the fibre. An optical isolator is also placed before the output fibre to attenuate the back reflected laser signals which could disturb the laser cavity.

In case of the laser chip, the setup is illustrated in Figure 3-3. The chip is placed on a copper plate which is temperature controlled. A 1 metre long pigtailed tapered fibre is used to couple the laser output into an optical fibre, a magnified view of the taper and the laser is shown in Figure 3-4. At the fibre end, a lens is formed out of the core and the coating. The fibre is the standard SMF-28 optical fibre with an FC/APC fibre connector.

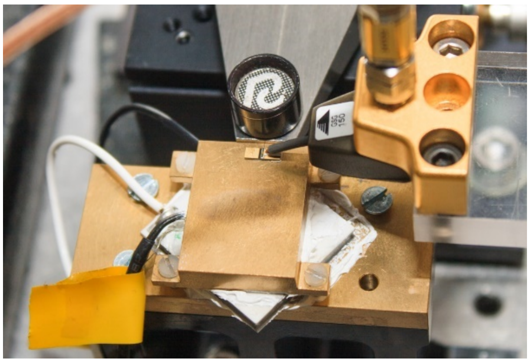

*Figure 3-3*
*MLL setup at UCL*

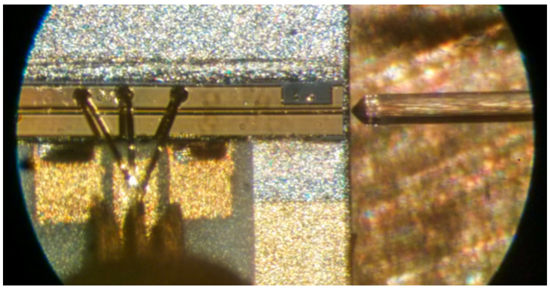

*Figure 3-4 magnified view of the lensed fibre at the laser output face*

APC (angled physical contact) connectors are polished to have an 8° angle of the fibre end surface, this tilt improves the return loss to 60 dB which is at least 10 dB improvement compared to the FC/PC (physical Contact) connectors. It is essential to use the APC connectors to minimize the unwanted back reflected light to reach the laser cavity. The temperature was controlled with a Peltier element, and a temperature sensor (resistive sensor) was placed inside the copper plate to give a feedback of the temperature to the controller device. The electrical bias and possible RF connection were applied simultaneously via a coplanar RF probe connecting to a stripline on the ceramic carrier. The whole stage of the laser chip was fixed, while two x-y-z positioner stages were used for the precise alignment of the lensed fibre and the RF-probe. In Figure 3-3 the setup constructed at UCL is illustrated, the same setup built at IMPE-LAHC in Grenoble is illustrated in Figure 3-5. Here, instead of a tapered fibre we used a pigtailed collimator lens to couple the laser into the fibre. Higher coupled optical power was achieved with this coupling solution compared to the tapered fibre. Using the collimator lens also has the advantage of the longer distance between the lens and the output of the laser cavity, so the back reflected light from the surface of the lens has a lower level at the laser output facet compared to the tapered fibre case.

In all the setups, after the 1 meter long pigtailed fibre a fibre based circulator was connected to prevent unwanted back-reflections from the fibre based optical network. The average optical power coupled into the fibre with the tapered end was around 4.5 dBm while with the collimator lens we reached 8 dBm.

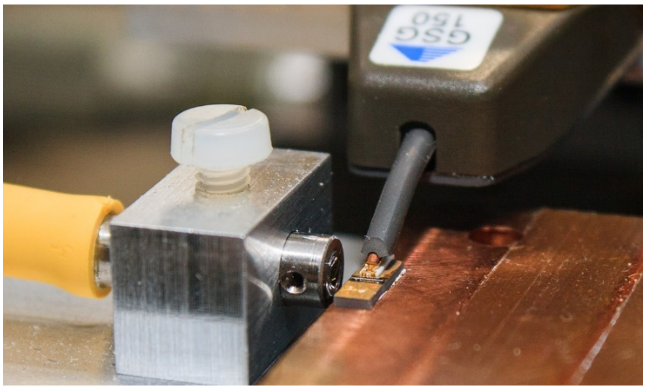

Figure 3-5
MLL setup at IMEP-LAHC with the collimator lens

### III/1.3. Laser optical properties

Both the packaged laser and the laser chip were characterized, and as they are identical, they showed the same performance. The small differences are only the result of the better laser to fibre coupling in case of the packaged option, and later we will see that the unpackaged laser is more useful for the stabilization experiments as the butterfly package has an isolator at the laser output. The characterization in this section and section III/1.4 was done with the packaged laser.

The temperature of the laser was set with a Newport Laser Diode Controller Model 6000, we used only the temperature controller (TEC) part of this device. It was possible to use this model for both laser setups. In case of the butterfly package, the temperature sensing and control were connected through the electrical pins of the package seen on the top of Figure 3-2. The bias was set with a Keithley 2401 Sourcemeter through the V-type connector. The next figure shows the output optical power at the end of the 1 meter fibre versus the bias current. The power was measured with a ThorLabs PM20 Optical Power Meter which fully integrates the laser spectrum.

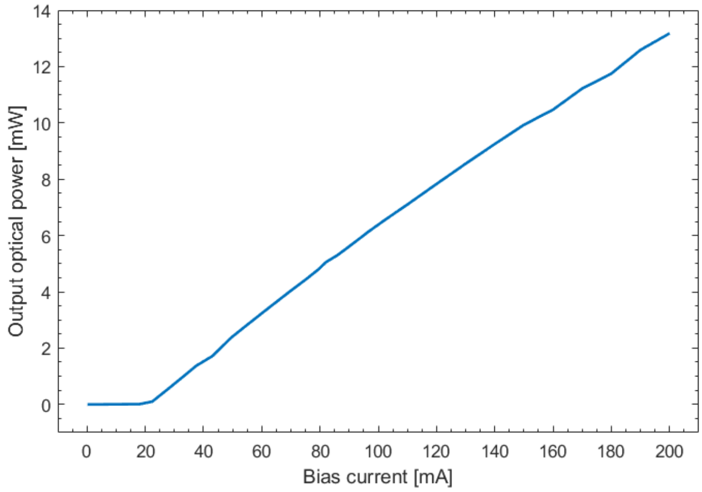

*Figure 3-6*
*Packaged laser optical power versus bias current*

The laser has a threshold bias current of 21 mA and a slope efficiency of 0.073 mW/mA. The output optical power with 100 mA bias is 6.5 mW (8.13 dBm), and 9.9 mW (9.9 dBm) with 150 mA, the maximum we measured is 13.2 mW (11.2 dBm) optical power with 200 mA, we did not apply higher bias currents in order not to damage the laser. The measurement was done at 21 °C. Analysing the optical spectrum with a Bosa 400 C+L Optical Spectrum Analyser, the wavelength distance between the adjacent modes is 0.202 nm, which translates to around 24.5 GHz in the 1570 nm range, the spectrum is illustrated in Figure 3-7, recorded with at 21 °C.

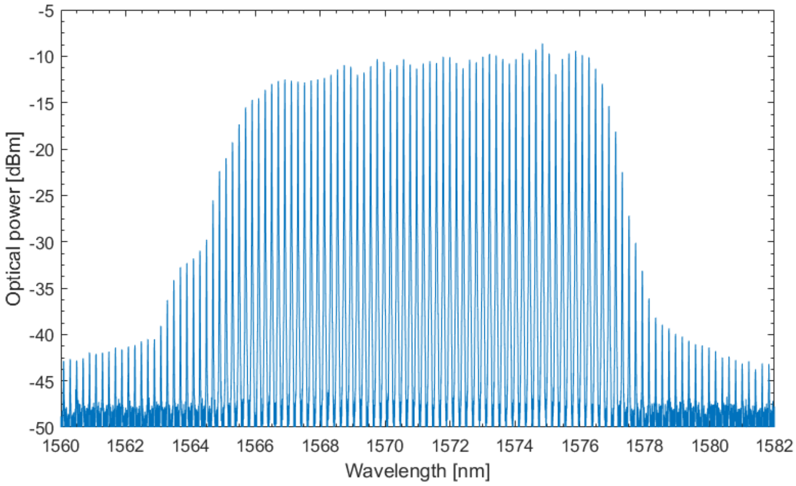

*Figure 3-7*
*Optical spectrum of the packaged MLL at 21°C and 130 mA bias*

The laser is emitting in the 1570 nm wavelength range and contains 40 optical modes in an 8 nm wide 3 dB bandwidth, therefore most of the spectrum lies in the optical L-band (1565-1630 nm).

We analysed how the optical spectrum is transforming with different temperatures and bias currents. In Figure 3-8 we draw the envelope of the optical modes for increasing temperature (17°C – 19°C – 21°C), it can be observed that the emitted spectrum is shifting towards longer wavelengths with a rate of around 0.3 nm/°C. This is an expected behaviour as with rising temperatures, the laser cavity is expanding and as the cavity length determines the oscillation frequency the longer cavity means lower oscillation frequency and longer emitted wavelengths.

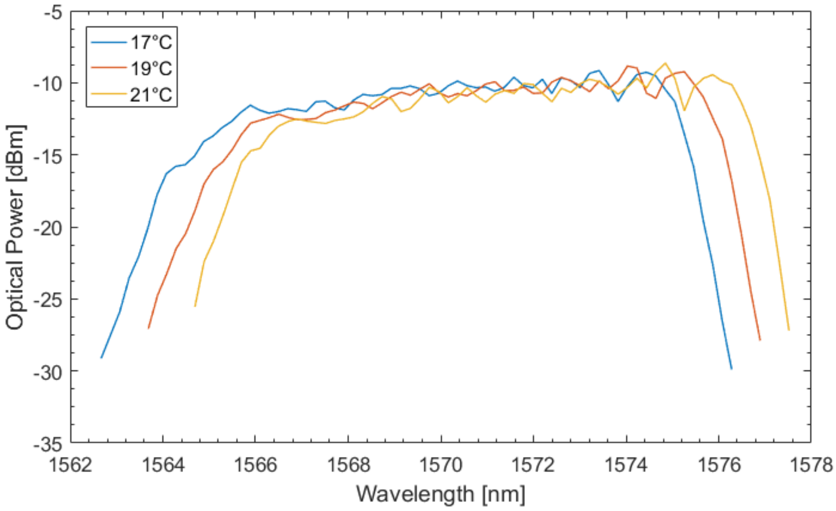

*Figure 3-8*
*Optical spectrum envelops versus laser temperature.*
*$I_{bias}$ = 130 mA*

The optical spectrum also depends on the applied bias current, not just the temperature. Increasing the bias current, we observed an increase of the power of all modes and a widening in the spectrum with an increasing number of modes in the 3 dB bandwidth. The optical modes for bias currents between 50 mA and 190 mA are illustrated in Figure 3-9. Applying 190 mA current, the optical bandwidth widens up to 10 nm, while for 50 mA bias the bandwidth is only around 5.6 nm.

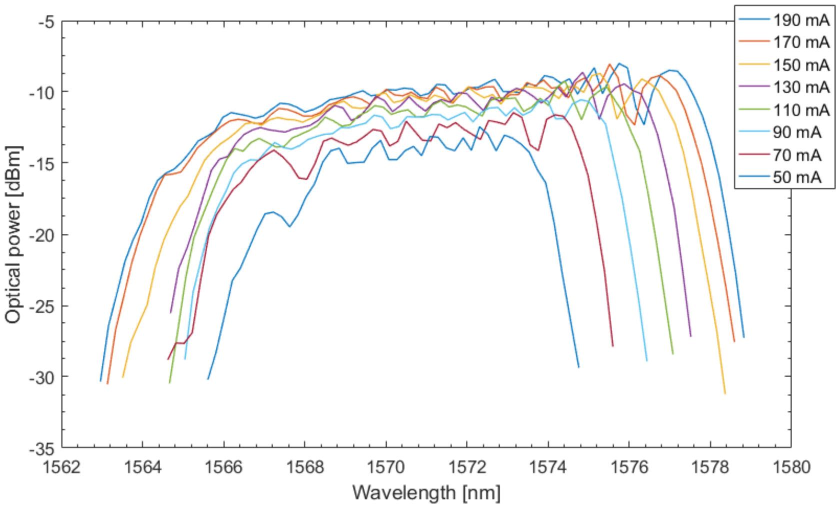

*Figure 3-9*
*Optical spectrum envelops versus bias current at 21°C temperature*

## III/1.4. Optical pulse characterization

We characterized the temporal length of the laser pulses generated by the semiconductor MLL. At the output of the laser diode the phase difference of adjacent modes is constant and not zero. This phase difference is produced by an intrinsic chromatic dispersion of the laser cavity, the emitted pulses have a positive chirp. This intrinsic effect can be compensated with the negative chirp caused by the propagation in standard single mode fibre (SMF-28. The dispersion in a certain length fibre can decrease the phase differences to zero. In this case all the modes interfere in phase and together produce a short optical pulse [97]. We determined the needed fibre length by measuring the laser pulse width while varying the fibre length.

The measurement was performed with the packaged fibre and the pulse width was measured with the Femtochrome FR-105XL autocorrelator [98] and an oscilloscope. In Figure 3-10 a top view of the autocorrelator is shown. This device incorporates an optical autocorrelator setup, a non-linear crystal for second harmonic generation, and a photomultiplier tube (PMT) is receiving the intensity autocorrelation signal. The delay between the two separated beams are introduced by a rotating parallel mirror. Twice in each rotation the delayed beam is reflected back through mirror M3 and focused in the crystal with mirror M2 together with the fixed beam, generating a third beam due to the second harmonic generation (SHG) phenomena (the SHG phenomena is describe in APPENDIX C). The fixed beam is reflected back with a corner mirror and mirror M1. The measurement principles are the same as in the setup we constructed and described in APPENDIX C for the femtosecond pulse dispersion in Optical fibres. The maximum duration of the measurable pulsewidth depends on how long the two beams are present together at the crystal, which time is determined by the parallel mirror sizes and their distance, in this case the maximum pulsewidth is 90 ps. During the rotation, when the position of the rotating mirrors enables the back reflection, a continuously increasing delay is introduced between the two beams. The rate of this change depends on the rotation frequency, in this device it is 10 Hz. In Figure 3-11 (Source: [99]) a schematic is illustrating the path of the laser beams.

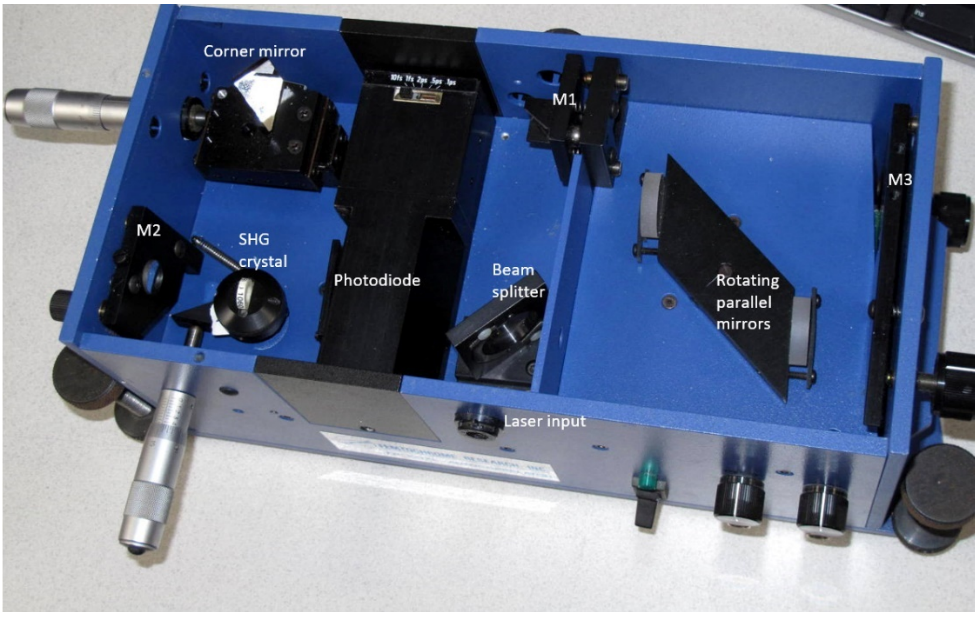

*Figure 3-10 Top view of the Femtochrome FR-105XL autocorrelator*

The equipment has a fibre adapter input which also couples the laser signal into free space. There are 4 adjustment knobs for the alignment of the mirrors inside the device. After the beam splitter, the re-joined delayed and fixed beams have to reach M2 lensed mirror as parallel beams, this can be set with the adjustment knobs. M2 is focusing the two beams into one spot in the non-linear crystal. The crystal is made of $LiIO_3$ working with 700-1800 nm wavelengths. The generated second-harmonic beam in the crystal is received by the PMT covering the wavelength range of 410 – 1800 nm, its sensitivity can be extended in the infrared range by using photodiodes.

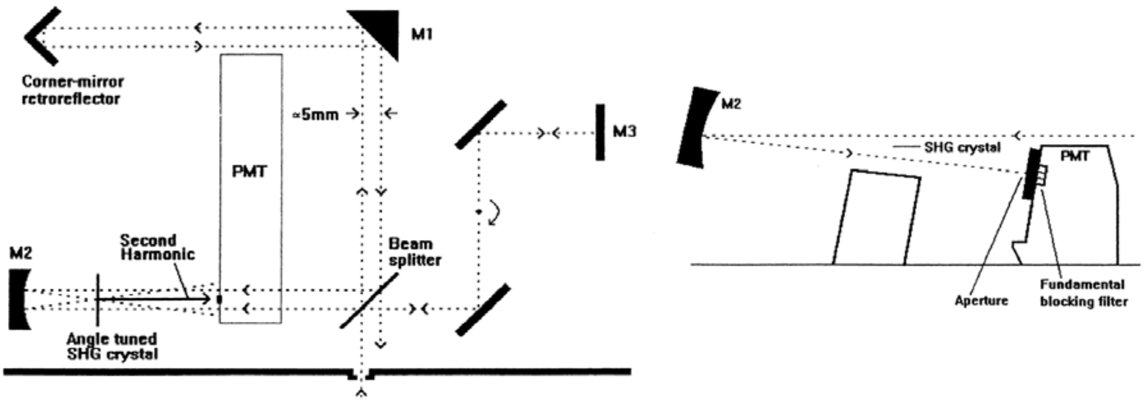

*Figure 3-11 Schematics of the laser beam paths inside the autocorrelator of Figure 3-10. Source: [99]*

The autocorrelator has two electrical outputs: one is for the signal output is the photodiode output, and the other output is a trigger signal providing the frequency of the rotating mirror for the synchronization with the oscilloscope. An Agilent Technologies DSO-X 3024A Oscilloscope was used to display the output signal, the trigger was synchronized with the autocorrelator trigger signal. In case we see a continuous signal on the oscilloscope, it means that our laser signal is continuous and not pulsed, or the duration of the pulses is longer than the time resolution of the autocorrelator. To measure the pulse width, we have to convert the oscilloscope time scale into a real time scale with calibration value. By adjusting the position of the corner-mirror retroreflector inside the autocorrelator results in a delay shift in the fixed length beam path, which is seen as a pulse shift on the oscilloscope's screen. We have to measure the pulse shift in the time-scale of the oscilloscope, and the position difference of the corner-mirror in micrometres (the adjustment knob has a scale). Knowing these values, we can calculate the calibration value with the following equation (31).

$$\frac{T}{t}=\frac{2x}{0.3s}\left[{}^{fs}/_{\mu s}\right] \tag{31}$$

Where $x$ is the translation distance in micrometres, and $s$ is the time-shift in the oscilloscope's scale in microseconds. For 100 µm translation, we measured 25.5 µs shift, which gives a calibration value of 26.14 fs/µs. It means that 1 µs on the oscilloscope equals to 26.14 fs in real time. This calculation assumes a linear delay change versus the parallel mirror rotation.

Performing the measurement by directly connecting the 1 m fibre of the packaged laser, we measured a flat signal, meaning that the laser emits a continuous intensity signal and the intrinsic dispersion of the laser have to be compensated for pulsed operation. Standard SMF-28 fibres can compensate this dispersion, Figure 3-12 shows the measured pulses with connected fibre lengths between 150 – 210 meters. The time scale of the figure is showing the real time and the pulses are normalized for comparison. The shortest pulsewidth is achieved with 200 m of optical fibre, the resulted pulse has a width of 1.33 ps at 1/e height. As the measurement gives autocorrelation pulses, a conversion is needed to calculate the real width: assuming that the pulses have a Gaussian shape, a conversion factor of 0.707 ($1/\sqrt{2}$) can be used. For 200 m fibre it means that the pulsewidth is 1.02 ps. Figure 3-13 shows the real pulsewidth change with the different lengths of fibres. For fibre length between 195 m and 205 m the pulse width stays below 2 ps. In these cases, the phase differences of the optical modes are minimal. The phase of each mode also depends on the bias current: for different bias currents, the needed compensation is different, therefore the needed fibre length as well. Figure 3-14 shows the pulse width change for several bias values, using 200 m optical fibre.

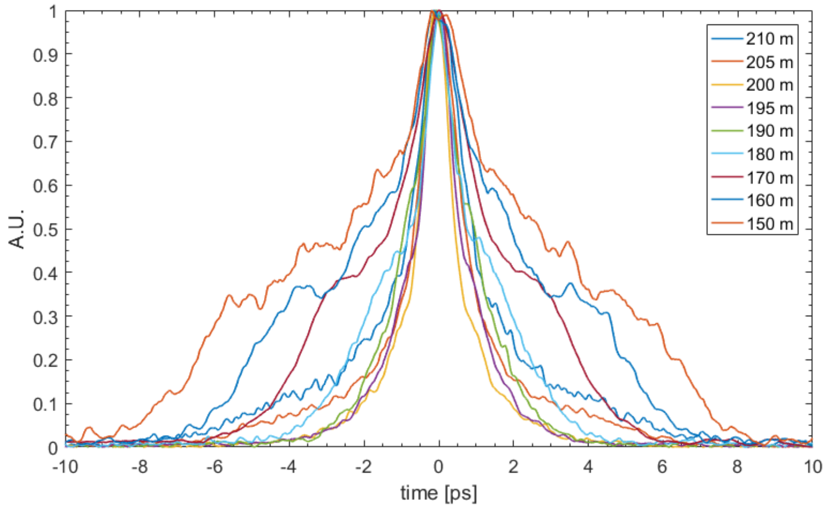

*Figure 3-12 Semiconductor laser pulsewidth with different lengths of optical fibre*

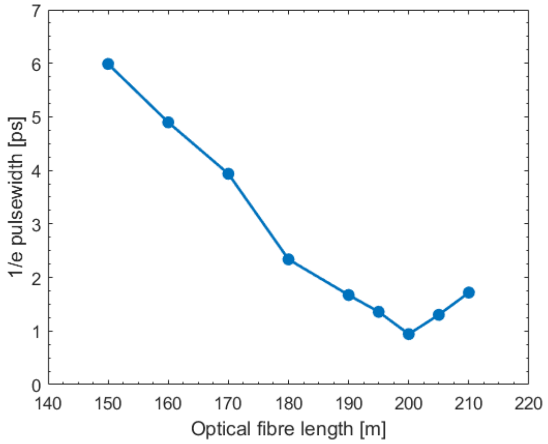

*Figure 3-13 MLL Pulsewidth versus optical fibre length at 140 mA bias*

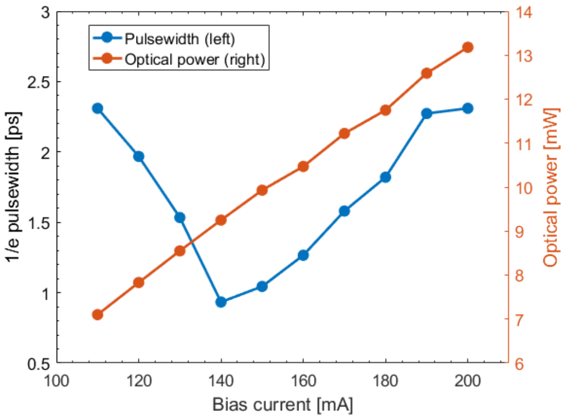

*Figure 3-14 Left axis, blue curve: MLL pulsewidth versus bias current with 200m optical fibre. Right axis, orange curve: optical power versus bias current*

This characterisation shows that if during the experiments we want to use a pulsewidth below 1.2 ps, which is in the range of the photoswitch response, we still have a freedom in choosing the bias currents between 135 mA – 155 mA.

### III/1.5. MLL heterodyning on a photodiode

Illuminating a high-speed photodiode (PD) with the laser light we can generate electrical RF signal. The PD output will contain electrical pulses with the same repetition rate as the MLL oscillation frequency, however the electrical pulsewidths are limited due to the frequency bandwidth of the PD. In the frequency domain, the optical beatings of the MLL's optical spectrum has a frequency difference of 24.5 GHz which translates from the wavelength's differences of 0.202 nm in the 1570 nm range. These optical beatings are generating electrical beatings on the photodiode at the fundamental frequency, and also at the harmonics. Figure 3-15 shows the fundamental electrical beating signal with 140 mA bias at 25°C temperature for our MLL. We received the laser signal with a Finisar photodiode (u$^2$t XPDV2320R) after 200 m optical fibre and measured the electrical signal with a signal analyser (Rohde&Schwarz FSQ 26, 20 Hz – 26.5 GHz). The peak power is at 24.5442 GHz, the PD has a frequency bandwidth of 50 GHz, therefore in the electrical spectrum we could observe only the fundamental beating and the 2nd harmonic (with an ESA with sufficient bandwidth) at 49.0884 GHz. In case using a higher bandwidth photodiode and ESA, generated electrical RF signals at higher harmonics would be also observable, e.g. at 73.6326 GHz, 98.1768 GHz and so on.

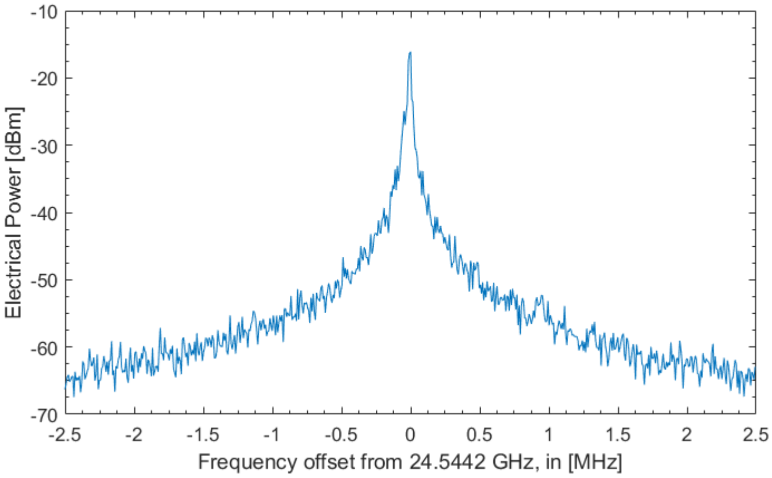

*Figure 3-15 Fundamental RF beating signal on a photodiode of the MLL, RBW: 3 kHz, VBW: 5 kHz*

The peak RF power of the signal is -16 dBm at the fundamental frequency, while the optical power was 9.8 dBm. The first couple of harmonics of the beating has similar RF power, which will be shown later in Chapter IV.

The oscillating frequency slightly depends on the laser temperature, because of the material expansion. Increasing the temperature, the laser cavity length is increasing. Therefore the higher the temperature, the lower the oscillating frequency is. Figure 3-16 is illustrating the relative change of the oscillating frequency in the 18°C – 30°C range, compared to the frequency at 25°C. We deduced a frequency shift of approximately 1.1 MHz/°C.

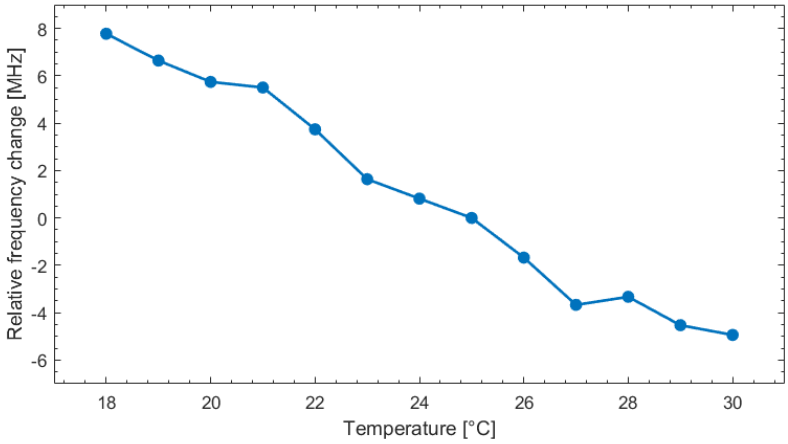

*Figure 3-16*
*Relative oscillating frequency change by temperature change of the MLL*

Using a fast photodiode to generate an electrical signal corresponding to the beating of the laser modes is a method of optical frequency generation of RF signals. The properties of RF linewidth, and RF phase noise, therefore the stability of an oscillator signal determines its usefulness for practical applications. Free-running MLL electrical beating signals usually have a Lorentzian shape with a finite linewidth [100], by fitting the appropriate equation we can measure the signal's linewidth. The spectrum of Figure 3-15 was recorded with a single sweep of 0.8 seconds with 3 kHz RBW and 5 kHz VBW. Fitting a Lorentzian curve on the peak we can measure a linewidth of 20 kHz. However, observing the beating signal continuously, we can notice a long term instability with our eyes. Figure 3-17 is showing the beating signal recorded with the "Max Hold" function of the ESA for 30 seconds. The 5 dB bandwidth of the curve is 280 kHz, measured with a 3 kHz RBW and 30 kHz VBW. This instability can be attributed to temperature and bias fluctuations.

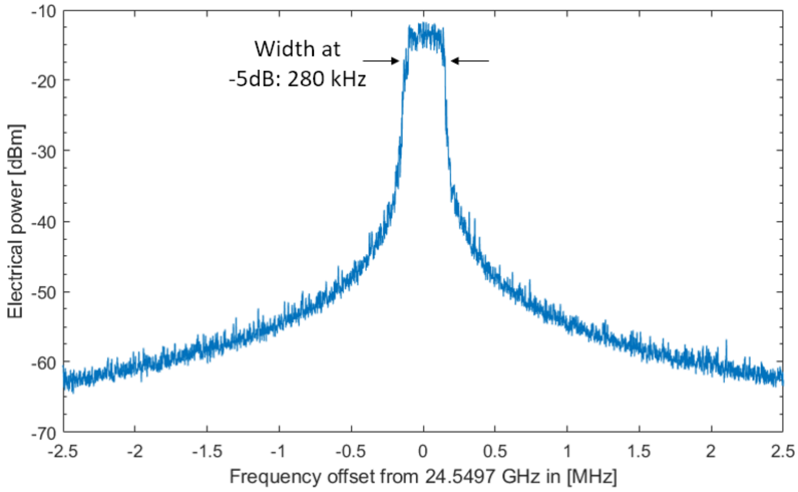

*Figure 3-17*
*Beating spectrum recorded for 30 seconds with ESA Max Hold option*

### III/1.6. Phase noise of the electrical beating signal

The single-side band phase noise (SSB-PN) generally written as $\mathcal{L}(\mathrm{f})$, is an important property of oscillator signals. It shows the phase instability, in other words the short term stability of the frequency, which is a fundamental limitation in systems. In the time domain we quantify phase noise as the jitter of the signal.

Phase noise is measured by taking the spectral power in a 1 Hz bandwidth $f_{offset}$ Hz away from the carrier frequency and dividing it with the total power of the carrier, as it is defined by the IEEE standard [101]:

$$\mathcal{L}(f) = \frac{Power\ density\ in\ one\ phase\ noise\ modulation\ sideband\ per\ Hz}{Total\ signal\ power} \tag{32}$$

The theory is illustrated in Figure 3-18. Equation (32) results in the single sideband phase noise referenced to the carrier power and measured in dBc/Hz. The PN curve is illustrated in an SSB-PN - frequency log-log plot. In many spectrum analysers there is a build-in measurement function to automatically measure and draw the PN curve of a signal in a given frequency offset range.

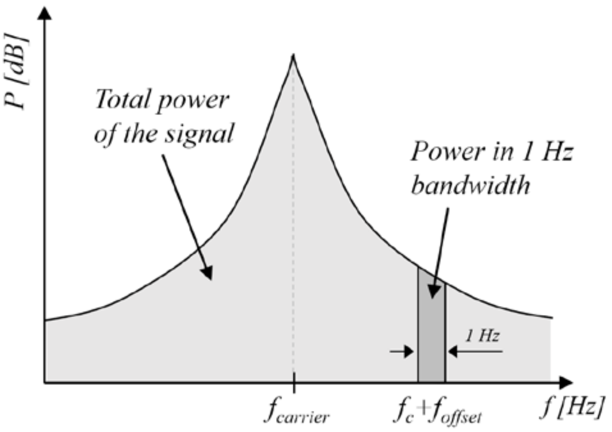

Figure 3-18
Illustration of the phase noise measurement

We characterized the electrical beating signal of the MLL to obtain its stability. In the following sections, we are analysing only the fundamental beating signal. Figure 3-19 illustrates the phase noise curves of the free-running laser RF beating for different bias currents. The curves are showing similar performance for bias currents between 80-140 mA except for 70 mA where a significant degradation is observable. The low bias current can be an explanation for this, here the optical power is just around 4 mW (6 dBm) and the 3 dB optical spectrum is 5 nm wide. For higher bias current of 160 mA we can observe a 2-3 dB higher phase noise values. As a measure, we are comparing the phase noise values at 100 kHz offset frequency, in case of 140 mA bias, it is -70 dBc/Hz, which as we found in the literature is a usual value for free-running mode locked laser diodes ([102][103][104]). However, these values are a few orders of magnitude larger than the SSB-PN observed in bulky diode pumped mode locked Ti:Sa laser running at 80 MHz, for which a typical value is -140 dBc/Hz as reported by Scott et al. [105].

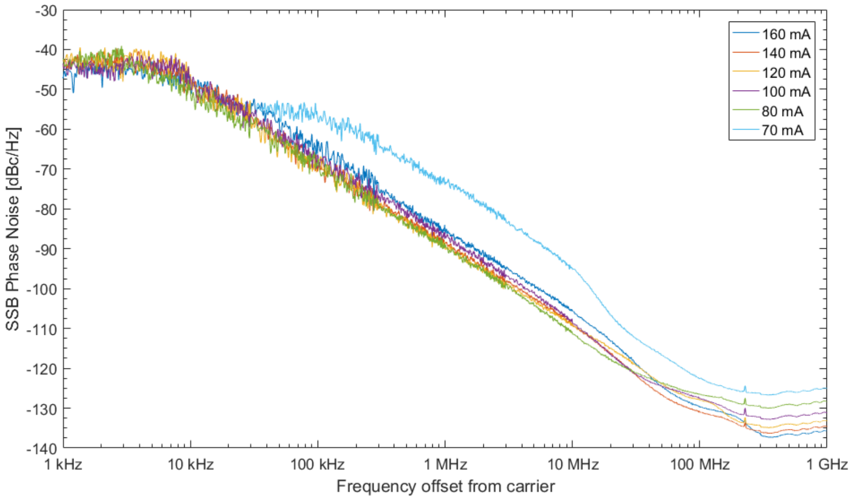

*Figure 3-19 Phase noise of the fundamental beating at 24.55 GHz of the MLL for different bias currents*

This curve can be converted into the integrated root-mean square (RMS) timing jitter ($\sigma_{RMS}$), which is the standard deviation of the timing accuracy of the signal. It is calculated by the integration of the SSB-PN curve and the result is measured in seconds, as it is used also in [100]:

$$\sigma_{RMS} = \frac{1}{2\pi f_{MLL}} \sqrt{2 \int_{f_{min}}^{f_{max}} \mathcal{L}(f) df} \qquad (33)$$

Where $f_{MLL}$ is the fundamental frequency of the laser, $f_{max}$ and $f_{min}$ are the integration limits of the phase noise curve, and $\mathcal{L}(f)$ is the SSB phase noise. The calculated timing jitter for the 140 mA bias current case is 3.7 ps integrated between 10 kHz and 1 GHz, we are going to use this range for comparisons in the following sections. The RMS jitter for the full frequency range for Figure 3-19 is 6.5 ps.

### III/1.7. Origins of phase noise

The noise in semiconductor mode-locked lasers can be attributed to several different sources and the phase noise curve we observe is the sum of the processes [106]. In this section, we are giving a short background of the phase noise origins of the electrical beating spectrum of the MLL signal.

In passively mode-locked lasers, like the lasers we are using in this work, an external source of timing is not required for mode-locking, the timing of each pulse depends on the previous one. The modulation is produced internally with the gain and absorber interaction with the optical pulses [107]. The noise of these semiconductor laser diodes is differing from the solid-state lasers like fibre lasers, Ti:Shapphire lasers or other lasers with slow gain dynamics [108]. This difference is originating from the short carrier lifetime in semiconductor lasers, therefore the gain fluctuations and timing of pulses is very important during one pulse round-trip in the cavity. If we consider the MLL as a free-running oscillator under uncorrelated timing noise, the optical pulses oscillating in the cavity are exhibiting timing noise within each round trip. The main source of this noise is the amplified spontaneous emission (ASE) directly coupling into the pulse [109]. This noise is causing the pulse shape to change which causes a shift in the pulse centre. This change is causing timing and frequency fluctuations in the pulse train. In [108], analytical expressions were derived for five identified fluctuations describing the noises of a semiconductor MLL: energy fluctuations, carrier phase fluctuations, frequency fluctuations, timing fluctuations and carrier population fluctuations. All, except the carrier population fluctuations can be described with linear differential equations driven by the ASE noise, the fifth fluctuation is driven by the shot noise. Equations for these fluctuations were first derived by *Haus and Marcozzi* in 1993 [110]. All these fluctuations can be modelled with a nonstationary random process, and they are due to the white noise properties of ASE noise. All together are leading to a Lorentzian electrical spectrum shape [100].

## III/2. MLL stabilization

Microwave signal generation with mode-locked laser is a practical solution, it has a simple setup providing a relatively stable RF signal with a fixed frequency. For certain applications, for example local oscillator signals for mixing or clock sources, the signal phase noise and timing jitter can determine the system performance and should be as low as possible. The previously shown values are considered high in advanced solutions and gives a limitation for their usage in the mentioned systems.

It is possible to improve the stability, therefore reducing the timing jitter, of self-oscillating semiconductor MLL signals with external manipulation. There are several methods to do so [109]:

- External direct modulation,
- Electro-optical feedback,
- All-optical feedback,
- External injection locking,
- A combination of the above is also possible.

In case of external direct modulation, the laser biasing field is directly modulated with a stable electrical RF source. Setting the RF frequency as the same as the MLL self-oscillation frequency, the laser output shows a higher stability, this method is also called as hybrid mode locking. The improvement depends on the external RF source signal quality. Usually high-power external modulation is needed, in one example by the team of *G. Carpintero* [111], the phase noise at 100 kHz offset frequency decreased with 25 dB, down to -105 dBc/Hz with a RF input power of 17 dBm, for a two section 10 GHz quantum dash MLL. The downside of this method is the requirement of the high power ang high quality external source, which can also be costly for high-frequency and good signal quality RF signals.

Electro-optical feedbacks are extracting a low percentage of the optical signal, which is then transformed into an electrical signal with a high-speed photodiode. Then this electrical signal is externally modulating the biasing voltage of the laser cavity. The setup does not need any external RF source, however it requires optical to electrical conversion. An external delay in the form of a fibre spool is added to the optical section of the feedback loop, it represents a high-quality (due to its length) external cavity. In section III/2.2.a, we will discuss about the role of the external optical loop. One example for this solution in [112] achieved a phase noise reduction of 20 dB, down from -55 dBc/Hz to -75 dBc/Hz at 10 kHz offset with a dual loop configuration.

For injection locking of the MLL, an external slave laser is required. The slave laser has to be a stable source with single or more optical modes in the MLL emission wavelength range, identical lasers can also be used as slave and master. The MLL can lock one of its optical modes into one of the injected optical modes of the slave laser. This technique can decrease the RF linewidth of the laser beating and allows a small tuning range of the RF beating frequency. The method usually is used with hybrid mode locked lasers as in [109].

All-optical feedback loops contain only optical elements in the feedback. The low power extracted signal from the laser signal is sent back into the laser cavity with the help of an optical circulator. Various components are placed in the feedback to alter the signal properties: attenuator, delay line, polarization controller, and optical fibres. An example for a semiconductor laser with 10 GHz self-oscillating frequency is demonstrated in [104].

This last solution is composed only of passive components, there is no additional electrical consumption due to the stabilization, only the useful laser power is decreasing due to the extracted feedback signal. It is also a simple and easily adjustable solution for lasers with different oscillation frequencies. The literature showed significant improvements in regard of stability ([102][104]), with at least 30 dB phase noise decrease at 100 kHz offset frequency. In section III/2.2 and III/2.3 we give a detailed description of this method and we are using it to stabilize our lasers.

## III/2.1. External direct modulation

Modulating the MLL cavity with an external stable periodical signal which has the same frequency as the MLL self-oscillation we can stabilize the laser's output signal. The experimental setup is illustrated in Figure 3-20. An Agilent E8257D PSG Analog Signal Generator was providing the RF signal, which is a pure sinusoidal with a frequency of 24.5449 GHz. A small tuning range around 30 kHz, where the MLL locked on the RF generator frequency was observed.

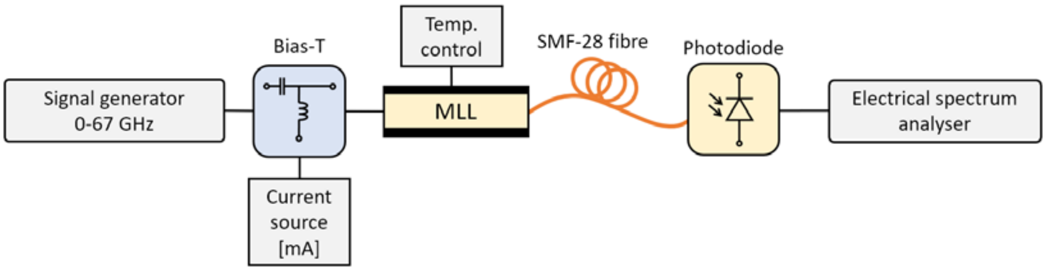

*Figure 3-20 Setup for the external RF modulation of the MLL*

In the setup, a bias-T was connected to the V-type connection of the packaged MLL to be able to bias and modulate the laser at the same time. A high speed photodiode (Finisar u$^2$t XPDV2320R) was receiving the laser signal after 200 meters of optical fibre, the PD was directly connected to an electrical spectrum analyser (Rohde&Schwarz FSQ 26).

Figure 3-21 illustrates the measured phase noise curve with different RF modulating power, a maximum of 19 dBm was used. We illustrate with the phase noise of the signal generator at 20 GHz with a black dotted curve, the data is taken from the datasheet. As the result of the stabilization, the curves are flattening in the lower offset frequency range, but above 100 kHz offset the stabilized curves are following the free running curve. The PN improvement is dependent on the power of the signal RF source, with the maximum modulating power, at 10 kHz offset the PN decreased to -70 dBc/Hz down from -52 dBc/Hz. Applying higher powers could further improve the PN, but the use of 19 dBm or higher powers is unrealistic for practical applications. The integrated phase noise for this curve is 0.889 ps in the 10 kHz – 1 GHz range. The signal generator has a phase noise of -110dBc/Hz at 100kHz offset, this value would be the theoretical minimum for the laser output with this setup. This solution requires a high power external RF source which makes it costly and not practical for real applications. Also, the improvement of the phase noise is not significant, we will see better results in the next section.

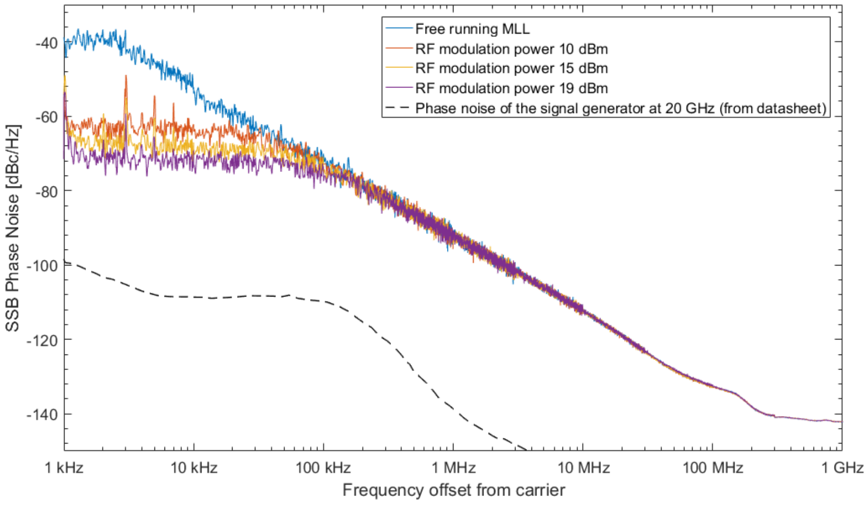

*Figure 3-21*
*Phase noise of MLL with external RF modulation*

## III/2.2. All optical feedback – single loop setup

### III/2.2.a Principles of stabilization

There are only a few researches were conducted on modelling the dynamics of a mode-locked laser behaviour with external optical feedbacks. A group from Darmstadt, Germany lead by *W. Elsäßer*, was focusing on the modelling of timing jitter reduction of different feedback methods [109]. They've built a time domain model relying on the effective interaction of the timing between the intra-cavity pulse and the time-delayed feedback pulse. The simulation and experimental results showed excellent agreement. It was found that the lengths of the external loop (external cavity) and internal cavity should be an integer multiple of the number of pulses inside the main cavity for effective feedback. A possible physical explanation was proposed in [109] to explain the timing jitter reduction under external feedback conditions. It is explaining it with the gain dynamics inside the MLL cavity. When the feedback pulse preceding the intra-cavity pulse, both assumed as gaussian shaped pulses, it experiences higher gain due to the non-linearity of the dynamical gain. This higher intensity pulse changes the centre of mass of the total pulse in time. After several round-trips, the pulse shape is reshaped back to a gaussian while keeping the changed timing. The internal and external pulses have the same time deviation distribution, the non-linear interaction between them leads to a smaller time deviation distribution, therefore the timing jitter is reducing [113].

From another point of view, the feedback loop is representing an external cavity, and can be also seen as an oscillator with the MLL, in which the Q-factor (the quality) is increasing as the delay length is increasing, which causes the RF linewidth to decrease. This effect was shown in [114] for different fibre lengths, where an increase of fibre length in the feedback loop from 28.5 m to 66 m reduced the linewidth from 3.6 kHz to 432 Hz. The longer feedback delay effect was also shown semi-analytically by *L. Jaurigue et al.* in [115]. They showed that the timing jitter is depending on the length of the feedback, a resonance occurs and the jitter is minimal when the loop delay is the integer multiple of the pulse repetition period. In addition, the feedback loop produces RF resonances in the spectrum, known as supermode noise resonances [116]. These resonances are separated by a frequency distance corresponding to the length of the feedback loop, which is also called as the free spectral range (FSR) of the loop. With a dual feedback loop, these resonances can be supressed if the additional loop modes coincide with the multiples of the modes of the main loop [114].

In the next section, first we construct a single loop feedback for the 24.55 GHz MLL, then we study the dual loop configuration in section III/2.3.

### III/2.2.b Stabilization setup

The laser self-injection is performed with a fibre based optical circulator and a fibre based optical splitter to extract part of the signal. This solution also means that the useful power of the laser is decreasing with the extracted power. For optimal stabilization low feedback power is sufficient, therefore, to minimise the splitting loss we used a 90:10 splitter, where the 90 % branch provides the stable laser signal for the experiments as the setup output, and the 10 % branch is the self-injection feedback loop. The loop contains various fibre optic elements: circulator, 90:10 splitter, 50:50 splitter, variable optical attenuator (VOA), variable optical delay line (VOD), polarization controller (PC) and a fibre spool with a long fibre. The setup for the stabilization is illustrated in Figure 3-22.

Since the packaged laser contains an optical isolator to prevent the unwanted feedback into the laser cavity, in case of using this laser the injected signal has an attenuation of at least 30 dB, which proved to be too high loss for proper stabilization. Due to this, we used the laser diode on a ceramic carrier configuration, seen in Figure 3-5.

After splitting the beam into two with the splitter, the 10 % branch first goes in a variable optical attenuator. The splitting adds 10 dB loss in this branch, and around 0.5 dB loss for the other branch, while the circulator has a loss of around 0.6 dB. A variable optical delay line is following the attenuator, this device is used to adjust a fine delay in the feedback, it can be set between 0 ps and 330 ps delay with a good precision using the manual knob for the adjustment. In the feedback loop the polarization of the signal also needs to be controlled with a 3-plate polarization controller. All the used fibres are single mode standard SMF-28 fibres which is not a polarization maintaining fibre, therefore it is needed to control the polarization in the feedback loop to have the same orientation when entering the laser cavity as it is at the laser output for optimal feedback. In the loop we also utilise a spool of fibre to add a long delay time in the ns - µs range. The feedback beam was injected back into the laser cavity through the lensed collimator thanks to the circulator. The 90 % branch of the splitter is followed by 200 m of fibre for the laser's intrinsic dispersion compensation and then the signal is received by a photodiode. Finally, the electrical beating signal quality was analysed by an electrical spectrum analyser. To assess the stabilization quality, we are comparing the electrical spectrum and the phase noise.

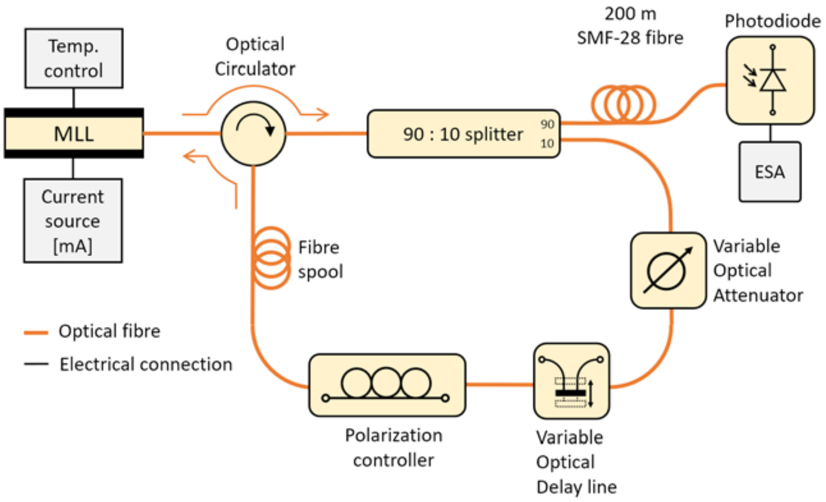

*Figure 3-22*
*Schematic of the single loop all optical feedback for MLL stabilization*

During the experiments we could distinguish 3 ranges of feedback power level regarding the stabilization results. If the injected power into the MLL is too high, so the attenuation in the feedback loop is less than 10 dB including the splitter loss, the laser output showed "chaotic" behaviour without a distinguishable electrical beating signal. In case of too low injected power, with more than 40 dB attenuation in the loop, the feedback has no effect on the signal. Between these power levels of the back injection, the laser output shows the effects of the stabilization at the right fine delay positions. By setting the optimum parameters for the feedback elements we can achieve maximum stabilization. The different ranges of feedback powers and delay line position was observed by *D. Arsenijević et al.* [102]. In their work they distinguished 5 different regimes, which are similar to our findings, with only one regime where phase noise reduction is achievable. An illustration from their results is seen in Figure 3-23.

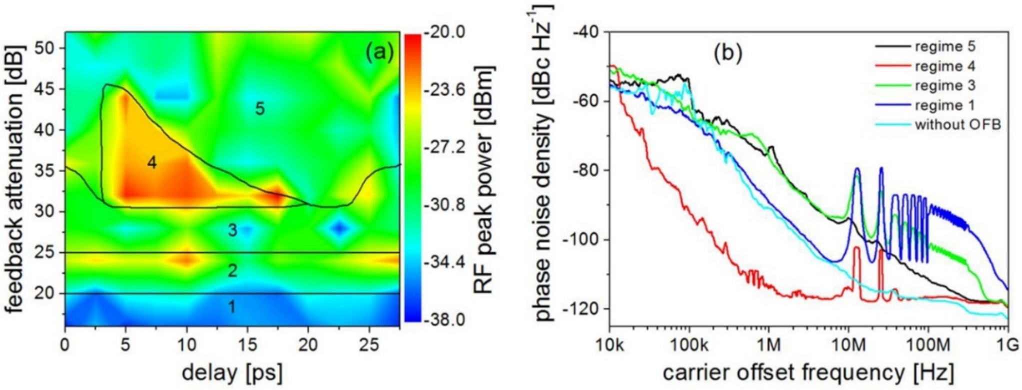

*Figure 3-23 Source: D. Arsenijević et al., IEEE Photonics Journal vol.6,No.2, 2014, [102].*
*Illustration of the different regimes of MLL stabilization for various feedback attenuation and delay.*

There are several working settings and combinations of adjustments. In case of using 100 meters or longer fibre in the feedback loop, the laser stabilization was achieved. Two possible combinations are presented here with fibre spool lengths in the feedback having 110 m and 200 m length.

The optimum feedback power measured before entering the circulator was around -27 dBm and -29 dBm, for the shorter and longer case respectively. Compared to the laser output power it means that there is an attenuation of 35-37 dB in the loop. The polarization controller and the delay line are adjusted to the optimal position. The stabilization is found to be more sensitive to the polarization of the feedback signal then the precision delay of the variable delay line. With the proper polarization, the stabilization occurs in a wide, 14 ps delay range. The behaviour is periodical with a period around 40 ps, which is directly related to the MLL pulse repetition rate of 24.55 GHz. This delay line sets the feedback signal’s phase to match the laser output signal. With the changing delay, also the peak frequency of the stabilized beating is shifting, the peak frequency shift with the delay change is illustrated in Figure 3-24.

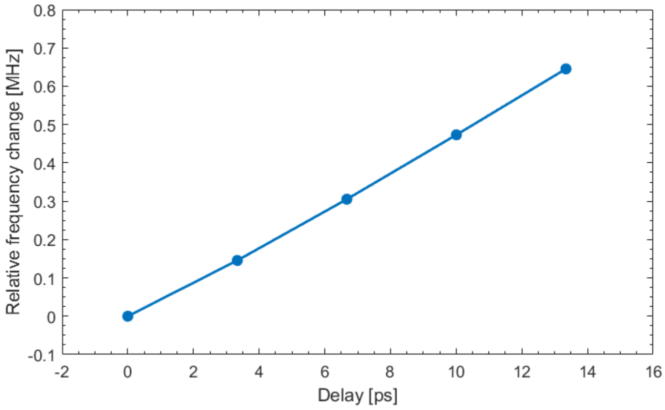

*Figure 3-24*
*Relative peak frequency change with the delay*

### III/2.2.c Stabilization results

The measured phase noise with the 2 examples of the stabilization feedback loop and the free-running phase noise is illustrated in Figure 3-25. The noise of the ESA at 25 GHz is also illustrated in the graph with dashed black curve. Its low level is showing that the ESA was not limiting the measured phase noise. The laser was biased with 147 mA and the temperature was set to 25°C. In the experiment the laser was sent to a high-speed photodiode (u$^2$t XPDV3120R) with 70 GHz bandwidth and a Keysight UXA N9040B Signal Analyser measured the output signal. The incident average optical power on the photodiode was 7.1 dBm. Figure 3-26 illustrates the electrical spectrum of the free-running and the stabilized laser. We can see a small frequency shift between the peaks with around 220 kHz. The stabilized peak can be shifted by adjusting the delay line position, there is around a 0.7 MHz range corresponds to the previously mentioned 14 ps where the output of the MLL is stabilized (see Figure 3-24).

The spurious peaks of the RF spectrum and phase noise curves in case of stabilization are corresponding to the free spectral range (FSR) of the feedback loop. For the 110 m case they are at 1.59 MHz, 3.18 MHz, 4.73 MHz and so on at higher harmonics, for the 200 m case they are at 0.93 MHz, 1.87 MHz, 2.82 MHz and so on. The FSR can be calculated with equation (34).

$$f_{FSR} = \frac{c}{n_{eff} L} \tag{34}$$

Where $c$ is the speed of light, $n_{eff}$ is the effective refractive index of the fibre, in case of SMF-28 it is 1.4682. $L$ is the length of the feedback loop in meters. Expressing $L$ form the above equation, we calculate the full length of the feedback loop for the measured two cases, the calculations gave 128 meters and 218 meters. This length includes the fibre spool and all the short input and output fibres of the fibre based devices, as all the components have around 1 meter fibres at their input and output.

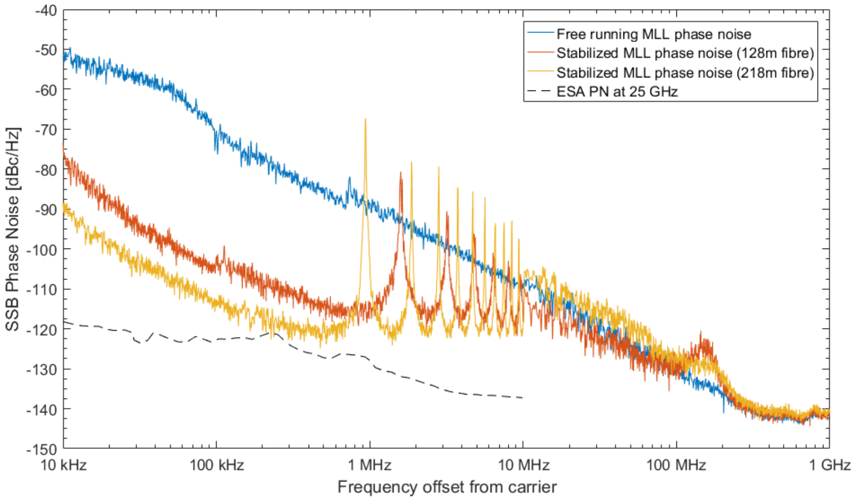

*Figure 3-25*
*SSB Phase noise curve before and after stabilization of MLL*

Comparing the phase noise to the free-running case, for the shorter loop we can observe an improvement of 35 dB at 100 kHz offset frequency, the value decreased from -70 dBc/Hz in the free-running case, down to -105 dBc/Hz in the stabilized case. For the longer loop the improvement is better, at 100 kHz offset, the PN is -113 dBc/Hz. However, the level of the spurious peaks is higher for this case, which can also be observed on the RF spectrum in Figure 3-26. The calculated integrated timing jitter for the above curves are 3.35 ps for the free-running case and 240 fs for the stabilized case with the shorter loop and 494 fs for the longer loop. The higher value of the shorter loop is mainly due to the spurious modes, their levels are higher, and they are closer to the fundamental signal. However, the ten-fold improvement of timing jitter for the shorter loop is already shows the advantage of stabilization.

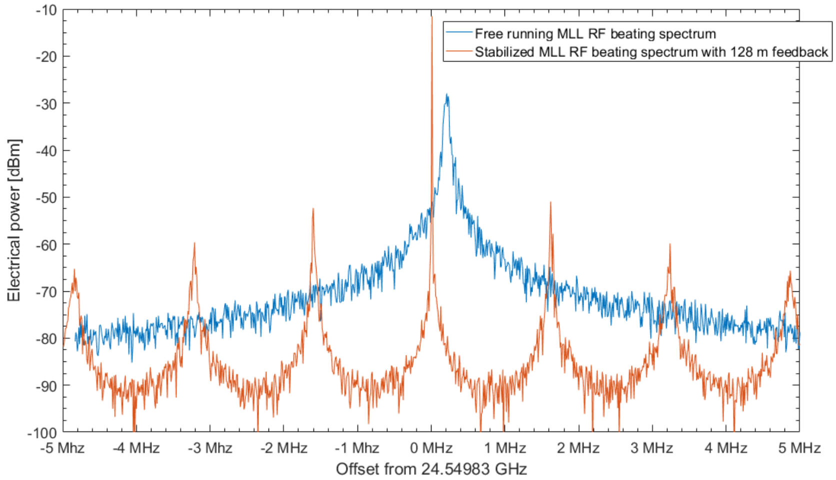

*Figure 3-26*
*RF spectrum of the beating before and after stabilization. RBW/VBW : 3kHz/3kHz*

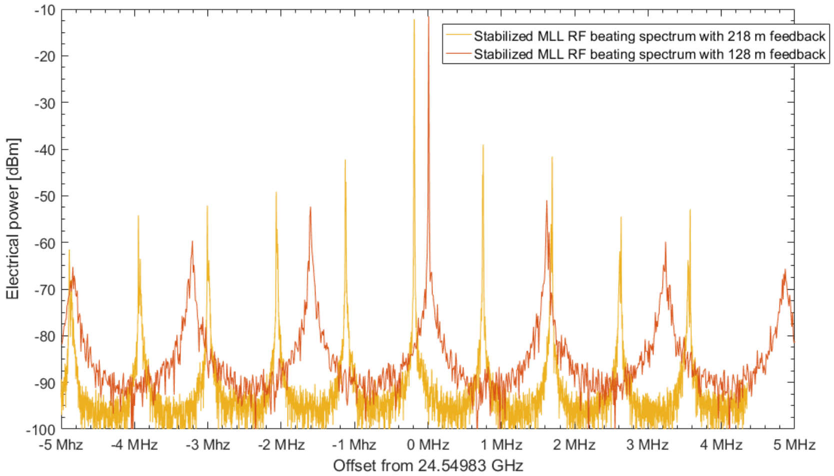

*Figure 3-27*
*RF spectrum comparison of two lengths of feedback loop for stabilization. RBW/VBW : 3kHz/3kHz*

The spurious peaks in the stabilized case have a power level around 40 dB below the main peak power for the shorter loop, which in the above picture is -11.5 dBm, and the closest spurious peaks are at -52.3 dBm and -51 dBm. For the longer loop the level difference is only 30 dB, the peak is at -12.17 dBm, and the side peaks are at -42.2 dBm and -39 dBm. Figure 3-28 illustrates a low span low RBW/VBW recording of the peak signal spectrum in case of the shorter feedback. We can measure a width of 2.77 kHz for a 10 dB bandwidth, this value suggests a 3 dB linewidth of below 1 kHz in case the shape is Lorentzian, which needs to be confirmed. The linewidth is in the same range for the longer feedback too.

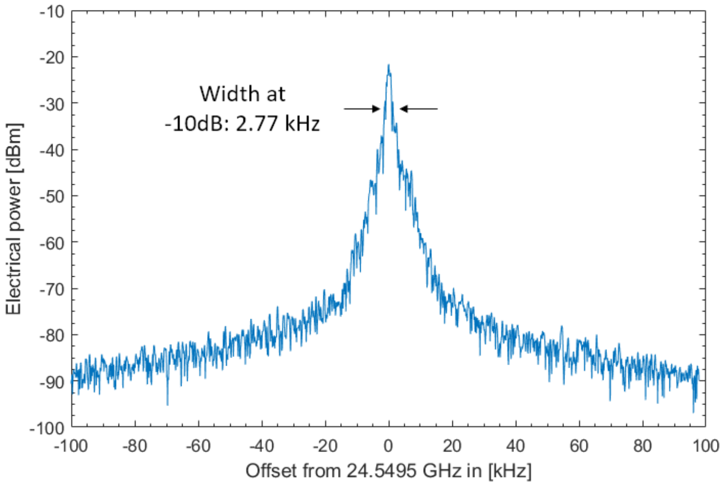

*Figure 3-28*
*Stabilized laser fundamental beating RF spectrum with 200 kHz Span and 300 Hz RBW and VBW*

The stabilization has an excellent quality. Once the stabilization occurs by setting the optimal values for the feedback, our observations shows that it can stay in the stabilized mode for at least half hour. It mainly depends on the temperature control stability and the environmental stability. The experiment was done in a temperature and humidity controlled room.

In the following Chapter IV, the preferred stabilization is with the shorter loop due to the lower spurious peak levels, and their higher distance from the fundamental peak.

### III/2.3. All optical feedback – dual loop setup

A method to further improve the stability of the MLL with all-optical feedback is to construct a second loop in the feedback. The main advantage of the dual-loop setup is that the previously observed spurious tones in the RF spectrum (see Figure 3-26 and Figure 3-27) of the stabilized laser can be suppressed. In [109], the reduction of the spurious levels was attributed to a mean destructive statistical averaging of the timing deviations of the returning noise originating from the two different length loops. The suppression occurs when the shorter loop's free spectral range (FSR) is the integer multiple of the longer loop's FSR. The setup can also be built as a dual opto-electronic loop, where the signals of the two loops are photodetected and added to the laser bias control as in [112].

In our constructed setup, illustrated in Figure 3-29, the two loops are starting at the output of a 50:50 coupler and then re-joined with another 50:50 coupler before the circulator. The two loops contain similar components: an optical attenuator, a long optical fibre, a polarization controller and a variable delay line which is present only in one of the loops. The fibre lengths in the two loops can be symmetrical, when both have the same length or asymmetrical in case of different lengths. A thoroughly investigation of this stabilization scheme was done by the group of *John G. McInerney* at *University College Cork*. The group was experimentally studying various combinations of different feedback power ratios [117], different feedback loop lengths [118] and the tolerance of delay phase mismatch [119]. They showed that in case of a symmetrical loop (equal delay in both loops) and unbalanced power ratio the signal linewidth can be up to 10 times narrower than in case the power ratios are balanced in the loops. The group also showed that using asymmetric feedback loops (the two loops have different lengths) can further reduce the level of the spurious tones. In [118] the first spurious mode can be reduced with 25 dB or can be completely eliminated with an optimal length of the second loop. This optimum occurs when the modes of the two loops are overlapping. As a downside of this optimization of the spurious tones, it causes that the signal linewidth is increasing from 2 kHz to 8 kHz. The stabilization can be further optimized to improve the tolerance of the phase delays in the loops as in [119], by selecting an optimum fine delay position for one loop, the stabilized linewidth stays below 4 kHz for almost the full fine delay range of the second loop. In our setup we are reconstructing the setup for this last case, as only one variable optical delay line is available.

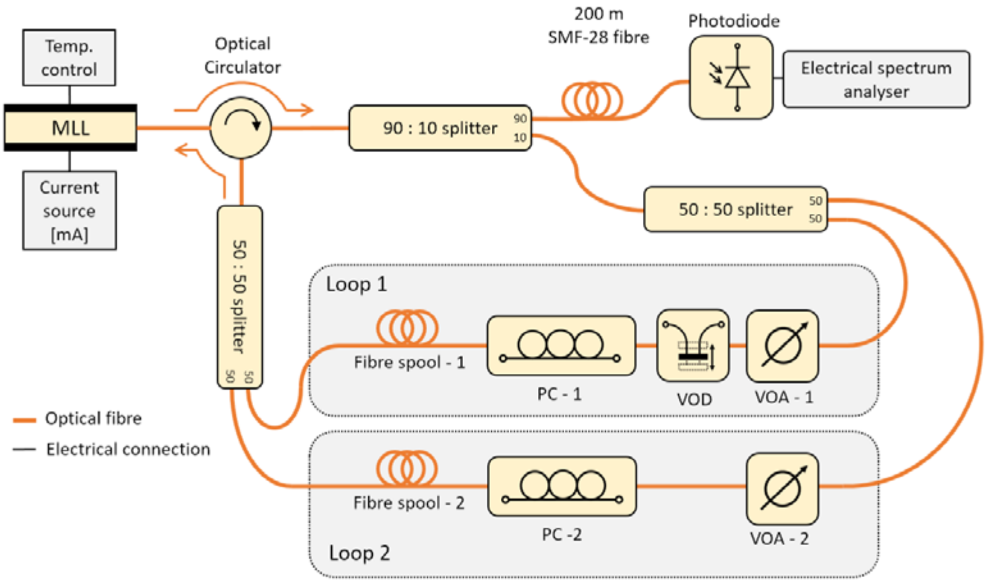

*Figure 3-29 Setup of the dual-loop all optical feedback.*
*PC: Polarization controller; VOD: Variable optical delay line; VOA: Variable optical attenuator*

In our setup the Loop-1 has 110 meter long fibre and Loop-2 has 210 meters. Calculating the feedback lengths with the component's short fibres, the Loop-1 length is around the half of Loop-2, which means that the modes of Loop-1 coincides with ever 2$^{nd}$ mode of Loop-2, which can be calculated from the FSR. We are setting the optical powers and polarizations to the optimal values while observing the fundamental RF beating signal with an electrical spectrum analyser after photodetection. Figure 3-30 shows the RF spectrum for a single loop setup and a dual loop setup. The single loop was recorded with disconnected Loop-2 and with optimized adjustments. The dual loop is recorded by connecting Loop-2 and readjusting the loop components for the optimum stabilization.

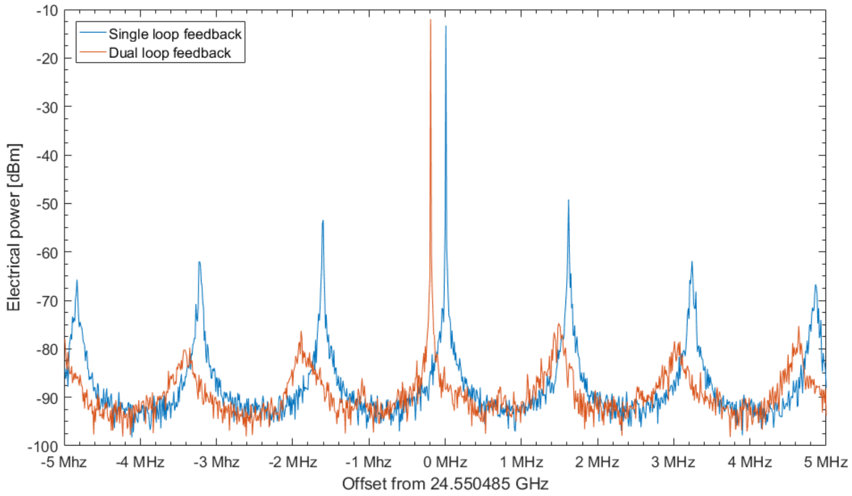

*Figure 3-30*
*RF beating spectrum of the single and dual loop feedback*

In the dual loop case, the peak power is -12 dBm and the closest side modes to the fundamental are at -74.7 dBm and -76.3 dBm. This means a side mode power level 62.7 dB lower, which is more than 20 dB improvement compared to the single loop setup. The SSB Phase noise curves corresponding to the previous spectrums are illustrated in Figure 3-31. The phase noise improvement is significant only around the levels of the spurious peaks, the level at 100 kHz offset frequency is -105 dBc/Hz for the dual loop, while for the single loop it is -100 dBc/Hz. In section III/2.2 with the single loop setup we also achieved to have -105 dBc/Hz for this offset frequency with a bit shorter fibre length in the loop too. Calculating the integrated timing jitter from the curves, we get 167 fs for the dual loop, and 188 fs for the single loop, which means the dual loop has around 10 % improvement in the timing jitter, mostly due to the suppressed spurious modes.

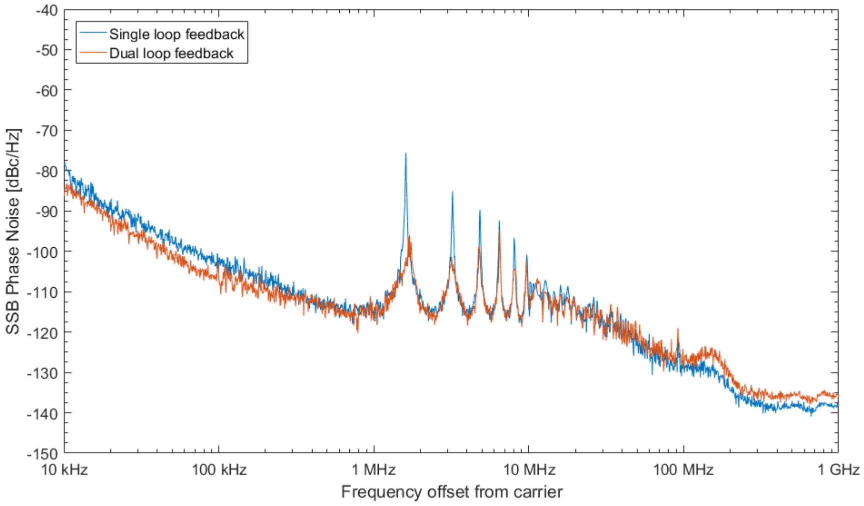

*Figure 3-31*
*Phase noise curve of the single and dual loop setup*

The main limitation of the dual loop setup is its short-term stability. In contrast with the single loop setup, we observed that the stabilization needs constant surveillance and fine tuning adjustments, while the single loop setup stayed in the stabilized mode without any intervention. During the experiment, when the stabilization occurs with dual-loop setup it can stay in that state for less than a minute in best case, before further adjustments are needed, so we mainly decide not to use this set-up as it was not convenient for day-to-day experiments and the single loop has already showed significant stability improvements compared to the free-running mode of the MLL.

## III/3. Stabilization summary

Table 7 details the main properties of the stabilization setups and the improvements in term of linewidth, phase noise and integrated jitter. The table details the feedback fibre lengths with the real calculated lengths considering also the component's short cables.

In a free-running mode, without any stabilization, the MLL beating at its fundamental frequency of 24.55 GHz has a linewidth of 20 kHz, and a phase noise of -70 dBc/Hz at 100 kHz offset frequency. This phase noise corresponds to an integrated timing jitter of 3.7 ps. The implemented stabilization loop improves these values significantly with a feedback fibre loop length of 128 m. The linewidth decreased below 1 kHz and the phase noise is down to -100 dBc/Hz. The stabilization introduced spurious tones in the electrical spectrum of the signal, which have a frequency distance from the carrier corresponding to the free-spectral range of the fibre loop length. Even though these spurs are present, the integrated timing jitter of the stabilized phase noise curve is 188 fs, which is a 20-fold improvement compared to the free-running case.

*TABLE 7. PROPERTIES OF STABILIZATION METHODS*

| | Linewidth | PN @ 100 kHz offset | Integrated Jitter | Loop-I fibre spool length | Loop-II fibre spool length |
|---|---|---|---|---|---|
| Free-running MLL | 20 kHz | -70 dBc/Hz | 3.7 ps | - | - |
| Single loop stabilization | < 1 kHz | -105 dBc/Hz | 240 fs | 118 m | - |
| Single loop stabilization | < 1 kHz | -100 dBc/Hz | 188 fs | 128 m | - |
| Single loop stabilization | < 1 kHz | -112 dBc/Hz | 494 fs | 218 m | - |
| Dual loop stabilization | < 1 kHz | -105 dBc/Hz | 167 fs | 118 m | 228 m |

The dual-loop setup further improves the signal quality, mainly by reducing the spurious modes level by 20 dB. However, the short-term stability of this setup and the constant need of adjustments of the feedback loop properties (delay and polarization) makes the dual-loop setup not practical for system measurements.

Considering the best achieved timing jitter value of 167 fs theoretically could allow to construct a single channel ADC with a sampler using this laser source at 24.5 GHz, with an ENOB value around 4 bits (according to the Walden-plot shown in Chapter I, Figure 1-28).

## III/4. Conclusions on Chapter III

In this chapter we first characterized an InP based semiconductor mode-locked laser (MLL) with a self-oscillating frequency of 24.55 GHz. The characterisation involved measuring the optical spectrum and power. The required standard optical fibre at the output of the laser for compensating the intrinsic dispersion was also determined through measuring the temporal pulsewidth of the laser pulses. The pulses are 1 ps long in case of using 200 meters of optical fibre. We measured the stability of the laser in term of single sideband phase noise (SSB-PN). At 100 kHz offset frequency, the PN is -70 dBc/Hz. We constructed an all-optical feedback loop to improve the laser stability. With a single loop configuration, the best achieved phase noise is -112 dBc/Hz at 100 kHz offset, with spurious peak levels of -39.5 dBc. An improved feedback with dual-loop improved the spurious peak level to -62.7 dBc, however in contrast with the single loop, considering the short term stability of the stabilization, the feedback loops need constant adjustments to stay in the stabilized regime. This makes the dual-loop feedback less practical for optoelectronic mixing experiments, therefore in the following chapter we are using the single loop setup for the experiments. Another figure-of-merit for the stabilization is the integrated timing jitter calculated form the SSB-PN curves. The best jitter achieved with the presented solution is 167 fs integrated in the 10 kHz – 1 GHz range, it is more than a 20-fold improvement compared to the free-running case.

# Chapter IV

# Photoswitch as an optoelectronic mixer

IV/1. Heterodyne mixer of narrowband signals .................................................... 103
  IV/1.1. Setup design........................................................................................ 103
  IV/1.2. Conversion loss ..................................................................................... 105
    IV/1.2.a Discussion about the high conversion losses ............................. 107
    IV/1.2.b Simulation of the conversion loss............................................... 109
  IV/1.3. Heterodyning of two DFB lasers ........................................................... 109
    IV/1.3.a Conversion loss........................................................................... 111
    IV/1.3.b Simulation of the conversion loss............................................... 112
    IV/1.3.c System characterization ............................................................ 112
    IV/1.3.d Heterodyne detection results..................................................... 114
IV/2. Optoelectronic mixer for data-stream downconversion ................................ 115
  IV/2.1. QPSK modulation format for the data-stream ...................................... 116
  IV/2.2. Data-stream demodulation – EVM and BER......................................... 117
  IV/2.3. Optically provided local oscillator - MLL................................................ 119
  IV/2.4. Optically provided local oscillator – DFB laser...................................... 124
  IV/2.5. Electrically provided local oscillator ..................................................... 126
IV/3. Study of switch non-linearities......................................................................... 129
IV/4. Applications of the optoelectronic mixer schemes ........................................ 132
IV/5. Conclusions of Chapter IV ............................................................................... 135

In Chapter II we characterised the photoconductive switches made of InGaAs. Then in Chapter III, we characterized and stabilized the semiconductor mode-locked laser. In this chapter, we are going to use the two devices together in an optoelectronic mixing scheme. The MLL beating signal is used as the local oscillator signal, which is mixed with an electrical signal at the input of the photoconductive switch. The output mixing signals are analysed to obtain the characteristics of the proposed scheme.

## IV/1. Heterodyne mixer of narrowband signals

Photoconductive materials have a broad wavelength sensitivity range which allows to use wide bandwidth signals in the optical domain. The operating bandwidth of the device is usually limited because of the electrical components of the system. In Chapter II, we measured the low equivalent capacitance of the photoswitches: 5 fF – 8.1 fF, and the AC dark resistance values of 2.1 kΩ – 5 kΩ. These values are giving an electrical characteristic time of 300 fs in case of 50 Ω load. This low value suggests a theoretical electrical bandwidth limit in the sub-Terahertz range. In the following experiment we are measuring the optoelectronic bandwidth of the used photoswitches by measuring a mixing product of an optical signal and an electrical signal. Due to the equipment limitation, we are measuring the properties only in the microwave frequency range.

### IV/1.1. Setup design

The setup is similar as before, the photoconductive switch is placed on an RF probe station, two coplanar probes are making the connection between the two sides of the switch and the electrical equipment. The laser signal is guided to the switch through an optical fibre. Two Cascade Microtech Infinity i67 RF probes were used and a third probe for the optical fibre. A photograph of the probe station setup is illustrated in Figure 4-1.

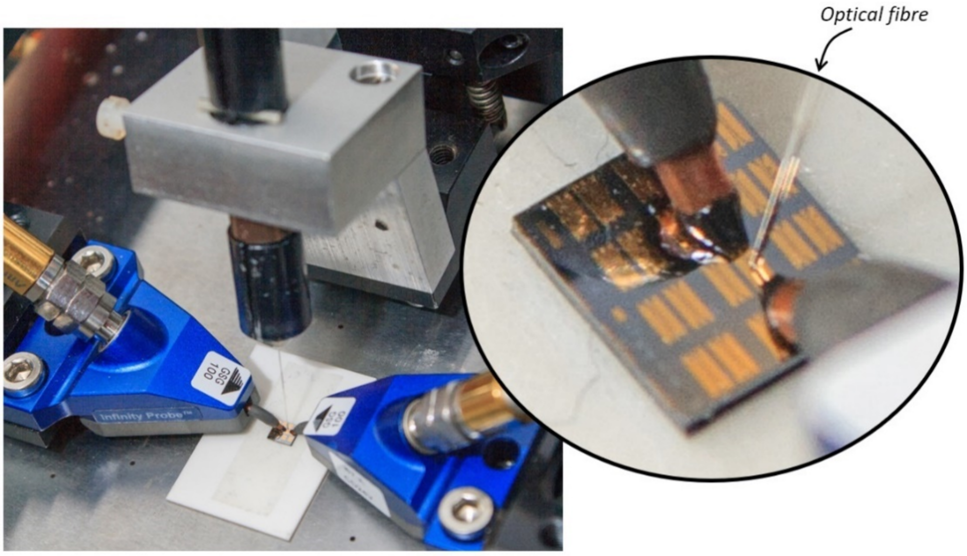

*Figure 4-1 Photoswitch sample in the RF probe station with two RF probes and fibre probe. Inset: magnified view of the connected switch*

We are using the semiconductor MLL, described in Chapter III, with the stabilization feedback. The setup schematics is illustrated in Figure 4-2. The average optical power illuminating the photoswitch was 7 dBm (5 mW), with 1 ps optical pulse duration thanks to the dispersion compensation of the 200 meters of SMF-28 fibre (see Chapter III, section III/1.4).

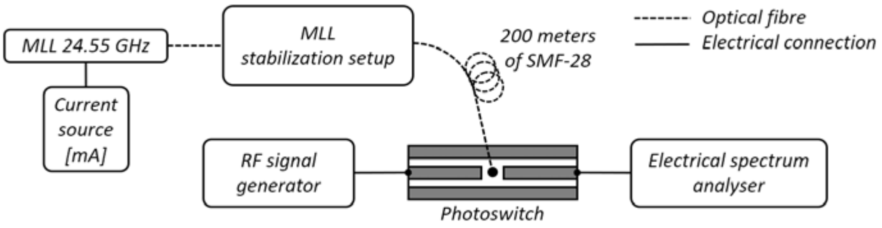

*Figure 4-2 Heterodyne mixer setup*

The photoswitch in all the following experiments of Chapter IV is unbiased. Using an additional DC bias, as expected did not have any effect on the performances in the different experiments presented. At the electrical input of the photoswitch an Agilent 8257D (250 kHz – 67 GHz) RF signal generator provides a variable frequency signal, while at the output, a Keysight UXA N9040B (2 Hz – 26.5 GHz) Signal Analyser is used for frequency domain analysis. In this configuration the photoconductive switch acts as an optoelectronic mixer. The periodic optical signal is creating an oscillating photogenerated carrier density in the InGaAs semiconductor. As we apply a sinusoidal signal at the input, an oscillating electric field is built up between the electrodes of the switch and together with the optical signal excitation it generates mixing products in the photocurrent. These mixed products can be measured at the output of the photoswitch.

The optically generated local oscillator signal is used to down- or upconvert the electrical signals, therefore creating a heterodyne mixer. In case the optical source is a mode-locked laser, providing an optical pulse train which has a large number of spectral components in the frequency domain, at the output we also measure a large number of mixing products between the electrical RF signal and the optical signal. The spectral components of the mixing are illustrated in Figure 4-3.

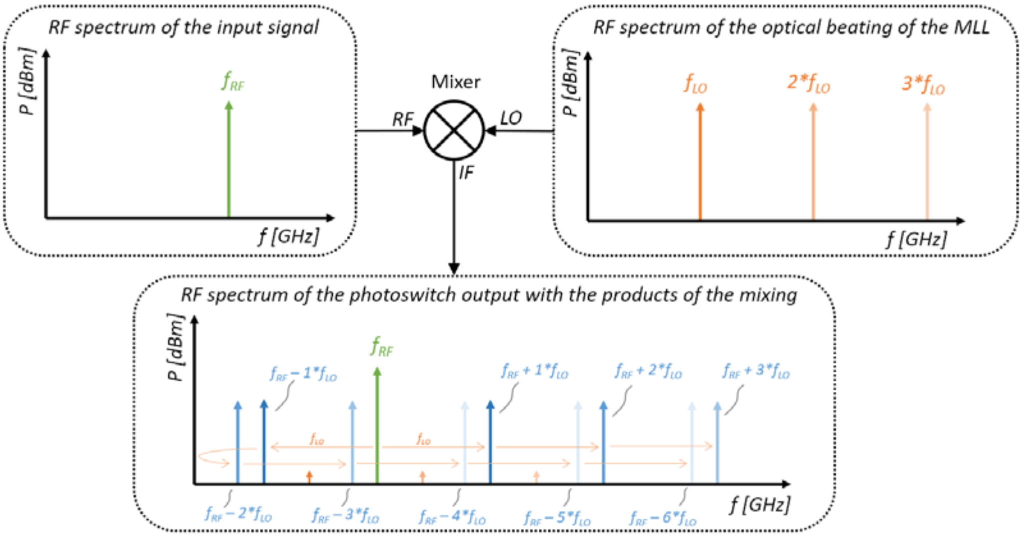

*Figure 4-3 Illustration of the mixing products of the proposed mixer scheme*

The local oscillator (LO) signal at $f_{LO}$ is generated by the MLL mode beatings, which means that the local oscillator signal is present also at the harmonics of $n * f_{LO}$, where $n$ is an integer. The first couple of harmonics have similar electrical power on the RF spectrum, as it was shown for a lower frequency MLL in [120]. The input RF signal at $f_{RF}$ is an electrical signal, in our experiments either a sinusoidal signal or a data-stream modulated signal with a defined bandwidth. In the following first experiments, it is a narrowband pure sinusoidal signal. At the output of the switch the mixing products can be measured at the intermediate frequencies (IF): $f_{IF} = f_{RF} \pm f_{LO}$, which in the MLL case is $f_{IF} = f_{RF} \pm n*f_{LO}$. Due to the switch non-linearities, and also due to the harmonics of the signal generator, mixing products can be found at the intermediate frequencies of $f_{IF} = m*f_{RF} \pm n*f_{LO}$, where $m$ is also an integer. These frequency components are not illustrated in Figure 4-3, they will be studied later on in this chapter in section IV/3.

In the following measurements, for every data point one single mixing product's power is measured, the conversion losses of the mixer can be deduced from these results. In the experiments were using a type 3:3 switch, which type showed the highest power for the IF signals.

### IV/1.2. Conversion loss

In mixers, the conversion loss (CL) is an important property, it shows the loss between the power of the input RF signal ($f_{RF}$) and the power of the output intermediate frequency signal ($f_{IF}$). We are measuring this value for a wide range of input frequencies with a fixed LO frequency provided by the MLL at its fundamental frequency of 24.55 GHz, and at its harmonics. The signal generator at the input is capable to generate frequencies up to 69 GHz, while the signal analyser at the output can detect signals up to 26.5 GHz. We note that the signal generator's calibrated operating range is up to 67 GHz, however we experienced no signal degradations at 68 GHz and 69 GHz. These equipment allowed us to measure the conversion loss with three LO frequencies: the fundamental beating signal, the 2nd and 3rd harmonic of the fundamental signal, for the following RF frequencies.

1. The fundamental beating signal at 24.55 GHz and input RF frequencies in the 1 GHz – 51 GHz range. Measured mixing product at $f_{IF} = f_{LO} - f_{RF}$.
2. The 2nd harmonic at 49.1 GHz and input RF frequencies in the 23 GHz – 68 GHz range. Measured mixing product at $f_{IF} = f_{RF} – 2*f_{LO}$.
3. The 3rd harmonic at 73.65 GHz and input frequencies in the 48 GHz – 69 GHz range. Measured mixing product at $f_{IF} = 3*f_{LO} - f_{RF}$.

In the above cases the IF frequency fell always in the bandwidth of the ESA (26.5 GHz). We measured the power of the IF signal in each case and calculated the conversion loss by taking into consideration the losses of the RF cables. At the input we used a coaxial cable calibrated in the DC - 67 GHz range, and at the output a coaxial cable calibrated in the DC - 40 GHz range. The losses $L$ of both cables are known by measurement or from the factory datasheet. The calculation was done with the formula in (35).

$$Conversion\ Loss = CL = \frac{P_{RF} - L_{67\ GHz\ cable}}{P_{IF} - L_{40\ GHz\ cable}} \qquad (35)$$

The cable losses were ranging from 0.74 dB to 6.4 dB for the 67 GHz cable, and 0.23 dB to 1.84 dB for the 40 GHz cable. The input RF power was set to 15 dBm, except above 60 GHz where the equipment limit is 14 dBm, for 68 GHz the limit is 13 dBm and for 69 GHz the limit is 12 dBm. The measured IF power with the ESA without any compensation calculation was in the range between -59 dBm and -68 dBm. All the data points were measured with 3 kHz/3 kHz RBW/VBW and 5 MHz Span settings. The mode-locked laser was in the stabilized state with a feedback fibre length of 110 meters and a stabilized timing jitter of 188 fs. For further details of the stabilization see Chapter III section III/2.2. The compensation calculation doesn’t contain the losses introduced by the RF probes, which is typically between 0 dB and -1 dB up to 67 GHz according to the probe data-sheet. The calculated CL dependence on the input RF frequency is illustrated in Figure 4-4 for the first 3 LO harmonics.

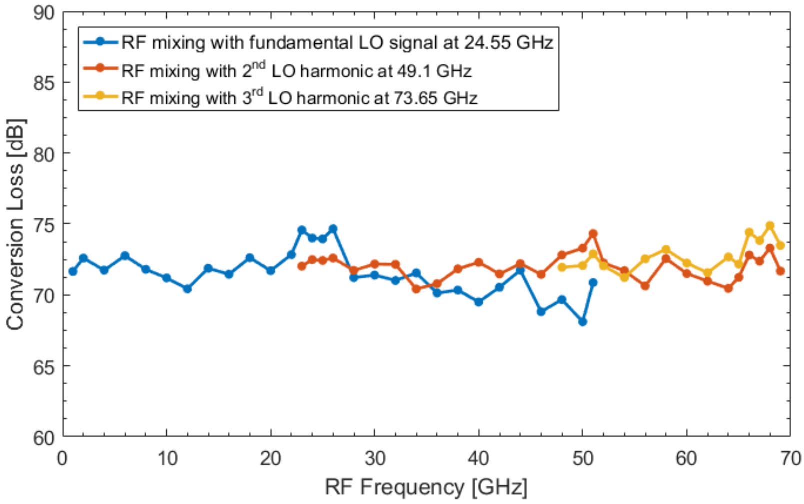

*Figure 4-4*
*Conversion loss of the photoswitch versus input RF frequency for the first 3 harmonics of the optical LO*

The results show that the conversion loss has a variation of 7 dB around 72 dB over the full 69 GHz wide RF frequency range. The performance is uniform for all three local oscillator harmonics, which shows that at least the first 3 beating signal of the MLL produces the similar RF power.

It is expected that higher harmonics have also similar power level, which we were able to confirm for the 4th, 5th and 6th harmonics thanks to a harmonic mixer (Keysight M1971E) extending the ESA input bandwidth into the 60 GHz – 90 GHz frequency range. The higher MLL harmonics are at the following frequencies: 4th: 98.2 GHz; 5th: 122.75 GHz and the 6th: 147.3 GHz. The input RF frequencies were once again swept from 0 GHz to 68 GHz. For different input frequencies the $f_{IF} = n*f_{LO} - f_{RF}$ intermediate frequency can be positioned in the harmonic mixer’s range. In this case the switch output was connected to the harmonic mixer (and ESA) with an RF probe (i110 Cascade Microtech) and a coaxial cable calibrated up to 110 GHz. The results show that the conversion loss between the higher harmonics of the MLL is also in the same range as with the fundamental signal and the 2nd and 3rd harmonics. This measurement indicates that also the 4th, 5th and 6th harmonic of the MLL have around the same amplitude as the fundamental. It is also showing that the photoswitch is able to detect optically generated signals at least up to 147.3 GHz (6th MLL harmonic), confirming its high optical bandwidth.

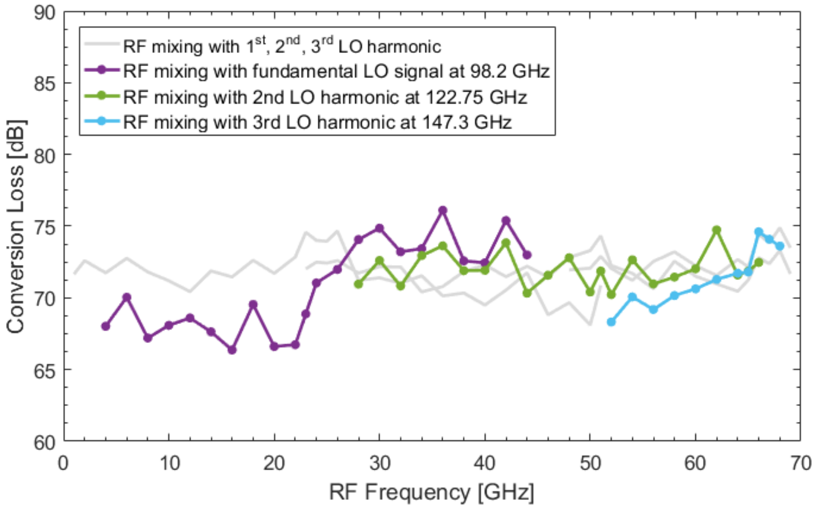

*Figure 4-5*
*Conversion loss of the photoswitch versus input RF frequency for the 4th, 5th and 6th harmonics of the optical LO*

As the efficiency of the optoelectronic mixing is depending on the switch's conductance, this conversion loss depends on the optical power of the MLL, therefore the local oscillator power. In Figure 4-6 we can see the dependence of the conversion loss on the average optical power illuminating the switch. The measurement was done at 10 GHz input RF frequency with 15 dBm power. The result shows a linear decrease of the conversion loss on the logarithmic scales with a decrease of 1.85 dB with every 1 dB increase of optical power, until the maximum available power of 7.1 dBm. During the first characterisations of the photoswitch at UCL, it was shown that the switch can handle higher optical powers too, in [29], 17 dBm (50 mW) optical power was used. Therefore, by increasing the optical power, the IF power would increase with the same rule as in Figure 4-6 if there are no saturation effects. The conversion loss would be as low as 53.5 dB if the MLL's optical power could be as high as 17 dBm.

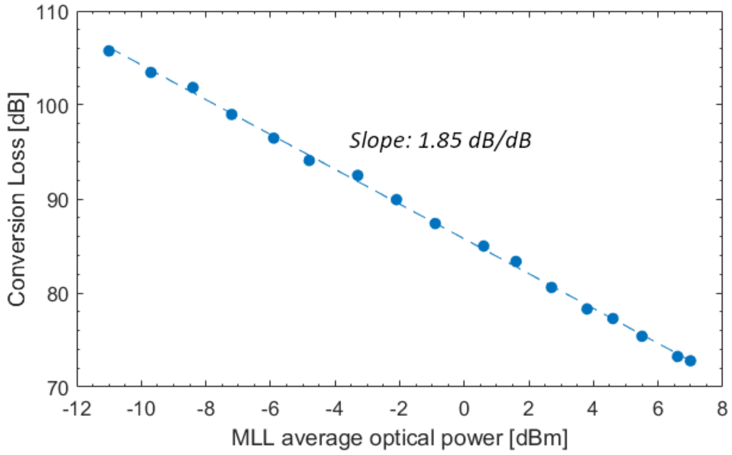

*Figure 4-6*
*Conversion loss dependence on optical power of the MLL*

It is difficult to predict the saturation value where the conversion loss would be the lowest, it is depending on semiconductor material properties and physical effects like the saturation of the generated photocarriers, and the approximation would require the exact knowledge of these.

### IV/1.2.a Discussion about the high conversion losses

The presented conversion loss of 72 dB (see Figure 4-4) is considered a high value for mixers. Comparing it to the more efficient and already developed GaAs photoswitch technology, we can find losses with orders of magnitude lower, as we reviewed it also in *Chapter I* sections *I/2.2* and *I/2.3*. An LT-GaAs device reported by *E. Peytavit et al.* [35] achieved a CL of 22 dB with 100 GHz input RF signal (with 9.3 dBm) and 20.7 dBm optical power. Their measured loss with 7 dBm optical power was around 46 dB, considering also the different RF input power, it presents a lower CL with 30 dB compared to our device. However, their GaAs switch was working with 800 nm wavelengths.

A work from *M. billet et al.* [39], also based on LT-GaAs photoswitch with an improved resonant structure for increased efficiency for 1550 nm wavelengths, achieved conversion losses in the same order as our InGaAs switch. They reported a CL of 66 dB for the same input frequency range as us using 17 dBm optical power emitted from an MLL with 90 MHz repetition rate. This loss performance is 12 dB higher than our solution (as our solution would have a CL of 53 dB with 17 dBm optical power), however it is important to note that it was achieved with LT-GaAs which has a low absorption efficiency at 1550 nm wavelengths.

InGaAs photoconductor performances at millimetre wave (mmW) frequencies is not a well-researched area, these devices are mainly used for THz generation. A work by *H. Song et al.* [66] was investigating the optoelectronic mixing performances of an InGaAs photoswitch. The achieved losses were greatly limited by the long lifetime of the used InGaAs material. A CL of 15 dB in case of an optical LO frequency of 100 MHz grew to 50 dB as the LO frequency increased to 10 GHz. Because of this low bandwidth, their solution can't be used at mmW frequencies.

To increase the efficiency of the photoswitch based optoelectronic mixer, it is essential to improve the quantum efficiency of the device. The discussed nanoplasmonic solutions as proposed in [30], and as we discussed in section I/2.3, are a promising technique to achieve low conversion losses. The enhanced optical absorption in the active region of the photoconductive material can dramatically improve the efficiency. Many of the ongoing researches now are mainly focusing on Terahertz frequencies, but these improvements are also affecting the performance in the lower mmW frequency range too.

The low conversion loss is also originating from the short pulsewidth of the used laser. In this work we are using 1 ps long optical pulses from the MLL, which means that the photoswitch is opening only just a bit longer than this period due to the carrier lifetime being in the same order, and it is closed for the main part of the repetition period (MLL repetition rate: 40 ps) until the next pulse arrives. A higher ratio of ON/OFF switch state could further improve the conversion loss with at least one order of magnitude, due to the longer opening time while a bigger portion of the electrical signal can pass. A theoretical study done by *Yann Desmet* from IEMN, Lille [121], made a comparison with the conversion losses using different pulsewidths with a 1 GHz repetition rate source. The calculations in his work showed that a conversion loss of 63 dB at 50 GHz input RF frequency in case of 1 ps optical pulses can decrease to 52 dB in case of using 4 ps optical pulses. However, the improvement is at the expense of the bandwidth, the 4 ps pulsewidth case has a loss of 72 dB at 200 GHz input RF, while with 1 ps optical pulses it is 64 dB at 200 GHz.

These solutions could improve the mixing efficiency of our device, however despite these high losses in our system, we were able to use it for optoelectronic mixing and data-stream downconversion. The experiments and results are described in the following parts of Chapter IV.

### IV/1.2.b Simulation of the conversion loss

The simulations shown in Chapter I and Chapter II can also be used to simulate the conversion loss of the photoconductive switch. In this case the input optical signal is a pulse train with the properties of the semiconductor MLL: 24.55 GHz repetition rate and 7 dBm (5 mW) optical power. The switch RF input is a sinusoidal signal with 0 dBm power and 30 GHz frequency, and the switch details (capacitance, dark resistance) is set for a type 3:3 switch. The simulation calculates the output signal for every time step of 1 fs in a 20 ns long time window. This output time domain signal is then Fast-Fourier Transformed (FTT) into the frequency domain for analysis. More details and description of the Matlab script used for the simulation can be found in Appendix A. Figure 4-7 is showing the spectrum of the input signal with dashed blue curve and the spectrum of the output signal containing the mixing components with orange curve.

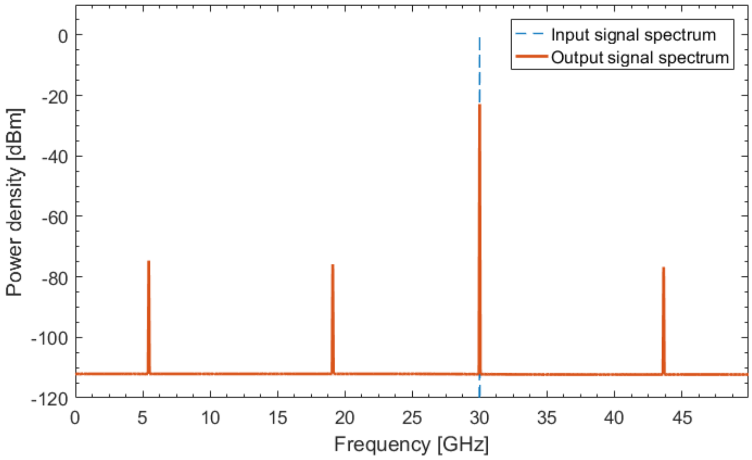

*Figure 4-7*
*Spectrum of the simulated switch output and input signals for mixing with MLL as LO source.*

The highest peak of the orange curve is the switch feedthrough signal, which corresponds to the measured values in section II/2.2. The three smaller peaks are the mixing products of $f_{RF} - n*f_{LO}$ between the input signal and 3 LO signals: the fundamental signal of the MLL and its 2nd and 3rd harmonic. The conversion loss of the input signal and these mixing products are: 74.63 dB, 75.83 dB and 76.71 dB (respectively for the 1st, 2nd, 3rd harmonic). This loss is in the same order as the measured values in the experiment.

## IV/1.3. Heterodyning of two DFB lasers

Another method of generating RF signals optically is the use of single mode lasers having different wavelengths. Illuminating a photoconductor with the two lasers we can generate electrical RF signal with the frequency difference of the two optical modes. The method requires laser sources with extremely stable wavelengths, a wavelength shift of 0.01 nm in one of the lasers will result in a generated signal frequency shift of 1.25 GHz at 1550 nm wavelengths. We tested the photoswitch capabilities of downconverting the optical beating of two continuous wave DFB lasers in a broad 164 GHz wide range. We used integrated glass lasers fabricated at IMEP-LAHC laboratory. The design, fabrication and characterization of the laser was performed by *Nisrine Arab* [122].

Distributed feedback (DFB) lasers integrated on erbium/ytterbium co-doped glass were providing the optical signals. They are composed of waveguides made by silver/sodium ion exchange, on top of them a Bragg grating is implemented by holographic exposure [123]. Each laser emits several milliwatts of optical power around the peak of the erbium spectrum at 1534 nm. As the beating frequency is determined by the difference between the two lasers wavelengths, several couples of single mode lasers emitting with varied wavelength difference ranging between 0.1 nm and 1.28 nm were used during the measurement. The wavelength of each laser was fixed during its fabrication by adjusting predetermined parameters.

The setup of the experiment is illustrated in Figure 4-8. The two lasers were emitting with $\lambda_1$ and $\lambda_2$ wavelengths and each output was coupled into a single SMF-28 fibre, and then the two signals were joined with a 3 dB fibre based coupler. The coupler output was guiding the laser signal to the photoswitch. We used the i67 probes for the electrical connections of the switch in case the IF signal is in the 0 – 26.5 GHz range of the ESA. For higher frequencies, we used a harmonic mixer (Keysight M1971E) with the ESA to be able to measure IF frequencies in the 60 GHz - 90 GHz range, in this case we used the i110 model for RF probe at the switch output. The input $f_{RF}$ signal was provided by an Agilent 8257D (250 kHz – 67 GHz) signal generator.

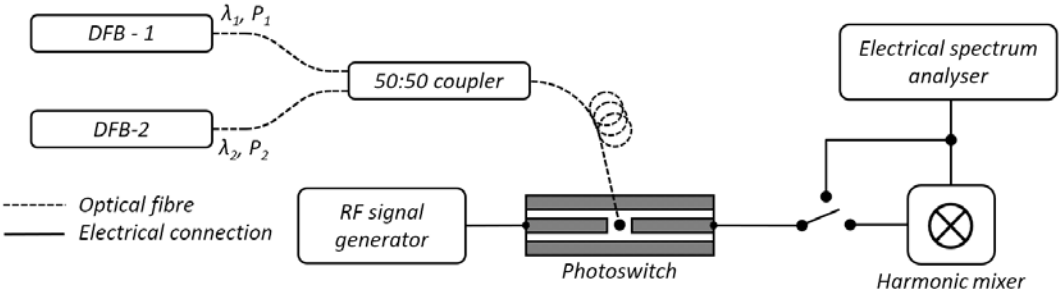

Figure 4-8 Setup for heterodyne detection of DFB laser signals

The $f_{LO}$ frequency is determined by the wavelength difference of the two lasers, calculated with equation (36).

$$f_{LO} = \left|\frac{c}{\lambda_1} - \frac{c}{\lambda_2}\right| \tag{36}$$

Where $\lambda_1$ and $\lambda_2$ are the wavelengths of the two lasers, and $c$ is the speed of light in vacuum. If the two DFB laser provides spectrally pure signals there is only one local oscillator signal in contrast with the several harmonics produced in case of the mode-locked laser. This means that we have two IF signals at $f_{RF} + f_{LO}$ and $f_{RF} - f_{LO}$. In our experiments we are considering only one of these mixing products for one measurement. The instantaneous total optical power ($P_t$) after joining the two laser beam can be describe with equation (37) [32].

$$P_t = P_1 + P_2 + 2\sqrt{mP_1P_2}[\cos(\omega_1 - \omega_2)\,t + \cos(\omega_1 + \omega_2)t] \quad (37)$$

Where $P_1$ and $P_2$ are the average optical powers, $\omega_1$ and $\omega_2$ are the angular frequencies of the two optical signals, and $m$ is a mixing efficiency ranging between 0 and 1.

The phase noise and linewidth of the heterodyne signal is depending on the optical linewidth of the two laser modes, a generated electrical RF signal linewidth of 600 Hz was reported in [124] with the lasers used also here.

In the next section IV/1.3.a we are measuring the conversion loss with a fixed optical frequency and swept electrical input signal frequency. In section IV/1.3.d, we sweep the optically generated frequency up to 164 GHz and measure the conversion loss for each of it. These measurements are aimed to show the electrical and optical bandwidth of the switch.

### IV/1.3.a Conversion loss

The first experiment is measuring the conversion loss of the photoswitch as an opto-electronic mixer for a fixed LO frequency. The method is identical as in section IV/1.2. We selected 39.4 GHz as $f_{LO}$ and measured the IF signal with swept RF input between 13 GHz and 65 GHz with 15 dBm power. The wavelengths of the lasers were $\lambda_1$ = 1533.242 nm and $\lambda_2$ = 1533.52 nm with optical powers of $P_1$ = 14 dBm and $P_2$ = 10 dBm. During this measurement we used the ESA directly connected to the switch output (Figure 4-8). The coupler and the fibre introduced losses which results in a total illuminating average optical power at the photoswitch of 11.9 dBm. Cable losses are considered in the conversion loss calculation, it was ranging from 4.4 dB to 8 dB depending on the RF and IF frequencies. The calculated Conversion Loss curve is illustrated in Figure 4-9.

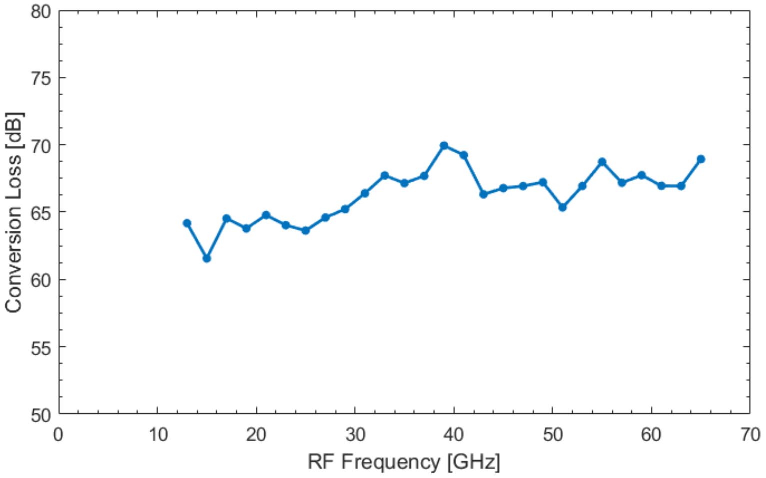

*Figure 4-9 Conversion loss of mixing with two DFB lasers as a local oscillator frequency source*

The measurement shows a conversion loss around 67 dB, which is slightly increasing with higher RF frequencies. The value is 5 dB better than in the case of the MLL laser (see Figure 4-4), which is also caused by the higher optical power used here. However, a complete comparison of the conversion loss could be misleading, because in the MLL case the RF signal is generated by the beating of more than 40 optical modes and higher harmonics are also generated, while in this case there are only 2 laser modes used.

### IV/1.3.b Simulation of the conversion loss

Similarly as in section IV/1.2.b, this experiment can be also simulated with the Matlab model detailed in APPENDIX A. In this case the optical signal is a sinus signal with the beating frequency of the two CW laser. In the simulation we set a 20 GHz frequency input RF signal with 0 dBm power. The beating frequency is at 35 GHz and the total illuminating optical power is 11.9 dBm. Figure 4-10 is illustrating the simulation results. The blue dashed curve is the spectrum of the input signal with a peak at 20 GHz. The orange curve is the spectrum of the output signal.

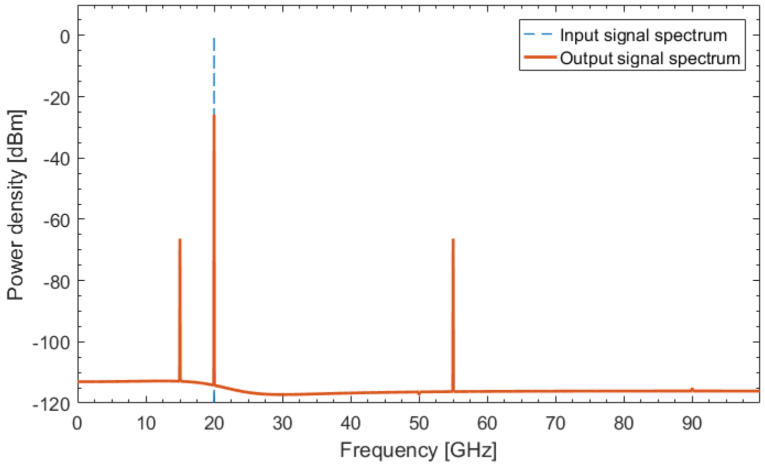

*Figure 4-10*
*Simulated spectrum of the switch input (blue) and output (orange) with optical beating as a LO*

The higher peak of the orange curve is the feedthrough signal from the input. The two lower peaks are the IF signals at 15 GHz ($f_{LO} - f_{RF}$) and at 55 GHz ($f_{LO} + f_{RF}$). Both of it has a power level of -66.3 dBm, which corresponds to 66.3 dB of conversion loss. This value is in the same range as our measurement, illustrated in Figure 4-9. See APPENDIX A for a detailed description.

### IV/1.3.c System characterization

We characterize the heterodyne detection system in a broad range of optical powers. Figure 4-11 is showing the IF power dependence on the total optical power reaching the switch. We used a variable fibre based attenuator to sweep the optical power, it was placed after the coupler directly before illuminating the switch (setup in Figure 4-8). A straight slope can be fit on the results which is showing a linear increase of the IF power in a wide optical power range from -10.2 dBm to 12.2 dBm. In this measurement the two lasers were selected to generate a frequency of 13 GHz ($f_{LO}$), and the input RF frequency was at 20 GHz ($f_{RF}$), with 15 dBm power. We measured the mixing product at $f_{IF} = f_{RF} - f_{LO} = 7$ GHz.

The linear fitting on the result curve has a slope of 1.9 $\mathrm{dB}_{\mathrm{electrical}}/\mathrm{dB}_{\mathrm{total.optical}}$. It means that with 1 dB increase in optical power, the IF power increases with 1.9 dB. We observed no saturation effects in the measured optical power range. This quadratic dependence was predicted by the theory described by *E. R. Brown et al* [32]. The photogenerated current, therefore the square root of the generated signal power is in proportion of the square root of the optical power. The instantaneous total optical power detected by the photoswitch can be described with equation (37). Here we are interested only in the third element containing both optical signals. The generated photocurrent of $I_{photo}$ is proportional to this part (equation (38)), and the power of the heterodyne signal to the square of this component (equation (39)).

$$I_{photo} \propto \sqrt{mP_1P_2}[\cos(\omega_1 - \omega_2)\,t + \cos(\omega_1 + \omega_2)t] \tag{38}$$

$$P_{electrical} \propto R * I_{photo}^2 \propto (P_1 * P_2) \tag{39}$$

Where *R* is the load impedance. All the optical powers in equations (37-39) are noted in mW. This connection in logarithmic scale would give a slope of 2, which is very close to our measurement. The maximum measured IF power is -53 dBm (without any compensation for the cable losses) for 12.2 dBm optical power.

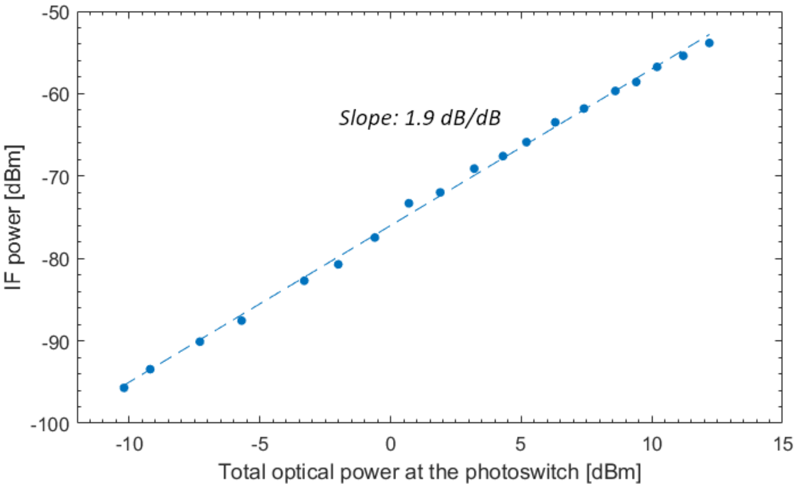

*Figure 4-11*
*IF power versus the total optical power illuminating the photoswitch*

A second system characterization experiment was aimed to measure the effect of unbalanced optical power variation. We were sweeping only one of the lasers optical power while the other was fixed at 3.5 dBm and 7.8 dBm. The selected optical frequency and the RF signal settings are the same as in the previous experiment: optically generated $f_{LO}$ = 13 GHz, input RF $f_{RF}$ = 20 GHz, with 15 dBm power and the measured mixing product at $f_{IF} = f_{RF} - f_{LO}$ = 7 GHz. We placed the fibre based attenuator after one of the lasers and before the 3 dB coupler and measured the IF power while adjusting the attenuator. The result curves are illustrated in Figure 4-12 for two fixed powers of one laser (*P(λ₁)*). The linear fitting in this case showed a slope of 1.04 $\mathrm{dB_{electrical}/dB_{P2\text{-}optical}}$, satisfying the theory in this case too (equations (38)-(39)). The same rule is also observed for fixed $P(\lambda_2)$ powers, for example at $P(\lambda_2) = 5$ *dBm* the IF power difference is 4.7 dB for a $P(\lambda_1)$ difference of 7.8 dBm – 3.5 dBm = 4.3 dB, which gives a rate of 1.09 dB/dB.

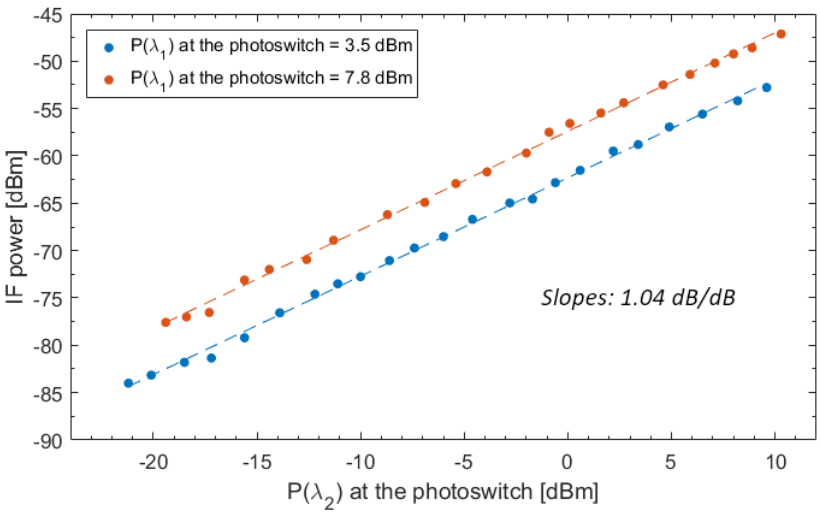

*Figure 4-12*
*IF power versus varied optical powers of one DFB laser*

### IV/1.3.d Heterodyne detection results

The photoswitch is expected to have a wide bandwidth for optically generated signals because of its picosecond carrier recombination time. The DFB lasers are emitting with a fixed wavelength, therefore we selected several laser pairs with wavelength differences (for one pair) ranging between 0.1 nm and 1.28 nm, corresponding to generated signals between 12 GHz and 164 GHz. For each measured laser pairs, the two lasers had different optical powers between 4.2 dBm and 14.9 dBm coupled into the optical fibre, the different powers were the result of sub-optimal laser to fibre coupling. The setup is illustrated at the beginning of this section, in Figure 4-8.

During the experiment we measured the IF power of one mixing product for each data point, while changing the laser pairs to generate different frequencies. The RF input frequency was adjusted for each laser pairs to position the intermediate frequency in the mixer’s (60 GHz – 90 GHz) or the ESA’s (up to 26.5 GHz) frequency range. The input power was set to 15 dBm, except in case of 69 GHz input frequency where it was limited to 13 dBm. All these varied settings for each data point require the post-processing of the data. Thanks to the previous system characterization (section IV/1.3.c), we can calculate an IF power value from the measurements, which is the equivalent IF power in case if the data points were obtained with equal optical powers. Then from this calculated IF power, the conversion loss is calculated, this calculated CL curve is drawn in Figure 4-13. The calculation steps are the following:

1. As the first step, we calculate the IF power change for the case of the two lasers are having equal power with the rule of the unbalanced optical powers experiment (Figure 4-12). In the calculation we adjusted the lower optical power to the higher one. As an example, if the two lasers have 9 dBm and 11 dBm optical powers, we calculated the IF power compensation for the case of 11 dBm optical power for both laser, which means we added 2.08 dB to the measured IF power.
2. In the second step, we calculated the compensation for equalized total optical powers, to have uniform values for all data points. For this we selected 10 dBm total power for

$P_1$+$P_2$ and calculated the compensation value with the rule found in Figure 4-11.

3. As the last step, we add or in some cases subtract the compensation values from the measured IF powers.

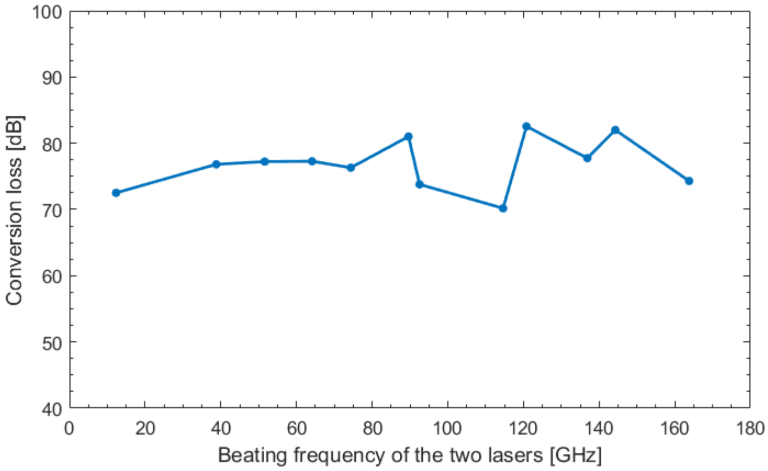

*Figure 4-13 Conversion loss of the beating of two DFB lasers versus the beating frequency*

The loss is showing a variation around 12 dB in the full measurement range of 164 GHz. A cut-off effect in the measured range is not reliably observable on the result curve, so it can be stated that with this measurement, we showed the photoswitch capability of detecting optically generated mmW frequencies with a nearly uniform performance up to 164 GHz. This confirms the very good performances in terms of bandwidth, due to the ultrafast behaviour of the photoconductive InGaAs switch.

## IV/2. Optoelectronic mixer for data-stream downconversion

The previous section showed the photoswitch mixing performance for a low bandwidth electrical RF signal. The experiment is also performed with wider bandwidths, where one of the mixer input signals is modulated with a digital data-stream as it would be the case in a real life system. The signal bandwidth depends on the data-stream's modulation format and bit-rate. The second input signal is the local oscillator, and at the intermediate frequency the output signal is the mixed product of the input RF and the LO, which contains the features of both signals. Therefore, the downconverted signal will preserve the modulated data of the RF signal only if the LO signal is a good quality, low linewidth signal. In this case the data can be recovered without errors with an ideal mixer and receiver. However, mixers usually have a flat conversion loss only in a limited bandwidth. If the conversion loss varies in the frequency range of the modulated data signal, the downconverted and recovered data could contain errors, which limits the useful bandwidth of the system. In this section we are demonstrating the photoswitch with high bandwidth data-stream downconversion.

We are performing the downconversion with 3 different setups and comparing the obtained results.

1. Section IV/2.3: The first setup is using the MLL laser signal as the local oscillator source. We are comparing the downconversion quality with the free-running and the stabilized laser case (see Chapter III, section III/2). The data-stream is modulating the input electrical signal.
2. Section IV/2.4: The second setup is using an intensity modulated continuous wave DFB laser as the local oscillator source. We are intensity modulating the laser with a sinusoidal signal which creates the LO frequency with periodically changing intensity. In this case too, the data-stream is modulating the input electrical signal.
3. Section IV/2.5: In the third setup the LO is provided electrically with an RF signal generator. Here the data-stream is intensity modulating a DFB laser optical signal.

The downconverted data-stream at the intermediate frequency is then analysed with a Digital Sampling Oscilloscope (DSO, Agilent 54855A Infiniium Oscilloscope). The DSO has an input upper frequency limit of 6 GHz, therefore the frequencies of the two input signals (electrical or optical) are chosen to position the IF signal frequency in this range.

The measurements were performed with the switch SD2-2, a type 3:3 switch with 4 fingers (characterisation results in Chapter II in section II/2 and II/3).

### IV/2.1. QPSK modulation format for the data-stream

In digital communications the data is represented by “0” and “1”, called bits. For signal transmission the data-stream containing the bits must be converted into an analog waveform, this conversion is done by modulation. An analog carrier signal with a given frequency and amplitude is modified (modulated) according to the modulation rules and the data bits. This modification of the analog signal can be in its phase, frequency or amplitude, the modulations are called phase shift keying (PSK), frequency shift keying (FSK) or amplitude shift keying (ASK) respectively. The modulations can be combined for higher modulation formats. In case at least two phases and at least two amplitudes are combined it is called quadrature amplitude modulation (QAM). Each particular phase, frequency and amplitude of the modulated signal is called a state and encodes one symbol representing $q$ number of bits. If we have $q$ bits/symbol the possible $M$ number of symbols are $M = 2^q$. The encoded Symbols/seconds is the symbol-rate of the modulation, we can also talk about data-rate which is the number of encoded bits/second.

In our experiments we choose the Quadrature Phase Shift Keying (QPSK) modulation format. QPSK is identical to 4-QAM in the final modulated signal shape. It has 4 different phase states: $\left(\frac{\pi}{4}, \frac{3\pi}{4}, \frac{5\pi}{4}, \frac{7\pi}{4}\right)$, with identical amplitudes, each representing 1 symbol with 2 bits in each: 00, 01, 10 or 11. Depending on the coding rules the bit couples are attributed to one phase state. During modulation, the bits in one symbol are coded separately. The first bit in each symbol are coded to a sine version of the carrier signal with π phase shifts, this is called the In-phase signal marked with an $I$. The second bit in the symbols are coded to a cosine (sine + π/2 phase shift) with π phase shifts, called Quadrature signal, marked with $Q$. These two signals are combined into one before transmission. The decoding is done in a similar way, the signal is separated into two branch and each of it is mixed with a sine or cosine to extract the encoded bits. Because of this separate encoding this modulation format (and all QAM too) can be represented in a two dimensional x-y diagram called a constellation diagram, as it is illustrated for QPSK in Figure 4-14. This complex diagram is showing the amplitude and the phase of the modulation states. The x axis is the In-phase (I) axis represents the cosine, and the y axis is the Quadrature (Q) axis representing the sine. Each state can be positioned in this diagram by its amplitude and phase.

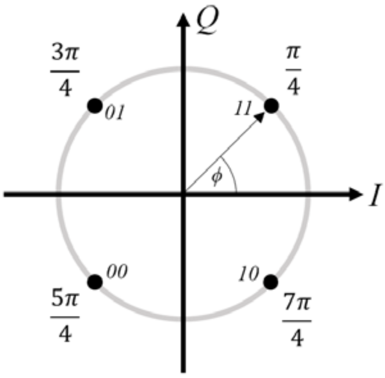

*Figure 4-14*
*Constellation diagram of QPSK modulation with the phases and the attributed symbols using Gray coding*

The data-stream used in the experiments contains random data and generated with an in-lab developed Matlab code. The script generates two files for the I and Q component and also a file for the combined modulated signal. These files can be loaded on an Arbitrary Waveform Generator (AWG, Tektronix AWG 7122B) which generates the electrical RF signal with a maximum sampling rate of 12 GSample/s. The Matlab code does not apply any signal shaping or filtering on the signal, the modulation is done with a square wave, therefore the AWG generated signals have spectral components in a wide bandwidth.

### IV/2.2. Data-stream demodulation – EVM and BER

During the transmission, additive white gaussian noise (AWGN) is added to the signal which can be present as amplitude or phase noise and losses are also present. All these effects are decreasing the signal to noise ratio. The DSO is sampling this noisy signal and demodulating it online. The demodulation results can be shown in a constellation diagram. Because of the added noise, the symbols are not exactly at the ideal position in the diagram, but with a vector of $P_{error}$ away from it, as it is illustrated in Figure 4-15. As a figure of merit of the downconversion, we are using the Error Vector Magnitude (EVM) value of the demodulated signal to obtain the performance. The EVM is the root mean square (RMS) of the symbol errors averaged over N number of symbols [125]. The value is often written in decibels or percentage and calculated with equation (40).

$$EVM_{RMS} = \sqrt{\frac{\frac{1}{N}\sum_{i=1}^{N} P_{error,i}^{2}}{\frac{1}{N}\sum_{i=1}^{N} P_{ref,i}^{2}}} \tag{40}$$

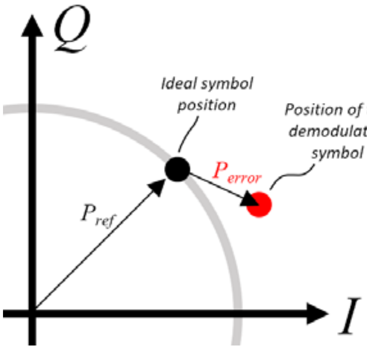

*Figure 4-15*
*Illustration of the symbol error*

We are recording the EVM percentage for different data-rates of QPSK modulation.

Another figure-of-merit of the quality of transmission in communication systems is the Bit Error Rate (BER). It shows the rate of bit faults in a given number of bits. For example, a BER of $10^{-3}$ means that during the transmission 1 bit was demodulated wrong in 1000 bits. The measurement is done by sending a known bitstream through the system and comparing it with the received and demodulated bitstream. The bitstream is usually a Pseudorandom binary sequence (PRBS). This measure gives a more accurate and widely used value of quality. When the BER measurement equipment is not available it can be estimated from the EVM values. Measuring EVM (and seeing the constellation diagram) has several advantages over the BER. The diagram can show the type of noise the system experiences, the phase and amplitude noise can be easily identified just by looking at the constellation. EVM also takes a shorter time to measure in case of very low BER values ($10^{-12}$ or below). The BER can be estimated from the EVM values with the following equation (41) [126].

$$BER = \frac{(1 - M^{-\frac{1}{2}})}{\frac{1}{2}\log_2 M} erfc\left[\sqrt{\frac{3/2}{(M-1)EVM_{RMS}^2}}\right] \tag{41}$$

Where *M* is the symbol number of the *M*-ary modulation, for QPSK *M = 4*. Knowing a BER value can give an indication of the performance compared to systems where only the BER is given. A short list of calculated BER values is given in TABLE 8 for QPSK modulation.

*TABLE 8 BIT ERROR RATE VALUES CALCULATED FROM ERROR VECTOR MAGNITUDE WITH EQ. (41)*

| EVM | 37 % | 29.5 % | 25.14 % | 20.15 % | 17.27 % | 15.33 % |
|---|---|---|---|---|---|---|
| BER | $10^{-2}$ | $10^{-3}$ | $10^{-4}$ | $10^{-6}$ | $10^{-8}$ | $10^{-10}$ |

## IV/2.3. Optically provided local oscillator - MLL

The first data-stream downconversion setup is using the MLL signal as the local oscillator source. The setup is illustrated in Figure 4-16. The AWG is generating the I and Q part of the modulated signal on its Channel 1 and 2. These outputs are connected to a wideband I-Q modulation inputs of a signal generator (Agilent 8267D, 250 kHz – 20 GHz), which is modulating the RF carrier signal with the data. The output of the generator is directly connected to the RF-probe touching the switch. The MLL signal was guided through optical fibres to illuminate the switch. We were using it both in free-running mode and stabilized mode. In the stabilized case the feedback had 110 m optical fibre, the signal properties for this stabilization setup are presented in Chapter III section III/2.2.c. In the free-running case the stabilization feedback is disconnected. For both cases, the illuminating optical power of the switch was 7 dBm (5 mW).

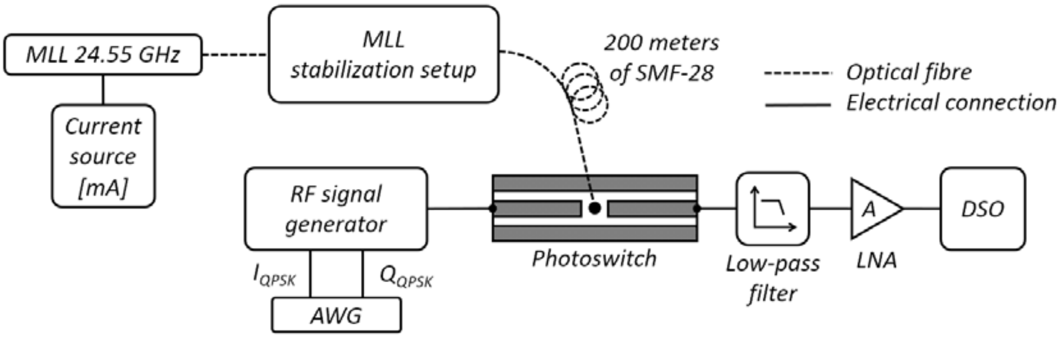

Figure 4-16 Setup of the data-stream down conversion experiment. Data on the electrical input signal, MLL as the local oscillator source.

At the output of the switch the use of a 5 GHz low-pass filter is needed, which is followed by a Low-noise amplifier (LNA) and then the sampling oscilloscope. The purpose of the filter is that it is reducing the level of the feedthrough RF carrier signal of the photoswitch in order not to saturate the amplifier and overload the DSO. The signal generator was set at a power level of 23 dBm, which is after the modulation is the full spectral power of the modulated signal considering all the sidelobes. The selected carrier frequency is at 20 GHz, which is the maximum allowed by the equipment. The LNA has a frequency limit of 18 GHz, and an amplification of 38 dB in 50 Ω network. The 18 GHz bandwidth of the LNA means it still has some amplification at the carrier frequency of the of the signal generator, and even with the attenuation of the switch feedthrough (around 20 dB at 20 GHz) this high power signal was overloading the DSO and saturates the amplifier if we do not use the filter. A typical electrical spectrum of a 1 Gbit/s QPSK modulated carrier is illustrated in Figure 4-17, the carrier frequency is at 20 GHz. We can observe the main lobe in a frequency range of 1 GHz around the carrier, this is the useful signal containing the data-stream. Two side lobes are also observed, which are the result of the modulation. It is possible to decrease the level of these sidelobes with signal shaping. In our case the signal is shaped of rectangular pulses representing the 1 and 0 transitions. By applying finer transitions, the sidelobe levels are reducing. This investigation was not part of the thesis, we were able to show the performance with the raw modulated signal without any spectrum optimization.

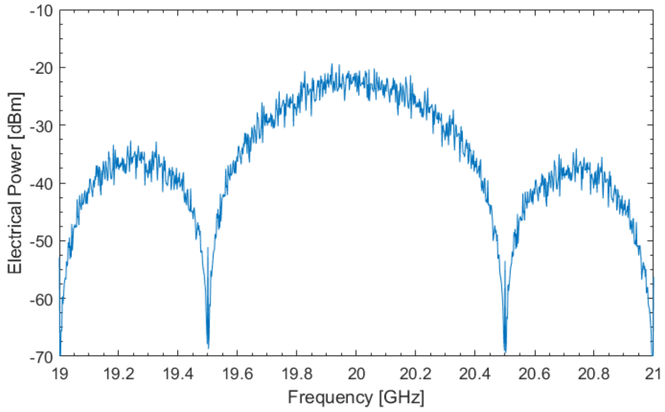

*Figure 4-17*
*Typical electrical spectrum of a QPSK modulated signal with 1 Gbit/s data stream*

The frequency settings for the RF and LO are positioning the IF signal to $f_{IF}$ =4.55 GHz ($f_{LO}$ = 24.55 GHz) centre frequency, which is inside the DSO's limit. The DSO is set to sample the signal and demodulate the QPSK data-stream. We were setting 8 different bitrates for the data-stream: 50-100-200-400-800-1200-1600-2000 Mbit/s. The measured EVM values are illustrated in a logarithmic scale of the bitrates for comparison. A reference back-to-back (B2B) measurement was also performed. We measured it by directly connecting the signal generator to the DSO with a carrier frequency of 4.55 GHz. In this case the signal power was set to have identical power as in the case of the IF signal at the switch output.

The result with this setup is illustrated in Figure 4-18, certain BER levels are also noted. The EVM values can be found in TABLE 9 along with the BER values for the stabilized case. As it was expected, we observed a better performance with the stabilized MLL signal. While the EVM is increasing with higher bitrates. The better performance mainly originates from the higher signal to noise ratio of the LO signal in the stabilized case and the better frequency stability.

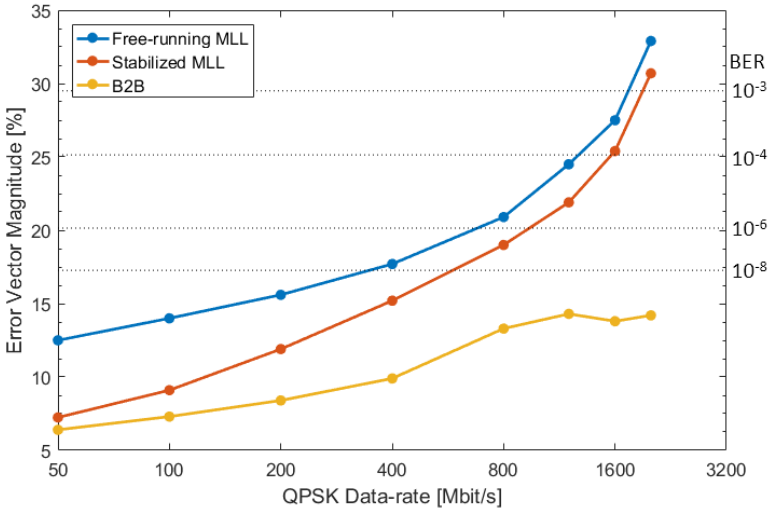

*Figure 4-18*
*Results of the data-stream downconversion and demodulation experiments in terms of the demodulated signal's Error Vector Magnitude. Certain BER values are also illustrated*

*TABLE 9 EVM VALUES FOR THE DOWNCONVERTING EXPERIMENT WITH THE MLL AS THE LOCAL OSCILLATOR*

| *Bitrate [Mbit/s]* | *50* | *100* | *200* | *400* | *800* | *1200* | *1600* | *2000* |
|---|---|---|---|---|---|---|---|---|
| *B-2-B [EVM %]* | 6.4 | 7.3 | 8.4 | 9.9 | 13.3 | 14.3 | 13.8 | 14.2 |
| *Stabilized MLL [EVM %]* | 7.24 | 9.1 | 11.9 | 15.2 | 19 | 21.9 | 25.4 | 30.7 |
| *Estimated BER for the stabilized MLL* | $< 10^{-10}$ | $< 10^{-10}$ | $< 10^{-10}$ | $< 10^{-10}$ | $2*10^{-7}$ | $7.2*10^{-6}$ | $1.2*10^{-4}$ | $1.6*10^{-3}$ |
| *Free running MLL [EVM %]* | 12.5 | 14 | 15.6 | 17.7 | 20.9 | 24.5 | 27.5 | 32.9 |

The EVM difference between the stabilized and the free running case is 5.2% for the lowest bitrate of 50 Mbit/s and this difference is decreasing to 2 % for 2 Gbit/s bitrate, showing that at higher frequencies the limiting of the LO phase noise is becoming less significant compared to other effects. Figure 4-19 and Figure 4-20 are illustrating typical constellation diagrams of the demodulated signals for two particular case: 100 Mbit/s and 1600 Mbit/s data rates, showing 500 sampled symbols represented by orange dots. In case of 100 Mbit/s, they are concentrating around the ideal symbol position, showing a very good quality of the demodulated signal. In case of the higher 1600 Mbit/s data-rate, the demodulated symbol points are spread in a wider area around the ideal point, which shows the higher noise of the signal. Despite the good EVM value, in the case of 100 Mbit/s we can still observe a low level of spreading of symbol points around a circle perimeter (which circle's perimeter contains the 4 ideal symbol points), creating an elliptic area of the demodulated data-points for each symbol. It is indicating a residual phase noise in the signal. This type of spreading is also present in the case of 1600 Mbit/s data-rate.

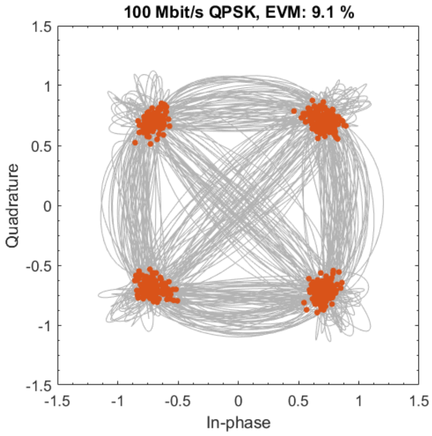

*Figure 4-19*
*Constellation diagram of the demodulated 100 Mbit/s data rate QPSK signal. LO is the stabilized MLL. EVM: 9.1 %*

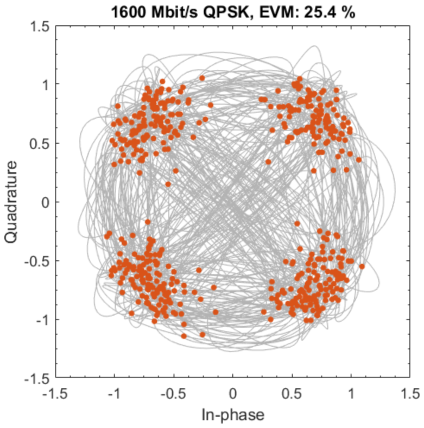

*Figure 4-20*
*Constellation diagram of the demodulated 1600 Mbit/s data rate QPSK signal. LO is the stabilized MLL. EVM: 25.4 %*

The calculated values of BER with the stabilized MLL as LO are below the value of $10^{-3}$ for data rates up to 1600 Mbit/s, in the literature this value is considered as a practical limit of error rate for telecommunication in case of using Forward Error Correction (FEC) coding. This coding type is using part of data for error correction bits created from the rest of the bits with a specific rule. Depending on the FEC type, this coding can decrease the error rate in exchange of the effective bitrate of the useful data for the user. The bit error means that after the symbol is sampled, the system decides that it is a different symbol due to the high level of noise. In the constellation diagram it means that it is closer to another symbol positions than to its original position. More details about the FEC coding can be found in [127], here we are not using this technique.

For higher bitrates the EVM values are increasing with a growing rate, indicating limitations in the setup. These limitations can be sourced from the following:

1. One limiting factor could be the standing waves between the signal generator 50 Ω output and the photoswitch. The CPW line of the switch is designed for 50 Ω characteristic impedance, however the switch has a much higher impedance as we measured it in Chapter II, which also changes with the illuminating power. This impedance mismatch creates standing waves, which deforms the modulated signal's spectrum and results in a lower quality signal. The same effect is possibly present at the output of the switch between the 50 Ω input of the filter and the photoswitch. These degradations have an increasing impact as the signal bandwidth broadens, as it is also seen from the EVM curves.
2. Other degradation can be sourced from the use of the 5 GHz low-pass filter, for bitrates higher than 1000 Mbit/s part of the spectrum is outside of its 3 dB cut-off frequency. Measurements showed that up to 5.5 GHz (the maximum frequency of the main lobe's spectrum for the highest bitrate of 2 Gbit/s) the attenuator has minimal difference in its transfer spectrum, so its effect can be minimal.
3. A third possible degradation can originate from the signal generator. The wide-band I-Q input is verified in the frequency range of +/- 1 GHz for carrier frequencies above 3.2 GHz. The datasheet shows [128] a performance with 4 dB variation in the verified spectrum for selected carrier frequencies (10-12-15-20 GHz). Even this low variation can affect the signal quality.

All these effects adding up can degrade the data-stream quality, but due to our equipment limitation we cannot make B2B measurement at 20 GHz carrier frequency to verify it directly. However, we performed a B2B measurement using the signal generator with the same output power level as it would be for the downconverted signal (-53 dBm) at the output of the switch, connected to the 5 GHz filter and the LNA and followed by the DSO. The carrier frequency was set to 4.55 GHz and we used the same coaxial cables. This B2B measurement, illustrated in Figure 4-21 with purple curve, shows the effect of the above mentioned limitations of the filter and amplifier compared to the direct B2B curve (yellow).

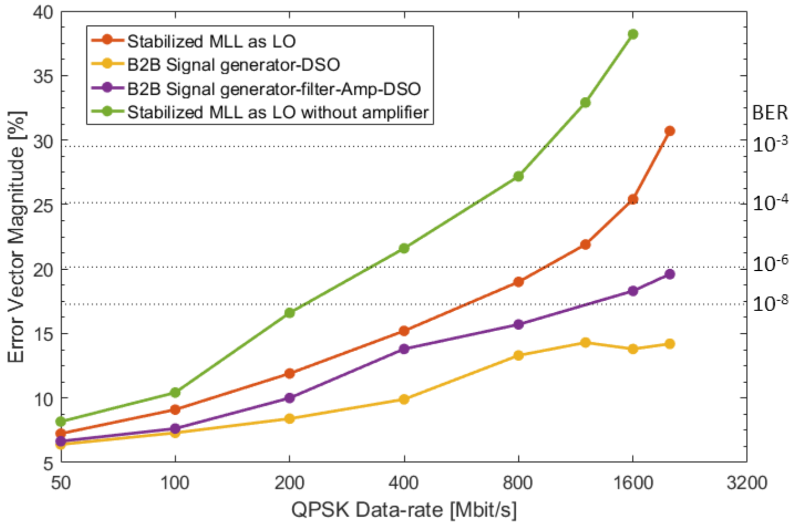

*Figure 4-21*
*EVM comparisons for different B-2B measurements and downconversion*

The downconverted result with the stabilized MLL is also illustrated with orange colour. The purple B2B measurement is closer to the downconversion result, suggesting that the filter and amplifier causes part of the signal degradations. This graph also shows a downconversion results without using the amplifier before the DSO (green curve). For low bitrates (≤ 100 Mbit/s) the results are almost the same as with the amplifier, but then the EVM difference grows to 5 % (200 Mbit/s) and even more to almost 15 % (1600 Mbit/s). This difference is still not as high as it would be expected after the amplification of 38 dB. There is still a significant difference compared to the B2B measurement, this difference is attributed mainly to the added noise and the standing waves in the coaxial cables due to the impedance mismatches. The measured EVM values illustrated in Figure 4-21 are listed in TABLE 10.

TABLE 10 EVM VALUES FOR BACK-TO-BACK MEASUREMENTS

| *Bitrate [Mbit/s]* | *50* | *100* | *200* | *400* | *800* | *1200* | *1600* | *2000* |
|---|---|---|---|---|---|---|---|---|
| *B-2-B [EVM %]* | 6.4 | 7.3 | 8.4 | 9.9 | 13.3 | 14.3 | 13.8 | 14.2 |
| *B-2-B with filter and amplifier [EVM %]* | 6.65 | 7.63 | 10 | 13.8 | 15.7 | - | 18.3 | 19.6 |
| *Stabilized MLL [EVM %]* | 7.24 | 9.1 | 11.9 | 15.2 | 19 | 21.9 | 25.4 | 30.7 |
| *Stabilized MLL without amplifier [EVM %]* | 8.17 | 10.42 | 16.6 | 21.6 | 27.18 | 32.9 | 38.2 | - |

In the next section we are using a different optically provided LO source and comparing the results with the MLL.

## IV/2.4. Optically provided local oscillator – DFB laser

In section IV/1 we were generating microwaves and millimetre waves optically with two methods, one is with a mode-locked laser generating optical pulses and the other is the beating of two continuous wave laser having a wavelength difference. A third method to generate signals optically is to intensity modulate a continuous wave source with the desired frequency. The modulation can be done directly, but in this case usually the low direct modulation bandwidth of the laser is limiting for high frequencies. With an external modulator this can be increased to tens of GHz. A plasmonic Mach-Zehnder modulator developed by *C. Haffner et al.* [129], showed no performance degradation in the frequency range 10 GHz – 70 GHz, indicating that its bandwidth can be even above this range (with 1550 nm wavelength optical signals). Here we are using an external Mach-Zehnder modulator (Sumitomo Osaka Cement co. Ltd, T-DEH1.5-40-ADC) with a modulation bandwidth up to 40 GHz. The modulator is used at its quadrature point with a DC bias around 5.5 V. The RF input signal is a pure sinusoidal from a signal generator (Agilent 8257D) with a frequency identical to the MLL frequency of 24.55 GHz. As a comparison we illustrate the phase noise of the signal generator controlled MZM output signal received with a photodiode at 24.55 GHz and the stabilized MLL phase noise in Figure 4-22.

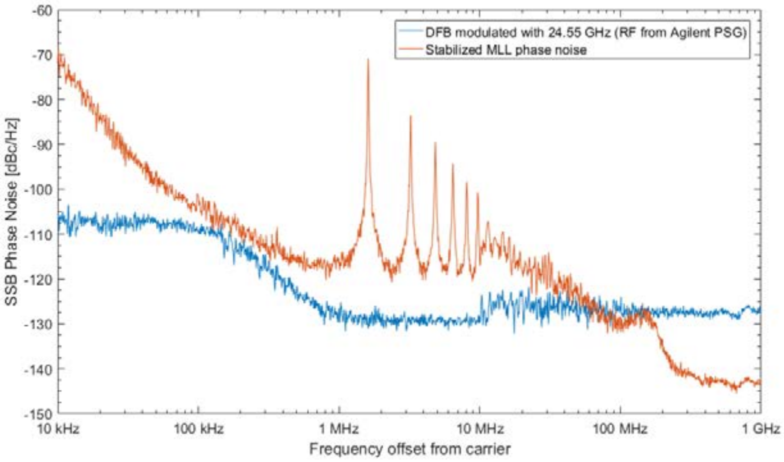

*Figure 4-22*
*Phase noise of generated RF signal with the intensity modulated DFB (blue) and the MLL (orange)*

The generated signal has a phase noise of -110 dBc/Hz at 100 kHz offset, which is very close to the MLL phase noise. Almost in the full measured offset range the signal generator has better phase noise values, than the MLL, showing that it generates a more stable signal.

At the RF input of the MZM we set the signal power to have the highest RF power after the photodetection of the MZM optical output, while still staying in the modulator’s linear regime. This was achieved with 18 dBm of RF power, which was attenuated with 3.6 dB by the RF cable loss at 24.55 GHz. As a continuous laser source, we used the previously presented integrated glass laser with 1534 nm wavelength and an optical power of 13.2 dBm. The optical power reaching the photoconductive switch after the modulator losses was 5.5 dBm. The input electrical signal was containing the data modulation the same way as in the previous setup with the same bitrates.

An illustration of the temporal shape of the modulated laser signal is shown in Figure 4-23, it is a sinusoidal with an offset and with a lower peak power than in case of the pulses.

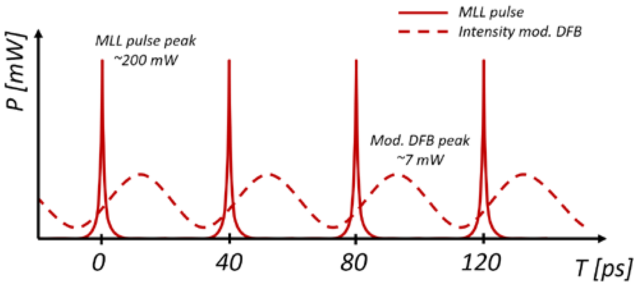

*Figure 4-23*
*Temporal shape of optical signals for the MLL pulses and the intensity modulated DFB laser*

As it can be seen from this figure, this type of modulation has a high level of continuous laser power and a low modulation depth resulting in a lower generated RF power after photodetection than in case of the MLL. Receiving the intensity modulated signal with a photodiode (u2t XPDV3120R) and a Keysight UXA N9040B Signal Analyser we can measure an RF signal power of -26 dBm at 24.55 GHz, while in the MLL case the peak power was at -12 dBm. The mixing with the photoconductive switch showed similar differences, the IF signal power was -67 dBm, 14 dB lower than in the case of the MLL. In the phase noise curve of Figure 4-22 the curve corresponding to the MZM output shows a better stability than in the case of the MLL, it has the same shape and level as the Agilent RF generator providing the modulating signal. This curve shows that the LO signal has a good quality and the limiting factor is due to the effects of the low modulation efficiency. The optoelectronic mixing setup is shown in Figure 4-24.

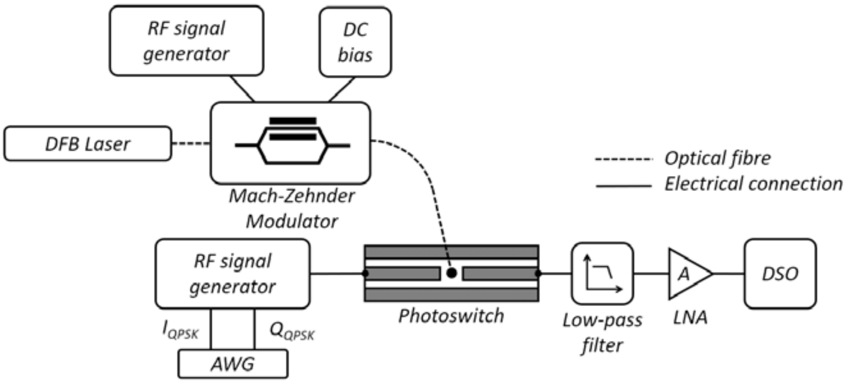

*Figure 4-24 Setup for the data-stream downconversion. Intensity modulated DFB laser signal as the local oscillator source*

Figure 4-25 is illustrating the results of this experiment. To compare the results to the MLL case we performed the previous experiment with attenuated MLL power of 5.5 dBm (dark red curve), to compare the results using the same optical power as the DFB case here. The B2B values are also remeasured with 1.5 dB less power, to correspond to the lower MLL power (yellow curve), but the EVM values showed no differences compared to the previous B2B measurement.

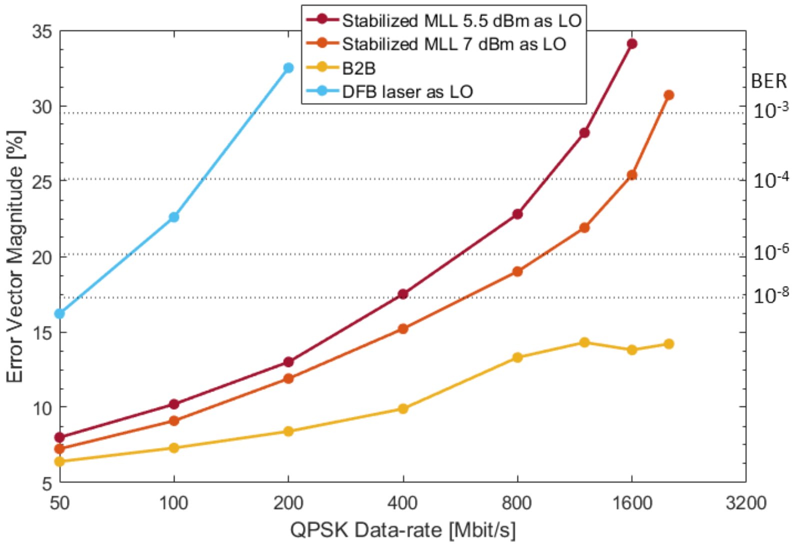

*Figure 4-25*
*Results of the data-stream downconversion and demodulation experiments in terms of the demodulated signal's Error Vector Magnitude. DFB laser setup compared to the MLL setup.*

The light blue curve shows the results of the modulated DFB as an LO. It has a significantly higher EVM performance compared to the MLL case, and bitrates above 200 Mbit/s were not possible to demodulate. This huge difference is mainly due to the low efficiency of the modulation and the 13 dB lower level of mixed electrical signals, which also introduces a much higher signal to noise ratio (SNR) in the downconverted signal. We can also observe the lower performance in case of the lower power MLL, it is showing a higher EVM difference for bitrates above 800 Mbit/s. The measured EVM values are detailed in TABLE 11.

TABLE 11 EVM VALUES FOR THE DOWNCONVERTING EXPERIMENT WITH THE DFB AS THE LO

| *Bitrate [Mbit/s]* | *50* | *100* | *200* | *400* | *800* | *1200* | *1600* | *2000* |
|---|---|---|---|---|---|---|---|---|
| *B-2-B [EVM %]* | 6.3 | 7 | 8.16 | 9.9 | 13 | 14 | 13.8 | 14.3 |
| *Stabilized MLL, 7 dBm [EVM %]* | 7.24 | 9.1 | 11.9 | 15.2 | 19 | 21.9 | 25.4 | 30.7 |
| *Stabilized MLL, 5.5 dBm [EVM %]* | 8 | 10.2 | 13 | 17.5 | 22.8 | 28.2 | 34.1 | - |
| *DFB as an LO [EVM %]* | 16.2 | 22.6 | 32.5 | - | - | - | - | - |

### IV/2.5. Electrically provided local oscillator

In the third setup, the DFB laser is used again as the optical signal for optoelectronic mixing. The setup is illustrated in Figure 4-26. Here, we are modulating the laser signal with the data-stream. The signal generator with the AWG was used the same way as before, here its output is connected to the Mach-Zehnder modulator, we were using an output RF power of 16 dBm and a carrier frequency of 20 GHz (the maximum of the equipment). The average optical power after the MZM was 3 dBm.

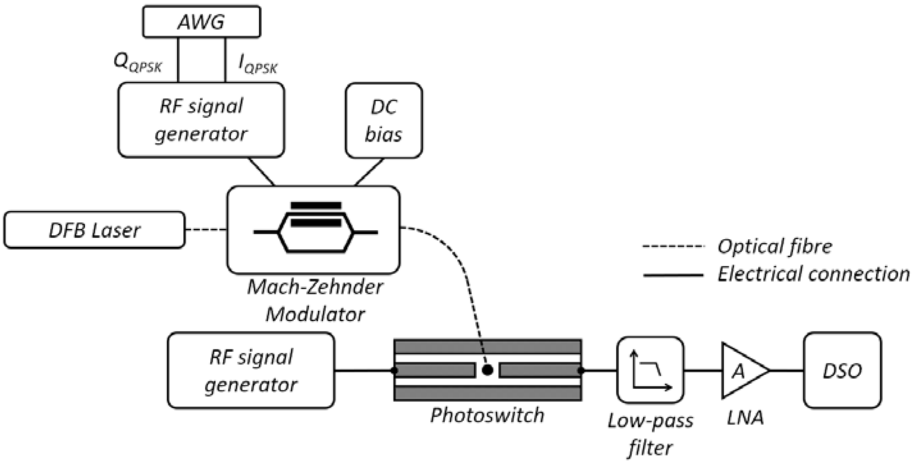

*Figure 4-26 Setup for the data-stream downconversion. Electrical signal as the local oscillator source, data-stream is intensity modulated on a DFB laser's signal*

The input electrical signal of the photoswitch is a pure sinusoidal serving as the local oscillator signal in this case. We set the output power to 19 dBm and the frequency to 24.55 GHz (so using the same LO frequency as before). The IF signal is at 4.55 GHz with the data, as in the previous cases.

The used electrical signal generator (Agilent 8257D), which is a laboratory equipment has a phase noise at 100 kHz offset at -110 dBc/Hz with 24.55 GHz carrier. Its phase noise curve is illustrated in Figure 4-27 along with the stabilized MLL. We can observe a difference of almost 40 dB at 10 kHz offset, and also for the full range it shows better values.

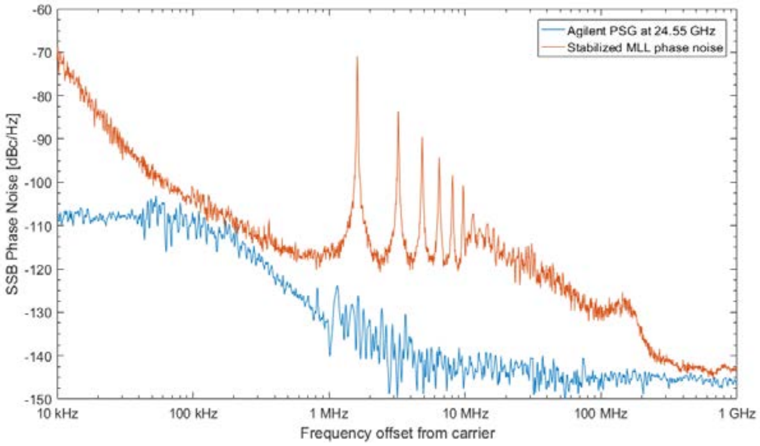

*Figure 4-27 Comparison of the PSG phase noise and the MLL phase noise*

The result in EVM of this mixing setup is illustrated in Figure 4-28 with blue colour, it is also compared to the previous two results with optical local oscillators. Light blue curve corresponds to the case of the modulated DFB laser used as an LO and the orange curve shoes the result in case the stabilized MLL is the LO. The yellow curve is the reference back-to-back measurement. TABLE 12 details the measured EVM values.

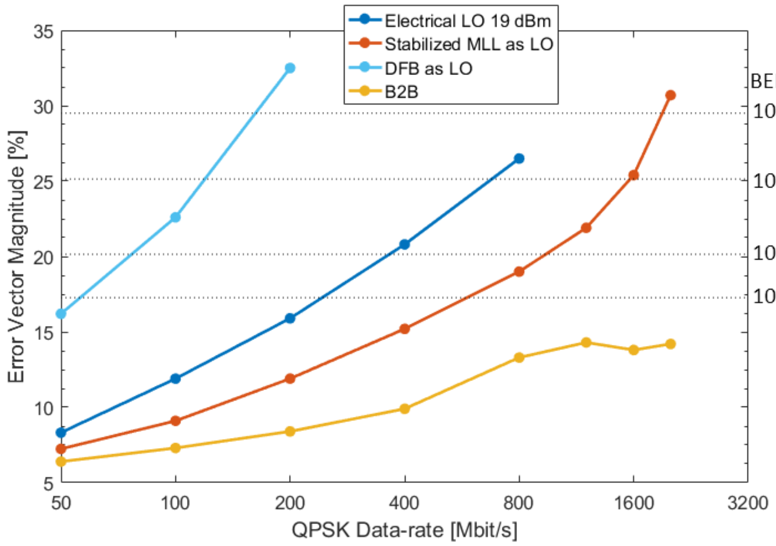

*Figure 4-28 Results of the data-stream downconversion and demodulation experiments in terms of the demodulated signal's Error Vector Magnitude. DFB laser setup compared to the MLL setup.*

*TABLE 12 EVM VALUES FOR THE DOWNCONVERTING EXPERIMENT WITH THE DATA MODULATED DFB SIGNAL*

| *Bitrate [Mbit/s]* | *50* | *100* | *200* | *400* | *800* | *1200* | *1600* | *2000* |
|---|---|---|---|---|---|---|---|---|
| *B-2-B [EVM %]* | 6.3 | 7 | 8.16 | 9.9 | 13 | 14 | 13.8 | 14.3 |
| *Stabilized MLL, 7 dBm [EVM %]* | 7.24 | 9.1 | 11.9 | 15.2 | 19 | 21.9 | 25.4 | 30.7 |
| *Electrical LO [EVM %]* | 8.32 | 11.9 | 15.9 | 20.8 | 26.5 | - | - | - |
| *DFB as LO [EVM %]* | 16.2 | 22.6 | 32.5 | - | - | - | - | - |

The performance is better than in the case when the DFB was providing the LO, as here we are using an LO which has no CW component, so all of its power is contributing to the mixing, unlike in the case of the DFB as an LO. The demodulation here was successful for bitrates up to 800 Mbit/s. The EVM difference to the MLL case is increasing over increasing bitrates, however as we used here a 4 dBm lower optical power, it was expected that the differences will be higher. This performance can be explained, that in this setup, the standing waves between the signal generator and switch does not affect the performance, because the signal generator provides only a pure sinusoidal signal, which has a very low bandwidth. And the MZM in the modulation bandwidth, which corresponds to a bandwidth in the optical domain of 0.013 nm in case of 800 Mbit/s, has a flat response which means that the data spectrum is not affected before reaching the photoswitch, unlike in the previous cases, where the standing waves deformed the spectrum. Only the downconverted signal is affected by the impedance mismatch.

All the previous downconverting experiments shows that the optoelectronic mixer scheme, despite the high losses, can be used in communication systems where the data-stream modulated signal can be either in the optical or electrical domain.

## IV/3. Study of switch non-linearities

The photoswitch has non-linear properties, which was seen on the I-V curve results in Chapter II, section II/2.6. These non-linearities are introducing high level harmonics in the sampled output signal of the photoswitch, which can be observed on the frequency spectrum of the switch output. In case of a high frequency carrier with a signal bandwidth being the fraction of the carrier frequency, the sampling can be performed with a much lower sampling rate than the carrier frequency ($f_{RF}$), this method is called undersampling, it was discussed in details in Chapter I, section I/3.3.a. During this process, replicas of the signal is positioned in the Nyquist bands (frequency ranges of $[m*f_s/2, (m+1)*f_s/2]$, where $f_s$ is the sampling frequency). If $f_s$ is selected appropriately, there are replicas of the signal at $f_{RF}-m*f_s$, where m is an integer. In case of the presence of high level of non-linearities, there are harmonics appear next to the fundamental replicas in each Nyquist band at frequencies of $n*f_{RF}-m*f_s$, *n* and *m* being an integer. If the levels of these harmonics are too high, it can interfere with the sampled signal and significantly decrease the dynamic range of the sampler. Figure 4-29 illustrates a measured switch output spectrum for an input RF signal of $f_{RF}$ = 123 MHz with 15 dBm electrical power, and with a pulsed illumination from the Menlo C-fibre mode locked laser with $f_{MLL}$ = 100 MHz repetition rate and 15.7 mW average optical power.

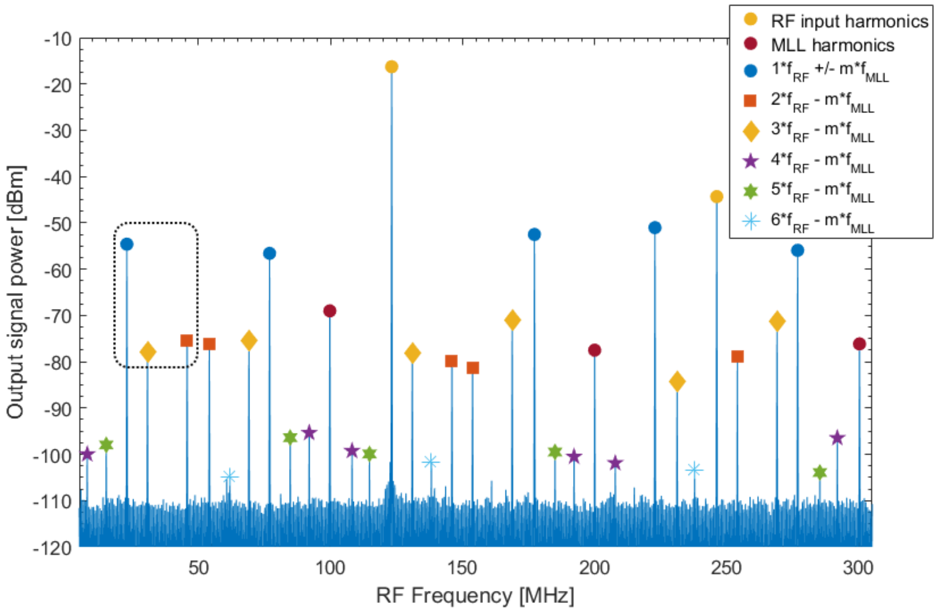

*Figure 4-29 RF spectrum of the switch output, Popt=12 dBm, P(RF)=15 dBm. VBW/RBW: 3 kHz/3 kHz*

The generated harmonics by the interaction of the input RF and optical signals are marked with the same marker, if they are produced with the same input RF signal harmonic. In the spectrum up to 305 MHz, we can observe mixing products produced with up to the 6th harmonic of the RF input. Each harmonic has one replica in each Nyquist bands, which are in this case the [m*50 MHz, (m+1)*50 MHz] frequency ranges. The first 3 harmonics produced by the MLL beating can be also observed in the spectrum (dark red circles). We measured the peak powers of selected harmonics and compared their values while we set different input powers. The harmonics of $2*f_{RF}-n*f_{MLL}$ and $3*f_{RF}-m*f_{MLL}$ (orange squares and yellow rhombuses respectively), are showing similar amplitudes, while the ones corresponding to the *{4, 5, 6}**$f_{RF}$ *-m**$f_{MLL}$ (purple star, green star, blue star respectively) products are also have similar amplitudes, but they are lower than the previous ones.

Figure 4-30 is comparing the generator harmonics signals of *2**$f_{RF}$ and *3**$f_{RF}$ to the fundamental frequency signal in dBc, measured directly at the output of the generator. And in Figure 4-31 we compared the levels of the harmonics in the first Nyquist band to see their evolution over different $f_{RF}$ input powers (from -15 dBm to +15 dBm). These harmonics are the $f_{RF}$*-1**$f_{MLL}$, *2**$f_{RF}$*-2**$f_{MLL}$ and *3**$f_{RF}$*-4**$f_{MLL}$, their positions marked with the black dotted square in Figure 4-29. The power difference between the terms $f_{RF}$*-1**$f_{MLL}$ and *2**$f_{RF}$*-2**$f_{MLL}$ is 30.5 dB at -5 dBm input power and it decreases to 20.8 dB difference with 15 dBm input power. While the generator's second harmonic signal at *2**$f_{RF}$ is at -65.6 dBc when the input is set at -5 dBm and -44.3 dBc for 15 dBm input power.

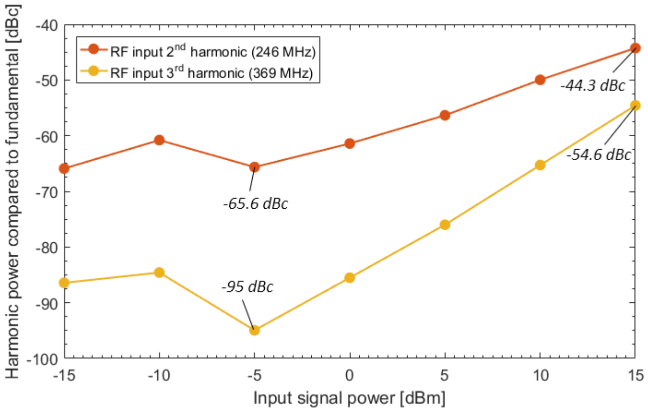

*Figure 4-30*
*Power levels of the input RF signal harmonics at the switch output.*
*$f_{RF}$ = 123 MHz, $P_{RF}$ = 15 dBm*

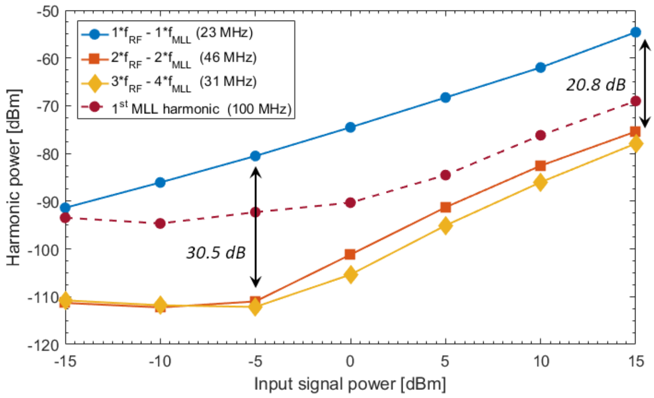

*Figure 4-31*
*Power levels of selected harmonics of the mixing products at the switch output. $f_{RF}$ = 123 MHz, $P_{RF}$ = 15 dBm*

This is showing that while the input signal's second harmonic power changes with 40 dB, the harmonics are changing with only 10 dB, indicating that due to the switch non-linearities high levels of harmonics are also generated from the input $f_{RF}$ signal.

Surprisingly, the PSW also acts as a simple photodetector even if it was not DC biased. The purple curve of Figure 4-31 is showing the evolution of the first MLL beating signal at 100 MHz over increasing input RF signal powers. We can observe that above 0 dBm input power the generated RF beating signal is increasing with a similar rate as *P(*$f_{RF}$*-*$f_{MLL}$*)* (blue curve).

Repeating the measurement with higher RF input frequencies we observed similar behaviour. Figure 4-32 and Figure 4-33 are showing the same measurement (with the Menlo fibre laser, 100 MHz repetition rate pulses, 15.7 mW average optical power) with an input frequency of 2.022 GHz. Figure 4-32 is a direct measurement of the signal generator output to show the generator's harmonics. We can see that the second harmonic has a level of maximum -66.7 dBc compared to the fundamental power. In Figure 4-33 the power difference between the products of $1*f_{RF}+32*f_{MLL}$ and $2*f_{RF}+10*f_{MLL}$ are only 22 dB, which is 44 dB lower and it is produced by the switch non-linearities.

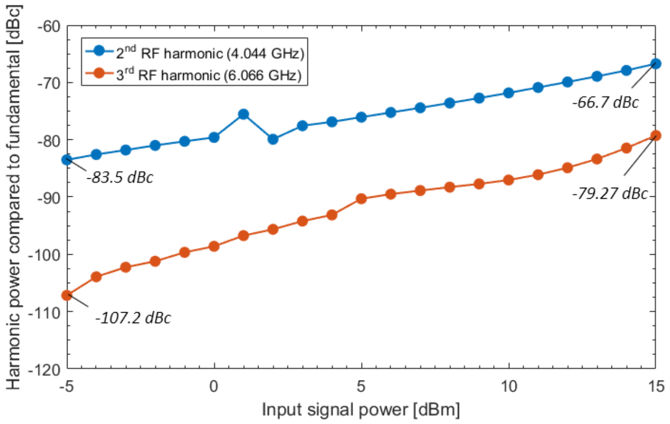

*Figure 4-32*
*Power levels of the input RF signal harmonics at the generator output.* $f_{RF}$ *= 2.022 GHz,* $P_{RF}$ *= 15 dBm*

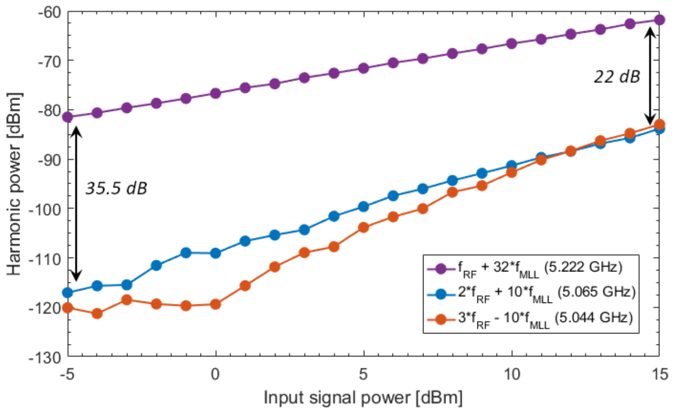

*Figure 4-33*
*Power levels of selected harmonics of the mixing products at the switch output.* $f_{RF}$ *= 2.022 GHz,* $P_{RF}$ *= 15 dBm*

These measurements are showing that the photoswitch non-linearities are causing a high level of harmonics at the output of the switch. These distortions are destructive for the sampling performance in case of using the switch as a sampler device for Analog-to-digital converters. This property, and also the low conversion loss measured at the beginning of this chapter are making the switch not suitable for the use in ADCs, the achieve resolution would be too low. Therefore, we did not perform further measurements in the ADC topic.

## IV/4. Applications of the optoelectronic mixer schemes

There are several advantages of optoelectronic mixers compared to the fully electrical ones: high isolation between electrical input signal and optical local oscillator signals, the optical signal's immunity to electromagnetic interference, the high bandwidth available in the optical domain and also the easy integration with the low-loss fibre based systems. One possible use of the proposed optoelectronic mixing schemes, presented here in Chapter IV, are in Radio-over-Fibre (RoF) systems. In this section we will propose concepts about the switch's function in such systems.

It is important to emphasize that the current photoswitch presents high levels of losses and using it in real life telecommunication systems would require the use of an excessive level of amplification, therefore it is essential to improve the efficiency of these devices before they are suitable for practical use.

In the previous experiments we were presenting signal down-conversion, where the data modulated carrier signal is downconverted into the baseband for signal processing. It is one of the potential applications, as in the new generation telecommunication systems, the carrier frequencies are increasing compared to the nowadays typically used telecommunication bands below 6 GHz for the 3rd and 4th generation of networks. One of the planned 5G network frequency band is around 25 GHz. While RoF systems are using even higher frequencies around 60 GHz. Despite these high carrier frequencies, the signal processing is still performed in the baseband, therefore the signal downconversion is needed. The photoswitch based downconverter can have a role in a wireless receiver, a simple schematic is illustrated in Figure 4-34, where the received signal is sent to the photoswitch after amplification and filtering. The photoswitch based mixer is downconverting the signal to the baseband with the LO signal provided by an MLL. Thanks to the flat response of the photoswitch over a high frequency range, measured it up to 67 GHz electrically, and optically detected signals up to 164 GHz, (measurements limited by the equipment bandwidth) gives a wide frequency range of the possible carrier frequencies.

Another advantage of the mixer is that both devices, the photoswitch and the semiconductor mode-locked laser are InP based, therefore it is possible to integrate the two on a single chip to further reduce the footprint of the mixer.

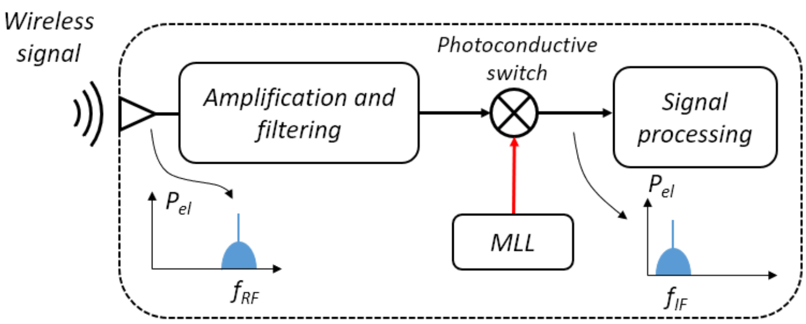

*Figure 4-34*
*Photoswitch based optoelectronic mixers used as a downconverter of high carrier frequency signals*

This mixer can also be used as a frequency up-converter in Radio over Fibre networks, in the next part we propose the possible use of the mixer in RoF systems.

*The RoF systems*

In the Radio-over-Fibre communication systems the data from the central station (CS) is sent to the remote base station (BS) as a modulated optical signal through the fibre network. The BS is converting the optical signal into the electrical domain (O/E: optical to electrical converter) for wireless distribution to the user. In common RoF scenarios, the wireless distribution networks are indoor environments like offices, shops or homes.

The CS is performing an electrical to optical conversion (E/O: electrical to optical converter) while the BS is converting the optical signal back to the electrical domain. The advantage of using the fibre networks for transmission is its low-loss, therefore the transmission distance can be tens of kms without significant loss. The fibre presents an ultrawide bandwidth in the frequency domain which allows the multiplexing of several wavelengths in the same optical fibre which reduces the required installation costs of such systems. The wireless link usually uses a high carrier frequency, for example a carrier around 60 GHz. This frequency band is the most anticipated for everyday use as in most parts of the world a 3.5 GHz - 9 GHz wide unregulated spectrum can be found around the 60 GHz frequency band [130]. Due to the free-space loss at this high carrier frequency, a higher number of BS is needed to cover an area with wireless connection compared to the mobile networks using the frequency bands up to 6 GHz . Because of the high number of BS, the cost of it is crucial in system designs, it should be as simple as possible without expensive components, the complicated functions should be placed in the CS. There are 3 main scenarios possible for the transmitted data signal through the fibre [50]. Schematics of the scenarios are illustrated in Figure 4-35 with the optical spectrum of the fibre transmission. The up- and down-link is illustrated as they are going through the same channel, but usually they are working with separate channels meaning the need of two mixers and separate E/O and O/E converters.

1. In Baseband-over-fibre systems, the baseband data modulates the optical signal with an electro-optical modulator or by directly modulating the laser. This option has the least complex CS, as only low bandwidth components (commonly up to 9 GHz bandwidths which is the maximum allowed band at 60 GHz) are needed for the modulation. This means that the more complex functions are placed in the BS: it has to up-convert the received baseband data for wireless distribution.

2. RF-over-Fibre systems are sending the already up-converted data in an RF carrier frequency through the optical signal. In this case, the BS receiver doesn't perform frequency mixing, it requires only a high-bandwidth photodiode for the optical to electrical conversion. This requires a very wide bandwidth optical detector (>60 GHz), which can increase the cost.

3. Intermediate frequency (IF)-over-fibre systems are similar to RF-over-fibre, they are transmitting the data signal on an IF carrier frequency, which can be in between the baseband and the RF frequency, for example at 30 GHz. The data is up-converted in the CS

into an intermediate frequency (IF), and then another up-conversion is needed in the BS. The conversion in the CS can be performed in the electrical domain, or in the optical domain also. In this scenario, the BS receiver requires a lower bandwidth optical receiver, than in RF-over-fibre case. However, the frequency mixer is also needed in the BS, but can be less complex as in the baseband solution, because the signal is already on a high frequency carrier and not in the baseband.

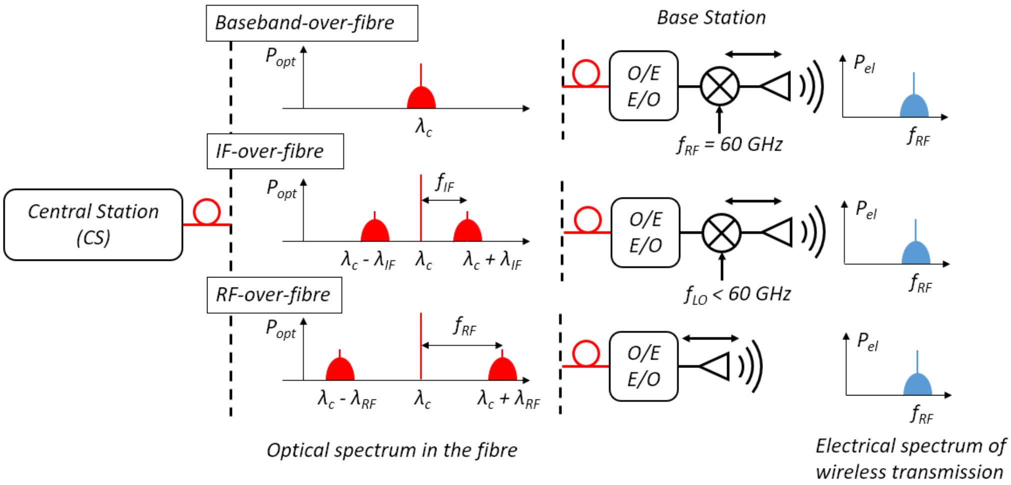

*Figure 4-35 Illustration of the 3 RoF scenario. O/E: Optical to electrical converter; E/O: electrical to optical converter*

The simplest BS can be achieved with the RF-over-fibre solution, where the data signal is sent through the optical network on the same carrier as the wireless transmission. The drawback of the second and third scheme is the dispersion of the optical fibres which has bigger effects in these broadband signals and limits the maximum distance of the fibre transmission.

The photoconductive based optoelectronic mixer can be used in the BS as the mixer to upconvert the signal into the RF carrier for the downlink direction toward the user for the baseband- and IF-over fibre case. This can be performed with a locally installed mode-locked laser as the local oscillator frequency source, or this LO signal can be distributed through the fibre network from the central station. Figure 4-36 is illustrating the two options, in case (A), each base station has an MLL providing the necessary frequency for up conversion, which can be 60 GHz in case of baseband-over-fibre, or a lower frequency MLL in case of IF-over-fibre. The setup can work in both downlink and uplink direction. In case of uplink from the user, the received wireless signal is downconverted with the photoswitch and the MLL, and after electrical to optical conversion the signal is transmitted through the fibre network. Case (B) simplifies the BS module by placing the LO source in the CS, and its signal is distributed through the fibre network in a secondary fibre next to the fibre containing the data. This setup was also proposed in [66] using a photoconductive switch as the mixer and the fibre network for LO distribution. The advantage of this scheme is that this LO signal from the MLL can be distributed to several BSs from a single laser source.

In Case B, it is also among the advantages that the presented stabilization loop to provide improved quality local oscillator signal can be constructed in the CS and the stabilized signal is distributed, as it would make the BSs too complex and costly to have a stabilization loop in all of it.

The needed 200 meters of fibre for the MLL intrinsic dispersion compensation and to achieve the maximal electrical RF beating power, can be extended to kilometres as the optimal compensation periodically occurs for longer fibre length [97]. In this setup, instead of a single MLL, two DFB lasers can be also used to optically generate an LO frequency, as we used the method in section IV/1.3. The advantage of the DFB beating signal is that the chromatic dispersion of the fibre network has much lower effect than in the case of the MLL.

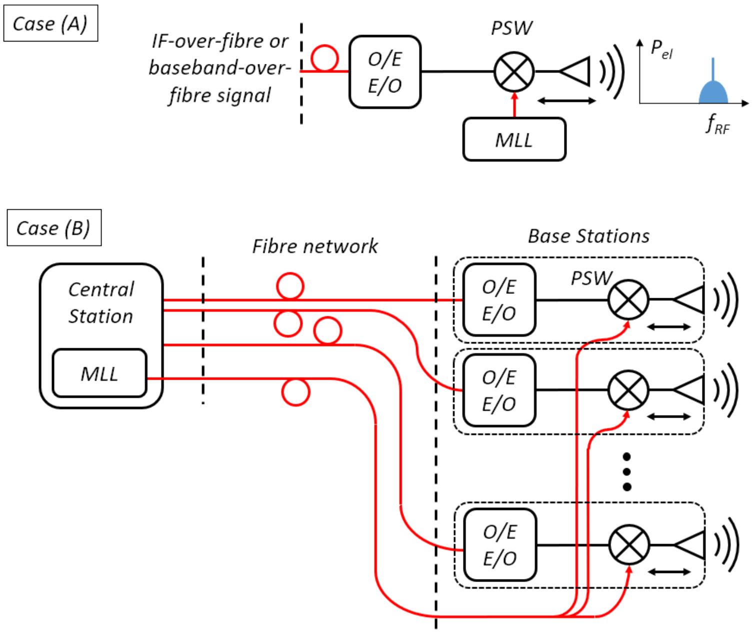

*Figure 4-36 Concepts of the photoconductive switch use in RoF networks. O/E: optical to electrical converter; E/O: Electrical to optical converter; PSW: photoconductive switch*

For both cases in Figure 4-36, the uplink from the user can also utilize the photoswitch based mixer in a way we presented in Figure 4-34. The mixer downconverts the received high carrier frequency signal for IF- or baseband-over-fibre transmission.

This mixing scheme therefor could simplify the RoF system in different ways. The local oscillator signal needed for the up conversion is a small footprint device, while it can provide LO frequencies in the millimetre wave range which also opens the possibility of RoF networks working in the mmW above 60 GHz. Also, using an optoelectronic mixer the complexity of the base station reduces as it is not necessary to use an optical to electrical converter for the distributed local oscillator signal for electronic mixers.

## IV/5. Conclusions of Chapter IV

This Chapter was focusing on the practical applications of the photoconductive switch. In sections IV/1.2 and IV/1.3.a we saw that the optoelectronic mixing scheme with the photoconductive switch presents conversion losses in the order of 65 dB – 72 dB. As these losses are considered as high values, we proposed solutions to reduce the switch losses. Despite the high losses, we used the switch in an optoelectronic mixing scheme with different setups. Two methods were presented for optically provided local oscillator, one is the use of an optical frequency comb, generated by a quantum dash semiconductor mode locked laser where the frequency difference between the optical modes corresponds to the generated local oscillator frequency. The other method is the use of two independent single mode lasers, where the two mode's beating frequency corresponds to the generated local oscillator frequency.

Using the MLL as the optical source for the mixer we demonstrated data-stream modulated signal down conversion. A QPSK modulated data signal on a carrier of 20 GHz was used as an input electrical signal to the switch while the MLL illuminating it provided the LO at 24.55 GHz. The mixing resulted in an IF signal at 4.55 GHz, which contained the down-converted data-stream. Receiving and demodulating this down-converted signal we analysed the data quality through the demodulated signal's Error Vector Magnitude for data-rates up to 2 Gbit/s. We also compared the down-conversion quality with the stabilized and free-running MLL signal and showing the improved down-conversion results through the EVM values. An EVM of 30.7 % was achieved with this highest bitrate of 2 Gbit/s with stabilized laser. Considering the high conversion losses, these values considered as good performance. We demonstrated an inverse setup too, where the data-stream was modulating a continuous wave optical signal from a DFB laser, and the LO was provided electrically for the photoswitch based mixer. We showed the performance up to 800 Mbit/s data-rates with a maximum EVM of 26.5 %.

In section IV/4 a brief study showed the switch non-linearities, which are turned out to produce too high level of harmonics, therefore the switch can be used as a sampler only with a low resolution.

The last section of this chapter proposed possible applications of the optoelectronic mixing scheme as a downconverter for wireless receivers. The presented setup provides a simple solution for the next generation of telecommunication networks, where the carrier frequencies are moving towards the mmW frequencies. Applications in Radio over Fibre systems was also proposed both as a downconverter and an upconverter in the base stations for the wireless distribution.

# General conclusions

This work was focusing on the characterization of a nitrogen ion implanted InGaAs photoconductive switch and on its practical applications as an optoelectronic device in the micro- and millimetre wave frequency range.

In the first Chapter, the photoconductive device physical properties are explained with the basic semiconductor equations and a numerical model of the switch is introduced based on these equations. A review of the state-of-the-art photoconductive devices was given and as the current devices are showing low quantum efficiency, improvement methods of the switch structure were proposed based on the literature. In this work we are focusing onto applications of the photoconductive device at frequencies in the 20- 200 GHz frequency range. Two applications are described, the use as an optoelectronic frequency mixer device and as a sampler device in photonic assisted Analog-to-Digital Converters. Utilizing an ultrafast photoconductive switch in these two applications may lead to better performances than the conventional all electrical solutions and offer more flexibility in the design of telecommunication systems thanks to the possible use of low loss fibre links.

The characterization of the photoconductive switch is described in the second chapter. Using the electrical response measurement results we were able to find an equivalent circuit model to obtain the switch electrical properties. For the 3 switch types with different finger and gap widths, equivalent capacitance of 5 fF – 8.1 fF was found, with AC dark resistance values around 2.1 kΩ – 5 kΩ. The photoswitch dynamic properties was also measured with an optoelectronic autocorrelation experiment. As the result of this measurement, we were able to obtain the ultrafast response of the devices and we attribute this response to the lifetimes of the photogenerated electron and hole in the semiconductor material. The autocorrelation of the response was measured, fitting a dual exponential on the curve we obtained the carrier lifetimes of 1.2 ps for the electrons and an average of 20 ps for the holes. These characterization measurement results of the short carrier lifetime and the low equivalent capacitance are suggesting a wide optoelectronic bandwidth for the switch with a cut-off frequency in the sub-THz range. In order to go further into the applications, we plan to use the photoswitch in combination with a semiconductor mode-locked laser as the optical signal source.

The third chapter is introducing a semiconductor mode-locked laser diode with a self-oscillation frequency of 24.55 GHz. We characterized the laser in the optical domain and analysed the beating signal in the electrical frequency domain produced by illuminating a photodiode. The properties of the free-running beating signal were obtained: 20 kHz RF linewidth and a phase noise of -70 dBc/Hz at 100 kHz offset. In order to improve the laser properties, an all-optical single feedback loop was constructed which stabilizes the laser output. As the result of the stabilization, the beating RF signal properties have improved: the phase noise showed a decrease down to -112 dBc/Hz at 100 kHz, this also corresponds to a 20-fold integrated timing jitter improvement down to 188 fs from 4 ps in case of the free-running laser. A dual loop stabilization feedback was also tested, which further improved the laser signal quality, however its long term stability restricted its usefulness in practical applications. This stabilized laser source based on a single-loop design will be then used in combination with the photoswitch in the next chapter.

Chapter IV is detailing the optoelectronic mixing experiments. The mode-locked laser served as the local oscillator source, and an electrical signal generator provided the input signal. First, we showed a relatively flat mixing performance over a wide electrical input bandwidth up to 67 GHz, and up to 164 GHz with optically generated signals. Conversion loss values in the range of 68-72 dB was obtained with these characterization experiments. These conversion losses are considered high values for a frequency mixer, this low efficiency is originating from the low quantum efficiency of the photoswitch. Possible improvements on new designs of the photoswitch are proposed in this chapter and also in Chapter I, however during our work the necessary technological resources were not available to improve the photoswitch structure.

The performance of the optoelectronic mixing scheme was demonstrated through the downconversion and demodulation of a QPSK modulated data-stream. There are 3 scenarios that were presented with different local oscillator sources.

- The first option used the MLL laser diode as the local oscillator source with a frequency of 24.55 GHz, we compared the results with the free-running and stabilized laser to show the advantages of the stabilization. With this setup we were able to downconvert data-streams with bitrates up to 2 Gbit/s on a 20 GHz carrier signal. The error vector magnitude value of the demodulated signal was used as the figure of merit of the mixing performance. The 2 Gbit/s data-stream had an EVM value of 30.7 % in case of the stabilized MLL. For all the measured bitrates, the stabilized laser showed better performance, however for increasing bitrates the difference decreased, showing that at wider bandwidth it is not the LO quality which limits the system performance. A discussion of the possible degradations effects was given to explain the performance limitations.
- The second optoelectronic mixing setup used an intensity modulated DFB laser as the local oscillator frequency source. With this setup the maximum bitrate, which was still possible to demodulate, was 200 Mbit/s (EVM : 32.5 %). This setup had limitations originating from the intensity modulated laser beam's low modulation depth.
- The third setup used the electrical input as the local oscillator source, while the data-stream was intensity modulating a continuous wave laser which was illuminating the photoswitch. The switch was able to downconvert this optically provided data signal with data-rates up to 800 Mbit/s with a maximum EVM in this case of 26.5 %. These measured maximum EVM values for the first and the third setups around 30 % are considered still acceptable in case the data is coded with Forward Error Correction, which can correct some of the bit errors after demodulation.

At the end of Chapter IV, an experimental study was given of the switch non-linearities. These were found to be too high, therefore the presented photoswitch application as a sampler device for photonic assisted ADCs is limited.

As the result of this work, we showed, that despite the high conversion loss of the photoswitch, the optoelectronic mixing scheme is still able to work with QPSK modulated data-streams up to 2 Gbit/s. Due to the switch advantages of simple operation and wide bandwidth they are promising candidates for use in Radio-over-fibre networks, as it was proposed in Chapter IV.

However, to utilize the switch in a real life application it is important to improve the quantum efficiency of the switch by redesigning the electrode structure. The described solutions in Chapter I for improved efficiency are promising technologies: the resonant structure or the nanoplasmonic structures to increase the absorbed photon number. Both solutions would improve the present photoconductive switch conversion losses, which is based on the nitrogen ion implanted InGaAs material having a low carrier lifetime to enable mmW operation. As we saw in Chapter IV, the switch has a stable performance in a wide opto-electronic bandwidth which presents a broad range of possible frequencies for the telecommunication system. To assess the mixing performance for the use in next generation of telecommunication networks, higher carrier frequencies, higher data-rates and complex modulation formats (QAM-16, OFDM etc.) has to be tested.

# References

[1] M. Martin, E. R. Brown, "Critical comparison of GaAs and InGaAs THz photoconductors," *Proc. SPIE 8261, Terahertz Technology and Applications V*, 826102 (23 February 2012); doi: 10.1117/12.914028

[2] D. H. Auston, "Picosecond optoelectronic switching and gating in silicon," *Applied Physics Letters*, 26(3), 101–103, 1975; doi: 10.1063/1.88079

[3] A. E. Iverson, D. L. Smith, "Mathematical modelling of photoconductor transient response," *IEEE Transactions on Electron Devices*, vol. 34, no. 10, pp. 2098-2107, Oct. 1987; doi: 10.1109/T-ED.1987.23203

[4] S. M. Sze, Kwok K. Ng, "Physics of Semiconductor Devices," 3rd edition, *John Wiley & Sons, Inc.*, Hoboken, New Jersey, 2007.

[5] H. Eusèbe, J. F. Roux, J. L. Coutaz, A. Krotkus, "Photoconductivity sampling of low-temperature-grown Be-doped GaAs layers," *Journal of Applied Physics*, 98(3), 2005; doi: 10.1063/1.2001151

[6] J. F. Roux, "Dispositifs à semi-conducteurs rapides pour la génération et la détection de signaux électriques GHz-THz," *Habilitation à diriger des recherches*, Université de Savoie, 2010.

[7] T. Hochrein, "Markets, Availability, Notice, and Technical Performance of Terahertz Systems: Historic Development, Present, and Trends," *J. Infrared Milli. Terahz. Waves,* 36: 235., 2015; Doi: 10.1007/s10762-014-0124-6

[8] N. M. Burford and M. O. El-Shenawee, "Review of terahertz photoconductive antenna technology," *Optical Engineering*, vol. 56, no. 1, p. 010901, 2017.; Doi: 10.1117/1.OE.56.1.010901

[9] T. Nagatsuma, G. Ducournau, and C. C. Renaud, "Advances in terahertz communications accelerated by photonics," *Nature Photonics*, vol. 10, no. 6, pp. 371–379, 2016; doi: 10.1038/nphoton.2016.65

[10] T. Nagatsuma, S. Hisatake, M. Fujita, H. H. N. Pham, K. Tsuruda, S. Kuwano, and J. Terada, "Millimeter-Wave and Terahertz-Wave Applications Enabled by Photonics," *IEEE Journal of Quantum Electronics*, vol. 52, no. 1, pp. 1–12, 2016.; doi: 10.1109/JQE.2015.2506992

[11] T. Kürner and S. Priebe, "Towards THz Communications - Status in Research, Standardization and Regulation," *Journal of Infrared, Millimeter, and Terahertz Waves*, vol. 35, no. 1, pp. 53–62, Jan. 2014.; Doi: 10.1007/s10762-013-0014-3

[12] T. Nagatsuma, S. Horiguchi, Y. Minamikata, Y. Yoshimizu, S. Hisatake, S. Kuwano, N. Yoshimoto, J. Terada, and H. Takahashi, "Terahertz Wireless Communications based on Photonics Technologies," *Optics Express*, vol. 21, no. 20, pp. 23736–23747, 2013.; doi: 10.1364/OE.21.023736

[13] G. Ducournau, P. Szriftgiser, F. Pavanello, E. Peytavit, M. Zaknoune, D. Bacquet, A. Beck, T. Akalin, J. F. Lampin, and J. F. Lampin, "THz Communications using Photonics and Electronic Devices: the Race to Data-Rate," *Journal of Infrared, Millimeter, and Terahertz Waves*, vol. 36, no. 2, pp. 198–220, 2015.; doi: 10.1007/s10762-014-0112-x

[14] P. R. Smith, D. H. Auston and M. C. Nuss, "Subpicosecond photoconducting dipole antennas," *IEEE Journal of Quantum Electronics*, vol. 24, no. 2, pp. 255-260, Feb. 1988.; doi: 10.1109/3.121

[15] F. W. Smith, H. Q. Le, V. Diadiuk, M. A. Hollis, A. R. Calawa, S. Gupta, M. Frankel, D. R. Dykaar, G. A. Mourou, and T. Y. Hsiang, “Picosecond GaAs-based photoconductive optoelectronic detectors,” *Applied Physics Letters*, vol. 54, no. 10, pp. 890–892, Mar. 1989.; doi: 10.1063/1.100800

[16] E. R. Brown, K. A. McIntosh, K. B. Nichols, and C. L. Dennis, “Photomixing up to 3.8 THz in low-temperature-grown GaAs,” *Applied Physics Letters*, vol. 66, no. 3, pp. 285–287, Jan. 1995.; Doi: 10.1063/1.113519

[17] S. Gupta, M. Y. Frankel, J. A. Valdmanis, J. F. Whitaker, G. A. Mourou, F. W. Smith, and A. R. Calawa, “Subpicosecond carrier lifetime in GaAs grown by molecular beam epitaxy at low temperatures,” *Applied Physics Letters*, vol. 59, no. 25, pp. 3276–3278, Dec. 1991.; doi: 10.1063/1.105729

[18] A. Krotkus, S. Marcinkevicius, J. Jasinski, M. Kaminska, H. H. Tan, and C. Jagadish, “Picosecond carrier lifetime in GaAs implanted with high doses of As ions: An alternative material to low-temperature GaAs for optoelectronic applications,” *Applied Physics Letters*, vol. 66, no. 24, pp. 3304–3306, Jun. 1995.; doi: 10.1063/1.113738

[19] A. Singh, S. Pal, H. Surdi, S. S. Prabhu, S. Mathimalar, V. Nanal, R. G. Pillay, and G. H. Döhler, “Carbon irradiated semi insulating GaAs for photoconductive terahertz pulse detection,” *Optics Express*, vol. 23, no. 5, p. 6656, Mar. 2015.; doi: 10.1364/OE.23.006656

[20] A. Krotkus, K. Bertulis, M. Kaminska, K. Korona, A. Wolos, J. Siegert, S. Marcinkevičius, J.-F. Roux and J.-L. Coutaz, “Be-doped low-temperature-grown GaAs material for optoelectronic switches,” *IEE Proceedings - Optoelectronics*, vol. 149, no. 3, pp. 111–115, Jun. 2002.; doi: 10.1049/ip-opt:20020435

[21] M. Tani, K.-S. Lee, and X.-C. Zhang, “Detection of terahertz radiation with low-temperature-grown GaAs-based photoconductive antenna using 1.55 µm probe,” *Applied Physics Letters*, vol. 77, no. 9, pp. 1396–1398, Aug. 2000.; doi: 10.1063/1.1289914

[22] C. Kadow, A. W. Jackson, A. C. Gossard, J. E. Bowers, S. Matsuura, and G. A. Blake, “Self-assembled ErAs islands in GaAs for THz applications,” *Physica E: Low-dimensional Systems and Nanostructures*, vol. 7, no. 1–2, pp. 97–100, Apr. 2000.; doi: 10.1016/S1386-9477(99)00314-8

[23] A. Takazato, M. Kamakura, T. Matsui, J. Kitagawa, and Y. Kadoya, “Detection of terahertz waves using low-temperature-grown InGaAs with 1.56µm pulse excitation,” *Applied Physics Letters,* vol. 90, no. 10, p. 101119, Mar. 2007.; doi: 10.1063/1.2712503

[24] D. C. Driscoll, M. P. Hanson, A. C. Gossard, and E. R. Brown, “Ultrafast photoresponse at 1.55 µm in InGaAs with embedded semimetallic ErAs nanoparticles,” *Applied Physics Letters*, vol. 86, no. 5, p. 051908, Jan. 2005.; doi: 10.1063/1.1852092

[25] N. Chimot, J. Mangeney, L. Joulaud, P. Crozat, H. Bernas, K. Blary, and J. F. Lampin, “Terahertz radiation from heavy-ion-irradiated In0.53Ga0.47As photoconductive antenna excited at 1.55µm,” *Applied Physics Letters*, vol. 87, no. 19, p. 193510, Nov. 2005.; doi: 10.1063/1.2126110

[26] B. Sartorius, H. Roehle, H. Künzel, J. Böttcher, M. Schlak, D. Stanze, H. Venghaus, and M. Schell, “All-fiber terahertz time-domain spectrometer operating at 1.5 µm telecom wavelengths,” *Optics Express*, vol. 16, no. 13, p. 9565, Jun. 2008.; doi: 10.1364/OE.16.009565

[27] R. B. Kohlhaas, R. J. B. Dietz, S. Breuer, S. Nellen, L. Liebermeister, M. Schell, and B. Globisch, “Improving the dynamic range of InGaAs-based THz detectors by localized beryllium doping: up to 70 dB at 3 THz,” *Optics Letters*, vol. 43, no. 21, p. 5423, Nov. 2018.; doi: 10.1364/OL.43.005423

[28] M. Suzuki and M. Tonouchi, “Fe-implanted InGaAs terahertz emitters for 1.56µm wavelength excitation,” *Applied Physics Letters*, vol. 86, no. 5, p. 051104, Jan. 2005.; doi: 10.1063/1.1861495

[29] C. Graham, R. Gwilliam, and A. Seeds, “Nitrogen ion implanted InP based photo-switch,” *Optics Express*, vol. 20, no. 24, p. 26696, Nov. 2012.; doi: 10.1364/OE.20.026696

[30] N. T. Yardimci and M. Jarrahi, “Nanostructure-Enhanced Photoconductive Terahertz Emission and Detection,” *Small*, vol. 14, no. 44, p. 1802437, Nov. 2018.; doi: 10.1002/smll.201802437

[31] Y. Chen, S. Williamson, T. Brock, F. W. Smith, and A. R. Calawa, “375-GHz-bandwidth photoconductive detector,” *Applied Physics Letters*, vol. 59, no. 16, pp. 1984–1986, Oct. 1991.; doi: 10.1063/1.106157

[32] E. R. Brown, F. W. Smith, and K. A. McIntosh, “Coherent millimeter-wave generation by heterodyne conversion in low-temperature-grown GaAs photoconductors,” *Journal of Applied Physics*, vol. 73, no. 3, pp. 1480–1484, Feb. 1993.; doi: 10.1063/1.353222

[33] E. Peytavit, C. Coinon, and J.-F. Lampin, “A metal-metal Fabry–Pérot cavity photoconductor for efficient GaAs terahertz photomixers,” *Journal of Applied Physics*, vol. 109, no. 1, p. 016101, Jan. 2011.; doi: 10.1063/1.3525709

[34] E. Peytavit, P. Latzel, F. Pavanello, G. Ducournau, and J.-F. Lampin, “Milliwatt output power generated in the J-Band by a GaAs photomixer,” *2013 38th International Conference on Infrared, Millimeter, and Terahertz Waves (IRMMW-THz)*, 2013, pp. 1–3.; doi: 10.1109/IRMMW-THz.2013.6665739

[35] E. Peytavit, F. Pavanello, G. Ducournau, and J.-F. Lampin, “Highly efficient terahertz detection by optical mixing in a GaAs photoconductor,” *Applied Physics Letters*, vol. 103, no. 20, p. 201107, Nov. 2013.; doi: 10.1063/1.4830360

[36] B. Heshmat, H. Pahlevaninezhad, Y. Pang, M. Masnadi-Shirazi, R. Burton Lewis, T. Tiedje, R. Gordon, and T. E. Darcie, “Nanoplasmonic Terahertz Photoconductive Switch on GaAs,” *Nano Letters*, vol. 12, no. 12, pp. 6255–6259, Dec. 2012., doi:10.1021/nl303314a

[37] C. W. Berry, N. Wang, M. R. Hashemi, M. Unlu, and M. Jarrahi, “Significant performance enhancement in photoconductive terahertz optoelectronics by incorporating plasmonic contact electrodes,” *Nature Communications*, vol. 4, no. 1, p. 1622, Dec. 2013.; doi: 10.1038/ncomms2638

[38] M. Billet, P. Latzel, F. Pavanello, G. Ducournau, J.-F. Lampin, and E. Peytavit, “Resonant cavities for efficient LT-GaAs photoconductors operating at λ = 1550 nm,” *APL Photonics*, vol. 1, no. 7, p. 076102, Oct. 2016.; doi: 10.1063/1.4954771

[39] M. Billet, Y. Desmet, F. Bavedila, G. Ducournau, S. Barbieri, J. F. Lampin, and E. Peytavit, “Ultrafast LT-GaAs photoconductors based on a Fabry-Pérot cavity designed for 1550 nm wavelength illumination,” in *2017 42nd International Conference on Infrared, Millimeter, and Terahertz Waves (IRMMW-THz)*, 2017, pp. 1–2.; doi: 10.1109/IRMMW-THz.2017.8066941

[40] David M. Pozar, “Microwave and RF Wireless Systems,” *John Wiley & Sons Inc*., 2001, ISBN: 0-471-32283-2

[41] Analog Devices Inc., “The Data Conversion Handbook,” 1st edition, *Elsevier*, 2005, ISBN: 0-7506-7841-0

[42] A. Khilo et al., “Photonic ADC: overcoming the bottleneck of electronic jitter,” *Optics Express*, vol. 20, no. 4, p. 4454, Feb. 2012.; doi: 10.1364/OE.20.004454

[43] P. A. Gamage, A. Nirmalathas, C. Lim, D. Novak, and R. Waterhouse, “Design and Analysis of Digitized RF-Over-Fiber Links,” *Journal of Lightwave Technology*, vol. 27, no. 12, pp. 2052–2061, Jun. 2009.; doi: 10.1109/JLT.2008.2006689

[44] R. G. Vaughan, N. L. Scott, and D. R. White, “The theory of bandpass sampling,” *IEEE Transactions on Signal Processing*, vol. 39, no. 9, pp. 1973–1984, 1991.; doi: 10.1109/78.134430

[45] U. R. Pfeiffer, C. Mishra, R. M. Rassel, S. Pinkett, and S. K. Reynolds, “Schottky Barrier Diode Circuits in Silicon for Future Millimeter-Wave and Terahertz Applications,” *IEEE Transactions on Microwave Theory and Techniques*, vol. 56, no. 2, pp. 364–371, 2008.; doi: 10.1109/TMTT.2007.914656

[46] A. Navarrini, A. L. Fontana, D. Maier, P. Serres, and D. Billon-Pierron, “Superconductor-Insulator-Superconductor Mixers for the 2 mm Band (129-174 GHz),” *Journal of Infrared, Millimeter, and Terahertz Waves*, vol. 35, no. 6–7, pp. 536–562, Jul. 2014.; doi: 10.1007/s10762-014-0076-x

[47] E. Novoselov and S. Cherednichenko, “Broadband MgB 2 Hot-Electron Bolometer THz Mixers Operating up to 20 K,” *IEEE Transactions on Applied Superconductivity*, vol. 27, no. 4, pp. 1–4, Jun. 2017.; doi: 10.1109/TASC.2017.2654861

[48] C. Wang, B. Lu, C. Lin, Q. Chen, L. Miao, X. Deng, and J. Zhang, “0.34-THz Wireless Link Based on High-Order Modulation for Future Wireless Local Area Network Applications,” *IEEE Transactions on Terahertz Science and Technology*, vol. 4, no. 1, pp. 75–85, Jan. 2014.; doi: 10.1109/TTHZ.2013.2293119

[49] J. A. Nanzer, P. T. Callahan, M. L. Dennis, and T. R. Clark, “Photonic signal generation for millimeter-wave communications,” *Johns Hopkins APL Technical Digest (Applied Physics Laboratory)*, vol. 30, no. 4, pp. 299–308, 2012.

[50] J. Capmany and D. Novak, “Microwave photonics combines two worlds,” *Nature Photonics*, vol. 1, no. 6, pp. 319–330, Jun. 2007.; doi: 10.1038/nphoton.2007.89

[51] A. Seeds, M. Natrella, H. Shams, L. Ponnampalam, K. Balakier, C. Graham, C.-P. Liu, H. Liu, C. Renaud, and M. Fice, “Microwave Photonics: Present Status and Future Outlook (Plenary Paper),” in *2015 International Topical Meeting on Microwave Photonics (MWP)*, 2015, pp. 1–6.; doi: 10.1109/MWP.2015.7356717

[52] G. Carpintero et al., “Microwave Photonic Integrated Circuits for Millimeter-Wave Wireless Communications,” *Journal of Lightwave Technology*, vol. 32, no. 20, pp. 3495–3501, Oct. 2014.; doi: 10.1109/JLT.2014.2321573

[53] J. Yao, “Microwave Photonics,” *Journal of Lightwave Technology*, vol. 27, no. 3, pp. 314–335, Feb. 2009.; doi: 10.1109/JLT.2008.2009551

[54] S. Preu, G. H. Döhler, S. Malzer, L. J. Wang, and A. C. Gossard, “Tunable, continuous-wave Terahertz photomixer sources and applications,” *Journal of Applied Physics*, vol. 109, no. 6, p. 061301, Mar. 2011.; doi: 10.1063/1.3552291

[55] R. A. Minasian, E. H. W. Chan, and X. Yi, “Microwave photonic signal processing,” *Optics Express*, vol. 21, no. 19, p. 22918, Sep. 2013.; doi: 10.1364/OE.21.022918

[56] J. Zhang, E. H. W. Chan, X. Wang, X. Feng, and B. Guan, “High Conversion Efficiency Photonic Microwave Mixer With Image Rejection Capability,” *IEEE Photonics Journal*, vol. 8, no. 4, pp. 1–11, Aug. 2016.; doi: 10.1109/JPHOT.2016.2592327

[57] K. Noguchi, O. Mitomi, and H. Miyazawa, “Millimeter-wave Ti:LiNbO/sub 3/ optical modulators,” *Journal of Lightwave Technology*, vol. 16, no. 4, pp. 615–619, Apr. 1998.; doi: 10.1109/50.664072

[58] P. O. Weigel et al., “Bonded thin film lithium niobate modulator on a silicon photonics platform exceeding 100 GHz 3-dB electrical modulation bandwidth,” *Optics Express*, vol. 26, no. 18, p. 23728, Sep. 2018.; doi: 10.1364/OE.26.023728

[59] A. Altaqui, E. H. W. Chan, and R. A. Minasian, “Microwave photonic mixer with high spurious-free dynamic range,” *Applied Optics*, vol. 53, no. 17, p. 3687, Jun. 2014.; doi: 10.1364/AO.53.003687

[60] C. K. Lin, C. W. Lin, Y. C. Wu, and H. C. Chiu, “An optoelectronic mixer based on composite transparent gate InAlAs/InGaAs metamorphic HEMT,” *Conference Proceedings - International Conference on Indium Phosphide and Related Materials*, vol. 28, no. 15, pp. 340–343, 2010.; doi: 10.1109/JLT.2010.2053696

[61] D. S. Shin, G. L. Li, C. K. Sun, S. A. Pappert, K. K. Loi, W. S. C. Chang, and P. K. L. Yu, “Optoelectronic RF signal mixing using an electroabsorption waveguide as an integrated photodetector/mixer,” *IEEE Photonics Technology Letters*, vol. 12, no. 2, pp. 193–195, Feb. 2000.; doi: 10.1109/68.823514

[62] S. A. Malyshev and A. L. Chizh, “p-i-n Photodiodes for Frequency Mixing in Radio-Over-Fiber Systems,” *Journal of Lightwave Technology*, vol. 25, no. 11, pp. 3236–3243, Nov. 2007.; doi: 10.1109/JLT.2007.906811

[63] H. Ito, T. Furuta, S. Kodama, and T. Ishibashi, “InP/InGaAs uni-travelling-carrier photodiode with 310 GHz bandwidth,” *Electronics Letters*, vol. 36, no. 21, p. 1809, 2000.; doi: 10.1049/el:20001274

[64] C. C. Renaud, M. J. Fice, L. Ponnampalam, M. Natrella, C. Graham, and A. J. Seeds, “Uni-travelling carrier photodetectors as THz detectors and emitters,” *SPIE Proceedings*, 2015, vol. 9370, no. February 2015, p. 93700B.; doi: 10.1117/12.2080195

[65] A. W. Mohammad, H. Shams, K. Balakier, C. Graham, M. Natrella, A. J. Seeds, and C. C. Renaud, “5 Gbps wireless transmission link with an optically pumped uni-traveling carrier photodiode mixer at the receiver,” *Optics Express*, vol. 26, no. 3, p. 2884, Feb. 2018. Doi: 10.1364/OE.26.002884

[66] H.-J. SONG, T.-W. KIM, S. J. JO, C.-H. LIM, K.-H. OH, S.-G. IHN, and J.-I. SONG, “Microwave Photonic Mixer Utilizing an InGaAs Photoconductor for Radio over Fiber Applications,” *IEICE Transactions on Electronics*, vol. E90–C, no. 2, pp. 457–464, Feb. 2007.; doi: 10.1093/ietele/e90-c.2.457

[67] G. C. Valley, “Photonic analog-to-digital converters,” *Optics Express*, vol. 15, no. 5, p. 1955, 2007.; doi: 10.1364/OE.15.001955

[68] R. Walden, “Analog-to-digital conversion in the early twenty-first century,” Wiley Encyclopedia of Computer Science and Engineering (Wiley, 2008), pp. 126–138.; doi: 10.1002/9780470050118.ecse014

[69] ONLINE – https://www.menlosystems.de/assets/datasheets/MENLO_CFiber-D-EN_2018-06_3w.pdf; last accessed: 22/01/2019

[70] F. J. Leonberger and V. Diadiuk, “High-speed InP-based photodetectors,” *1983 International Electron Devices Meeting*, 1983, pp. 460–463.; doi: 10.1109/IEDM.1983.190542

[71] R. Urata, L. Y. Nathawad, R. Takahashi, Kai Ma, D. A. B. Miller, B. A. Wooley, and J. S. Harris, “Photonic A/D conversion using low-temperature-grown gaas msm switches integrated with Si-CMOS,” *Journal of Lightwave Technology*, vol. 21, no. 12, pp. 3104–3115, Dec. 2003.; doi: 10.1109/JLT.2003.820054

[72] S. Formont, L. Menager, G. Baily, L. Morvan, and D. Rousset, “Direct sampling of Ka-Band signals using a photoconductive switch approach,” *2011 International Topical Meeting on Microwave Photonics jointly held with the 2011 Asia-Pacific Microwave Photonics Conference*, 2011, pp. 425–428.; doi: MWP.2011.6088762

[73] F. Lelarge et al., “Recent Advances on InAs/InP Quantum Dash Based Semiconductor Lasers and Optical Amplifiers Operating at 1.55 µm,” *IEEE Journal of Selected Topics in Quantum Electronics*, vol. 13, no. 1, pp. 111–124, 2007.; doi: 10.1109/JSTQE.2006.887154

[74] P. T. Callahan, M. L. Dennis, and T. R. Clark, Jr., “Photonic analog-to-digital conversion,” Johns Hopkins APL Tech. Dig. 30, 280–286, 2012

[75] M. P. Fok, K. L. Lee, and C. Shu, “4 x 2.5 GHz Repetitive Photonic Sampler for High-Speed Analog-to-Digital Signal Conversion,” *IEEE Photonics Technology Letters*, vol. 16, no. 3, pp. 876–878, Mar. 2004.; doi: 10.1109/LPT.2004.823696

[76] Yan Han and B. Jalali, “Photonic time-stretched analog-to-digital converter: fundamental concepts and practical considerations,” *Journal of Lightwave Technology*, vol. 21, no. 12, pp. 3085–3103, Dec. 2003.; doi: 10.1109/JLT.2003.821731

[77] F. Kärtner, A. Khilo, and A. Nejadmalayeri, “Progress in Photonic Analog-to-Digital Conversion,” in *Optical Fiber Communication Conference/National Fiber Optic Engineers Conference 2013*, 2013, p. OTh3D.5.; doi: 10.1364/OFC.2013.OTh3D.5

[78] D. J. Esman, A. O. J. Wiberg, N. Alic, and S. Radic, “Highly Linear Broadband Photonic-Assisted Q-Band ADC,” *Journal of Lightwave Technology*, vol. 33, no. 11, pp. 2256–2262, Jun. 2015.; doi: 10.1109/JLT.2015.2408551

[79] D. Arsenijevic, M. Kleinert, and D. Bimberg, “Breakthroughs in Photonics 2013: Passive Mode-Locking of Quantum-Dot Lasers,” *IEEE Photonics Journal*, vol. 6, no. 2, pp. 1–6, Apr. 2014.; doi: 10.1109/JPHOT.2014.2308195

[80] Hyoji Kim, Peng Qin, Youjian Song, Heewon Yang, Junho Shin, Chur Kim, Kwangyun Jung, Chingyue Wang, and Jungwon Kim, “Sub-20-Attosecond Timing Jitter Mode-Locked Fiber Lasers,” *IEEE Journal of Selected Topics in Quantum Electronics*, vol. 20, no. 5, pp. 260–267, Sep. 2014.; doi: 10.1109/JSTQE.2014.2298454

[81] F. X. Kärtner, P. Callahan, K. Shtyrkova, N. Li, N. Singh, M. Xin, K. Ravi, J. Notaros, S. Magden, D. Vermeulen, E. P. Ippen, and M. Watts, “Integrated rare-Earth doped mode-locked lasers on a CMOS platform,” in *Silicon Photonics: From Fundamental Research to Manufacturing*, 2018, no. May 2018, p. 14.; doi: 10.1117/12.2318010

[82] Hyunil Byun, A. Hanjani, D. Pudo, and J. Shmulovich, “Integrated Low-Jitter 400-MHz Femtosecond Waveguide Laser,” *IEEE Photonics Technology Letters*, vol. 21, no. 12, pp. 763–765, Jun. 2009.; doi: 10.1109/LEOS.2008.4688756

[83] C. Gosset, K. Merghem, A. Martinez, G. Moreau, G. Patriarche, G. Aubin, J. Landreau, F. Lelarge, and A. Ramdane, “Subpicosecond pulse generation at 134 GHz and low radiofrequency spectral linewidth in quantum dash-based Fabry-Perot lasers emitting at 1.5 µm,” *Electronics Letters*, vol. 42, no. 2, p. 91, 2006.; doi: 10.1049/el:20063868

[84] K. Merghem, A. Akrout, A. Martinez, G. Aubin, A. Ramdane, F. Lelarge, and G.-H. Duan, “Pulse generation at 346 GHz using a passively mode locked quantum-dash-based laser at 1.55 µm,” Appl. Phys. Lett. 94(2), 021107 (2009); doi: 10.1063/1.3070544

[85] A. Krotkus and J.-L. Coutaz, “Non-stoichiometric semiconductor materials for terahertz optoelectronics applications,” Semiconductor Science and Technology, vol. 20, no. 7, pp. S142–S150, Jul. 2005.; doi: 10.1088/0268-1242/20/7/004

[86] Simons, Rainee N. (2002). Conventional Coplanar Waveguide. In Coplanar Waveguide Circuits, Components, and Systems *Chapter 2* (eds K. Chang and R. N. Simons). doi:10.1002/0471224758.ch2

[87] D. Auston, “Impulse response of photoconductors in transmission lines,” IEEE Journal of Quantum Electronics, vol. 19, no. 4, pp. 639–648, Apr. 1983.; doi: 10.1109/JQE.1983.1071904

[88] ONLINE, Corning SMF-28 datasheet, last access: 11/04/2019 - https://www.corning.com/media/worldwide/coc/documents/Fiber/SMF-28%20Ultra.pdf

[89] Tektronix Technique Primer 47W-7209, Sampling oscilloscope techniques ; online available : https://www.tek.com/sites/default/files/media/media/resources/Sampling%20Oscilloscope%20Techniques.pdf; last accessed: 11/04/2019

[90] K. Grigoras, A. Krotkus, and A. Deringas, “Picosecond lifetime measurement in semiconductor by optoelectronic autocorrelation,” *Electronics Letters*, vol. 27, no. 12, p. 1024, 1991.; doi: 10.1049/el:19910637

[91] J.-F. Roux, J.-L. Coutaz, and A. Krotkus, “Time-resolved reflectivity characterization of polycrystalline low-temperature-grown GaAs,” *Applied Physics Letters*, vol. 74, no. 17, p. 2462, 1999.; doi: 10.1063/1.123881

[92] J. P. van der Ziel, W. T. Tsang, R. A. Logan, R. M. Mikulyak, and W. M. Augustyniak, “Subpicosecond pulses from passively mode-locked GaAs buried optical guide semiconductor lasers,” *Applied Physics Letters*, vol. 39, no. 7, pp. 525–527, Oct. 1981.; doi: 10.1063/1.92802

[93] Y. Silberberg, D. A. B. Miller, A. C. Gossard, W. Wiegmann, P. W. Smith, and D. J. Eilenberger, “Passive mode locking of a semiconductor diode laser,” *Optics Letters*, vol. 9, no. 11, p. 507, Nov. 1984.; doi: 10.1364/OL.9.000507

[94] M. G. Thompson, A. R. Rae, Mo Xia, R. V. Penty, and I. H. White, “InGaAs Quantum-Dot Mode-Locked Laser Diodes,” *IEEE Journal of Selected Topics in Quantum Electronics*, vol. 15, no. 3, pp. 661–672, 2009.; doi: 10.1109/JSTQE.2008.2012265

[95] E. U. Rafailov, M. A. Cataluna, and W. Sibbett, “Mode-locked quantum-dot lasers,” *Nature Photonics*, vol. 1, no. 7, pp. 395–401, Jul. 2007.; doi: 10.1038/nphoton.2007.120

[96] IPHOBAC Final Activity Report, Online, Last access: 11/04/2019; https://cordis.europa.eu/docs/projects/cnect/7/035317/080/publishing/readmore/Publishable-Final-Activity-Report-Reports-IPHOBAC-Y1-Y3-FAR.pdf

[97] F. Brendel, J. Poette, B. Cabon, T. Zwick, F. van Dijk, F. Lelarge, and A. Accard. “Chromatic dispersion in 60 GHz radio-over-fiber networks based on mode-locked lasers,” IEEE *Journal of Lightwave Technology*, 29(24):3810 –3816, Dec 2011.; doi: 10.1109/JLT.2011.2173902

[98] Online http://www.femtochrome.com/FR-103XL.htm, last accessed: 11/04/2019

[99] *FR-103MN Autocorrelator Instruction Manual by Femtochrome Inc., not available online*

[100] F. Kefelian, S. O’Donoghue, M. T. Todaro, J. G. McInerney, and G. Huyet, “RF Linewidth in Monolithic Passively Mode-Locked Semiconductor Laser,” *IEEE Photonics Technology Letters*, vol. 20, no. 16, pp. 1405–1407, Aug. 2008.; doi: 10.1109/LPT.2008.926834

[101] IEEE Standard Definitions of Physical Quantities for Fundamental Frequency and Time Metrology - Random Instabilities," in IEEE Std 1139-1999 , 1999, doi: 10.1109/IEEESTD.1999.90575

[102] D. Arsenijević, M. Kleinert and D. Bimberg, "Breakthroughs in Photonics 2013: Passive Mode-Locking of Quantum-Dot Lasers," in IEEE Photonics Journal, vol. 6, no. 2, pp. 1-6, April 2014, Art no. 0700306. doi: 10.1109/JPHOT.2014.2308195

[103] A. Stohr et al., “Millimeter-wave photonic components for broadband wireless systems,” *IEEE Transactions on Microwave Theory and Techniques*, vol. 58, no. 11, pp. 3071–3082, 2010.; doi: 10.1109/TMTT.2010.2077

[104] A. Akrout, A. Shen, A. Enard, G.-H. Duan, F. Lelarge, and A. Ramdane, “Low phase noise all-optical oscillator using quantum dash modelocked laser,” *Electronics Letters*, vol. 46, no. 1, pp. 73–74, 2010.; doi: 10.1049/el.2010.2886

[105] R. P. Scott, C. Langrock and B. H. Kolner, "High-dynamic-range laser amplitude and phase noise measurement techniques," in *IEEE Journal of Selected Topics in Quantum Electronics*, vol. 7, no. 4, pp. 641-655, July-Sept. 2001.; doi: 10.1109/2944.974236

[106] M. Endo, T. D. Shoji, and T. R. Schibli, “Ultralow Noise Optical Frequency Combs,” *IEEE Journal of Selected Topics in Quantum Electronics*, vol. 24, no. 5, pp. 1–13, Sep. 2018.; doi: 10.1109/JSTQE.2018.2818461

[107] D. Eliyahu, R. A. Salvatore, and A. Yariv, “Effect of noise on the power spectrum of passively mode-locked lasers,” *Journal of the Optical Society of America B*, vol. 14, no. 1, p. 167, 2008.; doi: 10.1364/JOSAB.14.000167

[108] L. A. Jiang, M. E. Grein, H. A. Haus, and E. P. Ippen, “Noise of mode-locked semiconductor lasers,” *IEEE Journal on Selected Topics in Quantum Electronics*, vol. 7, no. 2, pp. 159–167, 2001.; doi: 10.1109/2944.954125

[109] L. Drzewietzki, S. Breuer, and W. Elsäßer, “Timing jitter reduction of passively mode-locked semiconductor lasers by self- and external-injection: Numerical description and experiments,” *Optics Express*, vol. 21, no. 13, p. 16142, Jul. 2013.; doi: 10.1364/OE.21.016142

[110] H. A. Haus and A. Mecozzi, “Noise of mode-locked lasers,” *IEEE Journal of Quantum Electronics*, vol. 29, no. 3, pp. 983–996, Mar. 1993.; doi: 10.1109/3.206583

[111] G. Carpintero, M. G. Thompson, R. V. Penty, and I. H. White, “Low Noise Performance of Passively Mode-Locked 10-GHz Quantum-Dot Laser Diode,” *IEEE Photonics Technology Letters*, vol. 21, no. 6, pp. 389–391, Mar. 2009.; doi: 10.1109/LPT.2008.2011918

[112] F. van Dijk, A. Enard, X. Buet, F. Lelarge, and G. H. Duan, “Phase noise reduction of a quantum dash mode-locked laser in a millimeter-wave coupled opto-electronic oscillator,” *Journal of Lightwave Technology*, vol. 26, no. 15, pp. 2789–2794, 2008.; doi: 10.1109/JLT.2008.927608

[113] S. Breuer, W. Elsässer, J. G. McInerney, K. Yvind, J. Pozo, E. A. J. M. Bente, M. Yousefi, A. Villafranca, N. Vogiatzis, and J. Rorison, “Investigations of Repetition Rate Stability of a Mode-Locked Quantum Dot Semiconductor Laser in an Auxiliary Optical Fiber Cavity,” *IEEE Journal of Quantum Electronics*, vol. 46, no. 2, pp. 150–157, Feb. 2010.; doi: 10.1109/JQE.2009.2033255

[114] M. Haji, L. Hou, A. E. Kelly, J. Akbar, J. H. Marsh, J. M. Arnold, and C. N. Ironside, “High frequency optoelectronic oscillators based on the optical feedback of semiconductor mode-locked laser diodes,” *Optics Express*, vol. 20, no. 3, p. 3268, Jan. 2012.; doi: 10.1364/OE.20.003268

[115] L. Jaurigue, A. Pimenov, D. Rachinskii, E. Schöll, K. Lüdge, and A. G. Vladimirov, “Timing jitter of passively-mode-locked semiconductor lasers subject to optical feedback: A semi-analytic approach,” *Physical Review A*, vol. 92, no. 5, p. 053807, Nov. 2015.; doi: 10.1103/PhysRevA.92.053807

[116] F. Quinlan, S. Ozharar, S. Gee, and P. J. Delfyett, “Harmonically mode-locked semiconductor-based lasers as high repetition rate ultralow noise pulse train and optical frequency comb sources,” *Journal of Optics A: Pure and Applied Optics*, vol. 11, no. 10, p. 103001, Oct. 2009.; doi: 10.1088/1464-4258/11/10/103001

[117] H. Asghar, W. Wei, P. Kumar, E. Sooudi, and J. G. McInerney, “Stabilization of self-mode-locked quantum dash lasers by symmetric dual-loop optical feedback,” *Optics Express*, vol. 26, no. 4, p. 4581, Feb. 2018.; doi: 10.1364/OE.26.004581

[118] H. Asghar and J. G. McInerney, “An asymmetric dual-loop feedback scheme with optimized second delay time to suppress spurious tones and timing jitter of self-mode-locked quantum dash lasers,” *Optics Letters*, vol. 42, no. 18, p. 3714, Sep. 2017.; doi: 10.1364/OL.42.003714

[119] H. Asghar, E. Sooudi, P. Kumar, W. Wei, and J. G. McInerney, “Optimum stabilization of self-mode-locked quantum dash lasers using dual optical feedback with improved tolerance against phase delay mismatch,” *Optics Express*, vol. 25, no. 14, p. 15796, Jul. 2017.; doi: 10.1364/OE.25.015796

[120] Chang-Yi Lin, F. Grillot, Yan Li, R. Raghunathan, and L. F. Lester, “Microwave Characterization and Stabilization of Timing Jitter in a Quantum-Dot Passively Mode-Locked Laser via External Optical Feedback,” *IEEE Journal of Selected Topics in Quantum Electronics*, vol. 17, no. 5, pp. 1311–1317, Sep. 2011.; doi: 10.1109/JSTQE.2011.2118745

[121] Yann Desmet, “Echantillonnage de signaux radar par voie optoélectronique : étude des non-linéarités des photoconducteurs à cavité résonante”, Doctoral Thesis, IEMN, Lille, Online : http://theses.fr/2018LIL1I019, last access: 11/04/2019

[122] Nisrine Arab, “Optique intégrée sur verre pour la génération de fréquences radio”, Doctoral Thesis, IMEP-LaHC, Grenoble. Online : http://theses.fr/s136464 , last access 11/04/2019

[123] N. Arab, L. Bastard, J. Poëtte, “Co-integration of two DFB lasers on glass for millimeter-wave generation,” Proc. SPIE 10106, *Integrated Optics: Devices, Materials, and Technologies XXI*, 1010605 16 February 2017; doi: 10.1117/12.2250136

[124] N. Arab, L. Bastard, J. Poëtte, J.-E. Broquin, and B. Cabon, “Thermal coupling impact on an MMW carrier generated using two free-running DFB lasers on glass,” *Optics Letters*, vol. 43, no. 22, p. 5500, Nov. 2018.; doi: 10.1364/OL.43.005500

[125] R. A. Shafik, M. S. Rahman, and A. R. Islam, “On the Extended Relationships Among EVM, BER and SNR as Performance Metrics,” in *2006 International Conference on Electrical and Computer Engineering*, 2006, no. December, pp. 408–411.; doi: 10.1109/ICECE.2006.355657

[126] I. Fatadin, “Estimation of BER from Error Vector Magnitude for Optical Coherent Systems,” *Photonics*, vol. 3, no. 2, p. 21, Apr. 2016.; doi: 10.3390/photonics3020021

[127] Freeman, R. L. “Forward Error Correction,” Book Chapter in *Reference Manual for Telecommunications Engineering*, R. L. Freeman (Ed.); doi:10.1002/0471208051.fre023

[128] https://literature.cdn.keysight.com/litweb/pdf/5989-0697EN.pdf?id=473817 last access: 11/04/2019

[129] C. Haffner et al, “All-plasmonic Mach–Zehnder modulator enabling optical high-speed communication at the microscale,” *Nature Photonics*, vol. 9, no. 8, pp. 525–528, Aug. 2015.; doi: 10.1038/nphoton.2015.127

[130] S. K. Yong and C.-C. Chong, “An Overview of Multigigabit Wireless through Millimeter Wave Technology: Potentials and Technical Challenges,” *EURASIP J. Wirel. Commun. Netw.*, vol. 2007, pp. 1–10, 2007.; doi: 10.1155/2007/78907

# Publications

## International conference

[1] R. Horváth, J-F. Roux, J. L. Coutaz, J. Poëtte, B. Cabon and C. Graham, "Ultrafast InGaAs photoswitch for RF signal processing," *2017 International Conference on Optical Network Design and Modeling (ONDM)*, Budapest, 2017, pp. 1-5.; doi: 10.23919/ONDM.2017.7958541

[2] R. Horváth, J-F. Roux, J. Poëtte and B. Cabon, "Optoelectronic mixing with photoconductive switch and semiconductor mode-locked laser," *2018 11th International Symposium on Communication Systems, Networks & Digital Signal Processing (CSNDSP)*, Budapest, Hungary, 2018, pp. 1-3.; doi: 10.1109/CSNDSP.2018.8471845

[3] R. Horváth, N. Arab, J. Poëtte, J.-F. Roux, L. Bastard, and B. Cabon, “High bandwidth photoswitch for heterodyne detection of optically generated mm W signals using 1.5 μ m integrated glass lasers,” in *2018 International Topical Meeting on Microwave Photonics (MWP)*, 2018, pp. 1–4.; doi: 10.1109/MWP.2018.8552862

## French national conference

[4] R. Horváth, J-F. Roux, J. Poëtte and B. Cabon, "Photoconductive devices for the optoelectronic mixing of signals with mode-locked lasers: application for QPSK signal demodulation”, *Journée du Club Optique, Micro-ondes*, 2018 Toulouse

## Journal Publications

[5] R. Horváth, J-F. Roux, J-L. Coutaz and J. Poëtte, *“*Characterization of ultrafast InGaAs photoconductors and their application to signal processing in radio-over-fiber telecommunications*,” Lithuanian Journal of Physics.* 2018. Vol. 58 No. 1.; doi: 10.3952/physics.v58i1.3654

[6] Róbert Horváth, Jean-François Roux, Julien Poëtte and Béatrice Cabon, "Optoelectronic mixer with photoconductive switch for 1550 nm wavelengths", *Infocommunications Journal*, Vol. X, No 4, Dec. 2018, pp. 16-21.

# APPENDIX

## APPENDIX A : Numerical model of the photoswitch

In Chapters I, II and IV we are presenting simulation results of the photoswitch behaviour. This Appendix is detailing the used numerical model and its features. The model is a fitted model, where the variables were adjusted to the results of the different experiments: optoelectronic autocorrelation, I-V curves, mixing with MLL signal and heterodyned DFB lasers. The electron and hole lifetimes and mobilities can be verified from these simulation results. The simulation tool is a Matlab script and it was developed in-lab by *Jean-François Roux* [1].

The calculation is based on the semiconductor equations detailed in Chapter I, section I/1.1. The 4 equations of (1)-(4) (*Equations (13)-(16) in I/1.1.*) are describing the dynamic behaviour of the switch and TABLE 13 is detailing the different symbols.

$$\frac{\partial N(\mathbf{r},t)}{\partial t} = G(\mathbf{r},t) - \frac{N(\mathbf{r},t)}{\tau_N} \tag{1}$$

$$\frac{\partial P(\mathbf{r},t)}{\partial t} = G(\mathbf{r},t) - \frac{P(\mathbf{r},t)}{\tau_P} \tag{2}$$

$$\begin{aligned} I(t) &= \iint_S \vec{J}_{Total}\, dS = \left[\vec{J}_N(\mathbf{r},t) + \vec{J}_P(\mathbf{r},t)\right]\frac{W}{\alpha} \\ &= q[\mu_N N(\mathbf{r},t) + \mu_P P(\mathbf{r},t)]\frac{V(t)}{L}\frac{W}{\alpha} = \sigma(t)\frac{V(t)}{L}\frac{W}{\alpha} \end{aligned} \tag{3}$$

$$R(t) = \frac{V(t)}{I(t)} = \frac{\alpha L}{W\sigma(t)} \tag{4}$$

TABLE 13 SYMBOLS OF EQUATIONS (1)-(4)

| | | | | |
|---|---|---|---|---|
| $N(\mathbf{r},t)$ | Electron concentration | | $P(\mathbf{r},t)$ | Hole concentration |
| $G(\mathbf{r},t)$ | Electron-hole pair photogeneration rate | | $q$ | Electron charge |
| $\tau_P$ | Hole lifetime | | $\tau_N$ | Electron lifetime |
| $J_P$ | Hole current density | | $J_N$ | Electron current density |
| $\mu_N$ | Electron mobility | | $\mu_P$ | Hole mobility |
| $W$ | Switch width | | $L$ | Switch length |
| $V(t)$ | Switch input signal | | $1/\alpha$ | Photon penetration depth |
| $R(t)$ | Switch resistance | | $I(t)$ | Switch current |
| $\sigma(t)$ | Switch conductivity | | | |

The model is also taking into account the illuminated area of the photoswitch while calculating the electron and hole concentrations in order to precisely simulate the number of generated carriers. It is supposed that a round spot is illuminating almost the whole area of the switch, and the electrodes are shading 44 % of the area in a case of a type 3:3 switch. The simulation input values for $\tau_N$ and $\tau_P$ lifetimes are the ones we measured in *II/3.4.e*: $\tau_N = 1.2$ ps, $\tau_P = 20$ ps. The electron mobility is set to the value reported by Chris Graham [2]: $\mu_N = 6900$ cm$^2$/V/s. The hole mobility is set to $\mu_P = 450$ cm$^2$/V/s, this value is not known by measurement, however a good fit was obtained with this value.

To simulate the switch output signal with different inputs (bias voltage or RF signal) we placed the switch equivalent circuit in the electrical model illustrated in Figure 1. The $V_e$ source provides the input signal, $V_{switch}(t)$ (noted as $V(t)$ in Eq. (3)-(4)) is the voltage across the photoswitch which causes the current *i(t)* flowing through it. The switch output signal is analysed on the $R_L$ load resistance. The switch resistance *R(t)* is dependent on the illumination through the carrier concentrations, as it is defined in equation (1)-(4). $V_e$ can be a constant bias voltage in case of the switch temporal response simulation, or a continuous wave RF signal while simulating the mixing experiment.

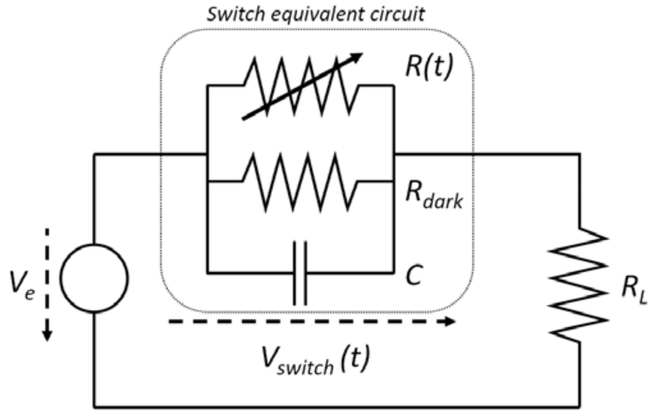

*Figure 1*
*Electrical circuit representation of the simulation model.*

$V_{switch}$ voltage is used to estimate the electrical DC field accelerating the photogenerated carriers. Using Kirchhoff's circuit law, we can write equation (5).

$$C\frac{\partial V_{switch}(t)}{\partial t} + \frac{V_{switch}(t)}{R_{eq}} = (V_e - V_{switch}(t))\frac{1}{R_L} \tag{5}$$

Where $R_{eq}$ is the equivalent resistance of the two resistance in the switch equivalent circuit, defined in equation (6).

$$R_{eq} = \frac{R_L * R(t)}{R_L + R(t)} \tag{6}$$

After calculating $V_{switch}$, the *i(t)* current can be calculated with equation (7).

$$i(t) = \frac{V_e - V_{switch}(t)}{R_L} \tag{7}$$

Starting from the RF electrical measurements done in Chapter II, the switch resistance and capacitance are defined for a type 3:3 switch: $R_{dark}$ = 2.3 kΩ , C = 7.5 fF. During the simulation, first the generated carrier concentration is calculated which is generated by the illumination. The illumination can be set as pulsed or continuous wave. At first, we simulated the pulse response of the switch, the parameters are set as the used femtosecond pulse during the characterisation in Chapter II, meaning a 100 fs pulse ($\tau_{pulsewidth}$) with 100 MHz repetition rate ($f_{laser}$), the average optical power is set at 1 mW ($P_{opt}$). The switch bias is $V_e$ = 1 V DC and a gaussian pulse is used. This illumination gives a generation rate of *G(t)* defined with Eq. (8)-(9).

$$G(t) = G_0 e^{-\left(\frac{t}{\tau_{pulsewidth}}\right)^2} \tag{8}$$

$$G_0 = \frac{P_{opt}}{\frac{hc}{\lambda} * f_{laser} * \tau_{pulsewidth} * \sqrt{\frac{\pi}{2}}} * \frac{1}{L * W * \frac{1}{\alpha}} \tag{9}$$

The carrier concentrations *N(t)* and *P(t)* can be calculated with the help of the above two and equations (1)-(2). Figure 2 shows the carrier concentration change in time after the optical pulse illuminates the switch at a time offset of 2 ps. The different lifetimes of the holes and electrons can be observed on the curves.

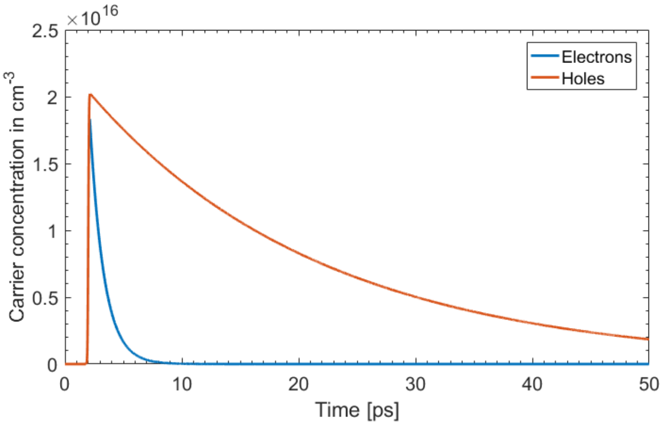

*Figure 2*
*Simulated electron (blue) and hole (orange) concentrations after illuminating the switch a 100 fs optical pulse.*

This carrier concentration change induces a drop in the switch resistance (or a jump in the conductance), it is illustrated in Figure 3 with the laser pulse.

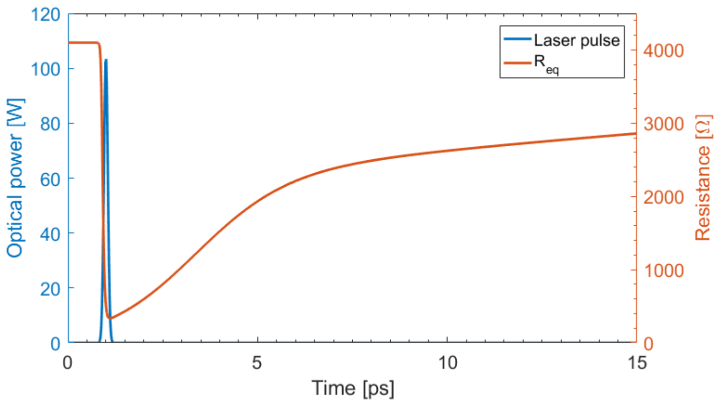

*Figure 3*
*Simulated resistance response (orange) after the optical pulse (blue) illuminates the switch.*

In the simulation the contributions of the holes and electrons are weighted thanks to the different mobilities (see below), as it was observed from our experiment in II/3.4.e. The resistance drop also results in a voltage drop on the switch, as seen in Figure 4 with blue curve, the orange curve shows the voltage at the circuit output on $R_L$.

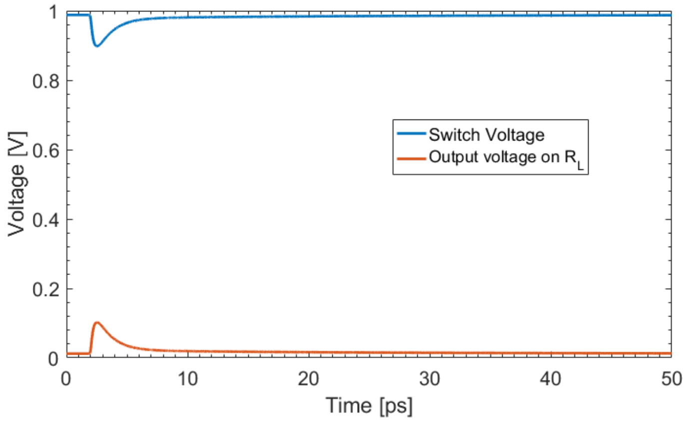

*Figure 4*
*Simulated voltage change on the switch (blue) and the load resistance(orange).*

And finally, the switch current is illustrated in Figure 5, as it is also seen in Figure 1-6 in Chapter I.

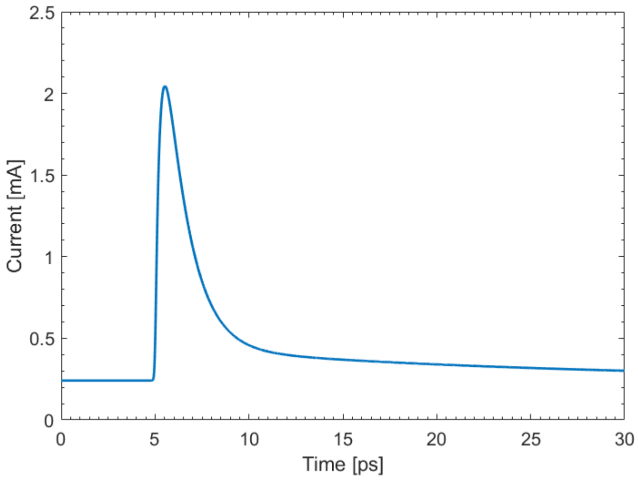

*Figure 5*
*Simulated switch current peak after optical pulse illumination of the switch.*

The autocorrelation signal resulted from the temporal response measurement (*section II/3.4*) is also simulated with the Matlab script, the result is shown in Figure 2-30 in Chapter II. The simulation is following the measurement principle: the output switch current was calculated step-by-step while adjusting the delay between the two optical pulses illuminating the photoswitch. The experimental result of the optoelectronic autocorrelation was numerically fitted by two exponential decaying function with 1.2 ps and 20 ps time constant. We assume that the fastest response is due to the electrons and the slowest to holes. So, fitting the experimental autocorrelation curve with the simulated curve obtained with the above physical model allow us to determine the electron carrier lifetime (1.2 ps) and the hole carrier lifetime (20 ps). From that fit, we also weighted the response of both carrier type which depends onto their respective mobilities: the relative weight of the mobilities was found to be in the ratio $\mu_N/\mu_P = 15$. The simulation curve is shown in Figure 6 together with the numerical fit that was obtained from the experiment (see Figure 2-37).

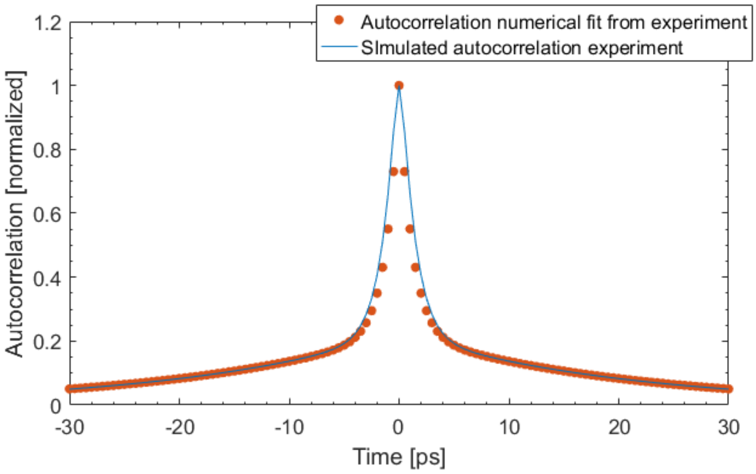

*Figure 6*
*Simulated autocorrelation experiment (M) and numerical fit from the experiment (A) (see Figure 2-37).*

Starting from this knowledge of the photogenerated carrier lifetimes, we are now able to estimate the conversion efficiency of the photoswitch, either in the case where the device is basically used as a photodetector (i.e. it is DC biased and illuminated by a CW laser beam) either in the case it is used as an optoelectronic mixer.

For a photodetector, dark current and CW responsivity are basics parameters. We know from the measurements (see Chapter II and reference [2]) that under a 1 volt DC bias, the dark current is in between 245 µA [2] and 65 µA (our measurements) and that the responsivity is in between 2.2 µA/mW and 3.2 µA/mW depending on the device. Starting from the model described above, the dark current is depending on the dark resistance and the responsivity rely on the geometry of the photoswitch, the mobility and lifetimes of the photogenerated carriers.

A first try of the simulation based on the parameters values given in TABLE 14 with the carrier mobilities extracted from [2] and a dark resistance of 4 kΩ [2] led to the correct dark current (240 µA). However, the calculated sensitivity was found to be ten times larger (24 µA/mW) than the measured one. A similar discrepancy was observed for the simulation of the mixing experiment. These results led us to reconsider the limitation of our model.

A first assumption that we have made is that the model is a linear model which assumes that the mobility is constant for any DC biasing field and also that the electrodes contacts act as Ohmic contacts. Other assumption is that every generated electrons and holes are contributing to the current: it is not taken into account that if they don’t reach the electrode they do not contribute to the current. A theory was proposed by *N. T. Yardimci and M. Jarrahi* [3], which explains the low efficiency of the photoconductive devices by the effect that not all the generated carriers reach the electrodes before being trapped, therefore not all are contributing to the current. Only the electrons in a few hundred nanometres distance to the electrodes are contributing to the current. So, in order to take this feature into account without modifying the overall physics of the model, we decided to “artificially” reduce the efficiency of the device. This has been done by lowering the mobility of the carriers. We could also have decided to reduce the actual number of generated carriers. This theory could explain, that for the accurate modelling of the results, also the previous temporal response measurement, Finally, a tenfold lower mobility had to be used for the electrons and holes than the one reported in [2]: the original mobility of $\mu_N$ = 6900 cm$^2$/V/s had to be reduced to 600 cm$^2$/V/s, and also the original $\mu_P$ = 450 cm$^2$/V/s is reduced to 45 cm$^2$/V/s. With these mobility values, given in TABLE 14, the simulation shows better accuracy for the mixing experiments and we were able to obtain a CW responsivity of 2.24 µA/mW. The true nature of the low switch efficiency is not confirmed by the measurements or the simulations

*TABLE 14 USED PARAMETERS IN THE SIMULATION*

| | | | |
|---|---|---|---|
| $W$ | 25 µm | $L$ | 25 µm |
| $\alpha$ | 1/12400 cm | $V_e$ | 1 V |
| $\tau_N$ | 1.2 ps | $\tau_P$ | 20 ps |
| *Original carrier mobilities [2]* | | | |
| $\mu_N$ | 6900 cm$^2$/V/s | $\mu_P$ | 450 cm$^2$/V/s |
| *Mobilities used for an accurate fit of the model* | | | |
| $\mu_N$ | 600 cm$^2$/V/s | $\mu_P$ | 45 cm$^2$/V/s |

Finally, we conclude this simulation approach by modelling the mixing experiment done in Chapter IV for the demodulation of data streams. Here, the optical signal is either optical pulses as in case of the MLL source, or the beating signal of two CW laser source. Simulations with the original mobilities [2], in case the optical signal is provided by the MLL (*see section IV/1.2.b),* shows a conversion loss of 54 dB, which is 22 dB lower compared to the "reduced" mobility where the loss is 76 dB in good accordance with the experimentation. Reducing the optical power to its tenth, 0.5 mW instead of 5 mW, while keeping the original mobilities, results in the same difference of conversion loss. The physics behind of the switch properties needs to be investigated deeply to be able to explain and model the behaviour with confidence.

In both mixing simulation cases, the Matlab script introduced the optical illumination code in the equation of the carrier concentration change by the time. In case of the MLL source, the following code is calculating the concentration change of electrons (`dn1dt`) and holes (`dp1dt`) for the current time step, which are added to the previous values (`n1, d1`). The equations are representing a gaussian pulse, which is repeated in every ~40.7 ps, corresponding to the 24.55 GHz repetition rate of the MLL.

```
dn1dt = Nmax*exp(-2*((time_forpulse-tpump)/pumpwidth)^2)-n1/taue1;
dp1dt = Pmax*exp(-2*((time_forpulse-tpump)/pumpwidth)^2)-p1/taup0;

n1=n1+dn1dt*dt;
p1=p1+dp1dt*dt;
```

The photoswitch resistance change by time with this pulsed illumination is illustrated in Figure 7.

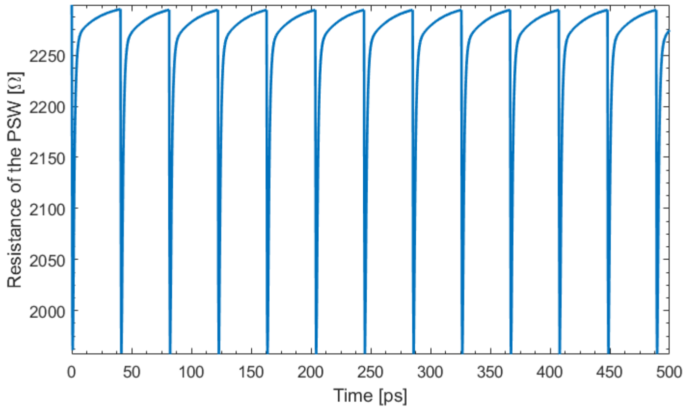

*Figure 7*
*Simulated resistance change of the photoswitch with a pulsed illumination source*

The simulated input and output signal in the frequency domain is illustrated in Figure 8. The input RF signal has 0 dBm power and a frequency of 30 GHz.

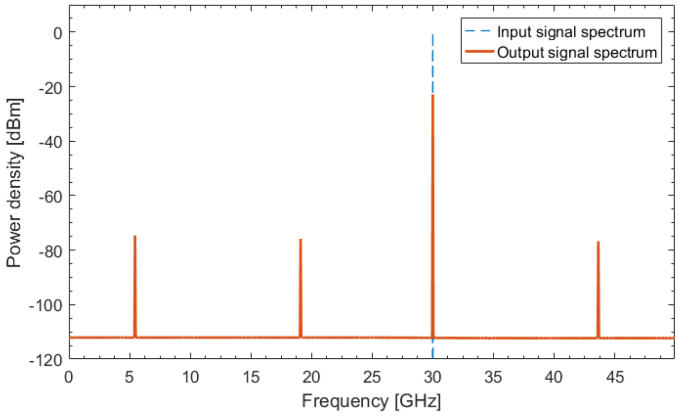

*Figure 8*
*Spectrum of the simulated switch output (orange) and input (blue) signals for mixing with the MLL as LO source.*

We can observe the mixing products at $f_{RF} - m*f_{LO}$, and the feedthrough signal too at 30 GHz.

The mixing simulation with heterodyned CW laser sources showed the same effects as in case of the MLL (*see section IV/1.3.b*). The simulated conversion loss was 66 dB, which is in the same order as the measurement. This value was obtained with the decreased carrier mobilities, with the original higher ones, the conversion loss is 46 dB. In this case the carrier concentration code in the Matlab script was the following:

```
    dn1dt = Nmax*(1+mopt*sin(2*pi*Fbeat*(time-tpump)))-n1/taue1;
    dp1dt = Pmax*(1+mopt*sin(2*pi*Fbeat*(time-tpump)))-p1/taup0;

  n1=n1+dn1dt*dt;
  p1=p1+dp1dt*dt;
```

Where `Fbeat` is the beating frequency of the two lasers, in our case we set it at 35 GHz, and the optical power is 15.5 mW (11.9 dBm). The resistance change of the photoswitch is illustrated in Figure 9. The simulated input and output of the switch in the frequency domain is illustrated in Figure 10. The input RF signal has a frequency of 20 GHz in this case, the two smaller peaks in Figure 10 are the mixing products at $f_{RF} \pm *f_{LO}$.

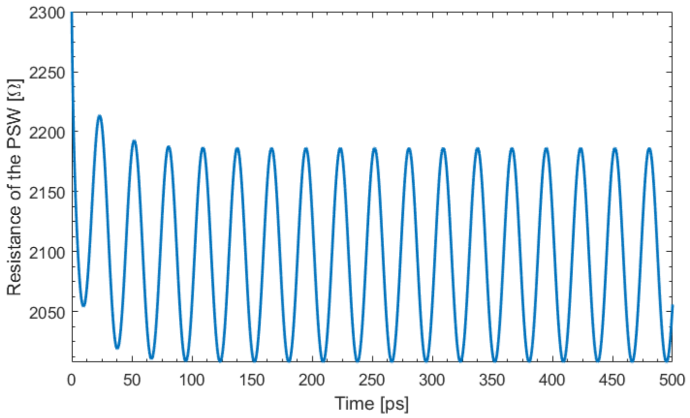

Figure 9
Simulated resistance change of the photoswitch with heterodyned CW laser illumination

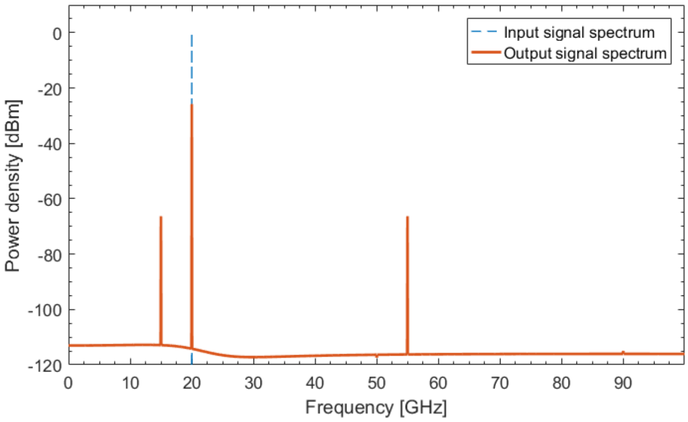

Figure 10
Simulated spectrum of the switch input (blue) and output (orange) with optical beating as a LO

## Appendix A References

[1] J. F. Roux, “Dispositifs à semi-conducteurs rapides pour la génération et la détection de signaux électriques GHz-THz,” *Habilitation à diriger des recherches*, Université de Savoie, 2010.

[2] C. Graham, R. Gwilliam, and A. Seeds, "Nitrogen ion implanted InP based photo-switch," *Optics Express*, 20, 26696-26703 (2012). doi: 10.1364/OE.20.026696

[3] N. T. Yardimci and M. Jarrahi, “Nanostructure-Enhanced Photoconductive Terahertz Emission and Detection,” *Small*, vol. 14, no. 44, p. 1802437, Nov. 2018.; doi: 10.1002/smll.201802437

# APPENDIX B : Chromatic dispersion in optical fibres

In optical fibres the propagating light suffers from dispersion effects. There are two main types, the chromatic dispersion and mode dispersion. The latter is present in multi-mode fibres, where several optical modes can propagate at the same time, in this work we are using only single mode fibres, so the mode dispersion is not present. Chromatic dispersion causes the ultra-short optical pulse to broaden through three effects: waveguide dispersion, material dispersion and polarization dispersion. The femtosecond laser has a linear polarization at its output, therefore we are not considering the effects of polarization dispersion as the polarisation dispersion of a 2 meters fibre is considered to be negligible. The other two dispersion have to be considered in order to compensate for the pulse widening. They are caused by the frequency dependence of the fibre material's refractive index. These two effects define the *D* dispersion parameter, giving the pulse broadening in time for a given propagation length and optical bandwidth, measured in [ *ps / (nm * km*) ]. This parameter is used commonly in fibre optics.

The D parameter is related to the β propagation constant [1], expanding this constant into Taylor series we get the following:

$$\beta(\omega) = \beta_0 + \beta_1(\omega - \omega_0) + \frac{1}{2}\beta_2(\omega - \omega_0)^2 + \cdots \tag{1}$$

Where $\omega$ is the angular frequency $2\pi f$, and $\beta_m$ are the derivatives of order $m$ of the propagation constant:

$$\beta_m = \left(\frac{d^m\beta}{d\omega^m}\right)_{\omega=\omega_0} \quad m = 1,2 \ldots \tag{2}$$

$\beta_1$ and $\beta_2$ are related to the refractive index of the material ($n$)

$$\beta_1 = \frac{1}{v_g} = \frac{n_g}{c} = \frac{1}{c}\left(n + \omega\frac{dn}{d\omega}\right) \tag{3}$$

$$\beta_2 = \frac{d}{d\omega}\beta_1 = \frac{d}{d\omega}\left(\frac{1}{v_g}\right) = \frac{1}{c}\left(2\frac{dn}{d\omega} + \omega\frac{d^2n}{d\omega^2}\right) \tag{4}$$

Where $c$ is the speed of light, $n_g$ is the group index and $v_g$ is the group velocity. The $\beta_2$ is called the group velocity dispersion (GVD), the second order dispersion, this causes the pulse broadening. It is measured in [$ps^2/km$]. Higher order dispersions like $\beta_3$, the third order dispersion (TOD) also have an effect on ultra-short pulses, their effect is considerable at $\lambda_d$, at the zero-dispersion wavelength. This wavelength is around 1.3 µm and $\beta_2$ is close to zero for the conventional SMF-28 fibre. We are working in the 1.5 µm wavelength range, therefore we are not taking into account the TOD. The dispersion parameter D is related to $\beta_1$ and $\beta_2$:

$$D = \frac{d\beta_1}{d\lambda} = -\frac{2\pi c}{\lambda^2}\beta_2 = -\frac{2\pi c}{\lambda^2}\frac{d}{d\omega}\left(\frac{1}{v_g}\right) = -\frac{2\pi}{\lambda^2}\left(2\frac{dn}{d\omega} + \omega\frac{d^2n}{d\omega^2}\right) \qquad (5)$$
$$or\ D = D_M + D_W$$

$D_M$ ad $D_W$ are the material and waveguide dispersion respectively. Figure 11 shows the contributions of these two dispersions.

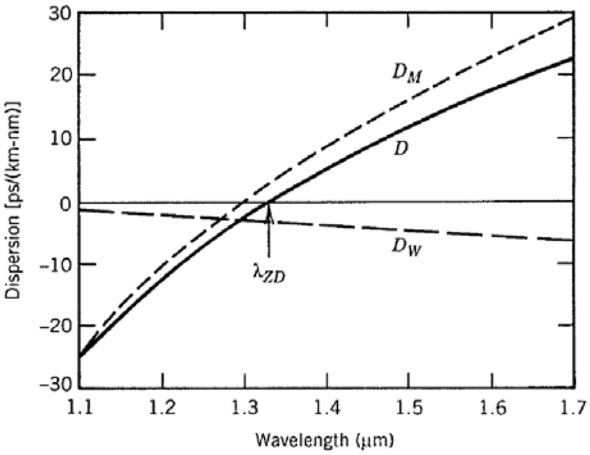

Figure 11
Waveguide and material dispersion curves for conventional fibre. Source: [1]

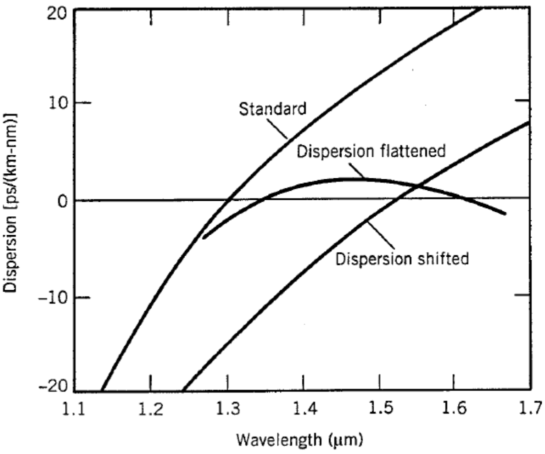

Figure 12
Different dispersion dependence of standard, dispersion flattened, and dispersion shifted fibres. Source: [1]

The waveguide dispersion component is dependent on the fibre-design: the core radius (*a*) and the core-cladding index difference (*Δ*). Changing these properties, the dispersion curve can be shifted to make zero-dispersion fibre at 1.55 µm. Shifting the zero-dispersion point even more, beyond 1.6 µm or more, the $\beta_2$ will have a large positive value. These fibres are called dispersion compensating fibres (DCF). Figure 12 shows usual dispersion curves for dispersion shifted fibres.

## Appendix B References

[1] Govind P. Agrawal, “Fibre Optic Communication Systems,” John Wiley & Sons, Inc., ISBN: 0-471-22114-7

# APPENDIX C : Chromatic dispersion measurement and compensation

## a. Theoretical calculation

Usual dispersion value for standard SMF-28 optical fibre is around 18 ps/(nm*km) at 1.55 µm. In our setup we are using a laser with a wide optical bandwidth (~70 nm) and 3 meters of fibre to guide the laser signal to the photoswitch. Due to this huge bandwidth the femtosecond pulse (~90 fs) from the laser can broaden to picoseconds after a short propagation in standard optical fibre. A theoretical broadening can be calculated for different propagation lengths with the help of the dispersion parameter, TABLE 15 contains the theoretical pulse widths after propagating through different length of fibre, starting from a laser pulse of 90 fs duration:

$$\Delta\tau(ps) = D(ps/(nm * km)) * L(km) * B(\mathrm{nm}) \tag{1}$$

$B = 70\ nm$

$D = 18\ ps/(nm*km)$

$T_{pulse,initial} = 90\ fs$

*TABLE 15 CALCULATED DISPERSED PULSEWIDTH AFTER FIBRE PROPAGATION*

| $L_{fibre}$ | 0.5 m | 1 m | 2 m | 3 m | 4 m | 5 m |
|---|---|---|---|---|---|---|
| $T_{pulse,L}$ [ps] | 0.83 | 1.42 | 2.69 | 4.03 | 5.37 | 6.4 |

## b. Optical autocorrelation setup for laser pulsewidth measurement

We performed an experiment to validate this theory. An optical autocorrelation setup was built with a BBO non-linear crystal to generate the second-harmonic of the pulse. The setup is illustrated in Figure 13, we used a similar setup to measure the photoswitch response (see Chapter II). The free-space output of the femtosecond laser was coupled into an optical fibre, in the experiment we varied the length of this fibre, and then we coupled the laser into free-space again with a collimator. Before coupling the laser beam into the fibre, we used an optical chopper to add a low frequency (500 Hz - 2 kHz) ON-OFF modulation to the beam. After the fibre the dispersed laser beam is split with a beam-splitter into two beams, one of the beam paths has a delay line with variable length. The two beams then joined with another beam splitter into two parallel beams directed into an optical lens to focus them into a beta barium borate (BBO) non-linear crystal. In the crystal a third beam is generated due to the second-harmonic generation (SHG) phenomena and it has a double frequency as the original signal. If the laser has a wavelength of 1550 nm (or a frequency of 193.4 THz) the generated pulse's wavelength is 775 nm (or the frequency is 386.8 THz). This third beam is directed to a photodiode and its electrical output is received by a Lock-In Amplifier (LIA).

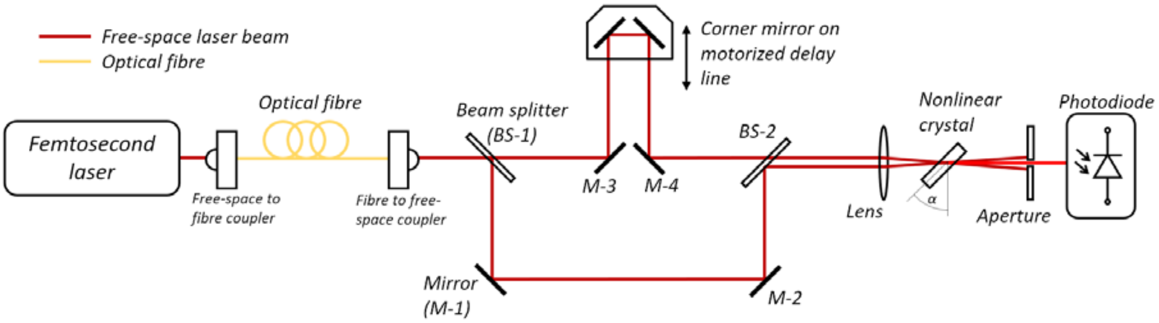

*Figure 13 Optical autocorrelation setup with second harmonic generation*

The LIA is locking on the optical chopper frequency and amplifies the signal only at this frequency. This frequency locking acts as a filtering in the frequency range, it can reduce the noise level and allows to measure very low signal levels. The output of the LIA is connected to a data-acquisition card (National Instruments USB-6221) and recorded with a PC which also controls the delay line position.

*SHG phenomena*

There are two types of SHG phenomena depending on the polarization of the beams. Type I SHG occurs when both of the beams have ordinary polarization relative to the crystal lattice. In case of Type II SHG, the beams have orthogonal polarization. In both cases the generated beam has extraordinary polarization. We used Type II SHG during the experiment. The delayed path had a polarization rotator, which forced a 90° rotation on the beam. The crystal is a birefringent medium, meaning that the refractive index depends on the direction of incidence and polarization. Also, like most of the materials there is a dependence in the refraction index by the wavelength. The incident and generated beams have to be phase-matched, this means that the refractive index of the medium “seen” by the IR beams have to be the same for the maximum intensity of the generated SHG signal so that the pump beams and the SHG generated beams travel at the same speed. An illustration of the connection between frequency, polarization and refractive index can be seen in Figure 14.

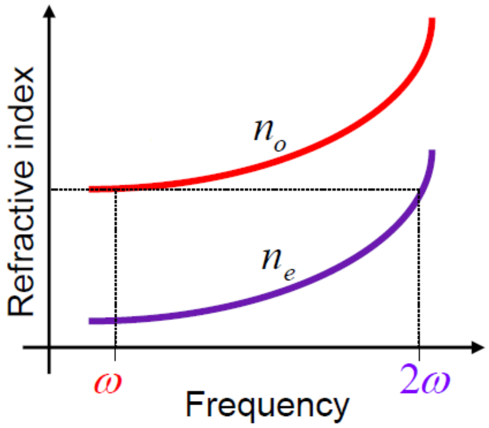

*Figure 14*
*Illustration if the refractive index dependence on frequency and polarization. Source: [1]*

The crystal lattice orientation is given by the manufacturer of the crystal. Rotating the crystal by an orthogonal axis to the crystal plane we can perform the phase matching. Figure 15 illustrates the phase matching degrees of BBO crystals for type I and II SHG. During the phase matching, we orientate the crystal lattice in a direction where the ordinary and extraordinary polarization has the same refractive index. This means that the original and the generated beams are travelling with the same speed inside the material and the generated photons added up constructively along the material length. As it can be seen in Figure 15, for type II SHG the phase matching degree is around 29° for 1550 nm wavelength.

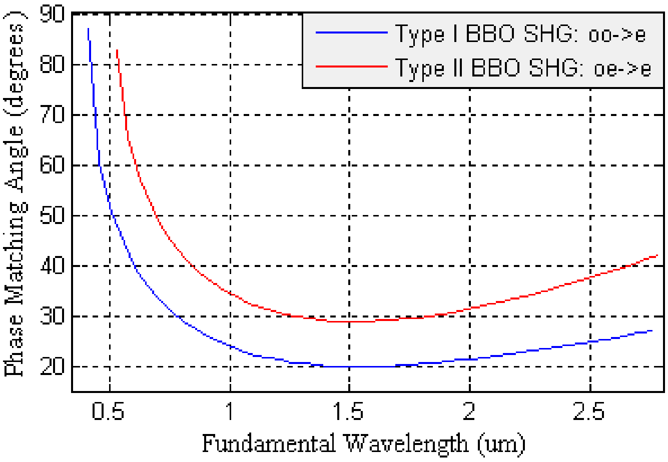

*Figure 15*
*Phase matching degrees of BBO type I and II SHG. Source: [2]*

The experiment was done with three BBO crystals with different thicknesses: 100 µm, 200 µm and 300 µm. The intensity of the generated beam is square-dependent on the thickness. In theory, the generated beam with the 200 µm thick crystal is four times higher than with the 100 µm crystal, and 9 times higher with the 300 µm crystal, our results have confirmed this.

*Measurement*

During one measurement we vary the delay line position around the zero-delay, the position where the two beams path have the same propagation time and mix together in the crystal. The second harmonic generation happens only when the two pulses are overlapping in time in the crystal. While they are moving closer to each other in time by adjusting the delay line, the third beam's intensity is increasing with each step due to a bigger part of the two pulses are overlapping. Therefore, the photodiode senses a higher signal intensity with each step. In this experiment we are measuring the intensity autocorrelation. The autocorrelation signal can be expressed with equation (2).

$$A^{(2)}(\tau) = \int_{-\infty}^{+\infty} I(t)I(t+\tau)\,dt \tag{2}$$

Where *I(t)* is the intensity of the pulse propagating in the fixed path, and *I(t+τ)* is the intensity of the pulse propagating in the delayed path. The number 2 in $A^{(2)}$ indicates that it is a second order function. The illustration in Figure 16 shows the positions of the two pulses for different points of the autocorrelation curve. The dark orange area is the overlap of the two curves, the third beam is generated in case of this overlap.

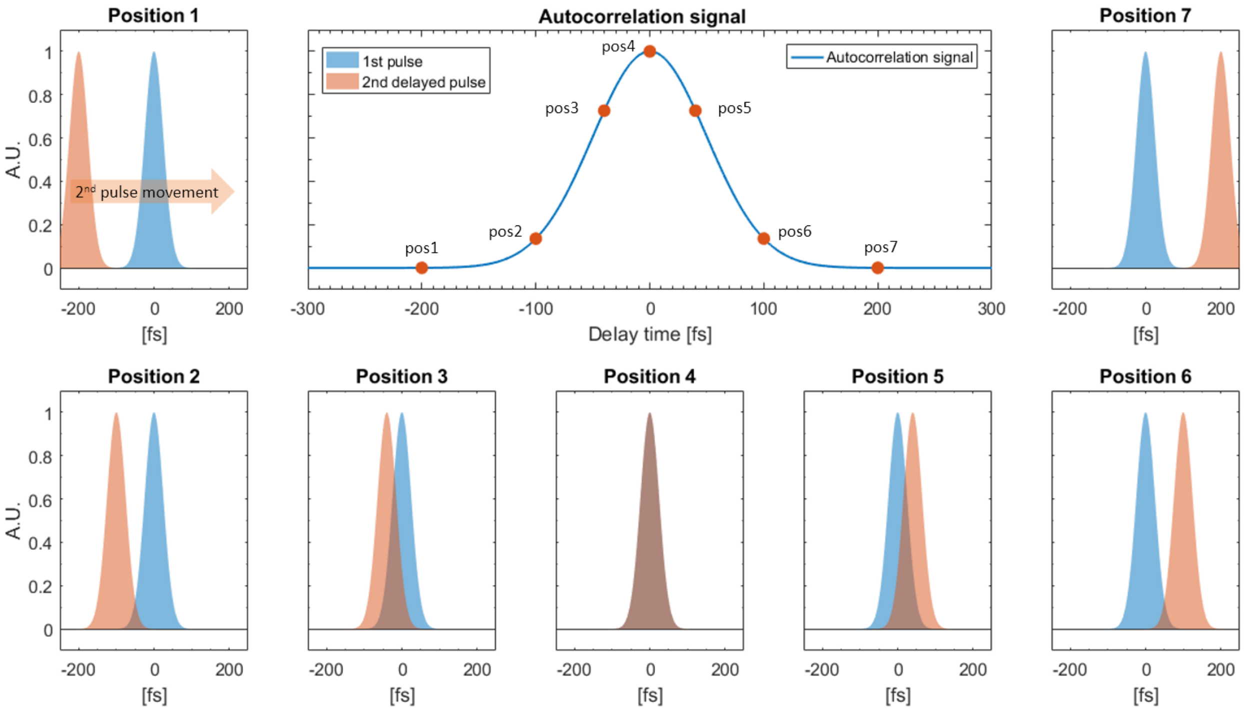

*Figure 16 Illustration of the autocorrelation signal between a fixed and delayed pulse shown in various positions*

The bigger the overlap is, the higher the average intensity of the third (SHG) beam, therefore the average output signal of the PD. Recording this signal (after the LIA) for each step we can draw the autocorrelation curve of the laser pulses. The software on the recorder PC is converting the movement of the delay line into a relative time delay, the temporal resolution of the measurement is limited by the delay line step resolution. The delay line is the same as it was used in Chapter II, if the delay line moves 1 µm, it means 2 µm change in the delayed beam path length (because of the corner mirror), this change translates to a delay time of Δt = 6.67 fs. The minimum step was 0.125 µm, which corresponds to 0.834 fs time delay. The obtained curves are intensity autocorrelation curves of the laser pulses, if we assume a Gaussian shaped laser pulse, which is a close approximation in this case, then the real pulse width is 0.707 ($1/\sqrt{2}$) times shorter than the measured width [3], this value is a conversion factor as the autocorrelation width is bigger than the real pulse.

## c. Measurement of dispersion in SMF-28 optical fibre

We measured the pulse shapes for several fibre lengths, the measured autocorrelation pulses are illustrated in Figure 17 and Figure 18 with amplitude normalized curves. The dark blue curve on both figures shows the autocorrelation of the original laser pulse.

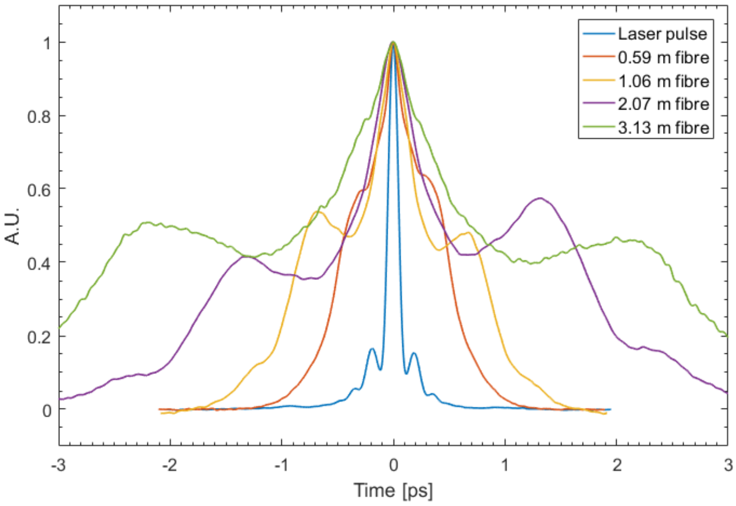

*Figure 17*
*Pulse broadening with different length of SMF-28 fibre (0.59m - 3.13m)*

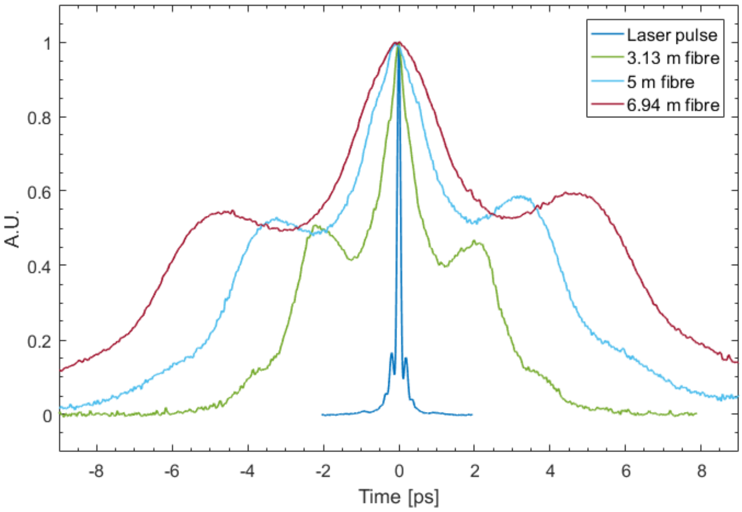

*Figure 18*
*Pulse broadening with different length of SMF-28 fibre (3.13m - 6.94m)*

A theoretical broadening was calculated for all the measured fibre lengths, the calculation was done assuming a gaussian pulse for sake of simplicity (despite the actual shape present some sidelobes) and with autocorrelated pulses (1/0.707 times the real width). Figure 19 shows the theoretical and measured pulsewidths. Measured pulsewidths are the 1/e autocorrelation widths, analyzing at this signal level is more useful for comparison as the FWHM, which cannot give precise values as the sidelobes of the pulses are around at half intensity. The theoretical values are calculated with a standard dispersion constant of D = 18 ps/(nm*km) and with 70 nm optical bandwidth of the laser pulses. The two curves have only a small difference, showing that the used SMF-28 fibres must have a dispersion constant close to the expected 18 ps/(nm*km) but not exactly that value, likely because of the various suppliers for the used fibres. Different suppliers are selling standard fibres with a dispersion around 16-18 ps/(nm*km).

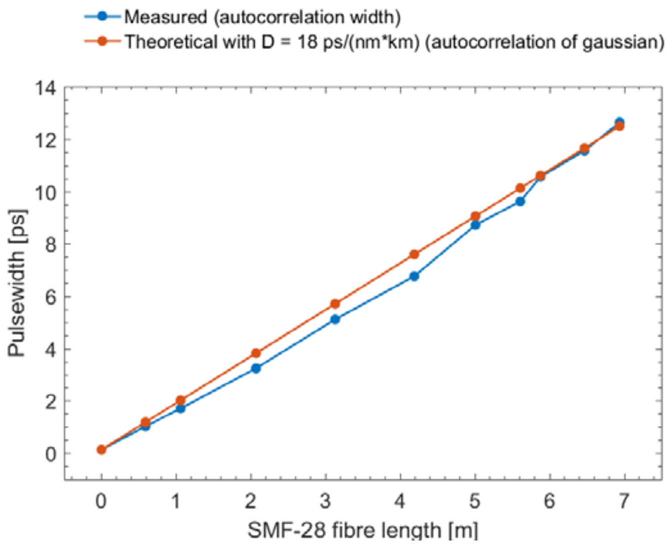

*Figure 19*
*Theoretical and measured 1/e pulsewidths for different length of fibre propagation*

*TABLE 16 MEASURED AND THEORETICAL DISPERSED PULSEWIDTH AFTER PROPAGATING IN SMF-28 FIBRE*

| Fibre length [m] | Measured width [ps] | Theoretical width [ps] |
|---|---|---|
| 0 | 0.128 | 0.128 |
| 0.59 | 1.018 | 1.178 |
| 1.06 | 1.705 | 2.016 |
| 2.07 | 3.24 | 3.816 |
| 3.13 | 5.11 | 5.705 |
| 4.19 | 6.76 | 7.594 |
| 5.01 | 8.72 | 9.056 |
| 5.61 | 9.62 | 10.125 |
| 5.88 | 10.56 | 10.606 |
| 6.47 | 11.56 | 11.658 |
| 6.94 | 12.64 | 12.496 |

## d. Measurement of dispersion compensation with DCF-38 optical fibre

In the experiment we observed that the pulse is broadening over 1 ps after propagation for 0.6 meters in an optical fibre. This broadened pulse is not practical for the temporal response measurement of the photoswitch, where we have to use pulsewidths as short as possible, preferably close to the original laser pulse width. For this purpose, we used a dispersion compensating fibre (DCF) to compress the broadened pulse. THORLABS was selling DCF fibre, specially fabricated to compensate the chromatic dispersion in SMF-28. Unfortunately, from October 2017 this product is no longer available anymore, an archive page can be found in their website with the fibre details: (last accessed 06/02/2019):

https://www.thorlabs.com/catalogpages/obsolete/2017/DCF38.pdf. Their DCF-38 fibre had a dispersion of -38 ps/(nm*km), and its dispersion slope was the opposite as for SMF-28 to achieve compensation in a broad wavelength range. This value of dispersion is suggesting that 1 metre of DCF fibre compensate for the dispersion of 2 metres of SMF-28 fibre. We check this feature experimentally.

In Figure 20 the blue curve is showing the pulse broadening inside 3.08 meters of the DCF fibre, as comparison the orange curve shows the broadening in SMF-28 fibre. We can see that a higher dispersion results in a broader pulse.

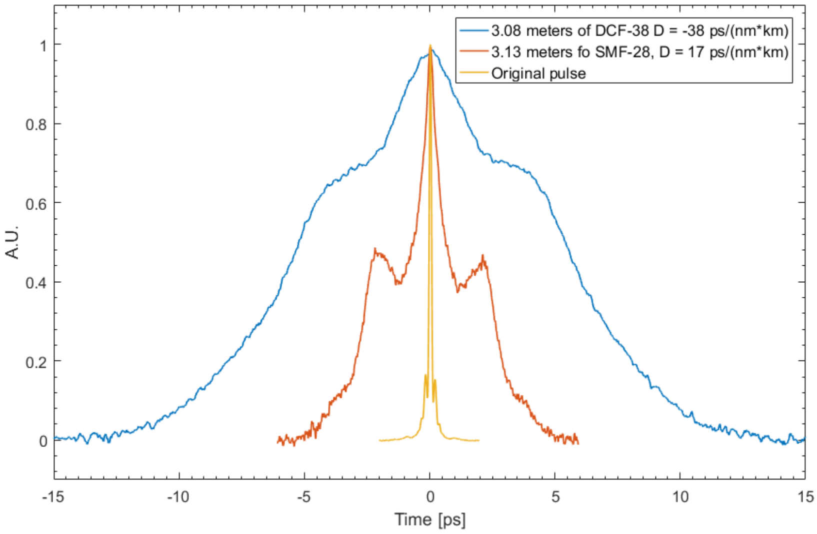

*Figure 20*
*pulse shapes after propagating in different dispersive fibres*

The pulse width after the highly dispersive DCF-38 became 8.85 ps (1/e bandwidth, assuming Gaussian pulse), while after SMF-28 it is 3.61ps. In the next experiment we determined the ratio of DCF and SMF fibre length needed to fully compensate the dispersion by connecting different lengths of SMF-28 to the 3.08 meter long DCF fibre. Figure 21 and Figure 22 are showing the results for a broad range of SMF lengths. It can be observed that by reducing the SMF-28 length from 9.6 meters, the pulsewidth is also reducing until 6 meters, then it starts to increase again. This suggests that the optimal ratio is close to 1:2, meaning that 1 meter of DCF can compensate the dispersion of 2 meters of SMF. Varying the length, we found a range of 30 centimetres between 5.88 meters and 6.21 meters, where the compensated pulsewidth is the same, close to the original width. In Figure 22, three options are illustrated around this optimum ratio of fibres.

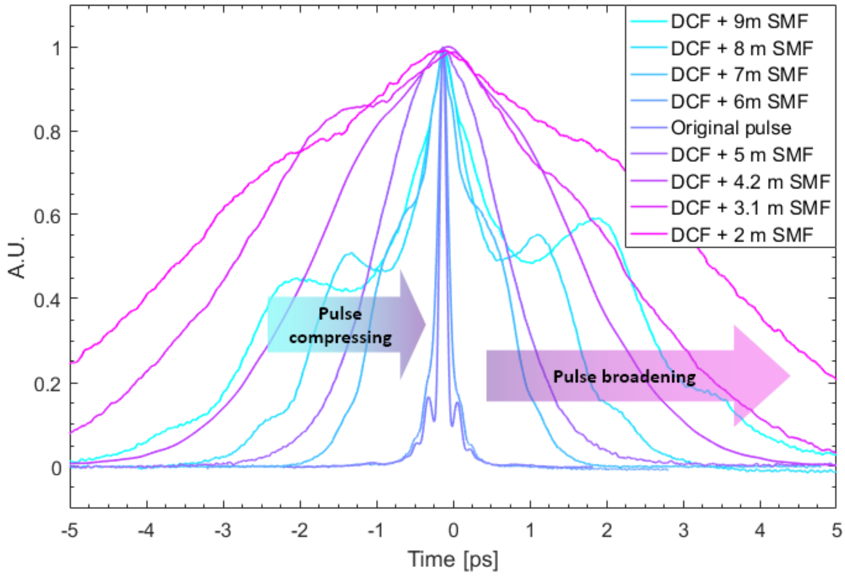

*Figure 21*
*Dispersion compensation with DCF and SMF fibre lengths of 9m - 2m*

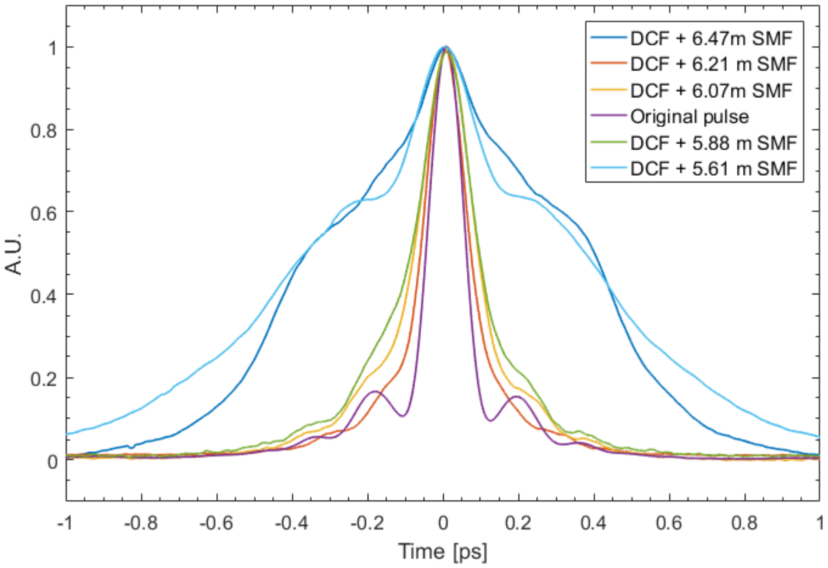

*Figure 22*
*Dispersion compensation with DCF and SMF fibre lengths of 6.47m - 5.61m*

Figure 23 and TABLE 17 details the measured pulsewidths (1/e, assumes Gaussian), with the calculated theoretical widths. The orange curve shows that the pulse is fully compressed in case of 6.47 meters of SMF-28, which equals to a DCF:SMF ratio of around 1:2.1. This difference can be explained by the variance of the dispersion constants, which can be slightly different from the datasheet. Calculating with a DCF dispersion of -36 ps/(nm*km), the optimum ratio agrees with the measurement. Which shows that the real dispersion of the fibre could be around this value.

In this experiment we determined the required ratio of SMF and DCF fibres to compress the dispersed laser pulse close to its original width. In the thesis, we cut the DCF fibre to its optimal length to compensate the dispersion almost totally. We use 1.53 meters DCF connected to 2.94 meters of SMF-28 fibre.

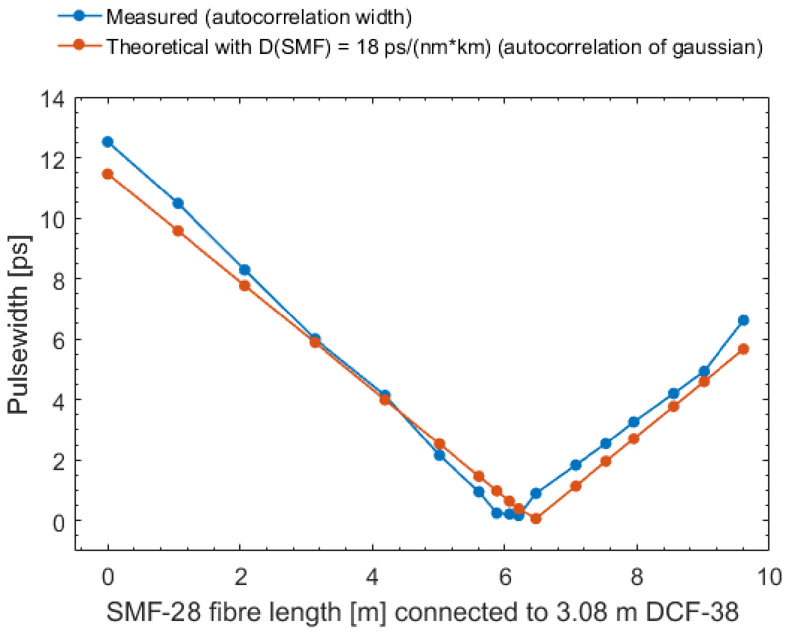

*Figure 23*
*Measured and theoretical pulsewidths for different lengths of SMF-28 fibre plus 3.08m DCF-38, D(SMF)=18, D(DCF)=-38*

*Table 17 Pulse widths with SMF-28 and DCF-38*

| SMF-28 length [m] | Measured width [ps] | Theoretical width [ps] |
|---|---|---|
| 0 | 12.52 | 11.460 |
| 1.06 | 10.48 | 9.571 |
| 2.07 | 8.29 | 7.771 |
| 3.13 | 6 | 5.882 |
| 4.19 | 4.14 | 3.993 |
| 5.01 | 2.155 | 2.532 |
| 5.61 | 0.95 | 1.462 |
| 5.88 | 0.25 | 0.981 |
| 6.07 | 0.219 | 0.642 |
| 6.21 | 0.169 | 0.393 |
| 6.47 | 0.899 | 0.069 |
| 7.07 | 1.833 | 1.139 |
| 7.53 | 2.545 | 1.959 |
| 7.95 | 3.265 | 2.707 |
| 8.55 | 4.203 | 3.776 |
| 9.01 | 4.935 | 4.596 |
| 9.61 | 6.615 | 5.665 |

## Appendix C References

[1] Lecture Notes, North Illinois University, Course title: Advanced Optics, Online material: http://nicadd.niu.edu/~piot/phys_630/Lesson22.pdf; last accessed: 13/02/2019

[2] Online - http://www.pmoptics.com/beta_barium_borate.html,; last accessed: 13/02/2019

[3] Rüdiger Paschotta, “Field Guide to Laser Pulse Generation, ” SPIE Press Book, published 30 October 2008, ISBN: 978081947248